A miniaturised hybrid ion-atom chip trap and the non-equilibrium statistical mechanics of trapped ions

Inauguraldissertation

zur

Erlangung der Würde eines Doktors der Philosophie

vorgelegt der

Philosophisch-Naturwissenschaftlichen Fakultät

der Universität Basel

von

Ian James Rouse

aus Birmingham, United Kingdom

Basel, 2018

Genehmigt von der Philosophisch-Naturwissenschaftlichen Fakultät auf Antrag von

Prof. Dr. Stefan Willitsch und Prof. Dr. Philipp Treutlein

Basel, den 13.11.18

Prof. Dr. Martin Spiess
Dekan

Abstract

Experiments involving trapped ultracold matter are of great interest to a diverse range of fields, from spectroscopy and quantum computing to ultracold chemistry. Hybrid traps allowing for the simultaneous confinement of charged and uncharged matter extend the scope of these experiments, but have not yet benefited from the miniaturisation of the trapping architectures demonstrated for traps which only confine either ions or neutral particles. This miniaturisation greatly enhances the spatial resolution of the forces with which the trapped particles are manipulated, and this thesis details the design and fabrication of a prototype miniaturised hybrid trap to take advantage of this increased precision. The co-trapping of ions and neutral particles leads to multiple mechanisms by which the energy distributions of the trapped ions may deviate from thermal statistics, which have previously been treated largely empirically. In this thesis, these effects are explored numerically and analytically to provide a theoretical framework for this behaviour through the formalism of superstatistics. The results derived here explain the deviations from thermal statistics observed in precision spectroscopy experiments and resolve outstanding questions about both the mechanism by which ions acquire a non-thermal energy distribution during buffer gas cooling with neutral atoms and the analytical form of this distribution. This significantly improves the ability to correctly interpret the results of experiments, and is applicable not only to the hybrid chip trap developed here, but to hybrid ion-neutral traps in general.

Acknowledgements

I would like to thank my supervisors, Professor Stefan Willitsch and Professor Philipp Treutlein, for the opportunity to study here in Basel and their guidance in the work presented here. The past and present members of the Willitsch group provided great company both in and out of university. Without them the time here would have been much less enjoyable, and much less would have been achieved. The patience and hard work of the staff of the mechanical and electronic workshops — Grischa Martin, Philipp Knöpfel and Georg Holderied — in translating my crude sketches and vague requests into reality was greatly appreciated, as was the construction of lasers by Dr Anatoly Johnson and Dr Andreas Jöckel.

The construction of the surface-electrode ion trap took multiple rounds of design and trials of different techniques, and I am very grateful to Dr Nadeem Rizvi of Laser Micromachining Ltd., Armin Stumpp and Beat Lüscher of the Fachhochschule Nordwestschweiz, and Dr Yves Pétremand of the Swiss Center for Electronics and Microtechnology for all their assistance and patience during this process. I must also thank Dr Cezar Harabula for his assistance with wirebonding and Dr Roman Schmied for his input during the chip design.

Funding from the Swiss Nanoscience Institute for this project (P1214) is gratefully acknowledged, as is funding from the Swiss National Science Foundation as part of the National Centre of Competence in Research, Quantum Science, and Technology (NCCR-QSIT) and Grant No. 200020_175533.

Last but certainly not least, thanks to my friends and family for supporting me throughout my time in Basel and reminding me that there is life outside of university.

Contents

List of Figures

Chapter 1

Introduction

1.1 Cooling and trapping particles

Everyday matter consists of a vast number of particles. A litre of water, for example, contains on the order of 3×10^{25} molecules constantly colliding with each other and undergoing random thermal motion. Under these circumstances, it is essentially impossible to investigate the behaviour of a single particle, and instead this must be inferred from the properties of the entire ensemble. The situation would be greatly improved if, instead of the unmanageably large number of particles present under typical conditions, the size of the collection of atoms or molecules could be limited to a much smaller number, or even a single particle. At room temperature, a free particle moves with a typical velocity of hundreds of meters per second, plus or minus a few more hundred. To be able to accurately measure the properties of the particle, it is therefore necessary to both slow the particle down and to reduce this wide spread in the range of velocities. That is, the particle must be cooled to as low a temperature as possible. Since the particle cannot be stopped entirely, it is necessary to ensure that it remains in a narrow region

of space. A collision with the walls of a container would lead to the particle thermalising with the container and regaining the energy removed by cooling, and thus a method of remotely applying a confining force to the particle is required. Thus, we conclude that to be able to precisely study a particle, it is necessary for the particle to be both cooled and trapped.

The first issue that must be overcome is cooling the particle to a sufficiently low temperature. One route to do so is through the supersonic expansion, in which the expansion of particles forced through a nozzle into vacuum results in an overall cooling, but a high forward velocity [1]. The resulting packet of particles must then be decelerated through some other means, e.g, through the application of time-dependent electric or magnetic fields [2–4]. Alternatively, the technique of laser cooling can be used to cool particles if they have a suitable transition between quantum states which can be excited by laser light. In this method, a force is generated due to the transfer of momentum during the absorption and re-emission of photons by the particle [5, 6]. The rate at which the particle absorbs photons, and thus the force experienced by the particle, is modulated by the Doppler effect, and by tuning the frequency of the laser such that the particle absorbs more photons when it is travelling towards the laser than when it is travelling away a net cooling force is produced. The force exerted on the atom due to the absorption of a single photon is minute, and so to achieve a measurable result requires the scattering of a large number of photons. For this process to work efficiently, the particle must return to its original state after emitting a photon with a probability of close to unity, i.e., it must have a closed optical cycle. If it does not, then the particle may become trapped in a metastable state, requiring the use of additional lasers to close the optical cycle and reducing the efficiency of cooling [6]. Consequently, laser cooling has so far been demonstrated only for certain atoms and molecules, typically, atoms with a single valence electron or molecules with favourable vibrational structure [6–8]. However, when it can be employed, laser cooling enables the cooling of particles to temperatures

of less than a millikelvin. Moreover, in contrast to the supersonic expansion, laser cooling is a continuous process and so ensures that the sample of particles remains cold for an extended period of time, and does not require the use of a decelerator to produce a sample which is both cold and slow.

We next move on to the issue of preventing the escape of the particle. There are a wide variety of possible routes to do so. A tightly-focused laser detuned from the resonance of a transition can be used to generate a confining potential through the optical dipole force [6, 9]. The scattering of photons from a laser, meanwhile, cannot directly trap particles, but when combined with an inhomogenous magnetic field the result is the magneto-optical trap, which simultaneously cools and traps particles. Neutral atoms which are sufficiently cold and are in a suitable hyperfine quantum state can be directly confined in a purely magnetic trap [10]. If the particle has a non-zero charge, then it is possible to apply strong forces to the particle using electric fields, however, a static electric field alone is not sufficient to provide three-dimensional confinement as a consequence of Maxwell's equations. There are two widely-used solutions to this issue. By combining a static, quadrupolar electric potential with a magnetic field the result is the Penning trap [11]. Stable trapping is also possible using an electric field oscillating at frequencies on the order of megahertz, as first demonstrated in the Paul trap and later generalised to a family of radiofrequency ion traps [11, 12]. These radiofrequency ion traps, along with the magneto-optical and magnetic traps, are discussed in more depth in Chapter 2.

As a general rule, the magnetic field generated by a current-carrying wire or the electric field from an electrode held at a certain potential decays as a power of the distance from the element generating it, with the characteristic length scale of this decay proportional to the size of the device. At greater distances, the forces generated become weaker. Moreover, at these large distances, the fields from neighbouring wires or electrodes are no longer well-resolved, and it is no longer possible to precisely manipulate the trapped

particles by applying different currents or voltages to these elements. Conversely, if the particle is too close to the device, then the force from one particular element is much greater than from the rest, and again the ability to precisely control the particle is lost. There is therefore great interest in miniaturising the devices, as this enables fine control at a much closer distances which, in turn, allows for greater forces to be applied to the trapped particles. This has lead to the development of miniaturised forms of the magnetic traps used for neutral atoms and the radiofrequency traps used for charged particles, referred to as atom chips and ion chips respectively [13, 14]. These planar devices trap particles at distances of less than a millimeter from the surface of the trap, and as such are capable of applying large, precisely shaped forces to the ions or neutrals.

The trapping techniques mentioned above typically work only for a narrow class of particles. Magneto-optical traps rely on the presence of a closed optical cycle at a wavelength which can be addresed using lasers, and only recently has this technique been extended from atoms to some molecules [15, 16]. Magnetic traps require atoms to be prepared in a particular hyperfine state, and the Penning and Paul traps both capture only charged particles. In order to study the interactions between different types of particles it is therefore necessary to combine these different mechanisms into hybrid traps. This can be achieved by constructing a device which produces two different traps simultaneously. In many cases, these hybrid traps are a combination of a radiofrequency ion trap with some mechanism for trapping neutral particles, as demonstrated by numerous groups [17–21]. As both the ion trap and neutral magnetic traps can be miniaturised into chip-based architectures to increase the precision with which they manipulate trapped particles, it seems a natural extension to combine these together to produce a hybrid chip trap. Such a device would be a useful tool for ion-neutral experiments with a higher degree of control than is achievable in the macroscopic hybrid traps, and this thesis presents the design and construction of a prototype of a hybird ion-neutral chip trap.

1.2 Applications of cold trapped particles

Having established that it is indeed possible to trap particles at low temperatures, we now address the issue of why this is desirable. A single atom in vacuum offers a system for which the quantum-mechanical behaviour can be calculated to a very high level of accuracy, and an experimental realisation of this system offers the ability to confirm these calculations. Not only does this allow for the validation of the underlying theories and the investigation of any potential modifications to the standard model, e.g. fifth forces, but it also enables the measurement of physical constants such as the electron-to-nucleon mass ratio and the fine structure constant and the detection of any changes in these values [22, 23]. The isolation from the environment is invaluable for studies of antimatter which would otherwise rapidly annihilate [24, 25], and for ordinary matter this isolation enables quantum states to be sufficiently long-lived that they may be used as a building block for quantum computers [26, 27].

The next logical step is to introduce a second particle, which need not be of the same type as the first. Since both particles are confined to the same region of space, they will eventually reach the same location and undergo a collision. At high energies, the collisions between particles can usually be modelled as that of two hard spheres bouncing off each other like billiard balls, but at the low energies achievable under these circumstances this is no longer the case [28]. The interaction potential between the two particles can be mapped to a cross-sectional area describing the effective size of one particle from the perspective of the other, and so determining how likely it is for a collision to occur. Depending on the relative velocity between the two particles, this cross section may increase or decrease, resulting in a rate of collisions which is highly dependent on the collision energy and the underlying potential describing the interactions between the two particles. If a collision does occur, then a variety of outcomes are possible, ranging from a simple transfer of energy to a change in the state of the particles, all of which

have their own cross section. It therefore may be the case that collisions at a particular range of energies mostly lead to a transfer of energy, wheras at other energies a reaction between the two particles is more likely. The possibility for a reaction to occur at very low temperatures gives rise to the field of ultracold chemistry [29]. Consider, for example, a collision between a charged particle A^+ and an uncharged particle B. This may lead to either a simple exchange of momentum, or it may result in A capturing an electron from B. This charge exchange reaction $A^+ + B \rightarrow A + B^+$ is one of the most elementary chemical reactions, and in an ion-neutral hybrid trap can be studied under precisely controlled conditions [30, 31]. The cross section is not measured directly in an experiment, and it is instead the rate of reactions which is measured. This quantity is averaged over the entire range of collision energies present in the system, and therefore the resolution is improved by decreasing this range as far as possible, i.e., working with cold particles. The theoretical rate constant is calculated by averaging the cross section over the distribution of collision energies, and compared to the experimentally measured value to assess the accuracy of the theory [28]. More complex reactions can also be investigated under conditions which would not be feasible in a traditional beaker filled with chemicals, enabling, for example, the study of the reaction rates of different spin isomers of water [32], the formation of exotic metal oxides [33], and the conformer-dependent reactions of isolated organic compounds [34]. It is also possible to construct molecules directly from their component atoms via photoassociation or Feshbach resonance [35, 36], offering another route to the production of ultracold molecules of interest to spectroscopy and quantum computing, amongst other applications [37].

There is no reason why this should stop at only two particles. For large ensembles of particles at the low energies considered here, states of matter occur which would not otherwise be observable. An ensemble of bosons at a sufficiently high phase-space density may undergo a transition to form a Bose-Einstein condensate and exhibit collective quantum behaviour [38].

When multiple ions are simultaneously confined, the resulting one-component plasma exhibits a variety of phases depending on the ratio of the average kinetic energy to the average distance between particles, and at sufficiently low temperatures an ordered crystalline phase known as a Coulomb crystal is formed, taking a variety of shapes from a string of ions to a series of concentric ellipsoidal shells depending on the number of trapped ions and the anisotropy of the trapping potential [39–44]. The ions are localised in discrete lattice sites and so may be individually addressed using tightly-focused lasers, and the rate at which ions are lost from the crystal used to measure rates of chemical reactions [45]. Co-trapping different species allows for the study of reactions as described above, but also enables the sympathetic cooling of particles which cannot otherwise be cooled. This may either be achieved in hybrid traps for, e.g., the cooling of ions by neutral atoms, or a single trap if this can be designed to confine two different masses simultaneously. This latter approach has been demonstrated for radiofrequency traps containing multiple species of ion, with a light laser-cooled ion used as a coolant for heavy ions lacking a closed optical cycle [46], and the sympathetic cooling of ions by atoms has also been achieved [19, 21, 47], but is limited in the range of masses which can be successfully cooled [48]. Hybrid traps in which the atoms have formed a Bose-Einstein condensate have also been the focus of some studies, with experiments investigating the rate of collisions and theory predicting the formation of mesoscopic structures of shells of increased atomic density around the ion [49–51].

As a result of the small particle numbers involved in trapping experiments, the conditions which typically lead to thermal equilibrium, i.e., a large number of weakly interacting particles, no longer hold. Consequently, it cannot be assumed that the familiar Maxwell-Boltzmann distribution (or, for very cold ensembles, the Fermi-Dirac or Bose-Einstein distributions) describes the velocity of trapped particles, and attempting to calculate reaction rates based on this assumption will lead to inaccurate values [52]. Likewise, any property

which depends to some extent on the velocity or the energy of the trapped particles will, when measured experimentally, reflect an average over the range of velocities or energies present in the system. It is therefore critical that when these distributions do not follow the standard thermal statistics, the actual forms for these distributions are known to ensure that the experimental results can be accurately compared to theoretical values. Ions held in radiofrequency traps, in particular, have been observed to show marked deviations from thermal statistics under a range of circumstances [19, 52–60]. Rare heating events significantly increase the energy of the trapped ions, which takes a finite amount of time to be removed by laser cooling. This leads to cycles of heating and recooling, with the result that the ions exhibit a non-thermal velocity distribution on experimental timescales [52, 57]. The time-dependent potential used for radiofrequency traps leads to a heating mechanism when a trapped ion collides with co-trapped neutral atoms, and the ion may gain energy even if the neutral atom is effectively at rest. This has been observed to produce a power-law energy distribution for the ion, and establishes an upper limit on the mass of the neutral buffer gas which can be used to cool the ion before a runaway heating mechanism leads to loss of the ion [19, 47, 48, 53, 54, 56]. Recently, it has been demonstrated that this runaway heating can be prevented by using a buffer gas with a non-uniform density by ensuring that collisions occur preferably at the centre of the trap [20, 21, 55]. It is therefore of interest to derive both how this occurs, and the resulting steady-state energy distribution of the ion to better interpret experimental results.

1.3 Outline of the thesis

This thesis has two complementary goals: the design of a miniaturised hybrid chip trap and the study of the dynamics of trapped ions under conditions other than thermal equilibrium. The former allows for the increased control

over ion-neutral systems by enabling more precise manipulation of the trapped particles, while the latter provides a more accurate interpretation of the result of experiments performed on trapped ions by finding the distribution of energies present. Taken together, this allows for the design of experiments with a high degree of control over the collision energies and an accurate knowledge of the spread of the values of these energies, greatly improving the ability to compare theory to experiment. Chapter 2 provides an overview of how the laser cooling and the trapping of both charged and uncharged particles to produce a hybrid system is performed, and gives a brief introduction to the formalism of superstatistics used to describe the statistical mechanics of non-equilibrium systems. In Chapter 3, the details of the design and fabrication of a miniaturised hybrid ion-atom chip trap is presented, and the molecular-dynamics simulations used to characterise the capability of chip to trap both charged and uncharged particles are presented in Chapter 4. The remaining two chapters, 5 and 6, discuss two different cases in which trapped ions may exhibit non-thermal energy distributions. In Chapter 5, these result from rare heating events due to the collisions of trapped particles with background gas of a high temperature, resulting in a cycle of heating and recooling that causes a deviation from thermal statistics on experimental timescales. Chapter 6 details the sympathetic cooling of an ion by an ultracold buffer gas and shows how micromotion interruption leads to a non-thermal distribution for the secular energy of the ion, with the form of this distribution analytically derived based on the change in energy during a collision for both a uniform buffer gas and a buffer gas held in a harmonic potential, such as that generated by the hybrid chip trap. Finally, the results of this thesis are summarised in Chapter 7 and it is briefly discussed how the hybrid chip trap can be used to investigate the range of distributions derived in Chapter 6.

Chapter 2

Theory of particle cooling and trapping

A number of different techniques must be employed simultaneously to produce an ensemble of ultracold particles, and the goal of this chapter is to introduce the theory behind these techniques. A semi-classical model of Doppler laser cooling is presented in Section 2.1 to establish the mechanism by which the particles may be cooled down through the application of off-resonant laser light. The means through which these ultracold particles may then be trapped in one location is discussed in Section 2.2, providing an overview of magneto-optical, magnetic, and radiofrequency electric traps. The forces through which trapped particles interact with each other and the effects of these interactions are discussed in Section 2.6. The chapter concludes with an introduction to the formalism of superstatistics used to describe the properties of systems with fluctuating temperatures.

2.1 Laser cooling

In most cases, if a laser is focused on an object, then the energy absorbed by that object is dissipated as heat, and the temperature of the object rises. Counterintuitively, under the correct circumstances a laser may be used to cool atoms down to temperatures a fraction of a degree above absolute zero [6, 61]. This effect relies on a combination of three properties: that atoms interact with light only at specific frequencies, that the frequency of light observed by an atom may be shifted by the Doppler effect, and that when an atom scatters a photon a small quantity of momentum is transferred from a fixed direction to a random direction. In the following sections, an overview of how these properties are combined to result in cooling of an atom is presented.

2.1.1 Interaction of light with a two-level atom

The scattering of light by atoms is an inherently quantum process and is linked to the transition of the system between discrete energy states. Consider a system with only two available energy levels: a ground state $|1\rangle$ and an excited state $|2\rangle$, separated by an energy $E = \hbar\omega_0$. In the absence of external forces, an atom prepared in one of the two states will remain there. A time-dependent potential, however, may couple these two states together, such that the atom's state is given by a superposition of these two states, $|\Psi\rangle = c_1 |1\rangle + c_2 |2\rangle$. To be specific, we will assume that this time-dependent potential is the electric field of monochromatic light of frequency ω_l, and that the two relevant states are the ground and first excited electronic state of an atom. The mathematical treatment of how the system evolves due to the light is non-trivial, and so here a summary of the main results from Ref. [62] are presented. The density matrix can be defined from c_1, c_2 as [62],

$$\begin{pmatrix} p_{11} & p_{12} \\ p_{21} & p_{22} \end{pmatrix} = \begin{pmatrix} c_1^* c_1 & c_1 c_2^* \\ c_1^* c_2 & c_2^* c_2 \end{pmatrix}, \tag{2.1}$$

where c^* is the complex conjugate of c. The diagonal elements of this matrix are the populations, that is, the probability for the atom to be in that state, while the off-diagonal elements are the coherences between the states. These are then expressed in terms of the components of the Bloch vector [62],

$$\begin{pmatrix} u \\ v \\ w \end{pmatrix} = \begin{pmatrix} p_{12}e^{-i\delta t} + p_{21}e^{i\delta t} \\ -i(p_{12}e^{-i\delta t} - p_{21}e^{i\delta t}) \\ p_{11} - p_{22} \end{pmatrix} \tag{2.2}$$

where $\delta = \omega_l - \omega_0$ is the detuning of the angular frequency of the light from the atomic resonance. The advantage of this form is that the time-evolution of u, v, w is given by a set of ordinary linear differential equations,

$$d/dt \begin{pmatrix} u(t) \\ v(t) \\ w(t) \end{pmatrix} = \begin{pmatrix} \delta v(t) \\ -\delta u(t) + \Omega_R w(t) \\ -\Omega_R v(t) \end{pmatrix}, \tag{2.3}$$

where Ω_R is the Rabi frequency defined in terms of the laser intensity I, the saturation intensity of the transition I_{sat}, and the natural linewidth of the transition Γ_{12} as,

$$\Omega_R^2 = \frac{1}{2}\frac{I}{I_{sat}}\Gamma_{12}^2. \tag{2.4}$$

The saturation intensity is given by [62],

$$I_{sat} = \frac{2\pi^2}{3}\frac{\hbar c}{\lambda^3}\Gamma_{12}, \tag{2.5}$$

where c is the speed of light and $\lambda_0 = 2\pi c/\omega_0$ is the wavelength of the transition.

Solving the differential equations given by Eq. (2.3) with the initial conditions $u = v = 0$, $w = 1$, corresponding to an atom initially in the ground

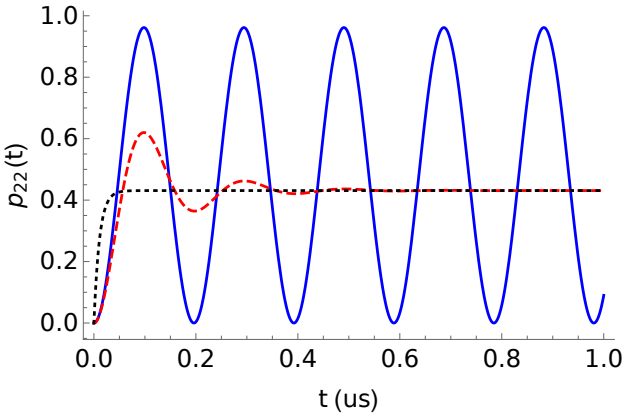

Figure 2.1: The population of the upper state due to transitions from the lower state caused by an applied electric field. Three cases are shown: the Rabi oscillations due to an applied field in the absence of noise (blue solid line), the result of adding spontaneous emission to the Rabi oscillations leading to damped oscillations (red dashed line), and a simplified rate-equation model (black dotted line). In all cases, the Rabi frequency is taken to be $5 \times 2\pi$ MHz, the detuning is given by $1 \times 2\pi$ MHz, and where appropriate, the lifetime of the upper state is $1 \times 2\pi$ MHz.

state, and using the normalisation condition $p_{11} + p_{22} = 1$ results in,

$$p_{22} = \frac{\Omega_R^2}{\Omega_R^2 + \delta^2} \sin^2\left(\frac{\sqrt{\Omega_R^2 + \delta^2}}{2} t\right) \tag{2.6}$$

from which it can be seen that the atom undergoes coherent oscillations, known as Rabi oscillations, between the ground and excited state, as depicted in Fig. 2.1. In practice, the atom does not continue to oscillate forever due to the presence of noise, which results in transitions from the excited state back to the ground state. This process of spontaneous emission occurs at a rate equal to Γ_{12}. The set of equations given by Eq. (2.3) may be modified

to include this decay, producing the Optical Bloch Equations (OBE) [62],

$$d/dt \begin{pmatrix} u(t) \\ v(t) \\ w(t) \end{pmatrix} = \begin{pmatrix} \delta v(t) - \frac{\Gamma_{12}}{2} u(t) \\ -\delta u(t) + \Omega_R w(t) - \frac{\Gamma_{12}}{2} v(t) \\ -\Omega_R v(t) - \Gamma_{12}(w(t) - 1) \end{pmatrix}. \tag{2.7}$$

The analytical solution for $p_{22}(t)$ is plotted in Fig. 2.1 to demonstrate the results of damping. As a consequence of the decay of the upper state, the initial oscillations rapidly die out, and the system tends towards a steady-state with the probability to be in the upper state given by,

$$p_{22}(t \to \infty) = \frac{\Omega_R^2/4}{\delta^2 + \Omega_R^2/2 + \Gamma_{12}^2/4}. \tag{2.8}$$

For understanding the mechanism of laser cooling, it is useful to view the atom as existing either in the upper state or the lower state, and undergoing discrete transitions between the two. In this model, three types of transition are possible, corresponding to the absorption or emission of a photon. In the ground state, the atom may absorb a photon and enter the excited state. Two types of emission from the upper state are possible, corresponding to the fact that the loss of population from the upper state can be due to either the coherent driving or random decay back to the ground state, refered to as stimulated and spontaneous emission respectively. In this discrete model, it can be useful to employ the Einstein rate equations to describe the evolution of p_{22} [62],

$$\dot{p}_{22} = \gamma_a(1 - p_{22}) - \gamma_e p_{22} - \Gamma_{12} p_{22}, \tag{2.9}$$

where $\gamma_a, \gamma e$ are the rate constants for absorption and stimulated emission respectively, and are equal for the two-level system considered here, $\gamma_a = \gamma_e = \gamma$, while the rate of spontaneous emission is given by Γ_{12}. By requiring that the steady-state value of p_{22} is equal to that predicted from the OBE,

the value for γ is found to be,

$$\gamma = \frac{\Gamma_{12}\Omega_R^2}{4\delta^2 + \Gamma_{12}^2}. \tag{2.10}$$

The solution to Eq. (2.9) is plotted in Fig. 2.1. By construction, it results in the same steady-state population, but the initial oscillations are missing and the initial rise in population occurs at a greater rate than it does in the solutions to the OBE. Nonetheless, these differences are only important for a very short period of time, and the rate equation model is particularly useful for numerical simulations of laser cooling, see Chapter 4.

Before proceeding further, a few complications should first be addressed. Any given atom has far more than two electronic states, and if the atom has multiple valence electrons it is very difficult to find a simple optical cycle as required here. For the most part, laser cooling is limited to either atoms of alkali metals, or the singly-charged ions of alkaline earth metals, although some exceptions exist for other atoms and some simple molecules. Even for the hydrogen-like atoms, it is fairly common for there to exist an energy level which is intermediate in energy between the two states used for laser cooling and which has the same parity as the ground state, see Fig. 2.2 for a schematic of the level structure. Consequently, transitions between this state and the ground state are forbidden, but the atom may spontaneously decay from the excited state into this state, where it becomes trapped. This may be overcome by introducing a laser to repump the atom from $|3\rangle$ back to $|2\rangle$, ensuring that the laser cooling may continue. Moreover, if the atom has a non-zero total angular momentum F in any of the electronic states, then this electronic level is split into $2F + 1$ Zeeman sublevels representing the different projections of this angular momentum onto a quantisation axis. The energies of these states are shifted in applied magnetic fields and by the electric field of the light itself, altering the scattering rate.

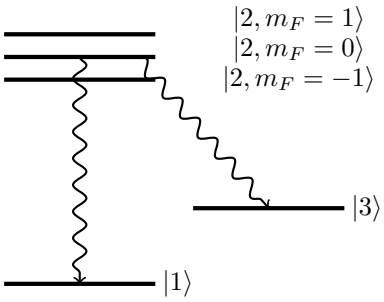

Figure 2.2: A schematic of the energy levels of a three level atom, showing the two levels used for lasing cooling and a third level which the excited state may decay into via spontaneous emission. The excited state is shown as being split into three Zeeman states, which are degenerate in the absence of a magnetic field but have been shown offset from each other for clarity. The curved arrows indicate possible routes for spontaneous emissions.

2.1.2 The scattering force

So far, the position and velocity of the atom have been neglected. As long as the atom has a reasonably large energy, these may be taken to be classical, continuous variables with well-defined values, which for simplicity are assumed to not vary during the absorption and emission of a single photon [62]. In the frame of reference of the atom, the frequency of the laser is altered due to the Doppler effect, with the result that the detuning from resonance depends on the velocity of the atom and is given by $\delta(\mathbf{v}) = \omega_l - \omega_0 - \mathbf{k} \cdot \mathbf{v}$, where $\mathbf{v}$ is the velocity of the atom and $\mathbf{k}$ is the wavevector of the laser. If the frequency of the laser is less than the frequency of the transition (red-detuned), then the light is brought back into resonance when the atom is moving towards the source of the light. Thus, the atom has a greater probability to be in the excited state when it is moving towards the laser than it does when the atom is moving away, see Fig. 2.3(a).

Each photon carries a small quantity of linear momentum, given by $\hbar k$, which must be conserved before and after both absorption and emission.

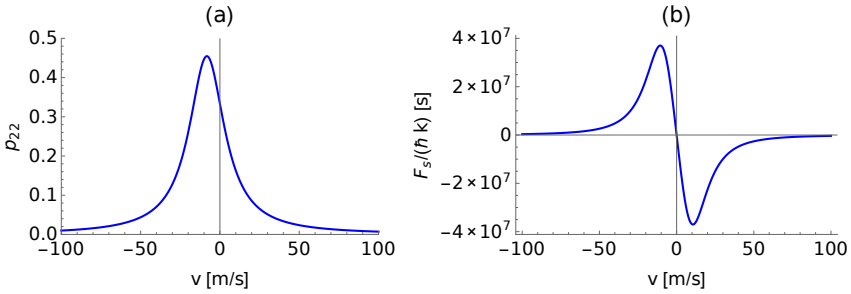

Figure 2.3: (a) The steady-state population of the excited state as a function of the velocity of the atom due to driving by an off-resonant laser. (b) The velocity-dependent force acting on a particle due to a pair of counterpropagating lasers, both of which are red-detuned from a transition at 397 nm. In both cases, the laser intensity is equal to the saturation intensity, the linewidth of the transition is taken to be $\Gamma_{12} = 20.7 \times 2\pi$ Mhz, and the detuning from resonance is $\delta = \Gamma_{12}$.

Hence, the momentum of the atom must also change by this amount whenever a photon is absorbed or emitted. When a photon is absorbed, this requires that the atom's momentum is increased in the direction in which the photon was travelling. The reverse is true for stimulated emission, since in this case conservation of momentum requires that the atom is accelerated in the opposite direction to the k-vector of the emitted photon. Thus, absorption followed by stimulated emission leads to no overall effect. Spontaneous emission, however, occurs in a random direction. By symmetry, the momentum change due to the spontaneous emission averages to zero, and so absorption followed by spontaneous emission leads to an overall change in the atom's momentum. Note that the momentum due to the emitted photon cannot be entirely neglected, as it establishes the minimum momentum of the atom at the recoil limit [62], and also leads to heating of the atom, see Section 2.1.3. To simplify the description of the cooling, we initially neglect these effects.

The rate at which photons are scattered by the atom is given by the rate of spontaneous emission from the excited state multiplied by the probability

for the atom to be in the excited state. Thus, the scattering rate is given by,

$$R_s(v) = \Gamma_{12} p_{22}, \tag{2.11}$$

where p_{22} is the population of the upper state taking into account the velocity-dependent detuning. Each scattering event causes the momentum of the atom to change by $\hbar\mathbf{k}$, and so the rate of change of the momentum, i.e. the scattering force, is given by,

$$\mathbf{F}_s = m_a \frac{d\mathbf{v}}{dt} = \hbar\mathbf{k} R_s(v), \tag{2.12}$$

where m_a is the mass of the atom. Substituting in the steady-state value for p_{22} produces [62],

$$\mathbf{F}_s = \hbar\mathbf{k}\frac{1}{2}\frac{\frac{I}{I_{sat}}}{4\frac{(\omega_l - \omega_0 - \mathbf{k}\cdot\mathbf{v})^2}{\Gamma_{12}^2} + \frac{I}{I_{sat}} + 1}. \tag{2.13}$$

The force acting on the atom due to absorption of photons is in the direction of travel of the laser, repelling the atom from the laser source. If the laser is red-detuned from resonance, then this force is largest when the atom is moving towards the laser, as this is when the Doppler shift cancels out the detuning. Conversely, if the atom is moving away from the laser, the force is significantly weaker, but some photons will still be scattered. As such, an atom initially moving towards the laser will be decelerated until it is brought to a standstill, then accelerated in the direction of the laser until it is sufficiently far from resonance that there is no longer any force acting on the atom. This can be prevented by employing a second, counter-propagating laser. Approximating that scattering from the two beams occurs independently of each other, the net force is given by adding together the scattering force from each beam, producing the result shown in Fig. 2.3(b). If both lasers are red-detuned by the same amount and of equal intensity, then the scattering will occur

preferentially from the beam opposing the motion of the atom, and so the net force decelerates the atom regardless of the direction in which it is moving.

To simplify the analysis of the cooling, we take a one-dimensional model in which the velocity and the wave-vector are parallel, and use scalar quantities v and k. Around $v = 0$, the scattering force from the sum of the two beams is approximately a linear function of v, and so a first-order Taylor expansion can be used to gain more insight into the cooling process. Eq. (2.13) is expanded for each laser with detuning δ_i and intensity I_i,

$$F_{s,i} \approx c_i - \lambda_i v, \tag{2.14}$$

where,

$$c_i = \hbar k_i \frac{\Gamma_{12}}{2} \frac{I/I_{sat}}{4\delta^2/\Gamma^2 + 1 + I/I_{sat}} \tag{2.15}$$

and,

$$\lambda_i = 4\hbar k_i^2 \delta/\Gamma_{12} \frac{I/I_{sat}}{(4\delta^2/\Gamma^2 + 1 + I/I_{sat})^2}. \tag{2.16}$$

The total scattering force is then given by $F_s = m_a \frac{dv}{dt} \approx c - \lambda v$, with $\lambda = \sum_i \lambda_i$ and likewise for c. It follows that the velocity of the atom evolves according to,

$$v(t) = c/\lambda + [v(0) - c/\lambda] e^{-\lambda t/m_a}, \tag{2.17}$$

i.e., an exponential decay with a rate of λ/m_a to an equilibrium value of c/λ. This would suggest that, if the two beams are of the same intensity and detuning such that $c = 0$, the velocity of the atoms is reduced to zero. In reality, this is prevented by the stochastic nature of the scattering force which ensures that the atom has some probability of having a non-zero velocity.

2.1.3 Heating effects

Two heating processes must be taken into account. The first of these is the recoil of the atom as a result of spontaneous emission. Every time a photon

is scattered, the velocity $\mathbf{v}$ along a given axis increases by,

$$\Delta\mathbf{v} = \frac{\hbar k}{m_a}(\cos\phi\sin\theta, \sin\phi\sin\theta, \cos\theta)^T, \tag{2.18}$$

where θ, ϕ are random variables describing the orientation of the direction of the emitted photon, and $k = |\mathbf{k}|$ is the scalar magnitude of the wavevector. Since the emission is isotropic, the mean increase in the velocity is zero, but the variance of each component of the velocity grows as a function of time. When the scattering is from a single laser, this is given by,

$$\langle v_j(t)^2\rangle - \langle v_j(t)\rangle^2 = \frac{1}{3}(\hbar k/m_a)^2 R_s(\mathbf{v})t \tag{2.19}$$

where the factor of $\frac{1}{3}$ reflects the fact that the spontaneous emission occurs isotropically and so the momentum increase is shared equally between the x, y, z axes [62]. The second effect is less immediately obvious and is a consequence of the fact that the absorption of photons is a random process [62], and applies only to the direction parallel to the k-vector of the laser, which we take to be the z axis. Consider an atom interacting with a single laser for a period of time t in which $R_s(v_z)$ remains constant, and the atom absorbs N_p photons. Excluding spontaneous emission, the change in the velocity of the atom is given by $N_p(0, 0, \hbar k/m_a)$. Since a random number of photons is scattered during this time, N_p is not a fixed number but instead is a random variable, and thus, $v_z(t)$ is also a random variable. Taking, for simplicity, $v_z(0) = 0$, the variance of $v_z(t)$ is given by,

$$\langle v_z(t)^2\rangle - \langle v_z(t)\rangle^2 = (\hbar k/m_a)^2[\langle N_p^2\rangle - \langle N_p\rangle^2]. \tag{2.20}$$

If each scattering event is independent of the others and the rate remains unchanged, then N_p follows Poisson statistics with a mean value of $\langle N_p\rangle = R_s(v_z)t$. The mean-square value for Poisson statistics is given by $\langle N_p\rangle^2 =$

$\langle N_p \rangle^2 + \langle N_p \rangle$ [63], and so,

$$\langle v_z(t)^2 \rangle - \langle v_z(t) \rangle^2 = (\hbar k/m_a)^2 R_s(v_z) t. \tag{2.21}$$

Thus, the width of the velocity distribution, and hence the temperature, increases due to the random number of photons scattered per unit time.

As a result of these stochastic terms, it is no longer possible to write down a simple expression for the velocity as a function of time. Instead, a statistical approach is used to calculate the probability distribution of v_j, denoted* $f_{v_j}(v_j)$, representing the probability for v_j to fall in the interval $[v_j, v_j + dv_j]$ [63]. During a period of time which is long compared to $1/\Gamma_{12}$, such that many photons are scattered, but short compared to $1/\lambda$ such that the velocity does not change significantly, the sum of the random changes in v_j may be approximated by a normal distribution by the central limit theorem. The evolution of the velocity of the atom may then be described in terms of a Langevin equation [6],

$$\frac{dv_j}{dt} = -\frac{\lambda}{m_a} v_j + \sigma \xi(t), \tag{2.22}$$

where $\xi(t)$ is white noise with a Gaussian distribution and zero mean, σ parameterises the strength of this noise, and it has been assumed that there are two counter-propagating beams of equal intensity and detuning to eliminate the radiation pressure term. This is an example of the Ornstein-Uhlenbeck process, and the steady-state probability distribution for v is given by [64],

$$f_{v_j}(v_j) \propto e^{-\frac{\lambda v_j^2}{m_a \sigma^2}}, \tag{2.23}$$

*This is an abuse of notation. Conventionally, a random variable X is distinguished from a possible value of this variable x, and the distribution is denoted $f_X(X = x)$. The shorthand is employed here to avoid either needing to find an unambiguous pair of upper and lowercase letters for each random variable or introducing additional subscripts, superscripts, or diacritical marks to distinguish between a random variable and a realisation of that variable.

i.e. v_j is distributed according to a Gaussian distribution. This is the distribution expected for a particle in thermal equilibrium with a heat bath at a temperature $T = \frac{m_a \sigma^2}{2k_B \lambda}$, where k_B is Boltzmann's constant, leading to the convention of referring to the width of the velocity distribution as a temperature. Three-dimensional cooling may be achieved through the optical molasses configuration, in which there is a pair of counterpropagating beams along each axis. Since these may well have different detunings or intensities, it is not necessarily the case that the same temperature is achieved for the motion along each axis, and the analysis is complicated by the fact that scattering from one beam necessarily reduces the rate of scattering from the others due to saturation of the transition. In the special case where all six lasers have identical detunings and intensities, and saturation effects can be ignored, the minimum steady-state temperature is given by [62],

$$T_D = \frac{\hbar \Gamma_{12}}{2k_B}, \tag{2.24}$$

referred to as the Doppler temperature. The actual temperature achievable may be much smaller than this due to the additional cooling mechanisms available from the interaction between multiple lasers and the fact that the atom is not a simple two level system [65]. If the atom has Zeeman structure in both the ground and excited states, then sub-Doppler cooling mechanisms are possible due to light-induced shift in the energies of these states [62], and exploiting these processes allows a reduction of the energy of the atom to close to the limit set by the recoil of a single photon [62].

2.2 Particle trapping

As discussed in Section 2.1.3, the velocity of a laser-cooled particle does not reach zero, but fluctuates around this value due to the stochastic nature of photon scattering. Thus, the particle diffuses away from its original position,

analogous to the Brownian motion of a particle in solution. After a sufficiently long period of time, it would leave the region of space in which it can interact with the lasers and become lost. This may be prevented by applying a position-dependent force to the atom to ensure that it remains trapped. A simple example of a suitable force is one which is a linear function of the distance from the centre of the trap, $F_x = -m\omega^2 x$, and which leads to harmonic motion of the trapped particles at a frequency ω. As long as $\omega << \Omega_R$, then the velocity of the atom can be treated as essentially fixed during each scattering event (the weak-binding approximation), and the theory discussed in the previous section is unchanged [66]. The evolution of the position and velocity of the atom is given by a pair of coupled Langevin equations [64],

$$\frac{dx}{dt} = v, \tag{2.25}$$

and,

$$\frac{dv}{dt} = -m\omega^2 x + \frac{c}{m} - \frac{\lambda}{m}v + \sigma\xi(t). \tag{2.26}$$

The steady-state probability distributions for x and v are given by Gaussian distributions [64], and so the position and velocity can both be described using thermal distributions. Any residual radiation pressure displaces the equilibrium position of the atom, but the mean velocity remains zero. Thus, if an external trapping potential is used, it is possible to cool the trapped atoms using only one laser per axis, or indeed a single laser if this has a non-zero component along each of the principle axes of the trap and the frequencies of these axes are non-degenerate [5, 67]. The question therefore arises as to how a suitable trapping potential can be generated. A wide range of different methods are possible, of which the three relevant to this thesis will be discussed: the magneto-optical trap, the magnetic trap, and the radiofrequency ion trap.

2.3 The magneto-optical trap

An elegant method to produce a trapping potential is by making the scattering rate depend on the position of the particle as well as the velocity, so that the lasers provide both cooling and a restoring force. This may be done by exploiting the change in the energy levels of the atom when exposed to a magnetic field through the Zeeman effect, resulting in the magneto-optical trap (MOT). For an atom with a total angular momentum F, there are $2F+1$ Zeeman sublevels labelled with $m_F = -F, -F+1, ..., F-1, F$, where m_f is the projection of the angular momentum onto the quantisation axis. In a weak magnetic field, which is assumed to define the quantisation axis, the potential energies of these states are given by [62],

$$E(m_F) = g_f \mu_B m_f |\mathbf{B}(\mathbf{r})| \tag{2.27}$$

where $|\mathbf{B}(\mathbf{r})|$ is the magnitude of the magnetic field at the location of the atom $\mathbf{r}$, μ_B is the Bohr magneton, and g_f is a proportionality constant. As a result of the fact that each of these sublevels has a different energy, the laser light is detuned from resonance by a different amount for each sublevel. Furthermore, if the magnetic field varies as a function of the position of the atom, then the scattering rate for each of the Zeeman states (except for $m_f = 0$) is position dependent. A suitable choice of field is the quadrupole field obtained from a pair of coils in the anti-Helmholtz configuration, see Fig. 2.4(a), which produces a field of the form,

$$\mathbf{B} = B_g(\frac{1}{2}x, \frac{1}{2}y, -z), \tag{2.28}$$

where B_g is the gradient and is usually on the order of 0.1 T/m [62].

To demonstrate how a field of this form alters the scattering rate, consider an atom at rest with ground state $F = 0$, excited state $F' = 1$, interacting with a laser of k-vector $(0, 0, -k)$. In this case, the scattering rate from each

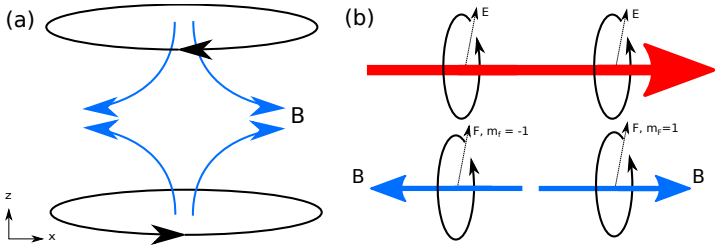

Figure 2.4: (a) A pair of current loops in the anti-Helmholtz configuration, producing a quadrupolar magnetic field B. (b) A schematic of the effects of circularly polarised light on the handedness of the precession of the angular momentum vector F around a quantisation axis defined by the local magnetic field B. In the lab frame, the direction of rotation of F matches that of the light used to drive the transition, but the handedness of the rotation around B, and hence the Zeeman shift, depends on the orientation of B.

m_f state is given by,

$$R_s(m_f, z) = \frac{\Gamma_{12}}{2} \frac{I/I_{sat}}{1 + I/I_{sat} + 4(\omega_l - \omega_0 - g_f \mu_B m_f B_g |z|)^2/\Gamma_{12}^2}. \tag{2.29}$$

As $|z|$ increases then the Zeeman shift leads to a change in the overall detuning from resonance, and so alters the scattering rate. If unpolarised light is used, the same scattering force is obtained at both z and $-z$ for a given final state m_f, that is, $F_s(m_f, z) = F_s(m_f, -z)$. This symmetry is broken by the selection rules for the transition if circularly polarised light is used, which cause only transitions to a certain value of m_f to be allowed. If the k-vector of the light points in the same direction as the quantisation axis and the electric field of the light rotates in a clockwise direction relative to its own k-vector, then transitions to the $m_f = 1$ state are driven, and those to the $m_f = -1$ state are suppressed [62]. At the opposite point in the trap, the quantisation axis is reversed, and so the same laser instead drives transitions to the $m_f = -1$ state, see Fig. 2.4(b). Consequently, although the $m_f = 1$ state may be in resonance with the laser at a pair of points $\pm z$, this transition can

only be driven at one of the two. Conversely, the transition to the $m_f = -1$ state is allowed at the opposite location, but as this has a different detuning from resonance the scattering rate is different. Thus, the scattering force is no longer symmetric with respect to inversion of z, and can be made to be weakly anti-trapping for $z < 0$, and restoring for $z > 0$. This situation is reversed for a laser with the opposite k-vector, and so the sum of the scattering force from the pair of lasers is overall restoring for all z. The combination of three pairs of counter-propagating lasers, as used in molasses cooling, and an anti-Helmholtz coil pair is sufficient to generate three-dimensional cooling and confinement, although the model of scattering presented above breaks down due to the interaction of the multiple lasers. Typically, the cooling is efficient enough that a MOT may capture atoms with velocities up to $v_c \approx 70$ m/s [62], enabling their loading from atomic vapour.

2.4 Magnetic traps

The random scattering of photons used to generate the magneto-optical trap also leads to a continuous rate of heating, thus limiting the achievable temperature. It would therefore be beneficial if, once the atoms have been cooled down to a sufficiently low temperature, they may then be trapped without requiring further scattering of photons and then potentially cooled to even lower temperatures. This may be done by again exploiting the Zeeman shift due to an inhomogenous magnetic field, as this produces a position-dependent energy. If the atoms are pumped into a state with $m_f > 0$ then trapping is possible around a point at which the field magnitude is at a minimum. Take, for example, the quadrupole field given by Eq. (2.28). For this field, $|B|$ has a value of 0 at $x = y = z = 0$ and increases linearly around this point. This would suggest that the quadrupole field can be used for purely magnetic trapping. There is, however, a significant disadvantage to the use of a quadrupole field. Close to the centre of the trap, the m_f states are very close in energy,

and so transitions may occur due to field fluctuations which cause transitions from m_f states which can be trapped to a state which cannot [38]. Thus, it is necessary to produce a field which has a non-zero minima. This may be achieved through use of the Ioffe-Pritchard trap which has a non-zero minimum [38, 62]. The disadvantage of this trap is that it requires large currents (≈ 100 A) to operate, as a result of the macroscopic scale of the trap.

The magnetic field gradient at a distance r generated by a wire carrying a current I decays as a function of I/r^2, and so achieving a significant force requires either a very high current or for the atom to be very close to the wire. If the atoms are sufficiently close then even a very low current of a few amperes may be sufficient to generate a magnetic trap. In this regime, three-dimensional trapping may be achieved through the use of a planar set of wires – an atom chip – in place of the macroscopic coils required for traditional magnetic trapping [68].

To illustrate how these traps works, first consider the magnetic field in the xz plane by a wire carrying current in the $+y$ direction. A homogenous bias field can be used to cancel out this field at a particular point, and around this point the field is approximately a quadrupole field, see Fig. 2.5. By itself, this does not offer confinement along the y axis, as the magnetic field has no component in this direction. It is therefore necessary to add an additional two wires carrying current in the x direction in order to provide axial confinement [68]. Two configurations for these wires are widely used. The first is the U-wire, shown in Fig. 2.6(a), in which one wire carries current in the $+x$ direction and the other in the $-x$ direction. In the plane equidistant between these two wires, the component of the magnetic field in the y direction is equal to zero, as the magnetic field from the two wires cancels at this point. The second configuration is the Z-wire (Fig. 2.6(b)), for which the two fields do not cancel and so provide axial confinement with a non-zero field minimum. Thus, the U-wire serves as an approximation to the quadrupole trap, while the Z-wire is equivalent to the Ioffe-Pritchard trap. These basic configurations

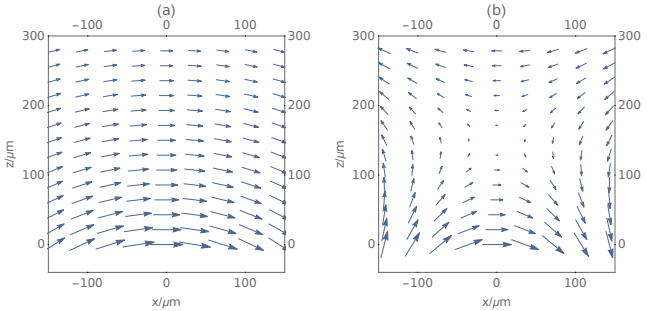

Figure 2.5: (a) The magnetic field in the xz plane created by a current passing through a wire parallel to the y axis, where the wire is located at $x = 0, z = -200$ μm and has a current of 4A. (b) The field shown in (a) combined with a homogenous bias field to produce an approximate quadrupolar field. The magnitude of this bias field chosen such that at $x = 0, z = 150\mu$m the total magnetic field is zero.

may then be combined and extended to produce a flexible variety of trapping potentials, see Chapter 3 for more details.

The depth of these traps is typically only on the order of a few millikelvin, and so loading cannot be performed directly from background vapour. It is therefore necessary to cool the atoms before they are trapped. The operation of a standard MOT is hindered by the fact that, unless a transparant substrate is used, the chip itself blocks the light which would be used to cool in the direction perpendicular to the surface of the chip. Fortunately, it is possible to achieve a three-dimensional MOT by reflecting two of the beams from the surface of the chip, see Fig. 2.7(a). The handedness of the circular polarisation of the beam is reversed by the reflection, and if the lasers are correctly aligned with a magnetic quadrupole field then this ensures that the total scattering force allows for confinement of particles [68]. In theory, the required quadrupole field may be generated by an on-chip U-wire in combination with a bias field. However, this is effectively only in a small region of space compared to the large quadrupole fields achieved through a pair of

external coils, limiting the efficiency with which atoms may be collected from background vapour. Consequently, either external coils or a specially designed U-wire must be used for the first MOT stage [69]. Once a sufficient number of atoms are collected they may be transferred into an on-chip MOT, which has the advantage of higher field gradients and more precise control of the location of the trapped atoms to optimise loading into a purely magnetic trap.

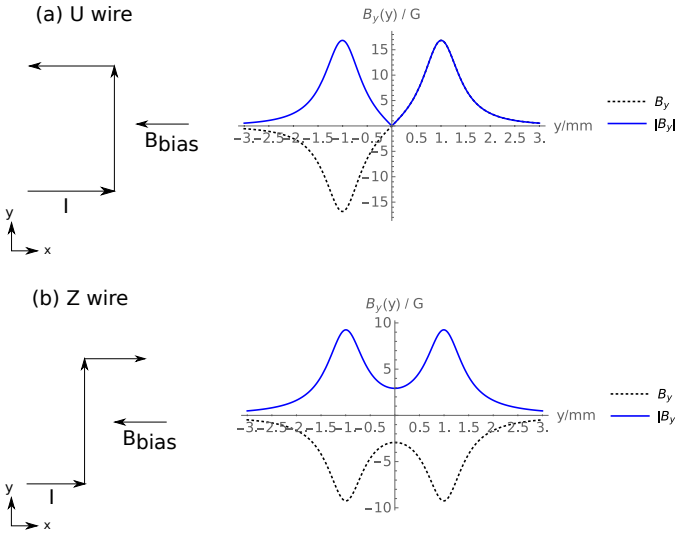

Figure 2.6: Schematics of the U (a) and Z (b) wires used for the generation of magnetic traps for neutral particles, and the magnetic field profile along the y axis generated by the wires parallel to the x axis.

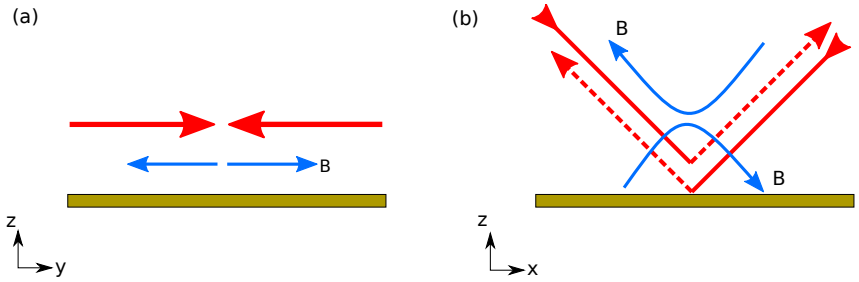

Figure 2.7: The configuration of lasers and the magnetic field used for the generation of a mirror MOT in (a) the yz plane and (b) the xz plane. Incoming lasers are shown as solid red lines and the reflected beams are dashed, while the blue lines indicate the magnetic field. For clarity, the lasers in (b) and the magnetic field have been offset from each other.

2.5 Ion traps

2.5.1 Radiofrequency ion traps

The magneto-optical and magnetic traps of the previous section share a common disadvantage that they are neither particularly deep, nor have particularly high trapping frequencies. Consequently, energetic particles are easily lost and the particles which remain are not especially well confined to the centre of the trap. The forces which can be achieved from applying electric fields to charged particles are much greater, and so these would seem the natural choice for confining particles. There is, however, a complication. For a potential $U(x, y, z)$ to be a minimum with respect to a given direction, it is necessary that the second derivative with respect to this direction is greater than zero, that is $d^2U/dj^2 > 0$ for each $j \in (x, y, z)$. However, this cannot be achieved by an electric field in free space as a consequence of Maxwell's equations. The divergence of an electric field in free space is required to be zero, $\nabla \cdot \mathbf{E} = 0$. Since the electric field is the gradient of the potential, $\mathbf{E} = -\nabla U(x, y, z)$, this implies that $\sum d^2U/dj^2 = 0$, which cannot be achieved if all three compo-

nents are required to be positive. Hence, any electric potential cannot be a minimum in all three directions simultaneously. If a point exists which is a minimum in one direction, it must either be a saddle-point or a maximum in the remaining directions.

If, however, the confining and anti-confining directions are rapidly switched by using a time-dependent potential, then it is possible to dynamically confine charged particles [11, 12]. This may be achieved using a radiofrequency (RF) ion trap, in which a combination of oscillating and static potentials are applied to a set of electrodes to generate an electric field with an oscillating saddle point in free space suitable for trapping charged particles. The motion of the ions in this potential is stable as long as certain criteria on the curvature of the electric potential, the mass of the trapped ion, and the frequency of oscillation are met, which will be discussed further in Section 2.5.2. Typically, the oscillating potential is at a frequency on the order of $1 - 100 \times 2\pi$ MHz, and the resulting trap is able to capture ions with kinetic energies up to a few electronvolts, i.e., a few thousand kelvin. The trapped ions may be laser cooled as before, and in fact the trapping potential may be exploited to reach temperatures below the Doppler limit through the method of sideband cooling [70].

The radiofrequency ion trap has the disadvantage that, due to the influence of the RF field, the trapped ion does not undergo simple harmonic motion but instead exhibits a complex motional spectrum, consisting of a slow "secular" motion and high-frequency "micromotion" components at frequencies close to multiples of Ω [11, 12]. This micromotion adversely affects laser cooling [71], and, if multiple ions are trapped simultaneously, causes heating of these ions [11, 12]. It is thus beneficial to use a radiofrequency field with no component along one axis so that there is no micromotion along this direction. One configuration of electrodes which results in this field is a set of four electrodes, parallel to the z-axis and symmetric when reflected in either the $y = 0$ or $x = 0$ planes, see Fig. 2.8(a), and which is known as the linear radiofrequency ion

trap. Applying a voltage to one pair of diagonally-opposite electrodes while applying the opposite polarity to the other pair results in the field shown in Fig. 2.8(b), which has essentially no component in the z direction close to the centre of the trap. Axial trapping is provided by applying a static voltage to each of the eight endcap electrodes, producing a static field which is confining along the z direction, but slightly reduces the efficiency of the dynamic trapping due to being anti-confining in the x, y directions.

In fact, a wide range of designs of electrodes can be used to generate a radiofrequency trap. The planar structure shown in Fig. 2.9 is of particular interest, due to the enhanced optical access of the trapped ions and the fact that it may be more easily miniaturised, allowing for a greater control of the ions [72]. These surface electrode ion traps, or ion chips, enable a wide range of trapping structures which cannot straightforwardly be achieved in a traditional macroscopic trap, much as the atom chip offers more flexibility than macroscopic magnetic traps for neutral atoms. To date, complex structures for shuttling ions from one region of the chip to another have been demonstrated for applications in quantum computing, as well as multi-zone traps for simulations of complex systems.

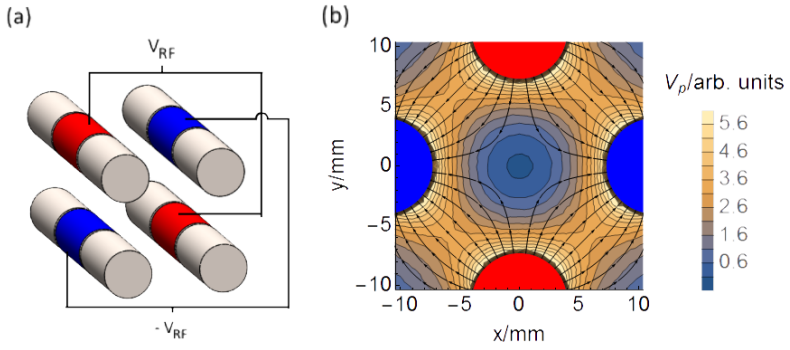

Figure 2.8: (a) Schematic of the electrodes used for a linear radiofrequency trap, based on the design used in Ref. [18]. The RF signal is applied to the four central electrodes with the sign of the voltage alternating between adjacent electrodes, while the remaining eight endcap electrodes are used for axial confinement and share the same static voltage. (b) The numerically calculated field (lines) and time-averaged pseudopotential (contour plot) in the plane perpendicular to the symmetry axis obtained by applying a 1V potential to the red electrodes, -1V to the blue electrode, and grounding the remainder. The numerical calculations were performed using the EMS package for SolidWorks [73].

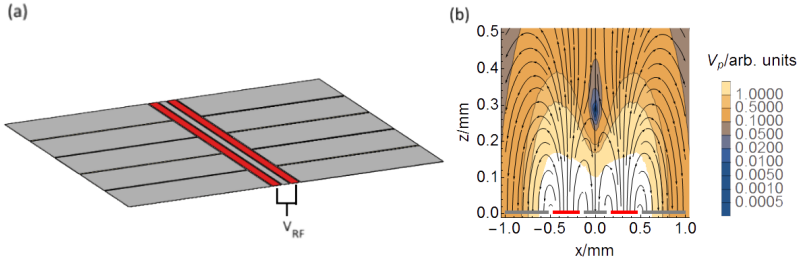

Figure 2.9: (a) Schematic of a surface electrode ion trap. (b) The numerically calculated field (lines) and time-averaged pseudopotential (contour plot) obtained by applying a 1V potential to the two electrodes shown in red and keeping the remaining electrodes grounded. The numerical calculations were performed using the EMS package for SolidWorks [73].

2.5.2 The Mathieu equation

A first approximation to the motion of an ion in a radiofrequency trap may be found using the pseudopotential approximation, in which the fast oscillations are averaged over to produce a time-independent potential. Briefly, if the instantaneous potential is given by the sum of a time-dependent (U_{RF}) and a static (U_{DC}) potential,

$$U(\mathbf{r}, t) = U_{RF}(\mathbf{r}) \cos(\Omega t) + U_{DC}(\mathbf{r}), \tag{2.30}$$

and Ω is much greater than the frequency of the slow motion of the ion, then the time-dependent component may be averaged over to produce a pseudopotential, such that the total potential is given by [74, 75],

$$\overline{U}(\mathbf{r}) = \frac{Q_i^2}{4m_i\Omega^2}|\nabla U_{RF}(\mathbf{r})|^2 + U_{DC}(\mathbf{r}) \tag{2.31}$$

where Q_i and m_i are the charge and mass of the ion respectively. The motion of the ion in this potential is the secular motion referred to in the previous section, and in this model the micromotion is neglected. The pseudopotential model provides a qualitative understanding of the motion of a trapped ion, and is useful to determine the maximum energy of an ion which can be trapped, i.e., the trap depth, and to estimate the frequency of the secular motion. However, the high-frequency micromotion can be reasonably expected to influence the behaviour of a trapped ion. It is therefore necessary to investigate the motion of the ion taking into account the time-dependence of the trapping potential. In the special case where both the RF and DC fields are linear around the centre of the trap, it is possible to obtain analytical solutions for the motion of the ion. The equation of motion for each axis $j \in (x, y, z)$ is given by,

$$m_i \frac{d^2 r_j(t)}{dt^2} = -(Q_i k_{DC,j} + \cos(\Omega t) Q_i k_{RF,j}) r_j(t), \tag{2.32}$$

where $k_{RF,j}$ is the gradient of the RF field at the centre of the trap, and likewise $k_{DC,j}$ is the gradient of the DC field. These factors are proportional to the applied voltages and typically scale as $1/d^2$, where d is the distance between the electrodes and the trap centre, but in general must be evaluated from numerical calculations of the trapping potential. Changing the independent variable from t to $\tau = \Omega t/2$ produces,

$$m_i \frac{\Omega^2}{4} \frac{d^2 r_j(\tau)}{d\tau^2} = -(Q_i k_{DC,j} + \cos(2\tau) Q_i k_{RF,j}) r_j(\tau). \tag{2.33}$$

From here on, we use $\dot{x}(\tau)$ to denote derivatives with respect to τ. Eq. (2.33) can be simplified by defining the dimensionless parameters,

$$a_j = \frac{4}{\Omega^2 m_i} Q_i k_{DC,j}, \tag{2.34}$$

and,

$$q_j = -\frac{2}{\Omega^2 m_i} Q_i k_{RF,j}. \tag{2.35}$$

In order to satisfy Maxwell's equations, the conditions $a_x + a_y + a_z = 0$ and $q_x + q_y + q_z = 0$ must hold. For an ideal linear radiofrequency trap with no component of the RF field along the z axis, $q_z = 0$ and so $q_x = -q_y$. Likewise, if the DC field is radially symmetric, $a_x = a_y = -\frac{1}{2} a_z$. For the configuration of electrodes shown in Fig. 2.8 with the zero-to-peak amplitude of the RF potential given by V_{RF} and a voltage of V_{DC} applied to each of the endcap electrodes, these parameters are given by,

$$a_z = \frac{8\kappa Q_i V_{DC}}{\Omega^2 m_i z_0^2}, \tag{2.36}$$

and,

$$q_x = \frac{4 Q_i V_{RF}}{\Omega^2 m_i r_0^2}, \tag{2.37}$$

where r_0 is the minimum distance between the centre of the trap and the RF electrodes, z_0 is one-half of the length of the RF electrodes, and κ is a geometric factor found either experimentally or from numerical calculations of the trapping potential [18, 76]. For the particular geometry on which Fig. 2.8 is based, $\kappa = 0.346$ [18], but in general this must be calculated for each individual geometry.

In terms of a_j, q_j, Eq. (2.33) reduces to the canonical form of the Mathieu equation,

$$\ddot{r_j}(\tau) - [a_j - 2q_j \cos(2\tau)]r_j(\tau) = 0. \tag{2.38}$$

This can be thought of as a generalisation of the equation of motion describing a harmonic oscillator, which corresponds to the case with $q_j = 0$ and $a_j > 0$, and is itself a special case of the more general Hill's equation [77]. Before discussing the exact solution to Eq. (2.38), it is instructive to first find an approximate solution under the assumption that q_j is sufficiently close to zero that the motion due to the RF field can be separated from the secular motion in the pseudopotential. In this adiabatic approximation, the secular motion of the ion is given by,

$$\tilde{r_j}(t) = A_j \cos(\omega_j t + \phi_j), \tag{2.39}$$

i.e., a harmonic oscillator of frequency $\omega_j \approx \frac{1}{2}\sqrt{a_j + q_j^2/2}\Omega$, and where the constants of integration are parameterised in terms of an amplitude A_j and a phase angle ϕ_j. The total motion including the micromotion is [11],

$$r_j(t) = A_j \cos(\omega_j t + \phi_j)[1 - \frac{q_j}{2} \cos \Omega t]. \tag{2.40}$$

Thus, to first order, the effects of the time-dependent potential produce a high-frequency modulation of the secular motion. Using the trigonometric identity $\cos A \cos B = \frac{1}{2}[\cos(A + B) + \cos(A - B)]$, the motional spectrum is given by the secular motion at ω_j, and a pair of micromotion terms at $\omega_j \pm \Omega$, the amplitude of each of which are smaller than the secular motion by a factor of $q_j/4$.

The exact solutions to the Mathieu equation may be found using Floquet theory. Since Eq. (2.38) is a linear function of r with periodic coefficients, a solution is given by [77],

$$\mathrm{me}_\beta(\tau) = e^{i\beta\tau} P_\beta(\tau), \tag{2.41}$$

and a second linearly independent solution is given by $\mathrm{me}_\beta(-\tau)$ [77]. Here, $P_\beta(\tau)$ is a function with period π, and β_j is the characteristic exponent, which is a function of a_j and q_j. The value of β_j can be calculated either using approximations when q_j, a_j are close to zero [78],

$$\beta_j \approx \sqrt{a_j - \frac{(a_j-1)q_j^2}{2(a_j-1)^2 - q_j^2} - \frac{(5a_j+7)q_j^4}{32(a_j-1)^3(a_j-4)}} \approx \sqrt{a_j + q_j^2/2}, \tag{2.42}$$

or by numerical integration of the Mathieu equation with the initial condition $r_j(0) = 1, \dot{r_j}(0) = 0$ and evaluating,

$$\beta_j = \mathrm{acos}[r_j(\pi)]/\pi, \tag{2.43}$$

noting that if $r_j(\pi) > 1$ the complex continuation of acos must be used [77]. If β_j has an imaginary component, then one of the two solutions diverges for $\tau \to \infty$ and so cannot correspond to stable trapping. The requirement that β_j is real is met only for certain regimes of values of a_j, q_j, giving rise to stability regions for different combinations of applied voltages and values of Ω [11]. We proceed assuming that β_j is purely real, which is usually true for $|q_j| < 0.5, a_j \approx 0$, and most ion traps operate in this regime. In this regime, $\beta_j \approx \sqrt{a_j + \frac{1}{2}q_j^2}$, allowing for a qualitative understanding of how the exponent changes as a function of the trapping parameters [11, 12].

Even when β_j is real, the Floquet solution is complex valued, and so it is useful to define a pair of real-valued solutions to the Mathieu equation. These may be obtained from $\mathrm{me}_\beta(\tau), \mathrm{me}_\beta(-\tau)$, analogously to how cos and sin may

be defined from the complex exponential solutions to the harmonic oscillator equation. These solutions are termed ce and se, meaning "cosine elliptic" and "sine elliptic" respectively, and have the Fourier series expansions [77],

$$\mathrm{ce}(a_j, q_j, \tau) = \mathrm{ce}_j(\tau) = \sum_m c_{2m,j} \cos[(\beta_j + 2m)\tau], \tag{2.44}$$

and,

$$\mathrm{se}(a_j, q_j, \tau) = \mathrm{se}_j(\tau) = \sum_m c_{2m,j} \sin[(\beta_j + 2m)\tau], \tag{2.45}$$

where the Fourier coefficients $c_{2m,j}$ depend on a_j, q_j and m, and are normalised such that $\sum c_{2m,j}^2 = 1$ [77]. For brevity, the j subscript for these coefficients is suppressed in the rest of this chapter. If $q_j = 0$, then $c_0 = 1$ and the remaining Fourier coefficients are all equal to 0, such that $\mathrm{ce}_j(\tau), \mathrm{se}_j(\tau)$ reduce to $\cos\beta\tau$ and $\sin\beta\tau$ respectively. For $q_j \neq 0$, the Fourier coefficients for $q_j \neq 0$ are defined by the recurrence relation [77],

$$q_j c_{2m+2} - [a_j - (\beta_j + 2m)^2]c_{2m} + q_j c_{2m-2} = 0. \tag{2.46}$$

When q_j, a_j are both close to zero, the recurrence relation may be approximately solved by setting all c_{2m} with $|m| > 1$ to zero. In this limit, the $m = \pm 1$ coefficients are given by,

$$c_{\pm 2} = \frac{q_j c_0}{a_j - (\beta_j \pm 2)^2}, \tag{2.47}$$

and c_0 is found by requiring that $c_0^2 + c_2^2 + {c_2}^2 = 1$. Furthermore, in this regime $\beta_j << 1$ and $a_j << (\beta_j + 2)^2$, such that these coefficients may be further simplified to $c_0 \approx 1$, $c_{\pm 2} \approx -q_j/4$.

The general solution to Eq. (2.38) may be written in terms of $\mathrm{ce}_j(\tau)$ and

$\mathrm{se}_j(\tau)$ as,

$$r_j(\tau) = A_j \cos\phi_j \mathrm{ce}_j(\tau) - A_j \sin\phi_j \mathrm{se}_j(\tau) = A_j \sum c_{2m} \cos[(\beta_j + 2m)\tau + \phi_j], \tag{2.48}$$

where the two constants of integration are parameterised in terms of an amplitude A_j and a phase angle ϕ_j as before. The position and velocity obtained from this solution of an ion in a trap defined by $q = 0.1$ and $a_j = 0$ is shown in Fig. 2.10 and compared to the trajectory predicted using the adiabatic approximation. It can be seen that, although the adiabatic approximation is adequate to describe most of the ion's trajectory, it is less accurate when $r(\tau) \approx 0$ due to miscalculating the velocity of the ion in this region, see Fig. 2.10(b). Thus, the exact solutions to the Mathieu equation will be used whenever possible. These solutions are valid for any values of q_j, a_j which correspond to stable motion, and it is not necessarily the case that the motion of the ion may be easily separated into a large slow component and small fast components. For this thesis, we simply define the secular motion as the result of truncating the infinite sum in Eq. (2.48) to include only the $m = 0$ term,

$$\tilde{r_j}(\tau) = A_j c_0 \cos(\beta_j \tau + \phi_j), \tag{2.49}$$

which is harmonic motion of an amplitude $A_j c_0$ at a frequency of (in terms of t rather than τ) $\omega_j = \frac{1}{2}\beta_j \Omega$, see Ref.[79] for a more thorough description of how the secular motion is related to $r_j(\tau)$. The remaining terms are the intrinsic micromotion at frequencies of $\omega_j + m\Omega$, with amplitudes given by $c_{2m} A_j$.

Although A_j, ϕ_j are defined by the initial conditions and remain unchanged in the absence of other factors, the energy of the ion is not a conserved quantity as a result of the time-dependent trapping potential. Two time-independent measures of the energy of an ion in a Paul trap are frequently used. The first is the secular energy, which is defined as for a harmonic oscil-

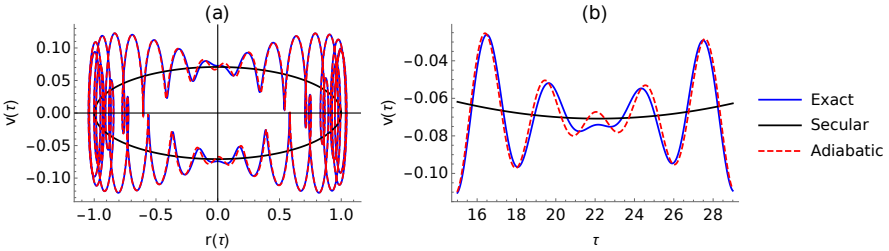

Figure 2.10: (a) The phase-space trajectory of an ion in a radiofrequency trap with $q_j = 0.1$ and the initial conditions $\phi_j = 0, A_j = 1$ in dimensionless units. Three forms of the solution are shown: the exact result using the solutions to the Mathieu equation (blue), the adiabatic approximation (red dashed) and the secular motion (black ellipse). (b) The velocity corresponding to the trajectory shown in (a) around the point where $r_j(\tau) = 0$.

lator of amplitude $A_j c_0$ and frequency ω_j,

$$E = \frac{1}{2} m_i \frac{\Omega^2}{4} A_j^2 c_0^2 \beta_j^2, \tag{2.50}$$

which includes contributions from both the potential and kinetic energy of the secular motion. This excludes the contribution of the micromotion, and so it is also useful to consider the time-averaged kinetic energy defined by [56],

$$\overline{E_{j,K}} = \frac{1}{2} \frac{\Omega^2}{4} m_i \lim_{L \to \infty} \frac{1}{2L} \int_{-L}^{L} \dot{r_j}(\tau)^2 d\tau. \tag{2.51}$$

The time derivatives of the Mathieu functions may be found through their Fourier series definitions [77],

$$\dot{\mathrm{ce}}_j(\tau) = -\sum_m c_{2m}(\beta + 2m) \sin[(\beta + 2m)\tau], \tag{2.52}$$

and used to evaluate this integral, producing,

$$\overline{E_{j,K}} = \frac{1}{2} m_i \frac{\Omega^2}{4} A_j^2 \frac{1}{2} \sum_m c_{2m}^2 (\beta_j + 2m)^2. \tag{2.53}$$

Notice that this definition of the energy has a very similar structure to the secular energy as defined by Eq. (2.50) and we may write,

$$\overline{E_{j,K}} = \frac{1}{2} E_j \sum_m \frac{c_{2m}^2 (\beta_j + 2m)^2}{c_0^2 \beta_j^2}, \tag{2.54}$$

to make the relation between the two clear. The factor of $\frac{1}{2}$ is a result of the fact that E_j contains both the secular kinetic and potential energy, wheras $\overline{E_{j,K}}$ only contains the kinetic energy. The sum in Eq. (2.53) describes the amount of kinetic energy present in each mode of motion. If $q_j = 0$, then all $c_{2m\neq 0}$ coefficients are equal to zero such that $\overline{E_{j,K}} = \frac{1}{2} E_j$, as expected for a harmonic oscillator. For $q_j \neq 0$ the micromotion terms also contribute energy. In the regime in which ion traps are usually operated, $0.1 < q < 0.5$, the micromotion terms with $|m| > 1$ can be neglected. If, in addition, $a_j \approx 0$, then the $m = -1, 1$ terms in the sum are each approximately equal to $1/2$, such that the total contribution from the micromotion is equal to the contribution from the secular motion. This result is frequently referred to as the equipartition of energy between the secular motion and micromotion. Moreover, in this limit, $\overline{E_{j,K}} \approx E_j$. Thus, the two definitions of the energy are approximately equivalent except when $q_j = 0$, for which $\overline{E_{j,K}} = \frac{1}{2} E_j$. For this thesis, the secular energy will be used to characterise the energy of the ion on the grounds that this ensures the same secular frequency and amplitude of motion corresponds to the same energy, regardless of whether or not q_j is zero for a given axis.

The inhomogenous Mathieu equation

In the above, it has been assumed that the only forces acting on the ion is that due to the trapping potential, which is a linear function of the position. In many cases, there are additional forces applied to the ion, which must be taken into account when calculating the ion's motion. If this force does not depend on the position of the ion, or at least does not change significantly over the region of space in which the ion moves, the equation of motion is given by the inhomogenous Mathieu equation,

$$\ddot{r_j}(\tau) + (a_j - 2q_j \cos 2\tau) r_j(\tau) = g_j(\tau). \tag{2.55}$$

The solution to this is given by,

$$r_j(\tau) = A_j \cos\phi \mathrm{ce}_j(\tau) - A_j \sin\phi \mathrm{se}_j(\tau) + r_{f,j}[g_j(\tau)], \tag{2.56}$$

which is the sum of the solution to the homogenous equation and an additional term $r_{f,j}[g_j(\tau)]$, which represents the response to the external force $g_j(\tau)$. By analogy to the forced harmonic oscillator, this term will be referred to as the forced motion, and in contrast to the intrinisic motion it is independent of A_j, ϕ_j. The forced motion can be calculated using the technique of the variation of parameters [80],

$$r_{f,j}[g_j(\tau)] = -\frac{\mathrm{ce}_j(\tau)}{W_j} \int \mathrm{se}_j(\tau) g_j(\tau) d\tau + \frac{\mathrm{se}_j(\tau)}{W_j} \int \mathrm{ce}_j(\tau) g_j(\tau) d\tau, \tag{2.57}$$

where W_j is the Wronskian [77, 80],

$$W_j = \mathrm{ce}_j(\tau)\dot{\mathrm{se}}_j(\tau) - \mathrm{se}_j(\tau)\dot{\mathrm{ce}}_j(\tau) = \mathrm{ce}(a_j, q_j, 0)\dot{\mathrm{se}}(a_j, q_j, 0). \tag{2.58}$$

Explicit forms for the forced motion may be found through the use of the Fourier series definitions of $\mathrm{ce}_j(\tau), \mathrm{se}_j(\tau)$. In principle, Eq. (2.57) can be used to evaluate the effects of a wide range of external forces. Here, we concentrate

on a force which may be written in terms of a Fourier series,

$$g_j(\tau) = g_{j,0} + \sum_i g_{j,i} \sin(\alpha_i \tau + \varphi_i), \tag{2.59}$$

on the grounds that this includes the most experimentally relevant cases and usually results in periodic motion of the ion. Eq. (2.57) is linear in terms of $g_j(\tau)$, and so the forced motion due to each term of Eq. (2.59) can be evaluated separately and the result summed to find the total forced motion. Thus, only the response to a constant force $g_j(\tau) = g_j$ and a sinusoidal force, $g_j(\tau) = g_j \sin(\alpha\tau + \varphi)$ need to be evaluated in order to determine the motion resulting from any external force which can be represented in terms of a Fourier series.

The simplest force to consider is one which is a constant, $g_j(\tau) = g_j$. In a harmonic potential with a static spring constant a_j, this force pushes the ion from the centre of the trap until it is counterbalanced by the restoring force at the equilibrium position $r_{eq} = g_j/a_j$. If the spring constant increases then the same force leads to a smaller displacement from equilibrium, and conversely a weaker spring constant causes a greater displacement. If the spring constant constantly varies as a function of time, then so does the equilibrium position. Consequently, a trapped particle will not remain at rest, but will instead be continuously accelerated towards the moving equilibrium position. It can therefore be expected that the combination of a constant force and the time-dependent potential of the ion trap leads to motion of the ion. Evaluating Eq. 2.57 using the Fourier series definitions of the Mathieu functions, we obtain,

$$r_{f,j}(\tau)[g_j] = \frac{g_j}{W_j} \sum_m \sum_n c_{2m} c_{2n} \cos[2(m-n)\tau]. \tag{2.60}$$

The terms with $m = n$ describe a constant offset of the ion's position, which is approximately given by $\Delta r \approx \frac{g_j}{\beta_j W_j} c_0^2$. The remaining terms are oscillations at frequencies of $m\Omega$ due to the moving equilibrium position. Since the frequency

of this motion is close to the frequency of the intrinsic micromotion, it is often known as "excess micromotion". There are, however, a number of significant differences between the intrinsic and excess micromotion, mostly arising from the fact that the intrinsic micromotion depends on the amplitude and phase of the secular motion, while the excess micromotion does not. Consequently, the excess micromotion may in fact be orders of magnitude larger than the secular motion, and cannot be cooled via laser cooling, which is demonstrated in the next section. Furthermore, the frequency of this forced motion is given by integer multiples of Ω, while the intrinsic micromotion is offset from Ω by the secular frequency, and so the two forms of motion may be distinguished via the Fourier transform of the ion's trajectory, see Fig. 2.11. It can be seen that the frequency components at $m\Omega$ require that an external force is present, while those at $\omega + m\Omega$ do not. Furthermore, the peaks corresponding to the intrinsic motion are unchanged by the introduction of the external force.

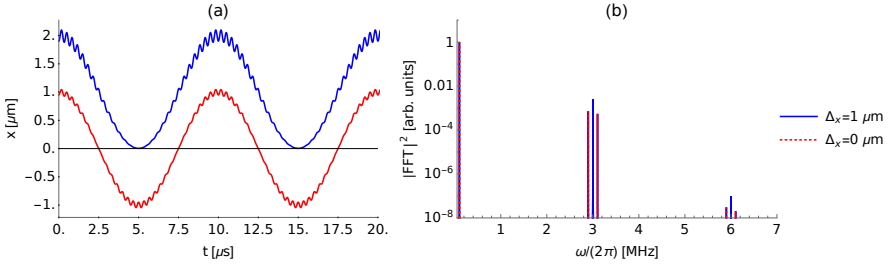

Figure 2.11: (a) The trajectory of a particle undergoing motion in a radiofrequency trap with (blue) and without (red) forced motion due to a uniform electric field. The amplitude of the secular motion is 1 μm, and the electric field is set to produce an offset of the ion's equilibrium position of 1 μm. (b) The Fourier transforms of the trajectories shown in (a).

A harmonic oscillator driven by an off-resonant, spatially-independent force is a standard textbook problem, and the result is motion at the driving frequency at an amplitude which increases as the driving frequency approaches the resonance frequency of the oscillator. When generalised to ra-

diofrequency traps, an off-resonant force of the form $g_j(\tau) = g_j \sin(\alpha\tau + \varphi_j)$ where $\alpha \neq \beta + m$, leads to forced motion of the form,

$$r_{f,j}(\tau)[g_j \sin(\alpha\tau + \varphi_j)] = \sum_{m,n} \frac{c_{2m}c_{2n}}{2W_j} \left[\frac{\sin(\tau(\alpha + 2m - 2n) + \varphi_j)}{(\alpha + \beta_j + 2m)} - \frac{\sin(\tau(\alpha - 2m + 2n) + \varphi_j)}{(\alpha - \beta_j - 2m)} \right] \tag{2.61}$$

The special case defined by $\alpha = 2, \varphi_j = 0$ corresponds to an external force of the form $\sin \Omega t$, which has previously been used as a model for the effects of a phase difference between RF electrodes [71], and which produces motion at frequencies of $m\Omega$.

Damping

In Section 2.1.2, it was shown that, at low velocities, the effects of laser cooling may be approximated as a constant force and a term linearly proportional to the velocity. In an ion trap, the frequency of the micromotion may be sufficiently high that the ion cannot be assumed to remain in the same position during the absorption and emission of a photon, and the effects of micromotion are known to alter the efficiency of the cooling [71]. Nonetheless, it is still useful to investigate how a velocity-dependent damping term alters the motion of an ion in a radiofrequency trap, as this also serves as a model for buffer-gas cooling of the ion if the buffer gas is much lighter than the ion. In both cases, the damping can be modelled by introducing a velocity-dependent term in Eq. (2.55),

$$\ddot{r}_j(\tau) - 2\mu_j \dot{r}_j(\tau) - (a_j - 2q_j \cos 2\tau) r_j(\tau) = g_j(\tau). \tag{2.62}$$

where μ_j is the friction term in dimensionless units. Defining $p(\tau) = e^{-\mu_j \tau} r(\tau)$ and substituting this into Eq. (2.62) produces,

$$\ddot{p}_j(\tau) - (a_j - \mu_j^2 - 2q_j \cos 2\tau) p_j(\tau) = e^{\mu_j \tau} g_j(\tau), \tag{2.63}$$

which can be seen to be an inhomogenous Mathieu equation as discussed in the previous section. The solution for $p_j(\tau)$ can be found as before,

$$p_j(\tau) = A_j \cos\phi_j \mathrm{ce}(\tilde{a_j}, q_j, \tau) - A_j \sin\phi_j \mathrm{se}(\tilde{a_j}, q_j, \tau) + p_{f,j}(\tau)[e^{\mu_j \tau} g_j(\tau)], \tag{2.64}$$

where $\tilde{a} = a_j - \mu_j^2$, and from here onwards the notation $\mathrm{ce}_j(\tau) = \mathrm{ce}(\tilde{a_j}, q_j, \tau)$ is used. The solution for $r_j(\tau)$ is,

$$r_j(\tau) = e^{-\mu_j \tau}[A_j \mathrm{ce}_j(\tau) \cos\phi_j - A_j \sin\phi_j \mathrm{se}_j(\tau) + p_{f,j}(\tau)[e^{\mu_j \tau} g_j(\tau)]]. \tag{2.65}$$

The part of this solution corresponding to the intrinsic motion can be seen to undergo exponential decay, confirming that both the secular motion and the intrinsic micromotion can be cooled by a friction-like force. This does not hold for the forced motion. If $g_j(\tau)$ is non-zero, then the forced motion $r_{f,j}[g_j(\tau)] = e^{-\mu_j \tau} p_{f,j}$ is given by,

$$\begin{aligned} r_{f,j}[g_j(\tau)] = \frac{e^{-\mu_j \tau}}{W_j} \Bigg[&- \mathrm{ce}_j(\tau) \int \mathrm{se}_j(\tau) e^{\mu_j \tau} g_j(\tau) d\tau \\ &+ \mathrm{se}_j(\tau) \int \mathrm{ce}_j(\tau) e^{\mu_j \tau} g_j(\tau) d\tau \Bigg]. \end{aligned} \tag{2.66}$$

Here, the Wronskian is defined as in the undamped case but with $\tilde{a_j}$ in place of a_j. Qualitatively, the evaluation of the integrals can be expected to produce terms which are proportional to $e^{\mu_j \tau}$ as a result of the properties of the exponential function with respect to integration. These cancel out the prefactor of $e^{-\mu_j \tau}$ which would otherwise lead to damping of the motion, and so if $g_j(\tau)$ does not itself decay, it can be expected that the amplitude of the

forced motion remains fixed. A constant force leads to motion of the form,

$$r_{f,j}(\tau)[g_j] = \frac{g_j}{W_j}\sum_{m,n}\frac{c_{2m}c_{2n}}{(\beta_j+2m)^2+\mu_j^2}\big\{(\beta_j+2m)\cos[2(m-n)\tau] - \mu_j\sin[2(m-n)\tau]\big\}, \tag{2.67}$$

where the effects of damping introduce a term proportional to $\sin[(m-n)\tau]$, i.e., motion which is out-of-phase with the RF drive, but in agreement with the above prediction there is no overall decay of the motion. In practice, unless the rate of cooling is on the same order of magnitude as Ω, then the damping has very little effect on the forced motion. In particular, regardless of the rate of cooling, the amplitude of the forced motion does not exhibit an exponential decay. It therefore cannot be cooled by laser cooling and must instead by eliminated by compensating the stray fields which generate it. This also holds when the forced motion is generated by a driving force with a sinusoidal time-dependency, $g_j(\tau) = g_j\sin(\alpha_j\tau+\varphi_j)$, which leads to,

$$\begin{aligned} r_{f,j}(\tau) = g_j\sum_{m,n}\frac{c_{2m}c_{2n}}{2W_j}\Bigg\{ &\frac{(\alpha_j+\beta_j+2m)\sin[\tau(\alpha_j+2m-2n)+\varphi_j]}{\big(\alpha_j^2+2\alpha_j(\beta_j+2m)+\beta_j^2+4\beta_j m+4m^2+\mu_j^2\big)} \\ &+\frac{\mu_j\cos[\tau(\alpha_j+2m-2n)+\varphi_j]}{\big(\alpha_j^2+2\alpha_j(\beta_j+2m)+\beta_j^2+4\beta_j m+4m^2+\mu_j^2\big)} \\ &+\frac{(-\alpha_j+\beta_j+2m)\sin[\tau(\alpha_j-2m+2n)+\varphi_j]}{\big(\alpha_j^2-2\alpha_j(\beta_j+2m)+\beta_j^2+4\beta_j m+4m^2+\mu_j^2\big)} \\ &+\frac{-\mu_j\cos[\tau(\alpha_j-2m+2n)+\varphi_j]}{\big(\alpha_j^2-2\alpha_j(\beta_j+2m)+\beta_j^2+4\beta_j m+4m^2+\mu_j^2\big)}\Bigg\}. \end{aligned} \tag{2.68}$$

If there are stochastic heating effects present, either the random emission of photons as described in Section 2.1.3 or recoil from collisions with a buffer gas, then the intrinsic motion of the ion is not damped to zero. Neglecting forced motion, the position and velocity of the ion in the presence of damping

and white noise are described by a bivariate normal distribution [81, 82],

$$f_{x,v}(x, v|\tau) \propto e^{-\frac{1}{2}[\frac{x^2}{\sigma_{xx}} + \frac{2xv}{\sigma_{xv}} + \frac{v^2}{\sigma_{vv}}]}, \tag{2.69}$$

where the σ_{ij} are time-dependent coefficients describing the second-order moments of the distribution [81, 82]. There are two important distinctions from the distributions obtained for laser-cooled particles in a harmonic potential. Firstly, the parameters σ_{ij} describing the width of this distribution are time-dependent, and so the "temperature" of the distribution depends on the current RF phase. Secondly, due to the term proportional to xv, this distribution cannot be written as the product of separate distributions for x and v, i.e., these two variables are not independent of each other. However, the position and velocity of the secular motion of the ion are typically found to follow independent distributions with a static temperature for both x and v and, consequently, may be treated as if they were in thermal equilibrium. It is also frequently the case that, even if the ion is cooled along a single axis only, the secular temperature is equal for the motion along each axis, whether due to non-linear terms in the trapping potential or collisions if multiple ions are trapped simultaneously.

2.6 Particle interactions

So far, it has been assumed that there is only one particle, or that if there are multiple particles they do not interact with each other. A full description of how a pair of particles interacts is beyond the scope of this thesis, and so only a brief overview is presented. For a pair of particles, there are six available degrees of freedom, three of which correspond to the position of the centre of mass of the system and may be neglected if the external potential does not alter the outcome of the collision. The remaining degrees of freedom may be expressed in spherical coordinates as the distance between the two

particles r, and a pair of angles θ, ϕ. A common representation of this interaction potential including the angular dependency is in terms of a multipole expansion,

$$V_{1,2}(r) = \sum_{n=1}^{n=\infty} C_n(\theta, \phi)|r|^{-n}, \tag{2.70}$$

where the $C_n(\theta, \phi)$ represent the strength of each term of the interaction and may be positive or negative, corresponding to repulsive or attractive interactions respectively. In the case of point particles with no other structure, the interaction is isotropic and so the two angles can also be neglected, and thus the interaction between the particles can be expressed as a function of the distance between them [83]. For the systems considered here, the charge-charge interaction ($n = 1$) and the charge - induced-dipole ($n = 4$) terms are typically the most significant, as these represent ion-ion and ion-neutral interactions respectively. This interaction potential must be modified to include the centrifugal barrier resulting from the relative angular momentum of the two particles by introducing an extra term of the form [83],

$$V_\ell(r) = \frac{\ell^2}{2\mu_r r^2}, \tag{2.71}$$

where ℓ is the magnitude of the angular momentum and μ_r is the reduced mass of the system.

Strictly speaking, the motion of a pair of particles interacting through a force of the form $1/r^n$ are coupled if the particles are at any finite distance from each other. In many cases, however, it is useful to view them as undergoing essentially independent motion until they become sufficiently close for the interaction energy to become significant compared to their kinetic energy. In this picture we may view the pair of particles as approaching each other, undergoing a collision if they are sufficiently close, and then (potentially) separating again. For point particles, the system may be described in terms of the impact parameter b and the collision velocity, as shown schematically

in Fig. 2.12 for a stationary target particle and an incoming particle. The

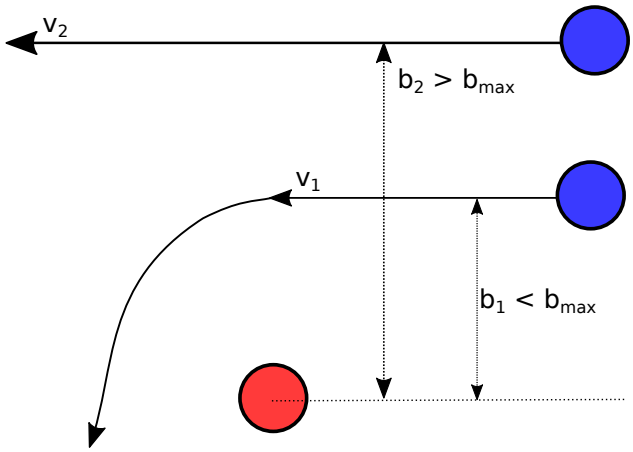

Figure 2.12: A schematic of the scattering of an incoming atom (blue) from a stationary target atom (red). If the impact parameter b is smaller than b_{max}, then a collision occurs, altering the trajectory of the incoming atom. If the impact parameter is larger, then the interaction potential is not strong enough to significantly alter the trajectory of the atom.

impact parameter describes the distance of closest approach, and if this is smaller than some critical value calculated from the interaction potential, a collision is said to occur. The effects of this collision may vary from an exchange of translational energy and momentum to the occurence of a chemical reaction. Closely related to this critical impact parameter is the cross section of the collision, which may be thought of as the effective size of the target particle as seen by the incoming particle. From the cross section, the rate constant may then be calculated from the number of particles which would pass through a surface with the same size per unit time,

$$k_c = \sigma_c v_{rel}, \tag{2.72}$$

where v_{rel} is the relative velocity. In general, the cross section depends on the

interaction potential and the collision energy. A simple model for collisions is the Langevin capture model, in which it is assumed that a collision occurs for any impact parameter less than b_{max}, and never occurs for greater impact parameters, and where b_{max} is determined by the centrifugal barrier. In this model, the cross section is given by [84],

$$\sigma_c = \left(\frac{n}{n-2}\right)^{1-\frac{2}{n}} \pi \left(\frac{nC_n}{\mu_r v_{\mathrm{rel}}^2}\right)^{2/n}. \tag{2.73}$$

For $n = 4$, i.e., ion-neutral collisions, the cross section scales as $1/v_{rel}$, and so the rate of collisions is independent of the collision velocity. Otherwise, the observed collision rate depends on the distribution of the relative velocity.

At the low energies, the classical model of collisions is no longer valid, and quantum effects begin to play a role. There is no longer a straightforward variation in the cross section as the impact parameter and collision velocity change, and additional structure is introduced due to the existence of resonances, e.g., the shape resonances which occur when the collision energy is approximately equal to the energy of a quasibound state of the interaction potential [28], see also Refs. [85, 86] for details of these effects for the $1/r^n$ interaction potential. For the work presented in this thesis, it is assumed that the energies of all particles remains sufficiently high that the collisions can be treated classically.

The collision model does not always fully describe the dynamics of the trapped particles, especially when the total interaction energy is of the same order of magnitude as the kinetic energy or when there are a large enough number of particles trapped that it is not feasible to resolve individual collisions. Thus, the remainder of this section will discuss some of the features of ensembles of cold particles which arise due to simultaneously trapping a greater number of particles.

2.6.1 Ion-ion interactions

The radiofrequency ion trap is sufficiently deep to allow for the confinement of a large number of trapped ions simultaneously, which interact through the long-range Coulomb potential. We may broadly distinguish three different regimes of interaction in terms of the relative magnitude of the average kinetic energy of the ions, i.e., the temperature, to the strength of the Coulomb interaction, parameterised by the coupling ratio [40],

$$\Gamma_c = \frac{1}{4\pi\epsilon_0}\frac{Q_i^2}{r_s k_B T}, \tag{2.74}$$

where r_s is the Wigner-Seitz radius, which parameterises the average distance between ions. When the temperature is sufficiently high that the Coulomb interaction is only significant at very short range ($\Gamma_c \to 0$), then the collision model holds, and we may view the ions as undergoing essentially independent motion in the trapping potential as before, with the inclusion of collisions which equalise the temperature between axes. As the temperature is reduced, the Coulomb repulsion between ions becomes more significant, and in this regime ($\Gamma_c \gtrsim 2$) the ions may be approximately viewed as a charged fluid of uniform density [39–41]. At very low temperatures corresponding to $\Gamma_c \gtrsim 170$, the kinetic energy is essentially negligible compared to the Coulomb and trapping potentials, and the combination of these results in the ions adopting an ordered structure known as a Coulomb crystal to minimise the total potential energy. The shape of this crystal depends on both the trapping potential and on the number of ions, ranging from a string of ions along the axis of weakest confinement to a series of ellipsoidal shells [42–44].

The motion of the ions still exhibits a separation into low frequency secular motion and high frequency micromotion, with a large amount of excess micromotion due to the force acting on each ion from all the other ions. Consequently, the total velocity of the trapped ions depends on their location in the crystal, and averaged over the trap it is highly non-thermal. The secular

velocity, however, is found to usually follow Maxwell-Boltzmann statistics, allowing for the definition of a secular temperature by fitting to this distribution [87]. The achieved secular temperature reflects the balance between cooling from e.g. Doppler cooling, and heating effects present in the trap. In addition to the heating from photon scattering, collisions between the ions leads to the effect known as RF heating, in which the collision transfers energy from the micromotion to the secular motion [88]. As the temperature of the ion cloud increases, so does the collision rate leading in turn to a more rapid increase in the temperature [89, 90]. However, as the ion cloud heats up it expands, reducing the density of the ions and thus the rate of heating [91]. Consequently, even a relatively small amount of cooling is sufficient to counteract this heating at large cloud sizes, or to maintain an ion crystal [91].

As previously mentioned, the collisions between ions allows for cooling to take place for all the degrees of freedom, even if only one axis is laser-cooled. In fact, it is possible to use this transfer of energy to sympathetically cool an ion which cannot be directly laser cooled by trapping it simultaneously with one which can [46]. This requires that the Matheiu parameters for both ions corresponds to stable trapping, but in practice this is usually achievable as long as the masses are reasonably close, which moreover results in more efficient cooling [88]. This technique greatly extends the scope of experiments that can be performed with ultracold ions, enabling spectroscopy and reaction studies of ions other than the limited number which may be laser cooled [92]. The presence of sympathetically cooled ions may be deduced from dark regions in the Coulomb crystal, as they displace the coolant ions but do not themselves fluoresce [93]. The mass of these sympathetically cooled ions may be estimated by their position in the crystal or, more accurately, by resonantly exciting their secular motion and calculating their mass from the excitation frequency.

2.6.2 Collective effects of uncharged particles

Neutral particles do not interact nearly as strongly as charged ones, and at the temperatures achievable through laser cooling ordered structures analogous to the Coulomb crystal do not form. Still, collective effects may be observed at sufficiently high densities and low temperatures. During the operation of a MOT, the light spontaneously emitted from an atom may be re-absorbed by another atom, and due to the conservation of momentum this leads to an effective repulsion between the pair of atoms, with the force proportional to $1/r^2$ [94]. This is much weaker than the Coulomb interaction, but leads to a crossover from the Gaussian distribution observed for dilute gases to a flat-topped distribution for denser ensembles [94]. Moreover, at very high phase-space densities, quantum statistics begin to play a role. At a sufficiently low temperature Bose-Einstein condensation may occur if the trapped atoms are bosons [38]. Typically, the formation of a BEC requires a phase-space density of particles much greater than can be achieved in a MOT, but is much more achievable in a magnetic trap due to the enhanced efficiency of evaporative cooling. This technique relies on the density of the atoms being sufficiently high that collisions between the neutral atoms result in a rapid thermalisation of the atoms [38]. If the trap were infinitely deep, and there was no external noise, the temperature of the trapped atoms would remain fixed. However, since the trap has a finite depth, atoms with a high energy may escape from the trap. If this escape is limited to atoms with a higher energy than the average energy, then every time an atom is lost the mean energy of the remaining atoms, and thus the temperature, decreases. This is referred to as the evaporative cooling of the trapped atoms, and may be taken advantage of to reach significantly lower temperatures than can be achieved through laser cooling. By deliberately lowering the trapping potential the more energetic atoms can be allowed to escape, and this procedure repeated until the sample reaches the desired final temperature, provided that a sufficiently high number of atoms was initially trapped. In practice, the removal of the energetic atoms

is done by applying an "RF knife" – a high-frequency signal which deliberately induces spin-flip transitions of energetic trapped atoms, causing them to be ejected from the trap [68]. This may be performed in a macroscopic magnetic trap, but the greater control over the trapping potentials achieved in a chip trap allows for more efficient evaporative cooling by increasing the density of the atoms.

2.6.3 Interactions in hybrid traps

As discussed in Chapter 1, there are many compelling reasons to co-trap charged and uncharged particles. Excluding reactions, the elastic collisions between ions and neutrals can be exploited in order to cool ions with lack a convenient transition for laser cooling. This requires that the mass of the neutral atom is much less than the mass of the ion in order to avoid a heating effect similar to RF heating, see Chapter 6 for more details. From a technical viewpoint, hybrid trapping can be achieved by superimposing the two separate traps on top of each other, subject to geometrical constraints and ensuring that the trapping fields used to contain one type of particle do not negatively impact on the other type [17].

2.7 Tsallis statistics and superstatistics

When multiple interacting particles are present, or when stochastic forces are acting on the particles, it is generally more appropriate to treat the properties of the system statistically rather than attempting to keep track of the individual energy or position of each particle. For a classical system at thermal equilibrium in the canonical ensemble, the probability for a particle to have a certain energy E is proportional to the Boltzmann factor $e^{-\beta E}$, where $\beta = 1/(k_B T)$ is the inverse temperature of the system. The proportionality factor is itself a function of E and depends on the nature of the system in question. In many cases, this factor is a power of E, such that the energy

distribution is given by a Gamma distribution [38, 63, 95],

$$f_E(E|\beta) = E^k \frac{\beta^{k+1}}{\Gamma(k+1)} e^{-\beta E}, \tag{2.75}$$

where $\Gamma(x)$ is the gamma function, $k > -1$, and the notation $E|\beta$ is used here to denote that this is a conditional probability for a given value of β [63]. The factor E^k is obtained from a consideration of the number of possible states with the same energy, i.e., the density of states [38].

The same form of the energy distribution can also be obtained under circumstances for which thermal equilibrium does not hold. If an energy ϵ_i can be related to a quantity x_i via a relation of the form $\epsilon_i \propto x_i^2$, and x_i follows a Gaussian distribution, then ϵ_i follows a Gamma distribution with $k = -\frac{1}{2}$ [63]. This applies, for example, to the position or velocity of a harmonic oscillator subject to white noise and linear friction. If there are N such degrees of freedom, e.g., $N = 6$ for a three-dimensional harmonic oscillator, and the mean energy for each of these degrees of freedom is equal, then the total energy is given by a Gamma distribution with $k = N/2 - 1$ [63]. For example, $k = 2$ for the three-dimensional harmonic oscillator, in agreement with the result predicted from the density of states [38]. Thus, thermal statistics may be observed even if the criteria for a thermal ensemble is not strictly met, as is approximately the case for a laser-cooled particle. If, however, there is neither a large ensemble nor linear friction and Gaussian noise, in general it cannot be expected that the energy distribution will follow thermal statistics. This is particularly significant for calculating the rate at which a process occurs from the cross section for that process, as this involves integrating over the distribution of collision energies [28]. If the assumption of thermal statistics is made incorrectly, then this leads to an inaccurate value for the rate constant, complicating the comparison of experiment to theory.

Due to the small particle numbers typically present in ion traps, ensembles of trapped ions are particularly sensitive to heating effects which lead to a

breakdown of the assumption of thermal equilibrium, resulting in energy distributions which deviate from Eq. (2.75) [19, 20, 52, 53, 57–60]. A commonly used model for these non-equilibrium systems is Tsallis statistics [96, 97], in which the exponential function of the Boltzmann factor $e^{-\beta E}$ is replaced by a q-exponential,

$$e_q(-\beta_q E) = [1 - (1-q)\beta_q E]^{1/(1-q)}, \tag{2.76}$$

where q describes the deviation from thermal statistics, β_q is the effective inverse temperature, and $q = 1$ recovers the standard exponential function [97]. The q-exponential is obtained from a maximisation of the Tsallis entropy [97], and it is not always immediately obvious why this particular form of the entropy should be used over the standard Boltzmann entropy. However, energy distributions exhibiting a functional form close to the q-exponential are known to arise from the formalism of superstatistics, which has a more straightforward interpretation. In this formalism, the temperature T or, equivalently, the inverse temperature $\beta = 1/(k_B T)$, is taken to be a fluctuating parameter, and the properties of the system found by averaging their fixed-temperature equivalent over the probability distribution for the temperature [98, 99]. For example, the energy distribution is given by,

$$f_E(E) = \int f_E(E|\beta) f_\beta(\beta) d\beta, \tag{2.77}$$

where $f_E(E|\beta)$ is the energy distribution for a fixed value of the inverse temperature, i.e., Eq. (2.75), such that,

$$f_E(E) = \int E^k \frac{\beta^{k+1}}{\Gamma(k+1)} e^{-\beta E} f_\beta(\beta) d\beta. \tag{2.78}$$

To establish the link to the q-exponential, we first consider the special case where β is described by a Gamma distribution with a mean value of $\langle\beta\rangle > 0$

and a shape parameter $n_T > 0$,

$$f_\beta(\beta) = \frac{\beta^{n_T-1}\left(\frac{\langle\beta\rangle}{n_T}\right)^{-n_T} e^{-\frac{\beta n_T}{\langle\beta\rangle}}}{\Gamma(n_T)}. \tag{2.79}$$

Evaluating Eq. (2.78) produces,

$$f_E(E) = \left(\frac{n_T}{\langle\beta\rangle}\right)^{-k-1} \frac{\Gamma(k+n_T+1)}{\Gamma(k+1)\Gamma(n_T)} \frac{E^k}{\left(\frac{\langle\beta\rangle E}{n_T}+1\right)^{k+n_T+1}}. \tag{2.80}$$

Eq. (2.80) has a functional form close to that of the q-exponential, and so systems which follow an energy distribution of this form will be referred to as following Tsallis statistics. Indeed, if the averaging is performed only on the Boltzmann factor, we find,

$$\int e^{-E\beta} f_\beta(\beta) = \left(\frac{E\langle\beta\rangle}{n_T}+1\right)^{-n_T}, \tag{2.81}$$

which is a q-exponential with $q = 1 + 1/n_T$. As a result of the inclusion of the factor of β^{k+1} in Eq. (2.78), the energy distribution given by Eq. (2.80) is not identical to this average Boltzmann factor multiplied by the density of states and then normalised, which has been suggested as an alternative method to produce superstatistical distributions [99]. However, the two are related through a change of parameters, and Eq. (2.78) has been demonstrated to be the correct method to calculate the energy distribution [99, 100]. In Fig. 2.13(a), the energy distribution obtained for a fixed inverse temperature $1/\beta = 10k_B$ mK, $k = 2$ is compared to a Tsallis distribution with $k = 2, 1/\langle\beta\rangle = 10k_B$ mK, $n_T = 0.5$. As a brief demonstration that this is the correct definition of the parameters for the Tsallis distribution, the distributions obtained numerically by sampling from Eq. (2.75) are also plotted in Fig. 2.13(a) for two cases. In the first case, the inverse temperature is kept fixed, producing thermal statistics. In the second case, the inverse

temperature is set to a random value for each value of the energy, with the inverse temperature distributed according to Eq. (2.79) with $1/\langle\beta\rangle = 10k_B$ mK, $n_T = 0.5$. It can be seen that Eq. (2.80) correctly represents the values of the energy obtained in this manner, and, moreover, there is a clear difference in the high-energy behaviour between the thermal and Tsallis statistics. In the limit $E \to \infty$, Eq. (2.80) asymptotically approaches a power law of the form $E^{-(n_T+1)}$, and the power-law exponent n_T will be referred to as the Tsallis exponent. Distributions with a power-law tail of the form $x^{-(1+n)}$ are normalisable for $n > 0$, and the values of the moments, $\langle E^m\rangle = \int E^m f_E(E)dE$, are defined for $m < n$. Thus if E follows Tsallis statistics with $n_T < 1$, the mean energy is not a well-defined quantity and cannot be used to characterise the distribution. The physical interpretation of this property is that, for $n_T < 1$, the mean energy calculated numerically from N values of the energy does not converge to a fixed value as N increases, as is demonstrated in Fig. 2.13(b) for $n_T = 0.5$.

The form of $f_\beta(\beta)$ depends on the dynamics of the system, and is not necessarily limited to a Gamma distribution. The results of evaluating Eq. (2.78) does not in general produce Tsallis statistics unless $f_\beta(\beta)$ is a Gamma distribution. However, in the limit where $E\sqrt{\langle\beta^2\rangle - \langle\beta\rangle^2} << 1$, i.e., the product of the energy and the standard deviation of β is small, the energy distribution approaches Tsallis statistics [99]. Thus, if the fluctuations in the temperature are small, then Tsallis statistics are typically observed, explaining their widespread empirical use. At high energies, $f_E(E)$ may deviate significantly from both thermal and Tsallis statistics, and does not necessarily approach a power-law. Two other forms of distribution for $f_\beta(\beta)$ are frequently considered in superstatistics in addition to the Gamma distribution: the inverse-Gamma distribution, leading to an asymptotic decay of the form $e^{-\sqrt{E}}$, and the log-normal distribution, leading to a decay of exponential form [101, 102]. In this thesis, the distribution of β is derived based on analytical models for the underlying heating and cooling processes. In Chapter 5, this leads to a

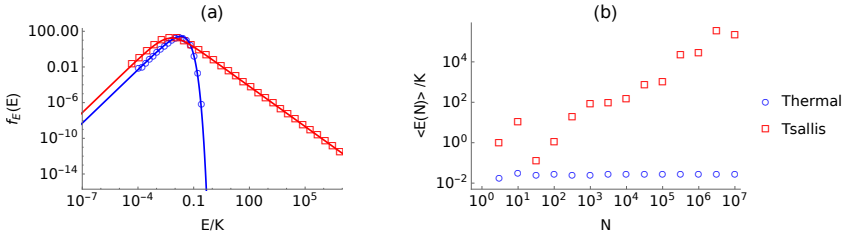

Figure 2.13: (a) The energy distributions for a thermal system (blue circles) and one which follows Tsallis statistics (red squares). The points show the distributions obtained through generating 10'000'000 random samples from thermal distributions with either a fixed inverse temperature $1/\beta = 10k_B$ mK or an inverse temperature chosen randomly for each value of the energy from a Gamma distribution as defined in the main text with $1/\langle\beta\rangle = 10k_B$ mK and $n_T = 0.5$, to illustrate how the Tsallis distribution arises as a superposition of thermal distributions. The solid lines show the analytical distributions for both cases. (b) The convergence of the mean value of the energy for thermal (blue) and Tsallis (red) statistics as a function of sample size N. The mean energy for a thermal distribution is a well-defined quantity and rapidly converges, wheras for the Tsallis distribution with $n_T = 0.5$, the mean energy does not converge.

distribution for β which does not fall into any of these three cases. Both the log-normal and the Gamma distribution are obtained in Chapter 6, and we also obtain a distribution which includes both Gamma and inverse-Gamma statistics as special cases.

Finally, the superstatistical formalism can be used to obtain the distributions of quantities oter than the energy by averaging their fixed-temperature forms over $f_\beta(\beta)$. For example, when the Cartesian component of the velocity of a particle v_i follows a Gaussian distribution at a fixed temperature, i.e., when Maxwell-Boltzmann statistics apply, the superstatistical distribution is given by,

$$f_{v_i}(v_i) = \int \frac{\sqrt{\beta m} e^{-\frac{1}{2}\beta m v_i^2}}{\sqrt{2\pi}} f_\beta(\beta) d\beta, \tag{2.82}$$

where m_i is the mass of the particle. In the special case where β follows

Gamma statistics as given by Eq. (2.79) the resulting velocity distribution is,

$$f_{v_i}(v_i) = \frac{\Gamma\left(n_T + \frac{1}{2}\right)\left(\frac{m\langle\beta\rangle v_i^2}{2n_T} + 1\right)^{-n_T-\frac{1}{2}}}{\sqrt{2\pi}\sqrt{\frac{n_T}{m\langle\beta\rangle}}\Gamma(n_T)}. \tag{2.83}$$

This has a similar form to a q-Gaussian, that is, a function of the form $e_q(-ax^2)$, and approaches $v_i^{-(1+2n_T)}$ for large values of v_i.

Chapter 3

A hybrid ion-atom trap on a chip

3.1 Background

Two distinct tracks have appeared in the development of the apparatus used for ultracold trapping experiments. The first consists of hybridising different techniques to allow for the studies of the interactions between different types of particles. A common version of these is the hybrid ion-neutral trap, which typically combines a magneto-optical trap (MOT) with a radiofrequency ion trap [17, 103, 104]. The other track is the miniaturisation of existing trapping mechanisms to increase the degree of control over the trapped particles [13, 72]. A miniaturised hybrid trap offers the best of both worlds, and would be a useful tool for the study of collisions between charged and uncharged particles at the temperatures achievable through evaporative cooling of atoms. In this chapter, I present the development and construction of a prototype hybrid ion-atom chip trap.

3.2 Design of the chip

3.2.1 Goals and constraints

The chip must be capable of the independent trapping and manipulation of both charged and uncharged particles and, ideally, should be capable of spatially separating the two in order to precisely control the state of the trapped particles before they are allowed to interact. The $^{40}Ca^{+}$ - ^{87}Rb system has previously been thoroughly characterised and a hybrid macroscopic trap demonstrated [45], and so for this chapter it is assumed that these are the two species to be trapped. In principle, however, the general design may be straightforwardly adapated for the confinement of other ions or particles with suitable Zeeman levels for magnetic trapping by altering the applied voltages and currents.

Trapped ions are highly sensitive to electric fields resulting from charges on exposed dielectric surfaces, and so the upper surface of the hybrid chip must be electrically conductive to minimize this effect. Moreover, this upper surface must also be reflective at the wavelength of light used for the laser-cooling of the neutral atoms to enable the generation of a mirror-MOT for the cooling of atoms prior to loading into the magnetic trap (Chapter 2). This suggests the use of a two-layer structure, in which the upper layer consists of an array of optically-reflective electrodes for the generation of the surface-electrode ion trap, and a lower layer containing current-carrying structures for magnetic trapping. This permits the device to be designed as a separate ion chip and atom chip, provided that the geometries of these two components are chosen such that the ions and neutrals can be trapped in the same region of space. In practice, the main constraint is that the height of trapping above the chip must be large enough to minimise the heating of ions through anomalous heating [105], but still small enough that the magnetic trapping of atoms can function efficiently without requiring large currents [68].

The operation of a mirror-MOT and imaging of the trapped particles requires optical access to the chip in directions both parallel and at a 45° angle to the surface of the chip. Moreover, the magnetic traps require the use of Helmholtz coil pairs to generate homogenous bias fields, which must be located as close to the chip as possible to minimise the required currents, and the chip itself requires a large number of electrical connections in addition to water cooling. Since trapping experiments require ultra-high vacuum (UHV) conditions, it is necessary for the vacuum chamber to be designed to allow

the high degree of optical access and enable all the electrical connections to be made while minimizing the total volume to ensure efficient pumping. This is achieved by incorporating the chip into a vapour cell [106, 107], and so the chip design must be compatible with this structure.

3.2.2 Ion chip

To maximise the symmetry of the chip, a five-wire configuration with RF electrodes of equal widths was chosen, similar to the design in Ref. [108]. A battery of ten control electrodes, five on each side of the chip, enables the axial confinement of the ion and the compensation of stray fields. Furthermore, these allow for the principle axes of the trap to be tilted to allow for efficient laser cooling of all three degrees of freedom simultaneously if a single ion is trapped.

Using the guidelines given in Ref. [109], the width of the central electrode was chosen to be 250 μm, and the widths of the RF electrodes to be 300 μm to optimise the depth of the trap and to produce the pseudopotential minima at a distance of $z \approx 270$ μm above the surface of the chip. This operating height was chosen as a trade-off between the requirement to be able to efficiently trap atoms at the same height, and the increased heating of trapped ions close to the surface of the chip [105]. The widths of the control electrodes, $w = 1.389$ mm were again chosen based on the recommendations given in Ref. [109]. The resulting geometry is shown in Fig. 3.1, including a large grounded electrode used to shield the ions from any electric fields which may build up on the atom chip and to provide an increased surface area for the mirror-MOT. The RF electrodes are chosen to be symmetric with respect to reflection in both the x and y axes to minimize the component of the RF field along the y axis, ensuring that the axial micromotion is minimized.

In order to confirm that the structure shown in Fig. 3.1 successfully traps ions, it is necessary to calculate the electric potential resulting from applying a set of voltages to the electrodes. This may be done by constructing a basis set of functions describing the electric potential obtained by applying a voltage of $1V$ to a given electrode while keeping the remainder grounded, then weighting each of these unit potentials by the actual potential applied to the electrode and summing these together to produce the total potential. The individual functions can be obtained either numerically by means of finite-element or boundary-element methods, or through a suitable analytical model of the trapping potential. The numerical methods have the advantage of requiring

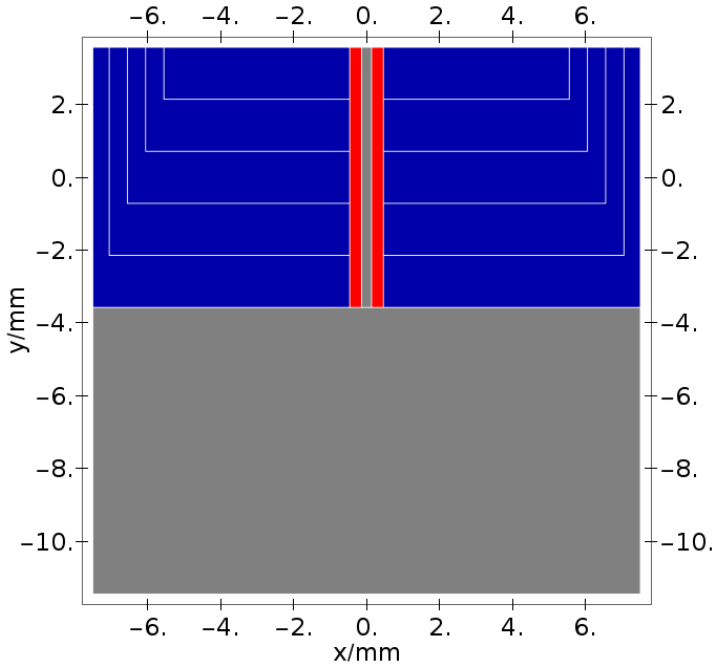

Figure 3.1: Schematic of the ion chip. Blue regions indicate DC control electrodes, red correspond to the RF electrodes, and grey regions are kept grounded. The nominal trap centre is at $x = 0, y = 0$ at a height of ≈ 260 μm above the surface of the chip.

fewer assumptions to be made, and do not require any simplification of the trapping geometry. However, calculating the potential for a given geometry may take an exceedingly large amount of computational resources, in terms of both time and available memory, and making a change to the geometry requires a recalculation of every basis function. In contrast, the analytical models require a few approximations to be made, but result in simple functional forms for the potential due to each electrode. A particularly useful model is the gapless plane model [109]. In this model, the gaps between the electrodes are ignored, and the assumption is made that the conductive surface occupies the entire xy plane. Under these conditions, the unit potential

for a rectangular electrode with corners at (a_1, b_1) and (a_2, b_2) with an applied voltage of 1V and all other regions in the plane kept at 0V is given by [109],

$$U_i(x, y, z, C_i) = \frac{1}{2\pi} \sum_{(m,n)\in(1,2)} (-1)^{m+n} U_c(x, y, z, a_m, b_n) \tag{3.1}$$

where C_i denotes the set of coordinates $\{a_1, a_2, b_1, b_2\}$ for electrode i and,

$$U_c(x, y, z, a, b) = \arctan\left[\frac{(x-a)(y-b)}{z\sqrt{z^2+(x-a)^2+(y-b)^2}}\right]. \tag{3.2}$$

The total electric potential is then found by summing over all electrodes,

$$U(x, y, z) = \sum_i V_i U_i(x, y, z, C_i). \tag{3.3}$$

This model may then be extended to include the effects of the gaps between electrodes, but the resulting corrections are typically only on the order of a few percent [109, 110]. The simplest such correction is found by enlarging each electrode to extend to the middle of each gap [109], and for the trapping geometry shown in Fig. 3.1, the potential for the RF electrodes calculated using this gap correction is a very good approximation to the numerical potential found using finite element methods, as can be seen in Fig. 3.2. Thus, this analytical model is used to calculate the properties of the ion chip to avoid introducing errors due to the limited resolution of the finite element calculations.

The pseudopotential minimum is located at a height of 261 μm above $x = 0$, $y = 0$, and to minimise the excess micromotion, the minimum of the DC potential used for axial confinement must coincide with this location. The method of Lagrange multipliers is used to calculate the voltages to apply to each DC electrode to produce an axial potential with a specified frequency under the constraints that the minimum is at the required position and that $\sum_i V_{DC,I}^2$ is minimised [111]. As an example, a target axial frequency of $120 \times 2\pi$ KHz is chosen, for which the required DC voltages are on the order of ± 1 V. Using the calculated DC voltages, and a nominal RF signal of zero-to-peak amplitude 200 V and frequency $20 \times 2\pi$ MHz, the Mathieu stability parameters can be calculated for an ion mass of $m_i = 40$ amu. As a result of the weakened symmetry of the surface electrode trap compared to

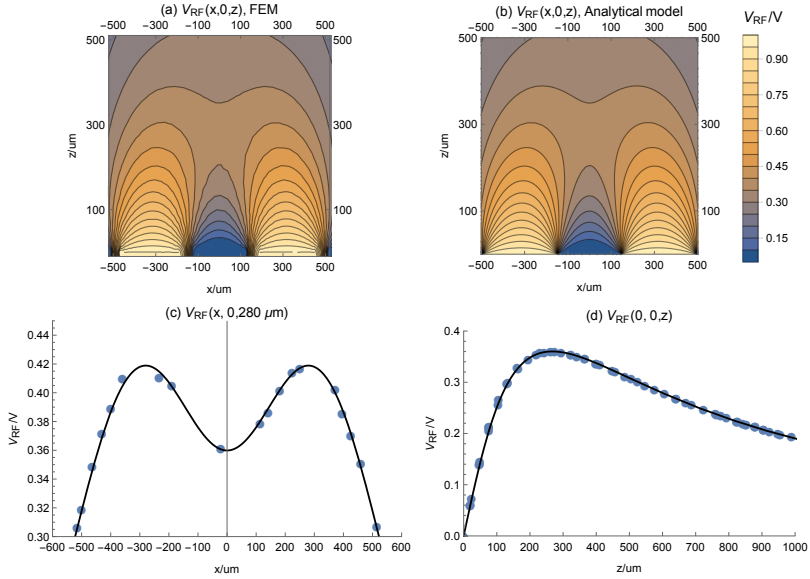

Figure 3.2: The potential generated by applying an electric potential of 1 V to the two RF electrodes of the surface electrode chip trap with geometry shown in Fig. 3.1, while keeping the remaining electrodes grounded. (a) Contour plot of the potential in the xz plane, calculated using a finite element method solver (EMS plugin for SolidWorks [73]), for a nominal gold thickness of 1 μm deposited on top of the ceramic wafer of thickness 200 μm, resting on a dielectric surface. (b) The analytical prediction for the potential in the xz plane, calculated using the model of Ref. [109] with the electrodes extended to meet in the middle of each gap to produce a gapless plane. (c) and (d) show a comparison of the numerical and analytical potentials at the saddle-point of the potential.

three-dimensional geometry, it is possible for there to be substantial coupling between the axes, and it is not known a priori that the motion of an ion can be treated independently for each axis. The generalised Mathieu parameters which take into account any possible coupling between the axes are given by,

$$q_{jk} = \frac{-2V_{RF}}{\Omega^2 m_i} \frac{d}{dj} \frac{d}{dk} U_{RF}(x, y, z), \tag{3.4}$$

and

$$a_{jk} = \frac{4}{\Omega^2 m_i} \frac{d}{dj} \frac{d}{dk} \sum_i V_{DC,i} U_{DC,i}(x, y, z), \tag{3.5}$$

for $j, k \in (x, y, z)$, where the derivatives are evaluated at the centre of the trap [109]. The resulting stability matrices are,

$$Q = \begin{pmatrix} 0.24853 & 0 & 0 \\ 0 & -0.00006 & 0 \\ 0 & 0 & -0.24846 \end{pmatrix}, \tag{3.6}$$

and,

$$A = \begin{pmatrix} -0.0005 & 0 & 0 \\ 0 & 0.00014 & 0 \\ 0 & 0 & 0.00035 \end{pmatrix}. \tag{3.7}$$

These matrices are diagonal and so the motion of a trapped ion can be treated independently for each of the three axes using the one-dimensional Mathieu equation as described in Chapter 2. The secular frequencies are found to be $(\omega_x, \omega_y, \omega_z) = (1.76, 0.120, 1.79) \times 2\pi$ MHz, and the depth of the pseudopotential was calculated as ≈ 151 meV. Since the axial frequency is much less than the radial frequencies, the equilibrium position of the majority of the trapped ions will lie on the trap axis, minimising the excess micromotion and the rate of RF heating. The combination of the pseudopotential and the static potential in the xz plane is shown in Fig. 3.3.

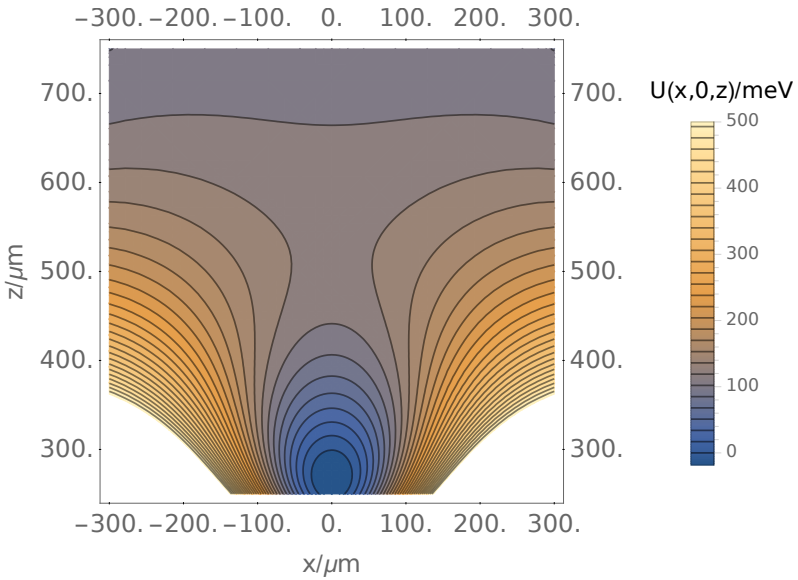

Figure 3.3: Contour plot of the sum of the time-averaged pseudopotential and the static potential for the ion chip using the parameters described in the main text, showing the centre of the trap at $z \approx 260$ μm and the saddle point at $z \approx 500$ μm.

3.2.3 Atom chip

To maximise the overlap between the trapped ions and atoms, the final magnetic trap must be generated at the same location as the pseudopotential minimum of the ion trap. Since these traps are very shallow, with typical depths on the order of 1 mK, it is necessary to precool the atoms in a magneto-optical trap (MOT). In this case, the cooling is achieved in a mirror-MOT using the electrodes of the ion chip as a reflective surface. To reduce the impact of charging of these electrodes due to the reflected laser and to reduce the heating of the ions due to elastic collisions with hot atoms, the mirror-MOT should be displaced from the ions and the cold atoms transferred to the trapping region once the MOT beams have been extinguished. The atom chip must therefore be designed to generate a flexible range of potentials to enable transfer from an initial magneto-optical trap into a wide magnetic trap, compression of the magnetically trapped atoms into a smaller trap to enhance the

efficiency of evaporative cooling, and transfer of the cold atoms to the position of the final trap. Fig 3.4 shows a schematic of the layout of the wires of the atom chip which, in combination with an external homogenous bias field, enables the generation of a range of magnetic traps. The necessary bias fields are provided by a coil cage, the design of which has not yet been finalised as this is constrained by the optical access required for lasers and cameras. Preliminary calculations indicate that for rectangular coils at separations of ≈ 7 cm consisting of 25 turns per coil using wires of rectangular cross section of width 2 mm, a current of ≈ 7 A is sufficient to produce the required field magnitude of 20G at the centre with a time constant due to self-inductance on the order of 1 ms [112].

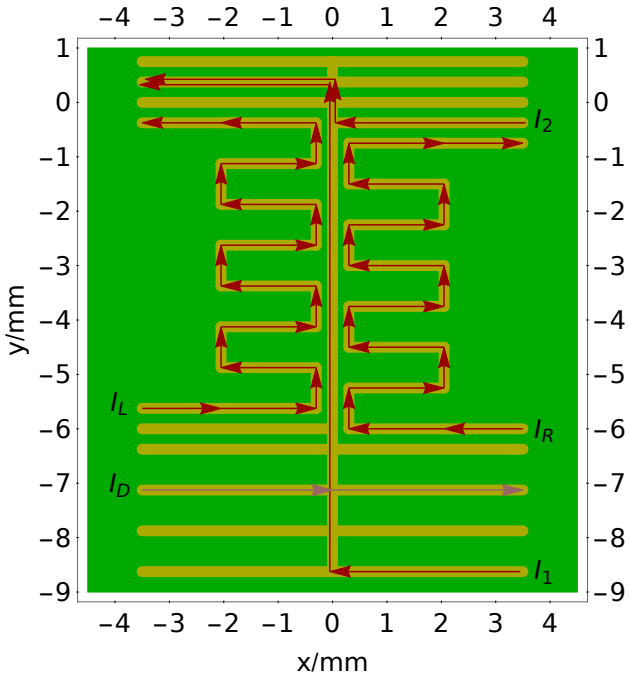

Figure 3.4: The central region of the atom chip, annotated with arrows indicating different current pathways used to produce the trapping sequence described in the main text.

By superimposing the magnetic fields resulting from passing currents through the on-chip wires with the bias field, a local minimum can be generated which is trapping in all three directions simultaneously. Two additional constraints must be met to ensure stable trapping. Firstly, the trap must be stable with respect to gravity, requiring that the minimum gradient in the direction perpendicular to the chip is 15 G/cm [68]. Secondly, to minimise the rate of Majorana transitions, it is required that the Lamor frequency $\omega_L = \mu_b g_f m_f |\mathbf{B}|/\hbar$ is large compared to the trap frequency in the radial directions [68]. These are typically on the order of a few hundred Hz, and so we require that at the centre of the trap $|\mathbf{B}| \geq 1$ mG.

In the present case, the distance between the wires used for generating the magnetic fields and the trapped atoms is typically large compared to the width of the wires. Thus, we use the thin-wire approximation to estimate the magnetic field generated for a current passing through a given wire segment [68]. For a wire of length ℓ carrying a current I from $(0,0,0)$ to $(\ell,0,0)$, the magnetic field is given by [113],

$$\mathbf{B}(x,y,z) = R(x,y,z)\frac{I\mu_0}{4\pi}\frac{1}{y^2+z^2}\begin{pmatrix}0\\ z\\ -y\end{pmatrix} \tag{3.8}$$

where $\mu_0 = 4\pi \times 10^{-7}$ H/m is the permeability of free space and,

$$R(x,y,z) = \frac{x-\ell}{\sqrt{(x-\ell)^2+y^2+z^2}} - \frac{x}{\sqrt{x^2+y^2+z^2}}. \tag{3.9}$$

This result can be translated and rotated as appropriate to calculate the field from each wire segment, and by summing over all the wire segments, the total magnetic field generated by the atom chip can be calculated. For the purposes of calculating magnetic fields in this section, only the fields due to the wire lengths visible in Fig. 3.4 are calculated. At the typical height of ≈ 500 μm of the atoms above these wires, the contributions from wires outside of the region shown are effectively negligible.

A simplified overview of the loading of the atom chip and transfer of atoms to the interaction region proceeds as follows. After an initial MOT is loaded using an external quadrupole field, an on-chip U-wire is used for a secondary MOT to optimise the location of the atoms relative to the chip, then switched off to allow for molasses cooling [107]. After the molasses cooling and opti-

cal pumping to a low-field seeking state, a Ioffe-Pritchard trap is formed by setting $I_1 = 4$ A, producing the axial potential shown in Fig 3.5. To enhance the rate of evaporative cooling, the trap is compressed in the axial direction by switching on currents in an additional wire, $I_D = 1$ A. Following evaporative cooling, the atoms are loaded into a magnetic conveyor belt formed by applying sinusoidal currents to the two meander wires I_L, I_R, with a phase difference of $\pi/2$ between the two wires [114]. Finally, harmonic confinement is provided in the interaction region using another Ioffe-Pritchard trap generated with $I_2 = 4$ A and all other currents switched off. A summary of the trap locations and harmonic frequencies, along with required homogenous bias fields is given in Table 3.1 for the static traps. These parameters are calculated using the thin-wire approximation for the magnetic field which, due to the height of the trapped atoms above the surface of the chip relative to the width of the wires, is an excellent approximation [68]. The trap locations and frequencies during the operation of the conveyor belt are not fixed, but typically the trapping height is ≈ 200 μm above the surface of the ion chip and the frequencies are on the order of 100 Hz, see Chapter 4 for more details.

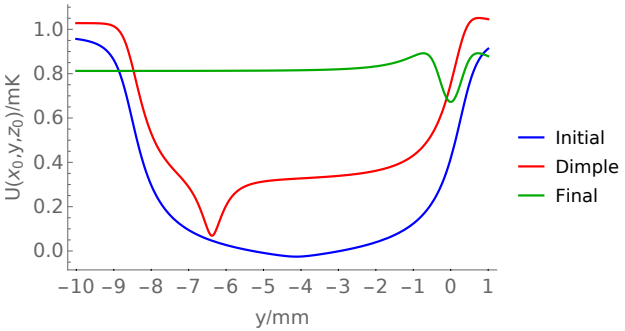

Figure 3.5: The axial potential generated by the magnetic chip trap in three of the trap stages. The initial trap (blue) is used to collect atoms from a magneto-optical trap, before compressing the atoms into a dimple trap (red) to allow for an enhanced rate of evaporative cooling. The final trapping potential (green) is used to maximise the overlap of the atoms with ions.

Stage	Trap centre/mm	$\mathbf{B}_{ext}$/G	$\omega_{x,y,z}/2\pi$
Initial	(0,-4.125,0.330)	(-15,0,0)	(1018,13.87,1023)
Dimple	(-0.0397,-6.377,0.312)	(-15,5,0)	(309.7,110.688,327.6)
Final	(0,0,0.27)	(-12.5,0,0)	(100.0,45.5,188.5)

Table 3.1: A summary of the locations and frequencies for the static magnetic traps generated using the atom chip in combination with an external bais field. All locations are given relative to the upper surface of the ion chip, with the wires of the atom chip located at 200 μm below this surface.

3.3 Construction

3.3.1 Ion chip

The first prototype of the ion chip was fabricated through laser-cutting of a stainless steel wafer, followed by electropolishing and electroplating with gold, see Fig. 3.6(a). During this initial design, it was envisioned that the ion trap would be loaded via backside loading, and so the central electrode has a small notch cut into it to facilitate this. However, the central electrode distorted during the laser-cutting process, resulting in a deformation which would negatively impact the trapping potential and use of the surface as a mirror for the trapping of neutral atoms. An attempt to eliminate this deformation by shortening the central electrode and eliminating the notch for backside loading was made, leading to the second prototype shown in Fig. 3.6(b), but this again proved unsuccessful. Moreover, due to the electrically conductive substrate it would be required that the electrodes were mechanically separated to produce electrical isolation between them, and no reliable process to do so without disturbing the alignment of the electrodes, causing damage to the atom chip, or contaminating the surface could be determined.

Consequently, the substrate was switched to a rigid aluminium oxide wafer of thickness 200μm, diced into squares of 20mm $\times$ 20mm (CoorsTek, 99.6% Al_2O_3), see Appendix 3.5 for the design of the final ion chip. Laser cutting of this wafer was performed to produce gaps of a nominal width of 45 μm (Fachhochschule Nordwestschweiz, Brugg-Windisch), with the result shown in Fig. 3.6(c). A titanium seed layer was evaporated onto the surface followed by the evaporation of gold to a nominal thickness 1 μm to produce the electrically conductive and optically reflective surface (Swiss Centre for Electronics and Microtechnology, Neuchâtel). The reflectivity of the gold surface in terms of

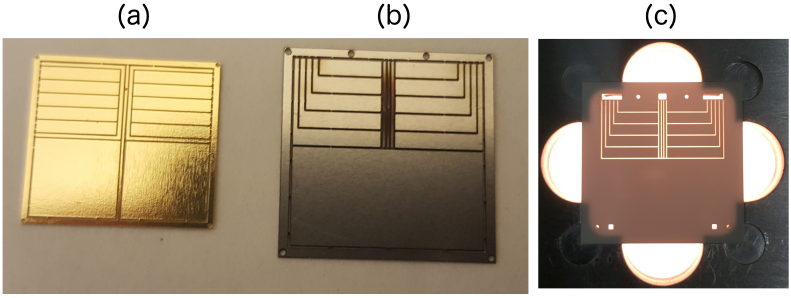

Figure 3.6: (a) The initial prototype of the ion chip constructed from laser-cut stainless steel after electropolishing and gold plating. (b) The second prototype, featuring a shortened central electrode with no hole for backside loading, an increased surface area, and electrodes connecting at the top of the chip rather than at the sides to avoid the blocking of lasers by electrical connections. (c) Microscope image of the laser-cut ceramic wafer used as the basis for the ion chip. The small circular cutouts are used as alignment holes to aid in aligning the ion chip to the correct position on the atom chip, and the rectangular cutouts are to provide access to the pads on the atom chip for electrical connections between the two chips.

the power of the reflected laser light compared to the incoming laser light was found to be $\geq 90\%$ at the wavelength $\lambda = 780$ nm used for operation of the rubidium MOT.

3.3.2 Atom chip

In addition to the wires required for the magnetic trapping, the atom chip provides connections between these wires and external current supplies, and likewise establishes electrical connections between the ion chip and voltage supplies, see Appendix 3.5 for the final design of the chip. The operation of the atom chip requires the use of relatively high currents (4 A) for extended periods of time, which leads to resistive heating of the atom chip and potential damage to the wires. Thus, it is necessary to ensure that the heat generated can be efficiently removed. Consequently, the atom chip consists of a printed circuit board (PCB) constructed from an insulated metallic substrate to provide a built-in heatsink and a high thermal conductivity. The PCB was manufactured by a commercial company (Beta Layout) using a

1.5 mm thick aluminium substrate with the conductive copper layer of thickness 35 μm separated from the substrate by a 100 μm thick layer of dielectric polymer. To ensure that these PCBs were vacuum compatible, four of the PCBs as recieved from the manufacturer were loaded into a vacuum chamber and baked at a temperature of ≈ 150°C, finding no significant alteration in the pressure achieved following cooldown. All current carrying wires have a minimum width of 200 μm and are made wider outside the centre of the chip to minimise the total resistance of the wires, which were typically found to be $< 1\Omega$. All external connections are made in the corners of the chip to ensure that there is good optical access along the x and y axes, and are designed to be compatible with header pins with spacing at standard pitch. A photograph of the atom chip is shown in Fig. 3.7.

3.3.3 Heatsink and U-bar

Although the atom chip is able to generate a quadrupole field for the operation of a MOT, this field is distorted from that of an ideal quadrupole and so does not efficiently capture atoms from background vapour [69]. An improved quadrupole field is provided by flattening out the central part of the U wire leading to an increased capture velocity and density of collected atoms [69]. This structure is included in a watercooled heatsink mounted to the back of the atom chip, with the additional benefit that this structure allows for removal of the heat generated during operation of the atom chip [107]. Both the U-bar and the heatsink are machined from copper using a design based on that of Ref. [107], with watercooling connections on the reverse of the heatsink, see Fig. 3.8

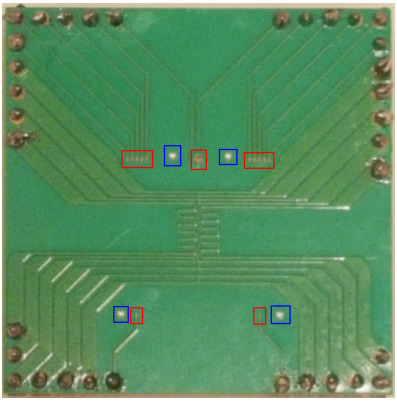

Figure 3.7: A photograph of the printed circuit board used as the atom chip, showing the wires used to generate the series of magnetic traps. The exposed copper areas outlined in red are used to establish electrical connections to the ion chip, while the circular regions marked in blue are milled regions to aid in aligning the ion chip into the correct position on the atom chip. The connections around the outside of the chip are soldered connections to header pins to connect the current and voltage carrying wires to external sources.

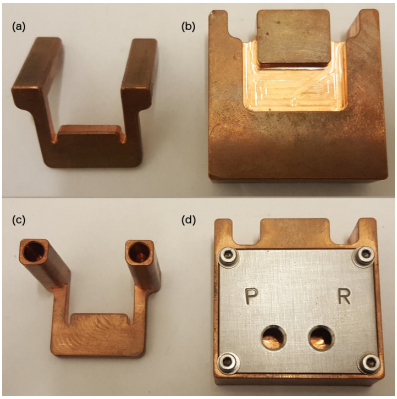

Figure 3.8: (a) and (c): The U-bar structure used to generate the quadrupole field required for the mirror-MOT. The holes in the reverse side (c) are sized to fit standard banana plugs for connection to a current supply. (b) and (d): The copper heatsink, with groove for the integration of the U-bar visible in (b) and connections for water-cooling shown in (d).

3.3.4 Assembling the hybrid chip

A small amount of Torr Seal was used to attach the two chips together, using the holes cut into the ion chip to guide the alignment process. The assembled hybrid chip is shown in Fig. 3.9(a). To establish electrical connections between the chips a wedge wirebonder was used (Devoltec, aluminium wire of thickness 50 μm) to connect between the upper surface of the electrodes and the copper pads exposed on the base PCB. Sample wirebonds can be seen in Fig. 3.9(b). Electrical testing confirmed that voltages could be applied to each electrode individually with no short-circuits.

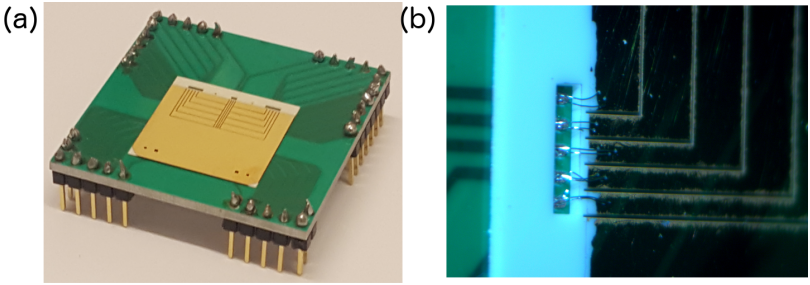

Figure 3.9: (a) Photograph of the hybrid chip with header pins soldered around the outside to enable electrical connections to external current and voltage supplies. (b) Microscope image of the wirebonds connecting the ion chip to the atom chip. Some damage to the ends of the gold coating is noticeable due to cleaning and failed wirebonds.

One of the key advantages of the hybrid chip is that, instead of being mounted inside a vacuum chamber, it may be directly used as the wall of a miniaturised vacuum chamber [106, 107]. This has two main benefits. Firstly, the optical access to the chip is greatly increased compared to a traditional setup of a large vacuum chamber with optical viewports. Secondly, all of the electrical connections may be made in air rather than through electrical feedthroughs. This is especially beneficial for the connection between the RF electrodes and the external RF signal, as it results in a short path length and so a small total capacitance. The vapour cell is constructed by gluing a fused silica cuvette of inner dimensions 3cm × 3cm × 3cm and thickness 2.5mm (see Appendix 3.5) onto the atom chip using vacuum-compatible epoxy, as shown in Fig. 3.10. The cuvettes were manufactured by Hellma Analytics,

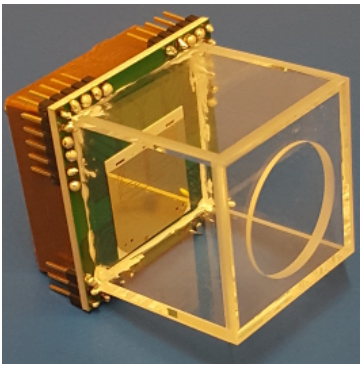

Figure 3.10: Photograph of the completed hybrid chip vapour cell assembly with the copper heatsink mounted on the reverse.

Zumikon and feature an open face with a hole of diameter 23 mm drilled into the opposing face. Initially, the attachment of a cuvette to a hybrid chip was performed using a heat-curing epoxy (EpoTek ND-353) with a multi-day cure schedule [107]. Unfortunately, due to the differential in the heat expansion coefficients of the base PCB and the quartz, this was not successful and lead to fracturing of the two cuvettes used to trial this procedure. The replacement of ND-353 by an epoxy which did not require a heat cure (Agilent Torr Seal) allowed for the attachment of the cuvette to the hybrid chip without cracking of the cuvette. However, only one out of the three cells glued in this manner produced a hermetic seal. Moreover, in this case the epoxy layer was sufficiently thick to reduce the optical access to surface of the chip. To test the achievable vacuum pressure for this cell, a glass-to-metal adaptor (Kurt J Lesker GMQS125F3) was attached using Torr Seal to the face of the cuvette opposite the chip to enable flanging to a vacuum system.

3.3.5 Vacuum system

The small trapping volume also allows for a reduction in the required pumping capacity to reach ultrahigh vacuum conditions, with a schematic of the vacuum system used shown in Fig 3.11. The vacuum system is constructed around a central six-way cube (Kurt J Lesker CU6-0275M) attached to a four-way cross (KJL C-0275) to provide connections for all the required com-

ponents. In order to provide isolation from the environment and increased optical access to the chip, the vacuum system is designed to be mounted below an optical table (ThorLabs, 1m × 1 m surface area), see Fig. 3.11(b). The glass-to-metal adapter of the vapour cell is connected to the cube via a nipple (KJL FN-0275S) through a central hole in the optical table of diameter 75mm, with the total length between the cell and the cube chosen to be slightly longer than the thickness of the optical table to ensure that there is sufficient optical access to the cell.

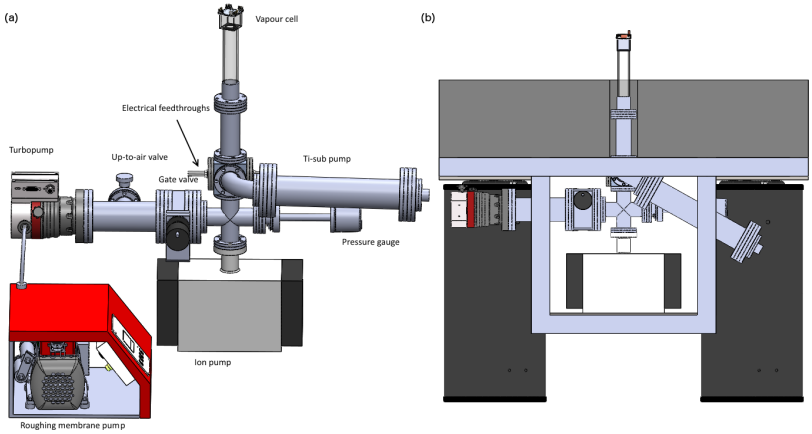

Figure 3.11: (a) Annotated schematic of the vacuum system used for the hybrid chip experiment. (b) Schematic of the vacuum chamber mounted to a framework suspended under the optical table. For clarity, a cut-away of the optical table is shown to depict the central hole through which the vapour cell is connected to the vacuum system, and two of the legs supporting the optical table have been removed. The ion pump is bolted to the framework to provide mechanical stability.

The initial vacuum is achieved through use of a membrane pump and a turbopump, supplied as a single unit (Pfeiffer HiCube Eco 80). These pumps, however, introduce vibrations to the system which may couple to the motion of the trapped atoms and lead to heating [13]. As a result, after the base vacuum is achieved these pumps are sealed off by closing the gate valve and then switched off. The vacuum is then maintained by a combination of a 40 L/s ion pump (Agilent VacIon Plus 40) and a titanium sublimation pump (Agilent 9160050) mounted in a custom nipple (KJL), and attached to the

system via an elbow to minimise the flux of titanium into the central cube. The surface area of the vacuum chamber surrounding the sublimation pump is fairly low, and the titanium film saturates in a few days requiring frequent deposition of a new layer. A set of electrical feedthroughs in the central cube enables connections to calcium and rubidium ovens (AlvaTec). The pressure of the vacuum chamber is monitored using a cold cathode gauge (Pfeiffer IKR270) mounted on the cross near the ion pump.

There is a large distance between the pressure gauge and the vapour cell, and so it cannot be assumed that the measured pressure accurately corresponds to the pressure in the experimentally relevant region. Using the simulation software Molflow+ [115, 116], the ratio of the pressure in the vapour cell to that measured at the pressure gauge can be estimated for the geometry shown in Fig. 3.11. It is assumed that the only gas present is molecular hydrogen H_2, and that this is absorbed either by the ion pump operating at the quoted pumping rate for H_2 of ≈ 60 L/s, or by a freshly deposited titanium layer with a sticking coefficient of 0.06 [117]. The outgassing rate of hydrogen from stainless steel is highly dependent on the bakeout temperature and on the previous treatment of the surface [118]. Thus, we consider the two limiting cases in which the desorption is either entirely from the steel regions of the vacuum chamber or entirely from the fused silica. The pressure reported by Molflow+ is proportional to the total outgassing rate, and to eliminate this dependency the ratio of the pressure at two points is calculated. In this case, we are interested in the ratio of the pressure at the cell to the ratio of the pressure at the vacuum gauge, p_{cell}/p_{gauge}. When the outgassing is primarily from the stainless steel we find $p_{cell}/p_{gauge} \approx 1$. Conversely, when the outgassing from the fused silica is much greater than the outgassing from the steel, we find $p_{cell}/p_{gauge} \approx 6$, indicating that in this regime the measured pressure is not a reliable indicator of the pressure in the vacuum cell beyond an order-of-magnitude estimate.

Bakeout of the system is performed using a procedure designed to minimise the risk of thermal damage to the cuvette [107]. An initial bakeout is performed using a blind flange in place of the glass-to-metal adaptor at a temperature of up to 150C, monitored from three points on the vacuum chamber. Once the pressure has stabilised, the temperature is gradually reduced until room temperature is achieved. The chamber is then flooded with nitrogen through the up-to-air valve, and the blind flange removed to allow for attachment of the hybrid chip. This is then baked at a low temperature of ≈ 100 C using multiple layers of insulation to ensure that no severe thermal

gradients are present. Using this procedure, the lowest pressure achieved with the vapour cell attached was measured to be 3×10^{-9} mbar after one week, including two 24 hour bakeout cycles. Baking for an extended period of time would likely be sufficient to further reduce this pressure, but could not be verified due to the development of a leak at high temperature.

3.3.6 Optical setup

The laser cooling of calcium ions requires light at 397 nm to address the $4^2S_{1/2} \rightarrow 4^2P_{1/2}$ transition used for the cycling transition, and an additional laser at 866 nm to prevent the accumulation of population in the metastable $3^2D_{3/2}$ state due to spontaneous emission from the excited state [119]. Cooling along a single axis is typically sufficient to cool all the modes of a crystal due to the rapid exchange of energy through Coulomb collisions. In order to avoid charging of the electrodes by the UV light [120], this axis should be parallel to the surface of the chip and the beam sufficiently well collimated to minimise the stray light which reaches the surface. Moreover, to eliminate the impact of micromotion on the laser cooling, the laser should be aligned with the symmetry axis of the trap, with the additional benefit that since this is the axis of weak confinement, the overlap of the ions with the central region of the laser is maximised. Thus, both the 397 nm and 866 nm lasers are set such that they are parallel to the y axis and pass through the centre of the trap to optimise cooling.

In contrast, the trapping of the neutral rubidium atoms is more complex, and requires multiple lasers addressing the $5^2S_{1/2} \rightarrow 5^2P_{3/2}$ transition at different frequencies to target the correct states, see Fig. 3.12(a) for an overview of the states and required lasers. The frequencies and lifetimes of these transitions are compiled elsewhere, see e.g. [121].

Trapping the rubidium in the initial MOT stage requires that all the degrees of freedom are addressed by a pair of counterpropagating lasers red-detuned from the $F = 2 \rightarrow F' = 3$ transition, which for the mirror MOT configuration requires one pair in the axial direction and two further lasers reflected from the surface of the chip. As a result of off-resonant excitation to the $F' = 2$ state followed by spontaneous emission to the $F = 1$ state, leading to the accumulation of population in this state and requiring the use of a repumping laser addressing the $F = 1 \rightarrow F' = 2$ transition to close the optical cycle. Transfer of atoms to the $F = 2, m_f = 2$ hyperfine state suitable for magnetic trapping can be done by addressing the $F = 2 \rightarrow F' = 2$ transition

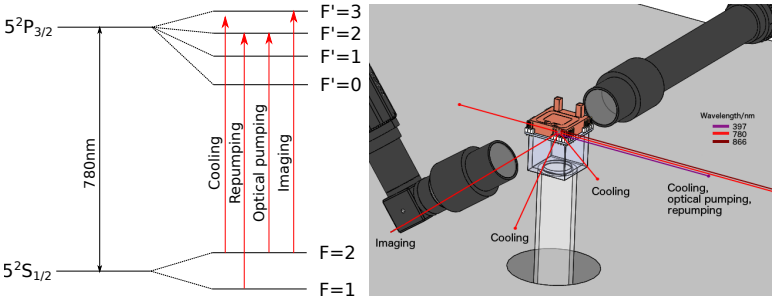

Figure 3.12: (a) Level structure of ^{87}Rb showing the required transitions required for the magneto-optical and magnetic trapping, adapated from Refs. [107, 121]. Gaps between states are not to scale. (b) Schematic of the paths of the lasers and the camera setup, annotated with the functions of the multiple lasers at wavelengths of 780 nm, see text for details. The laser at 397 nm is used for the laser-cooling of calcium ions, and the 866 nm laser is a repumper to prevent the accumulation of Ca^+ in the metastable $3^2D_{3/2}$ state.

with circularly polarised light [107]. Since there is no fluorescence during the magnetic trapping stage, the rubidium must be imaged by absorption spectroscopy, requiring an additional laser set to the resonant frequency of the $F = 2 \rightarrow F' = 3$. Thus, four cooling beams, a repumper, an imaging beam, and an optical pumping beam are required. Since the $F' = 2$ and $F' = 3$ states are separated by only ≈ 267 MHz [121], the required frequencies to address $F = 2 \rightarrow F' = 2, 3$ transitions can be generated through the use of a single laser locked to a suitable frequency, split into multiple beams, and the precise frequency set using acousto-optical modulators. For this purpose, a laser seeded using light from the $1, 3$ crossover resonance was provided by A. Johnson. The repumping from the $F = 1$ state requires a separate laser due to the large energy difference between the $F = 1$ and $F = 2$ states. A schematic of the optical setup in the region around the vapour cell is shown in Fig. 3.12(b) and annotated with details of the lasers.

Imaging of the trapped particles is achieved using a pair of telescopes consisting of an EM-CCD camera (Rolera EM-C2), an objective lens (Nikon MM200, 5x magnification), and an adjustable telescopic mount to control the distance between the objective and the camera. One telescope is mounted to allow for imaging in the plane perpendicular to the trap axis, while the other is angled to produce a view of the remaining plane without blocking the

optical access required for the lasers, see Fig. 3.12(b).

3.3.7 Electronics

Initial tests with a helical resonator by K. Najafian demonstrated that an RF signal at 20 MHz and an amplitude of 200V could be successfully applied to the RF electrodes of the hybrid chip. The voltages for the static confinement are on the order of ± 1 V and so may be output directly from a digital-analogue converter, filtered to eliminate noise, and applied to the control electrodes of the ion chip. Multiple current sources are required for the trapping of neutral particles, all of which were obtained from commercial suppliers. The U-bar used for the initial generation of a MOT requires a high current of up to 60 A (B&K Precision 1693). The atom chip itself requires only currents up to 4 A at most, but these must be as stable as possible to avoid heating of the trapped neutrals due to current fluctuations [68]. A set of current sources capable of outputting the required ± 4 A with current noise $< 10^{-6}$ A were obtained from a commerical supplier (High Finesse). The currents in the external coils to generate the required homogenous bias fields are supplied from a three-channel current supply (HAMEG HMP4030) capable of generating currents up to 10 A with a residual RMS ripple of < 1 mA.

3.3.8 Experimental control

The procedure for loading of the magnetic trap requires a precise sequence of currents applied to both the on-chip wires and the external coils used to produce homogenous bias fields, and for the lasers responsible for trapping and imaging to be switched off at the correct time. To this end, a simple interface for the control of the voltages applied to the electrodes and signals sent to the current generators was written in C++ using the Qt GUI library. This software directly interfaces with the current supply for the bias coils, and controls an Omega DAC card for the output of the voltages used to control the current output from the other current supplies. Pre-programmed routines for the generation of specific current sequences are then implemented in C++ as a simple series of functions, enabling rapid development and optimisation of the magnetic trapping sequence, and which may be extended to interface with the rest of the experiment to ensure that the lasers are switched on and off at the correct times.

3.4 Conclusions

A miniaturised hybrid ion-neutral trap was designed, fabricated, and assembled into a vapour cell, achieving a vacuum pressure on the order of 3×10^{-9} mbar after a short bakeout procedure. With further baking and a refinement of the procedure to attach the fused silica cuvette to the atom chip without blocking optical access to the chip, the device designed here would greatly increase the flexibility of experiments in ion-neutral trapping.

3.5 Appendix: Technical drawings

For reference, technical drawings of the ion chip, atom chip, and fused silica cuvette are included here.

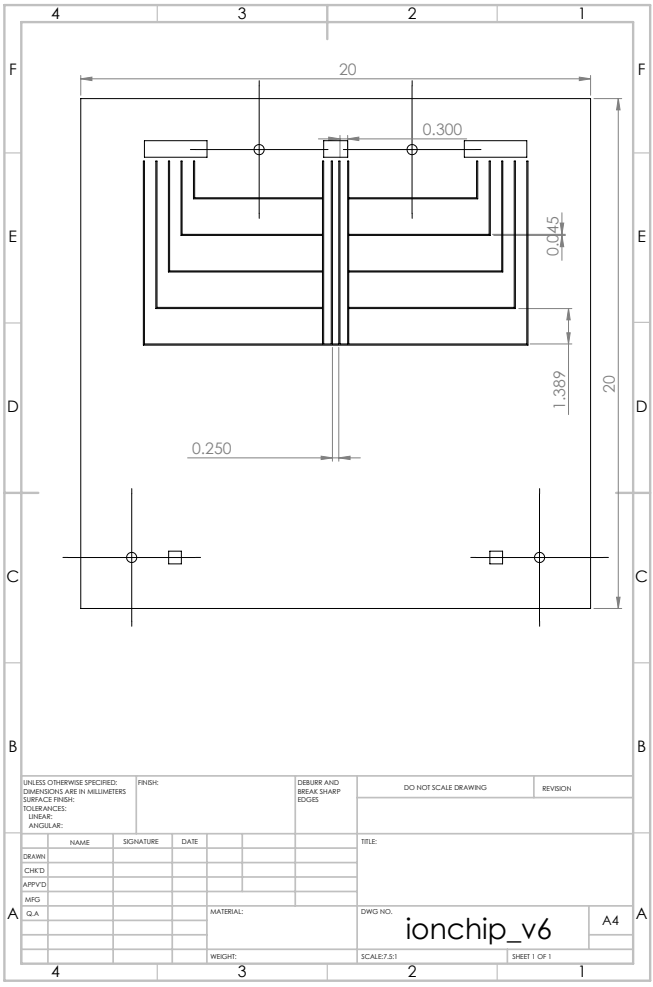

Figure 3.13: The final design of the ion chip showing the electrode widths, dimensions of the wafer, and the locations of gaps used for alignment and electrical connections. All dimensions are in mm.

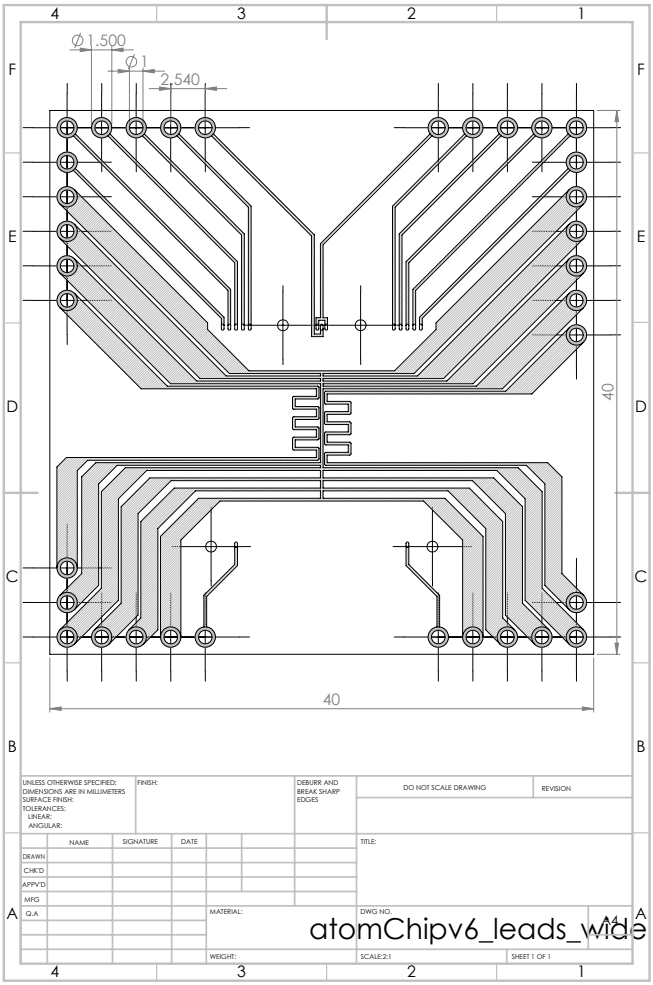

Figure 3.14: The layout of the wires on the PCB used as the atom chip. Shaded regions indicate wires, with darker shading indicating exposed copper. All dimensions are in mm.

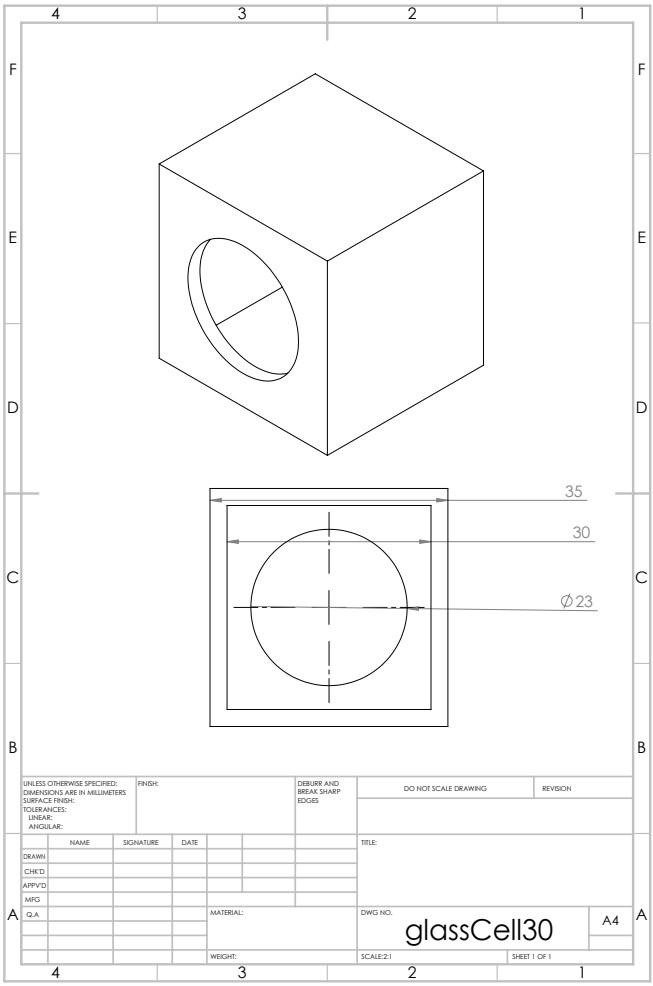

Figure 3.15: The design of the fused silica cuvette used as the vacuum chamber. All dimensions are in mm.

Chapter 4

Numerical simulations of trapped particles

4.1 Motivation

For a single particle moving in a simple (e.g., harmonic) potential subject to deterministic forces, it is often possible to solve the equations of motion analytically. When multiple interacting particles are present, the potentials are more complicated, or stochastic forces are present, the equations of motion are significantly more complicated and frequently may not possess analytical solutions. In order to characterise the behaviour of particles in the hybrid trap, an alternative approach is therefore required. In this chapter, I discuss how the force acting on particles in the hybrid trap may be implemented in molecular dynamics simulations, and present the results of these simulations performed to characterise the hybrid chip.

4.2 Implementation of molecular dynamics simulations

The general equation of motion considered for these simulations for the particle number i is given by,

$$m_i \ddot{\mathbf{r}}_\mathbf{i} = -\nabla[U(\mathbf{r}) + \sum_j U_{i,j}] + F_{scatt} + F_{stoch.} \tag{4.1}$$

where m_i is the mass of the particle, $\mathbf{r_i}$ is the position of the particle, $U(r)$ is the trapping potential, F_{scatt} is the force due to interaction with lasers, $\sum_j U_{i,j}$ is the interaction potential with all other particles indexed by j, and $F_{stoch.}$ represents any stochastic heating forces which may be acting on the trapped particles. These forces are in general non-linear, and so finding an analytical solution is not always possible. Instead, by considering the force acting on a particle with a known position and velocity during a small period of time δt, updated values for the position and the velocity can be calculated. Thus, Eq. (4.1) can be numerically integrated from a set of initial conditions to calculate the trajectories of the particles up to a later point in time. For these simulations, the numerical integration is performed using the Velocity Verlet algorithm, chosen for its simplicity, computational speed, and the important property that it is stable for oscillatory motion [122, 123]. The timestep δt is chosen to be much less than the smallest timescale relevant for the dynamics, either based on the motional frequencies or the model of laser cooling used.

4.2.1 Trapping potentials

In Chapter 3, it was demonstrated that the trapping potential of the surface electrode ion trap could be approximated to a high degree of accuracy using simple analytical functions [109]. Likewise, due to the distance between the neutral atoms and the wires of the atom chip, the magnetic fields can be calculated using the thin-wire approximations [68]. Thus, in both cases, the trapping potential and the forces acting on the particle can be calculated analytically based on these models, with the expressions for the electric potentials and magnetic fields given in Chapter 3. The primary benefit is that this avoids the requirement to fit a high-order, multidimensional polynomial to the potential calculated numerically. This ensures that the potential obeys the correct boundary conditions, i.e., that at large distances from the trap centre

it smoothly decays to a constant value, wheras a polynomial diverges to infinity. Moreover, using the analytical models ensures that all the anharmonicities and asymmetries of the trapping potential are automatically included, rather than having to ensure that the polynomial includes a sufficient number of terms to reproduce these effects. Finally, there is an additional benefit in that trapping potentials can be rapidly altered to take into account changes in geometry without having to first perform a time-consuming finite element method calculation.

4.2.2 Laser cooling

A number of routes are possible to simulate the process of laser cooling and the associated heating. Typically, in molecular dynamics simulations, a fixed temperature is enforced through methods such as rescaling of the velocities or applying a combination of friction and heating to the particles involved [87, 123]. For the simulations described here, it is preferable to use a more physical model for the heating and cooling of the particles, especially if these can be directly implemented by simulating the scattering of photons. The scattering rate for a particle at a position $\mathbf{r}$ and velocity $\mathbf{v}$ due to a laser of frequency ω_l and k-vector $\mathbf{k}$ exciting a transition with frequency ω_0 is given by [62],

$$R_s(\mathbf{r},\mathbf{v},\Delta m_f) = \frac{\Gamma_{12}}{2}\frac{I/I_{sat}}{1+I/I_{sat}+4(\omega_l-\omega_0-g_f\mu_B\Delta m_f|\mathbf{B}(\mathbf{r})|-\mathbf{k}\cdot\mathbf{v})^2/\Gamma_{12}^2}. \tag{4.2}$$

where $\Delta m_f = m'_f - m_f$ is the change in the quantum number for the Zeeman sublevel during the absorption of a photon. The values of the transition wavelength $\lambda_0 = 2\pi c/\omega_0$ (where c is the speed of light) and Γ_{12} relevant for the laser cooling of ^{87}Rb and $^{40}Ca^+$ are given in Table 4.1. The saturation intensity can be calculated from these values using Eq. (2.5) and is also listed in this table, but in practice for the simulations described in this chapter we instead simply define the intensity of the laser in units of the saturation intensity such that this value does not need to be calculated, as only the ratio I/I_{sat} enters the scattering rate. In this section, three methods are outlined to simulate the laser cooling of particles based on this scattering rate. For brevity, in this section it is assumed that there is no magnetic field and so the Δm_f parameter is irrelevant and thus is suppressed, see Section 4.4.1 for the scattering rate taking into account a magnetic field.

Parameter	^{87}Rb	^{40}Ca^{+}
λ_l/nm	780	397
Γ_{12}/s^{-1}	38.1×10^6	132×10^6
τ/ns	26.2	7.6
I_{sat}/W m^{-2}	16.7	431

Table 4.1: Parameters for the laser cooling of ^{87}Rb and ^{40}Ca^{+}, taken from Ref. [121] and [124] respectively. For convenience, the lifetime of the upper state $\tau = 1/\Gamma_{12}$ and the saturation intensity are also shown.

Continuous model

If the scattering rate is very high compared to the other forces acting on the particle, it may be appropriate to model it as a continuous force. This is found by multiplying the change in momentum with each absorption event by the average scattering rate,

$$F_s = \hbar k \langle R_s(\mathbf{r}, \mathbf{v}) \rangle. \tag{4.3}$$

This expression may either be used directly or, if the velocity of the particles is known to remain low, expanded in terms of a Taylor series to first order in v produce a friction-like force [87]. The friction force, however, leads to an overestimation of the rate at which paticles are cooled as discussed further in Chapter 5. In both cases, the heating due to spontaneous emission and fluctuations in the rate of absorption needs to be artifically added by including a noise term. For a single laser parallel to the z axis, the temperature of the motion along axis $j \in (x, y, z)$ increases according to [62]

$$\frac{1}{2} k_B \frac{dT_j}{dt} = (\delta_{z,j} + \frac{1}{3}) R_s(\mathbf{r}, \mathbf{v}) \frac{1}{2} m v_r^2, \tag{4.4}$$

where $\delta_{z,j}$ is the Kronecker delta and $v_r = \hbar k/m$ is the recoil velocity [62]. Summing over j, then assuming that an additional process (e.g. collisions between particles) exists to equalise the temperature for each axis such that $T_x = T_y = T_z = T$ produces,

$$\frac{3}{2} k_B \frac{dT}{dt} = m R_s(\mathbf{r}, \mathbf{v}) (v_r)^2. \tag{4.5}$$

The same heating rate can be achieved by applying one kick per timestep if the magnitude of this kick is set to $v_k = \sqrt{2\delta t R_s(\mathbf{r}, \mathbf{v})} v_r$, where δt is the length of the timestep. This generates an isotropic heating of the motion along each axis, which for laser cooling is valid when collisions between the trapped particles are sufficiently frequent to ensure that thermal equilibrium exists, or when multiple weak lasers are used to cool all axes simultaneously. If the heating is not isotropic, then the magnitude of each component of the kick vector should be calculated separately to produce the required heating rate. In practice, v_k is frequently set simply to a fixed value independent of the scattering rate, and tuned to reproduce experimentally observed temperatures, including the contributions from other heating effects [87]. This has the benefit of being computationally fast and straightforward to implement, but has the drawback of making it imposible to distinguish the heating to due to the photon scattering from heating due to other sources. Furthermore, if this method is employed, the heating rate is decoupled from the scattering rate, and so a particle sufficiently far from resonance that it no longer scatters photons would be heated at the same rate as if it was in resonance.

Stochastic scattering

As an alternative to artificially including a heating term and ensuring that this correctly reflects the rate of heating for each component of motion, we next consider the possibility of generating the heating due to photon scattering at the same time as the cooling force. Two methods are employed to do this, with the first used for simulations of cooling in a magneto-optical trap, and the latter for simulations of the cooling of ions in a radiofrequency trap. In the first case, the product $R_s(\mathbf{r}, \mathbf{v})\delta t$ is interpreted as the mean number of photons scattered during a given timestep, $\langle N_p \rangle$. Under the assumption that the photons are scattered independently of each other, and that the rate of scattering remains constant within a timestep, the number of scattered photons follows Poisson statistics [63],

$$f_{N_p}(N_p) = \langle N_p \rangle^{N_p} e^{-\langle N_p \rangle} / (N_p!). \tag{4.6}$$

For each laser-cooled particle at each timestep, $\langle N_p \rangle = R_s(\mathbf{r}, \mathbf{v})\delta t$ can be calculated and used to determine a random number of scattering events to apply. Each event consists of a change of the ion's momentum by one step of $\hbar k$ in a fixed direction, and one step of the same magnitude but in a

random direction. This produces the momentum change representing the cooling and heating due to spontaneous emission, and since the number of events is random, this also results in the heating due to fluctuations in the number of events. This implementation was used for simulations of a moving magneto-optical trap (MOT) finding good agreement with experiment [125]. This model is also used for the simulations of a MOT generated using an on-chip U-wire, see Section 4.4.1.

The scattering of photons is not a purely independent process due to the finite time between the absorption and re-emission processes, during which the atom cannot absorb another photon, and as such some deviation from Poisson statistics is expected. We therefore next take the case in which the lifetime of the excited state is large compared to the size of the timestep, and $R_s(\mathbf{r}, \mathbf{v})\delta t << 1$ such that absorption and emission are both rare events. In this case, the particle cannot be assumed to instantaneously decay from the excited state, but may remain there for a finite number of timesteps. To account for this, each particle is assigned a variable stating whether it is in the ground or excited state. At each timestep, if the particle is in the ground state it has a probability to make a transition to the excited state. Conversely, if it is in the excited state, it has a probability to undergo either spontaneous or stimulated emission back to the lower state. In each case, the transition is accompanied by an appropriate change in the ion's momentum, according to whether it is an absorption, spontaneous emission, or stimulated emission. The relevant probabilities may be calculated using the Einstein rate equation model for laser cooling discussed in Chapter 2, in which the population of the upper state is described by a differential equation of the form [62],

$$\dot{p}_2 = \gamma_a(1 - p_2) - \gamma_e p_2 - \Gamma_{12} p_2 \tag{4.7}$$

where Γ_{12} is the natural linewidth and γ_a is the rate constant for absorption and γ_e is the rate constant for spontaneous emission. For a two-level system with no degeneracies, $\gamma_a = \gamma_e = \gamma$, where γ is given by,

$$\gamma = \frac{\Gamma_{12}\Omega_R^2}{4\delta_d^2 + \Gamma_{12}^2}, \tag{4.8}$$

to ensure that the steady-state value of p_2 is equal to that predicted from the optical Bloch equations. Here, δ_d is the total detuning from resonance and Ω_R is the Rabi frequency defined in terms of the intensity I and the saturation

intensity of the transition I_{sat},

$$\Omega_R^2 = \frac{1}{2}\frac{I}{I_{sat}}\Gamma_{12}^2. \tag{4.9}$$

Typically, the intensity is of the same order of magnitude as the saturation intensity, and so $\Omega_R \approx \Gamma_{12}$ is on the order of megahertz for the transitions considered here. The probability for a ground-to-excited state transition during a time δt is approximately given by $\gamma\delta t$, and equivalently if a particle is in the excited state it decays via stimulated emission with a probability $\gamma\delta t$, and via spontaneous emission with probability $\Gamma_{12}\delta t$. In each timestep, the probability for the atom to undergo a transition is calculated based on its current state, position and velocity, and compared to a random number in the interval $[0, 1)$ to determine if it occurs, and the variable recording the state of the atom updated accordingly. If the atom is in the ground state, then only absorption is possible, wheras if the atom is in the excited state the probabilities for spontaneous and stimulated emission are calculated and used to determine both the likelihood of emission and which of the two mechanisms takes place. As shown in Fig. 4.1(a) this procedure correctly reproduces the steady-state population of the upper state as predicted from the OBE, and therefore generates the correct rate of both spontaneous and stimulated emission. The oscillatory behaviour during the first tens of nanoseconds is not reproduced, but given that typical simulations last for orders of magnitudes longer this has no significant effect.

In addition to updating the state, each transition also results in a change in the momentum of the particle, with the magnitude of this change given by $\hbar k$ and the direction either chosen isotropically for spontaneous emission, in the direction of travel of the laser for absorption, or opposite to the direction of travel of the laser for stimulated emission. The resulting change in temperature over time is shown in Fig. 4.1(b) in comparison to the friction model. For the friction model in this case, the heating rate is chosen at each timestep for each particle based on the calculated scattering rate. The rate of cooling and steady-state temperature achieved at low intensities are close to those predicted using the simple friction model, see Fig. 4.2. A modification to the state-tracking model in which the possibility for stimulated emission is neglected but the rate of spontaneous emission is kept fixed results in a slightly lower steady-state temperature. This is likely a result of the fact that the presence of stimulated emission inhibits spontaneous emission, resulting

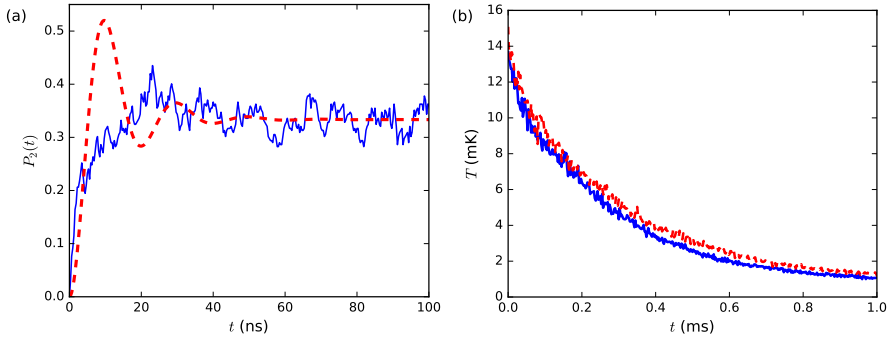

Figure 4.1: (a) Population P_2 of the upper state of a two-level atom as a function of time t given by the solution to the optical Bloch equation (black dashed line) and fraction of ions in the upper state of an ensemble of 262 Ca^+ ions undergoing discrete transitions between a lower and upper state according to the "state-tracking" model described in the text (blue solid line). (b) Secular temperature T as a function of time t of a system of 262 ions undergoing laser cooling at an intensity of $0.2I_{sat}$ and a detuning $\delta_L = \Gamma_{12}$ for the friction-force (black dashed line) and state-tracking (blue solid line) models of laser cooling.

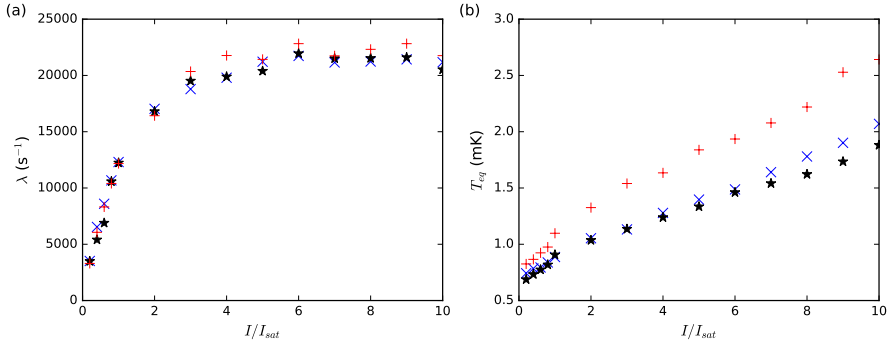

Figure 4.2: (a) Cooling rate λ and (b) equilibrium temperature T_{eq} of a cloud of 262 Ca^+ ions using the friction-force model (red +), the present state-tracking model (blue ×) and the state-tracking model without stimulated emission (black ⋆) as a function of laser intensity at a detuning $\delta_L = \Gamma_{12}$. See text for details.

in less efficient cooling and thus a higher temperature.

This model is only appropriate if the probability for the particle to undergo both absorption and emission in the same timestep can be neglected. This typically requires very small values of δt to ensure that $\delta t R_s$ is small, which may be computationally inefficient if the scattering rates are high or if a long period of time must be simulated. In general, $R_s \lesssim \frac{1}{2}\Gamma_{12}$ [62], in turn requiring that δt is much less than the lifetime of the excited state, $\tau = 1/\Gamma_{12} \approx$ 1–100 ns. For trapped ions, the timestep must also be small compared to the period of the RF motion, $2\pi/\Omega \approx 50$ ns, and so the requirement that the timestep is small compared to τ leads only to a modest increase in the number of timesteps required to simulate a given timespan. Moreover, the trapped ions are cooled by a single laser for which the state-tracking model as given above can be directly implemented, and therefore this method is used to simulate the laser-cooling of ions in this thesis with the timestep set to 50 ps. An equivalent state-tracking model has also been used for the simulation of laser cooling by other ion-trapping groups, again for the case of ions interacting with a single cooling laser [57, 126]. For the simulations of the laser cooling of atoms in the on-chip MOT, however, a much larger number of particles are simulated for greater periods of time, and the atoms interact with multiple cooling lasers. For reasons of computational efficiency, and to avoid the requirement to extend the state-tracking model to take into account the competing scattering processes from each laser, the cooling of atoms in the on-chip MOT is simulated by calculating the average scattering rate and assuming a Poisson distribution for the actual number of photons scattered by each atom as discussed above. This requires only that the velocity changes sufficiently slowly that the scattering rate does not appreciably change during a timestep, i.e. $R_s(\mathbf{r}(t), \mathbf{v}(t)) \approx R_s(\mathbf{r}(t+\delta t), \mathbf{v}(t+\delta t))$. This enables the use of much greater timesteps, with very close results found in Section 4.4.1 for timesteps of 10 ns and 1 μs.

4.2.3 Particle interactions

As discussed in Chapter 2, a generic model for the interaction between a pair of particles is given by a multipole expansion of the interaction potential $U_{i,j}(\mathbf{r_i}, \mathbf{r_j})$,

$$U_{i,j}(\mathbf{r_i}, \mathbf{r_j}) = \sum_{n=1}^{n=\infty} C_n(\theta, \phi) |\mathbf{r_i} - \mathbf{r_j}|^{-n}, \tag{4.10}$$

where $|\mathbf{r_i} - \mathbf{r_j}|$ is the distance between the two particles and $C_n(\theta, \phi)$ is a coefficient describing the strength of the interaction, which may depend on the relative orientation of the two particles as parameterised by the angles θ, ϕ. This potential must be evaluated once for each pair of atoms, and so the time taken to calculate the forces resulting from these interactions scales on the order of the number of particles squared. It is therefore computationally beneficial to neglect this interaction if at all possible, typically when the particle densities are low and the forces resulting from this interaction are weak and short-ranged.

The dominant interaction between ions is the Coulomb interaction, $n = 1$, which for the typical temperatures and densities of particles in a radiofrequency ion trap is sufficiently strong that it cannot be neglected. Thus, this is included in all simulations of trapped ions in order to correctly reproduce the structure of the Coulomb crystals and the phenomena of RF heating. It is assumed that this force is sufficiently stronger than the remaining terms in the multipole expansion to allow for the neglect of all other interactions. This is further justified by the fact that the atomic ions considered here are spherically symmetric and the distance between ions is much greater than the radius of the ions. Under these conditions, no permanent higher-order multipole moments exist, while induced multipole moments are short-ranged compared to the $n = 1$ interaction and hence may be neglected at typical ion-ion distances on the order of microns [127, 128]. Thus, the ions may be modelled as point particles interacting solely through the Coulomb potential, where C_1 is independent of θ, ϕ.

The interaction between neutral atoms is much weaker, and is neglected for simulations of atoms in magnetic traps due to the low densities considered here. However, in dense magneto-optical traps, an effective repulsion force arises between atoms due to photon rescattering, which leads to a change in the density distribution from a Gaussian distribution to one which is essentially flat. In Ref. [94] the force due to this rescattering is shown to be proportional to $1/r^2$ and so it may be straightforwardly included by including a term analogous to the Coulomb interaction. This is not performed for the simulations considered here, as again it is assumed that the MOT operates in the low-density regime. Due to the large difference in time scale between the motion of the ions and the neutral atoms, no simulations were performed in which both the ions and neutrals were simultaneously present, and so no attempt to parameterise the force acting between them was made. The interactions between an ion held in the hybrid trap colliding with a co-trapped

neutral gas are studied in more detail in Chapter 6, using an alternative technique to evaluate the trajectory of the ion over a greatly extended period of time than can be reasonably achieved in molecular dynamics simulations.

4.2.4 Background gas

An additional source of heating is that due to collisions between trapped particles and residual background gas in the vacuum chamber. Neutral particle traps are shallow and so these collisions usually lead to loss of the trapped particle. For the simulations performed in this chapter this effect is neglected as it is assumed that the atom is lost without transferring a significant amount of energy to the rest of the ensemble. Ion traps, however, are sufficiently deep that the energetic ion remains trapped and redistributes the energy obtained from the collision to the remainder of the ions. If a large number of ions are trapped simultaneously, then this results in an effectively constant heating rate, which may be implemented through a series of random kicks. In smaller crystals, however, the energy gain per ion is larger, and the rate of collisions lower, such that this approximation no longer holds. This results in a time-dependent temperature which is explored in Chapter 5.

4.2.5 Trap imperfections

During operation of the ion trap, the deposition of metal or metal oxides leads to the formation of small regions on the electrodes at a different potential to the remainder of the electrodes. These patch potentials lead to additional forces acting on the ions, which may either directly cause heating or lead to an increased amount of excess micromotion, which in turn leads to an increase in the rate of RF heating [71, 129]. Surface electrode ion traps are especially sensitive to the anomalous heating caused by fluctuating fields on the trap surface, although at the surface-to-ion height of 300 μm these are less significant than in traps operating closer to the surface [130]. Trapped atoms, meanwhile, are sensitive to current noise in the wires, which alters the trap position and frequencies and so cause heating [131]. For the simulations performed to characterise the hybrid chip trap, these effects are neglected as they cannot be accurately quantified in the absence of experimental results, but the achieved temperatures should be taken as lower bounds on the values on the values which would be observed experimentally.

4.3 Simulations of ions in the hybrid trap

All simulations of trapped ions are performed using the time-dependent electric potential rather than applying the pseudopotential approximation. Although this requires a much shorter timestep and so increases the amount of computational time required, the time-dependent potential is necessary in order to reproduce the heating of ions due to collisions in the RF field (RF heating) [48]. Consequently, the trajectories of the ions include both the secular motion and the micromotion. For a single ion in an idealised model of the potential, the amplitude of motion, and thus the secular energy, can be obtained by fitting the exact solutions to the Mathieu equation to the numerically calculated trajectory. When multiple ions are trapped, or when the potential is not an ideal quadrupolar potential, this is no longer possible. Instead, averaging the position of the ion over a single RF period produces a very good approximation to the secular position (Appendix 4.A). By calculating the secular position at each RF period over an extended duration, the secular velocity can be obtained as the numerical derivative of the secular position. The secular velocity is usually found to follow Maxwell-Boltzmann statistics (see Chapter 5), and so it is possible to assign a secular temperature to the ions based on this distribution from the mean secular kinetic energy.

Initially, simulations of the ions were performed using ProtoMOL [132], with additional code introduced to simulate the trapping potential due to the surface electrodes and implement the state-tracking method of laser cooling. Further software was developed using the OpenMM [133] library to take advantage of GPU acceleration and to provide a graphical interface to aid in setting up simulations. Simulations performed with 1000 ions on OpenMM using single GPU acceleration (nVidia GeForce GTX 650) proved to be four times faster than the ProtoMOL code running on four CPU cores (Intel Xeon CPU E5-2687W), wheras for smaller numbers of trapped ions the computational speed was approximately equal for both. For the generation of the data sets reported here the ProtoMOL software was primarily used due to the wider range of outputs, wheras the OpenMM software was used to investigate the effects of changing trapping and laser cooling parameters.

To characterise the ion trap, a simulation of 200 trapped ions at an assumed background pressure of 10^{-9} mbar of hydrogen molecules was performed. A time-dependent voltage of 0-to-peak amplitude 200V and frequency $20 \times 2\pi$ MHz was applied to the two RF electrodes to produce the radial confinement. Static voltages were applied to the control electrodes as calculated

in Chapter 2 to produce an axial secular frequency of 120 KHz. The laser cooling is modelled using the state-tracking method, taking a detuning from resonance of Γ_{12}, see Table 4.1 for this value, and assuming $I/I_{sat} = 1$. At this background pressure and number of trapped ions, a collision occurs once every ≈ 39 ms [134]. For this size of crystal and the laser cooling parameters used here, if an ion undergoes a head-on collision with a hydrogen molecule of velocity 1775 m/s, corresponding to a temperature of 300K, the crystal is recooled to equilibrium within ≈ 0.5 ms, see Fig. 4.3. The equilibrium secular temperature is given by $T_{eq} = 1.3$ mK, calculated from the period 2–3ms of Fig. 4.3. If we assume that the temperature remains at this value until the next collision, averaging the temperature over the entire 39ms interval produces a value of $\overline{T} = 1.5$ mK. In this case, although the collisions lead to a slight change in the temperature compared to the equilibrium value, this is effectively negligible in comparison to the heating due to the scattering of photons. In Chapter 5, a system for which the laser cooling is much less efficient is investigated, and it is found that the collisions lead to a significant impact on the dynamics of the ion crystal.

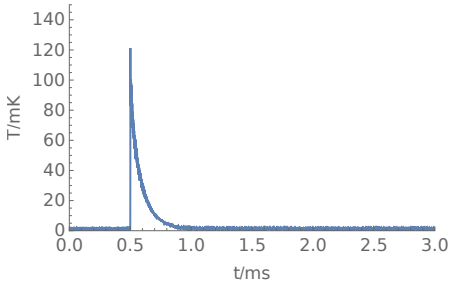

Figure 4.3: The evolution of the secular temperature of a crystal of 200 ions confined in the surface electrode chip trap following a head-on collision with a hydrogen molecule of velocity 1775 m/s at $t = 0.5$ ms.

Experimentally, the ions are imaged by means of a CCD camera collecting the light emitted during laser cooling. The depth of field of the imaging systems used is typically small enough that ions above or below the focal plane appear blurred, and due to the long exposure time of the CCD camera of a few hundred milliseconds, the ions are further blurred as a result of their motion. Comparing the results of numerical simulations to experimental images, therefore, requires that both of these effects are taken into account

when generating a simulated CCD image [87, 135]. This may be achieved as follows. At the start of the simulation, a three-dimensional histogram is initialised. At each timestep, the position of each ion is assigned to a bin of the histogram, and the value of each bin increased by the number of ions present in it at that timestep. After a sufficiently long amount of simulation time, this produces the average density distribution of that ensemble of ions. The histogram may then be converted into a two-dimensional image by choosing an imaging plane, e.g., yz, and separating the three-dimensional histogram into a set of two-dimensional histograms based on that plane. Each of these planes is a different distance away from the focal plane, and by applying a Gaussian blur to each plane based on this distance and the resolution of the imaging system, then superimposing the results, an image can be constructed with the correct blur due to the depth of imaging and the motion of the ions, and used as a comparison to experimental data. By altering the number N and the temperature T of the ions in a numerical simulation, the closest match to a given experimental image can be found, providing an estimate for the experimental values of N and T. The resulting simulated CCD image for the crystal of 200 ions is shown in Fig. 4.4 in the absence of collisions with background gas. As a result of the fact that the axial secular frequency is much less than the radial secular frequency ($\omega_y = 120 \times 2\pi$KHz, $\omega_z = 1.8 \times 2\pi$MHz), the crystal is highly elongated, and the majority of the ions lie close to the line on which the RF field nulls.

Figure 4.4: A simulated CCD image of 200 ions trapped in the potential generated by the surface electrode chip trap. The image represents the three-dimensional density distribution collapsed into the yz plane corrected for the finite imaging resolution, see text for details. The parameters for the image shown here are based on the experimental imaging system used in Ref. [136], for which the spatial resolution is given by 0.53 μm/pixel and the standard deviation of the Gaussian blur is given by $\frac{1}{7}$ multiplied by the distance of the plane from the central plane in pixels.

4.4 Simulations of atoms in the hybrid trap

During the purely magnetic trapping stage, the only forces acting on the trapped atoms are those resulting from the magnetic potential, gravity, and collisions between atoms. At the low temperatures relevant for magnetic trapping, the displacement of the atoms from the equilibrium position is small, and in the Ioffe-Pritchard traps used the potential in this regime is effectively harmonic. The average time between elastic collisions for a given atom due to collisions with the other atoms, τ_{el} is given by [38],

$$1/\tau_{el} = n_0 \sigma_{el} \sqrt{2} \sqrt{16 k_b T} \pi m, \tag{4.11}$$

where n_0 is the particle density at the centre of the trap and σ_{el} is the elastic cross section, $\sigma_{el} = 7.9 \times 10^{-16}$ m^2 [137]. For a harmonic trap with trapping frequencies $\omega_x = \omega_y = \omega_z \approx 100 \times 2\pi$ Hz, n_0 can be calculated assuming a Gaussian density distribution, and at a temperature of $T = 10$ μK this leads to $\tau_{el} \approx 34000/N$ s, where N is the number of atoms. For these collisions to become significant requires either a very long simulation time or a very high number of trapped particles, both of which are not computationally feasible . We thus limit ourselves to the regime in which collisions can be neglected. In this case, the molecular dynamics simulations are most useful for characterising either stochastic forces acting on the ions, or time-dependent potentials. In this section, two such cases are presented: the operation of a magneto-optical trap (MOT) using an on-chip wire and the long-range transport of atoms in the magnetic conveyor belt sequence. In both cases, all simulations are performed in ProtoMOL.

4.4.1 On-chip MOT

In these simulations, the force acting on the atoms is calculated by finding the average scattering rate from each beam and using this to generate a random number of photons to scatter in each timestep under the assumption that this follows Poisson statistics, as described in Section 4.2.2. Due to the distortion of magnetic fields generated by on-chip wires from the ideal quadrupole (see Chapter 2), the scattering rate was corrected to take into account the angle between the lasers and the magnetic field direction as described in Ref [138]. In short, for each atom and each laser the angle θ between the local magnetic field and the k-vector of the laser is calculated and used to determine the

relative probabilities for transitions for each possible change in m_f based on the polarisation of the laser. Defining $h = 1$ for a laser with circularly polarised light with a clockwise direction of rotation relative to the k-vector of the light, and $h = -1$ for anticlockwise rotation, these probabilities are given by [138],

$$\begin{aligned} P(h, \Delta m_f = \pm 1) &= \frac{1}{4}(1 + h\Delta m_f \cos\theta)^2 \\ P(h, \Delta m_f = 0) &= \frac{1}{2}\sin^2\theta. \end{aligned} \tag{4.12}$$

If the k-vector of the light is aligned with the local magnetic field, $\theta = 0$, and $\Delta m = +1$ transitions only occur if $h = 1$, i.e., if the light has a clockwise circular polarisation, and likewise $\Delta m = -1$ transitions can only occur from the laser with anticlockwise circular polarisation. If the k-vector and the field are not aligned, then scattering is possible from other beams. The scattering rate from a given laser is then given by the sum of the scattering rates from each m_f state taking into account the Zeeman shift due to the magnetic field and the Doppler shift due to the velocity of the atom (Eq. (4.2)), and weighted by these relative probabilities,

$$R_s(\mathbf{r}, \mathbf{v}) = \sum_{\Delta m_f = -1,0,1} P(h, \Delta m_f) R_s(\mathbf{r}, \mathbf{v}, \Delta m_f). \tag{4.13}$$

The scattering from each laser is treated independently, but the scattering rate is calculated using an empirical correction of the saturation parameter in the denominator of Eq. (4.2), $I/I_{sat} \to 6I/I_{sat}$, to take into account the total of six lasers [138].

For the simulations performed here, the 1/e beam radius for each laser is set to 1 cm, the intensity is set to $I = \frac{I_{sat}}{2}$, and the detuning to $3\Gamma_{12}$, with the natural linewidth taken from the literature (see Table 4.1) [121]. The timestep is initially set to 10 ns, which is of the same order of magnitude as the lifetime of the excited state (28 ns). It is assumed that the reflectivity of the surface is sufficiently high that the intensity of the beams reflected from the surface is equal to that of the incoming beams. The magnetic fields are calculated using the analytical expressions for thin wires, using an on-chip U-wire carrying a current of 4A. The applied bias field was set to produce an approximate quadrupole field at a height of 3 mm above the uppermost surface of the hybrid chip, at an offset of 260 μm from the central wire. Atoms which

fall below the surface of the chip are removed from the simulation. To save computational time, it is assumed that the MOT operates in the low-density limit such that the repulsive force between atoms due to the rescattering of photons can be neglected. In the absence of experimental results with which to validate the simulations for the mirror-MOT and due to the number of approximations made in the simulations, the results obtained here should be taken only as order-of-magnitude estimates for the achieved temperatures and densities, as these will depend on the exact magnetic fields and laser intensities and detunings. In particular, note that the model for the MOT used here does not account for the requirement of a repumper for the rubidium, sub-Doppler cooling due to polarisation gradients, and the possibility for absorption from one beam and emission into another [62, 138].

To investigate the steady-state distribution of trapped atoms, simulations are performed with the atoms initial velocities sampled from arbitrary thermal distributions of temperatures 1 μK, and the positions sampled from thermal distributions corresponding to a harmonic oscillator of frequencies 100 Hz for each axis and a temperature of 1 μK. This results in a much colder and denser cloud than the steady-state, ensuring that none of the initial trajectories would lead to immediate loss of the atom, with only 15 atoms lost due to collisions with the surface of the chip during the simulation. The phase-space distributions recorded after 100 ms of simulation time, i.e., once the steady-state had been reached, are shown in Fig. 4.5 with the temperature estimated to be $T = 519 \pm 3$ μK. Here, the temperature is calculated as $T = \frac{1}{3}(T_x + T_y + T_z)$, with the temperature for each axis calculated from the standard deviation of the velocities. The reported value and standard error are calculated via the bootstrap method as the mean and standard deviation of 10'000 bootstrap replicates [64]. For an idealised model of molasses cooling using six orthogonal cooling beams with a detuning from resonance of $\delta_l = \omega_0 - \omega_l$, the steady-state temperature is given by [62],

$$k_B T = \frac{\hbar \Gamma_{12}}{4} \frac{1 + (2\delta_l/\Gamma_{12})^2}{2\delta_l/\Gamma_{12}}, \tag{4.14}$$

producing a value of $T = 449$ μK for a detuning of $3\Gamma_{12}$, which is in reasonable agreement with the value found here. With the detuning set to $\Gamma_{12}/2$ the steady-state temperature is reduced to $T = 308 \pm 2$ μK. This is again larger than the predicted value ($T = 144$ μK), and the deviation is assumed to be a result of the increased scattering rate from beams which are not correctly

aligned with the magnetic field vectors, as this enables scattering events (and thus heating) which do not cool or contribute to the restoring force. For both detunings, we find approximately the same steady-state temperatures when the timestep is increased by a factor of 100 to 1 μs, with $T = 527 \pm 4$ μK for a detuning of $3\Gamma_{12}$, and $T = 308 \pm 2$ μK for a detuning of $\Gamma_{12}/2$, implying that the deviation is not due to the length of the timestep.

It is also useful to perform simulations with an initially more energetic ensemble of atoms to determine the phase-space acceptance of the MOT, for which the timestep is again set to 10 ns. The phase-space acceptance plots are shown in Fig. 4.6 for the initial conditions of a uniform density distribution in a box the size of the vapour cell, and velocities uniformly sampled from the interval $[-20, 20]$ m/s. It can be seen that the on-chip MOT can only trap particles with a low initial velocity of less than 15 m/s, and so loading from background gas would be inefficient. This highlights the requirement for the initial MOT to be generated using a modified U-bar to increase the efficiency of loading [69].

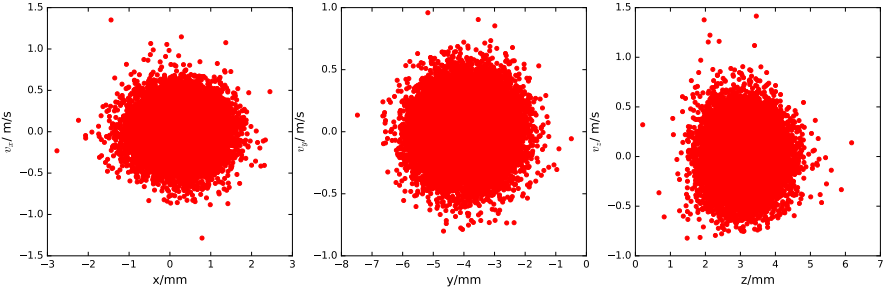

Figure 4.5: Steady-state phase space distributions for rubidium atoms trapped in a mirror-MOT with the magnetic field generated using an on-chip U-wire and a laser detuning of $3\Gamma_{12}$. The initial conditions are chosen such that the atoms start effectively at rest at the centre of the trap to ensure that the loss of atoms due to energetic initial trajectories is minimised.

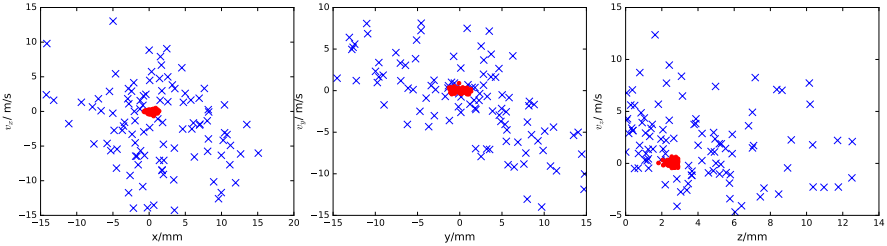

Figure 4.6: Phase space acceptance plots for rubidium atom trapped in a mirror-MOT with the magnetic field generated using an on-chip U-wire. Red points indicate the position and velocity of the 103 particles which remained trapped after 100 ms, while blue crosses give the initial position and velocity of these particles. 50'000 particles are initially generated with a uniform spatial distribution and velocities uniformly sampled in the range $\pm$20m/s, and atoms which collided with the walls of the vapour cell or the surface of the chip are not shown.

4.4.2 Magnetic conveyor sequence

After the atoms have been transferred to a Ioffe-Pritchard trap following the MOT and molasses cooling, they must be moved to a region in which they may interact with the trapped ions. This may be achieved by applying sinusoidal currents to the two square-wave shaped wires with a $\pi/2$ phase difference between the two wires [114]. This leads to an axial potential consisting of a series

of local minima, with the location of these minima advancing as a function of time as shown in Fig. 4.7. To confirm that atoms could be successfully transported in this potential, molecular dynamics simulations were performed using the time-dependent trapping potential calculated using the analytical expressions for the magnetic fields generated by the applied currents. The conveyor is operated using currents of $I_1 = 4$, $I_R = -2\cos(\omega_c t)$ and $I_L = 2\sin(\omega_c t)$ A, where $\omega_c = 5/(2\pi)$ is the conveyor frequency, with homogenous bias fields of $(-15, 5, 0)$ G applied to produce a set of Ioffe-Pritchard traps. The initial positions and velocities of 2000 atoms are generated assuming a temperature of 10 μK at a position and harmonic frequencies corresponding to the initial minima closest to the location of the dimple trap (see Chapter 3), with the trap centre at $(-0.0482, -6.06, 0.257)$mm, and harmonic frequencies of $(225, 47, 229) \times 2\pi$ Hz. The transfer from the dimple trap to this initial trap has not yet been optimised, but for this simulation we are primarily interested in the heating during the long-range transfer of atoms and so we assume the atoms start in this initial minima.

Fig. 4.8(a) shows the average position of the atoms along the y axis as a function of time, demonstrating the successful transport of atoms. The temperature of the atoms is calculated from the standard deviation of their velocity distribution along this axis and is shown in Fig. 4.8(b). Both the position and the temperature are calculated from the distributions of the 1875 atoms that are trapped in the final potential after 1 s. It can be seen that during the operation of the conveyor ($t = 0$ to $t = 600$ ms) the rise in temperature is small, confirming that this is a suitable method to transfer the atoms from the initial loading region to the interaction region. As with the initial loading from the dimple trap into the conveyor, the transfer of atoms from the conveyor to the final trap also requires optimisation to ensure that the atoms are not heated during this process. As such, the operation of the conveyor is halted at a location of $y = -1.4$ mm such that the change in temperature arises purely from the conveyor sequence. At present, this halting seems to contribute the largest amount to the increase in temperature, as can be seen in the sharp rise in Fig. 4.8(b) at $t = 600$ ms. Decelerating the conveyor rather than simply halting it may reduce the temperature increase, but this has not yet been investigated.

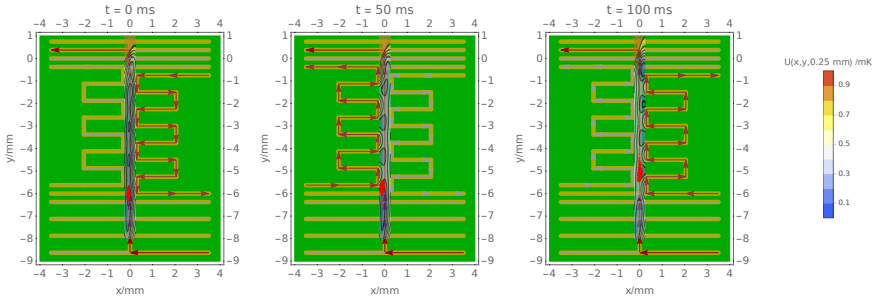

Figure 4.7: A schematic of the atom chip with the wires used to generate the magnetic conveyor sequence shown, superimposed with contour plots of the resulting potentials. The positions of atoms calculated through molecular dynamics simulations of this transport are shown as red points.

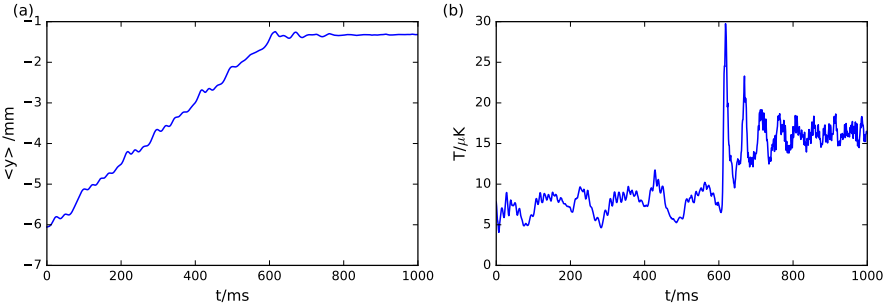

Figure 4.8: The evolution of the mean position along the axis of transport and temperature of atoms during the magnetic conveyor belt sequence, calculated using molecular dynamics simulations as described in the text for a sample of 2000 atoms at an initial temperature of 10 μK. The temperature is calculated from the standard deviation of the velocity along the y-axis. Both the position and the temperature are calculated from the sample of atoms which remain confined once the magnetic conveyor is halted at $t = 600$ ms.

4.5 Conclusions

Using molecular dynamics simulations, it was demonstrated that the hybrid chip designed in Chapter 3 is theoretically capable of trapping both charged and uncharged particles. Two models for laser cooling were investigated as alternatives to the simple model of a friction force coupled with a stochastic heating term, finding realistic values for the achieved temperatures. The long-range transport of atoms in a magnetic conveyor belt was simulated, confirming the ability to transfer atoms from an initial loading zone to a region of space in which they can interact with the ions. The ion chip was demonstrated to be able to contain 200 ions at a temperature of ≈ 1.5 mK in the presence of RF heating, collisions with background gas, and laser cooling.

4.A Numerical approximation to the secular motion

In Chapter 2, the motion of an ion in a radiofrequency trap was shown to consists of a spectrum of frequency components, primarily at the secular frequency ω, the RF frequency Ω, and the micromotion frequencies $\Omega \pm \omega$. From this, we wish to find the ion's secular motion, $\tilde{r}_j(t) = A_j \cos(\omega_j t)$. This can be done by averaging over an RF period to eliminate the fast motion of the ion. Analytically, this is achieved by means of an integral over the interval $[t - \Delta t/2, t + \Delta t/2]$, where $\Delta t = 2\pi/\Omega$ is the length of one RF period,

$$\overline{r}_j(t) = \frac{1}{\Delta t} \int_{t'=t-\Delta t/2}^{t'=t+\Delta t/2} r_j(t')dt'. \tag{4.15}$$

This integral may be evaluated using the Mathieu solutions as given in Chapter 2, but the results are more concise when the adiabatic approximation is used, and this suffices to illustrate the general principle. In this approximation, the motion of an ion in the presence of excess micromotion due to a constant force is given by, [71],

$$r_j(t) = [r_0 + A_j \cos(\omega_j t)][1 - \frac{q}{2} \cos \Omega t], \tag{4.16}$$

where r_0 is the equilibrium position of the ion and A_j is the amplitude of the ion's motion. Evaluating this expression using Eq. (4.16), we find,

$$\begin{aligned}\overline{r}_j(t) =& r_0 + \frac{\Omega A_j \cos(\omega_j t)\sin\left(\frac{\pi\omega_j}{\Omega}\right)}{\pi\omega_j} \\ &+ \frac{\Omega A_j q_j \sin\left(\frac{\pi\omega_j}{\Omega}\right)\left(\Omega\sin(\Omega t)\sin(\omega_j t) + \omega_j\cos(\Omega t)\cos(\omega_j t)\right)}{2\pi\left(\omega_j^2 - \Omega^2\right)}.\end{aligned} \tag{4.17}$$

The excess micromotion, i.e., the oscillating term proportional to r_0, is eliminated, and the intrinsic micromotion is greatly reduced. Using the small-angle approximation for $\omega_j << \Omega$, $\sin\pi\omega_j/\Omega \approx \pi\omega_j/\Omega$ simplifies this expression to,

$$\overline{r}_j(t) \approx r_0 + A_j\cos(\omega_j t) + \frac{A_j q_j \omega_j\left(\Omega\sin(\Omega t)\sin(\omega_j t) + \omega_j\cos(\Omega t)\cos(\omega_j t)\right)}{2\left(\omega_j^2 - \Omega^2\right)}. \tag{4.18}$$

The leading term of this expression gives the secular motion of the ion around its equilibrium position, subject to a small perturbation due to the intrinsic micromotion, i.e., the $\cos(\omega_j t)\cos(\Omega t)$ term found when expanding Eq. (4.16). In practice, this is sufficiently small compared to the secular motion that it can be neglected, and so this time-averaging procedure enables the extraction of the secular motion. For numerical trajectories, the integral may be approximated by a sum of the recorded values of the position during one RF period. The secular velocity can then be found by numerical differentiation of the secular position, and used to calculate the secular temperature.

Chapter 5

Superstatistics of ion crystals due to rare heating events

5.1 Introduction

It is typically assumed that an ensemble of trapped ions can be adequately described by a fixed secular temperature, such that the secular velocity of the ions follows Maxwell-Boltzmann statistics. This temperature is established as the equilibrium between the cooling of the ions due to laser or sympathetic cooling and the heating due to, e.g., patch potentials, RF heating, and collisions of the ions with residual background gas [87]. For this equilibrium to exist, these heating processes must be effectively continuous to prevent sudden increases in the secular temperature.

In molecular dynamics (MD) simulations, these heating processes are typically replaced by a single effective heating force, the strength of which is obtained by fitting to experimental data [45, 87, 139–141]. This approach neglects the underlying physical details of the heating sources and, in particular, replaces rare events which lead to strong heating with a continuous, weaker heating process. This converts the system from one which samples a broad range of temperatures into one in which the ions remain at an essentially fixed temperature after reaching equilibrium with only small displacements

from the mean.

Using the framework for MD simulations described in Chapter 4, it is demonstrated that collisions of only a single ion of the ensemble with a background gas molecule can lead to significant deviations of the secular velocities of all trapped ions from a Maxwell-Boltzmann distribution, and that the linear friction model of laser cooling is not appropriate when these collisions are present. We compare the present theoretical results to experimental data finding excellent agreement and invoke superstatistics to provide a simple explanation for the appearance of the non-Maxwellian behavior. Finally, we discuss the relevance of our results to the determination of reaction rate constants and put them into context with other recent theoretical work on the collisional dynamics of trapped ions [53, 56]. Following the original publication of these results as Ref. [52], it has since been experimentally confirmed that a combination of cooling and rare heating events in an ion crystal leads to the effects presented here [57].

5.2 Force model

The details of molecular-dynamics simulations used to characterise the trapping of ions in a radiofrequency trap were discussed in depth in Chapter 4, and the same framework is used here. Briefly, each ion is subject to a combination of forces,

$$F_i = -\nabla U(x,y,z,t) + F_{Coulomb} + F_{background} + F_{scatt}, \tag{5.1}$$

where $U(x,y,z,t)$ is the time-dependent trapping potential and $F_{Coulomb}$ is the sum of pairwise Coulomb forces acting between the ions. These two terms also implicitly account for heating by ion-ion collisions [90]. $F_{background}$ is a term representing elastic collisions with the background gas, and F_{scatt} is the force arising from interaction of the ions with near-resonant light, calculated using the state-tracking model described in Chapter 4. Heating due to experimental imperfections was neglected in the present treatment (see below). The trapping potential was formulated as [109]:

$$U(x,y,z,t) = \frac{\Omega_{RF}^2 m}{8} \sum_{i=x,y,z} (a_i - 2q_i \cos(\Omega_{RF} t)) u_i^2. \tag{5.2}$$

All simulations performed in this work use the potential of the surface-electrode chip trap described in [136] defined by $\Omega_{RF} = 8 \times 2\pi$ MHz, $q_x = 0.0824, q_y = -0.0806, q_z = -3 \times 10^{-4}$ and $a_x = -16 \times 10^{-4}, a_y = 11 \times 10^{-4}, a_z = 4 \times 10^{-4}$, where the a_i and q_i parameters were derived from numerical trapping potentials [136]. Due to a numerical error, the values of a_j, q_j used for simulations are given by these nominal values multipled by 0.964, although this does not effect the interpretation of the results and moreover does not appear to alter the agreement with experiment.

5.2.1 Collisions with background gas

Even at the ultrahigh vacuum of lower than 10^{-9} mbar usually used in cold-ion experiments, there is a significant rate of elastic collisions of ions with residual background gas, typically H_2. These collisions are primarily caused by the long range interaction between the ion and the induced dipole of the neutral molecule, and so the collision rate constant can be approximated by Langevin theory [134]:

$$k_{el} = 2\pi n_n \sqrt{\frac{\alpha'_n e^2}{4\pi\epsilon_0 \mu}}, \tag{5.3}$$

with background particle density n_n, polarizability volume α'_n and the reduced mass of the collision μ. As already shown in Ref. [87], a collision of an ion with a background gas molecule imparts momentum to the ions ejecting it from the crystal for a number of oscillation periods until it is recooled. Kinetic energy is transferred from the hot ion to the remaining ions in the crystal through ion-ion collisions resulting in an increase of the secular temperature followed by laser-recooling to equilibrium. In our simulations, the assumption is made that the collisions are purely elastic following a hard-sphere model. This is a reasonable approximation for an ion interacting with a weakly polarizable neutral particle. Although alternatives could certainly be considered, we emphasize that the effects described later in this chapter do not depend on the choice of collision model.

For a crystal consisting of 262 ions interacting with H_2 molecules at a temperature of 300K and partial pressure of 10^{-9} mbar, i.e., the one obtained experimentally in Ref. [141], an average of one collision event per 30ms takes place. A single simulation covering this period of time took approximately 10 hours. Thus, it would take a prohibitive computation time to average over the large number of collisions which occur on the timescales of typical

experiments (seconds to minutes). One method of overcoming this problem is to increase the rate and decrease the size of the momentum kicks imparted in the collisions so that the average heating rate remains the same [87]. In this way, a steady-state is reached in the simulations in only a few milliseconds of simulation time. This approach, however, does not accurately reproduce the underlying dynamics of the crystal as it creates a system which remains close to equilibrium temperature with only minor deviations which is accurate only for large crystals in which collisions are frequent [87]. The effect of rarer background gas collisions is to cause a sharp rise in the temperature followed by a slow recooling to equilibrium. In Section 5.3, we will describe an approach which preserves the essential features of the realistic heating mechanism and cooling dynamics while remaining computationally tractable.

Typically, the majority of ions in the trap remain at low secular velocities for which the linear expansion inherent in the friction force applies. However, after a head-on Ca^+ - H_2 collision at a mean relative velocity of 1775 m s^{-1}, the calcium ion is accelerated to a velocity of 170 m s^{-1}, for which the friction model is no longer valid. The force applied to an ion at this velocity by the friction term can be up to two orders of magnitude larger than the maximum scattering force for a near-optimum detuning equal to the natural linewidth of the transition used for laser cooling Γ_{12}. Consequently, the kinetic energy gained by the ion is rapidly removed before it can be transferred to the remainder of the crystal. This results in a decrease in the peak temperature and an unrealistically fast recooling to equilibrium, as can be seen in Fig. 5.1. The present state-tracking model does not rely on the friction approximation and so allows the role of collisions to be more accurately investigated.

In order to confirm that the present MD framework successfully reproduces experimental results, simulations of Coulomb crystals obtained in a surface-electrode RF ion trap used previously [136, 141] were performed. The laser intensity and detuning were set to the experimental values of $I \approx 9I_{sat}$ and $\delta_L \approx 13\Gamma_{12}$. The effect of collisions with background gas molecules at room temperature was simulated by applying a kick to a single ion at the mean collisional velocity and impact parameter at a fixed point in time (see Sec. 5.3). Simulations were carried out for a time interval equal to the mean period between collisions with background gas molecules. We obtained simulated images in a good agreement with experiment and previous simulations (Fig. 5.2) confirming the validity of the present MD approach.

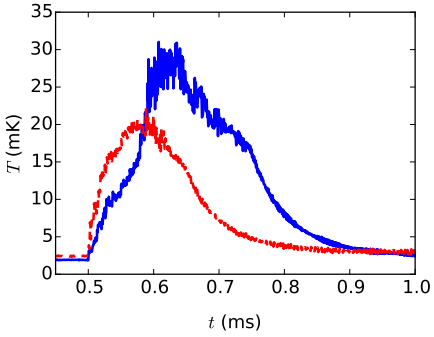

Figure 5.1: The secular temperature T as a function of time t of an ion crystal of 262 Ca^+ ions following a collision of an ion with a H_2 molecule using state-tracking (blue solid line) and friction-force (red dashed line) models of laser cooling averaged over 20 simulations. The friction model yields an unrealistically fast cooling rate resulting from a breakdown of the linear approximation to the scattering force.

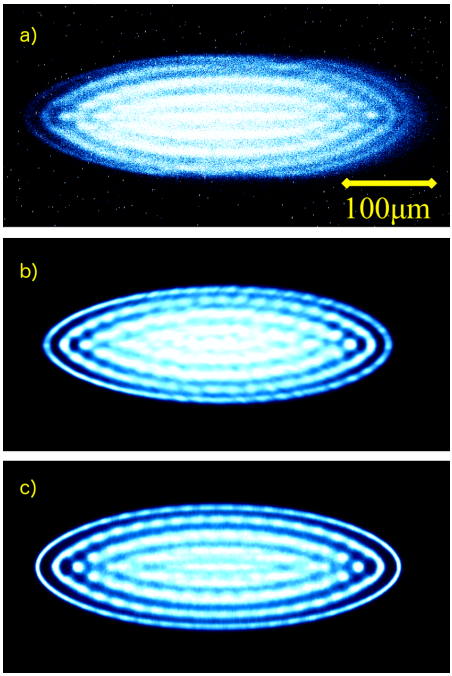

Figure 5.2: (a) Experimental and (b) simulated CCD image of 262 Ca^+ ions in the six-wire trap as previously reported in [141]. (c) Simulated image of 262 ions based on the present MD implementation described in the text.

5.3 Temperature fluctuations

Assuming that the ion motions are strongly coupled, the system is in an instantaneous thermal equilibrium (see Section 5.3.1) and so may be described by a temperature $T(t)$. Since, in thermal equilibrium, the velocity distribution for a given axis has a maximum at 0, the majority of the ions will be in the low-velocity regime for which the friction model is approximately valid, such that their mean energy decreases exponentially [62, 64]. As a result of the fact that the system is in thermal equilibrium, the mean energy is proportional to the temperature. Thus, the temperature following an increase at a time t_0 is approximated by an exponential decay to equilibrium [87, 90, 126]:

$$T(t) = T_{eq} + \Delta T(v_c, b) \exp[-\lambda(t - t_0)]. \tag{5.4}$$

Here, $\Delta T(v_c, b)$ is the increase in temperature from T_{eq} due to a collision occurring with a collisional velocity v_c and impact parameter b. It is assumed that collisions take place sufficiently infrequently such that the system recools to equilibrium in between which is the case here. Since both λ and T_{eq} are independent of the strength of the collision, they can be extracted from a set of trial simulations performed at a constant collision strength. Averaging over ten simulations, the best fit parameters were found to be $\lambda = 151$ s^{-1} and T_{eq} = 7.78 mK.

To establish values for $\Delta T(v_c, b)$, a total of $\approx$ 350 simulations were performed to sample over the range of collision velocities at an H_2 temperature of 300 K at impact parameter $b = 0$. The values of $\Delta T(v_c, b = 0)$ thus obtained are plotted in Fig. 5.3 as a function of the kinetic energy of the colliding H_2 molecules. Assuming an instantaneous energy transfer between the ions and that equipartition of energy applies, the temperature increase of the crystal should be a linear function of the kinetic energy transferred in the initial collision with the background gas molecule [48, 56, 88]. We observe this to be the case when the laser cooling is switched off following the collision, but not when the cooling remains active (see Fig. 5.3).

This phenomenon appears to be caused by the fact that at higher velocities, the transfer of energy from the ejected ion to the crystal is not instant and instead occurs over an extended period of time as shown in Fig. 5.4. The ejected ion moves on a large orbit in the trap transferring energy to the colder ions only through infrequent collisions when passing through the centre [87]. Laser cooling causes additional loss of kinetic energy reducing the radius of

the orbit. After the ion reaches a low enough energy at which it can no longer escape from the crystal, it quickly equilibrates through collisions with the other ions. In Fig. 5.4, the re-capture of the ejected ion by the crystal occurs at approximately 2 ms in the presence of a cooling laser, and is visible as a sharp maximum in the temperature of the crystal (Fig. 5.4 (a)) and steep drop in the velocity of the ejected ion (Fig 5.4 (b)). Without laser cooling, recapture occurs later and the overall increase in temperature of the crystal is also larger. From these results we conclude that the nonlinear trend in Fig. 5.3 is caused by the laser cooling process dissipating energy during the extended time between the collision and the re-thermalization of the ion which also results in a lower temperature increase of the crystal.

For a full characterization of the collision dynamics, it is necessary to consider collisions at all possible impact parameters. The average temperature increase due to collisions is then given by:

$$\overline{\Delta T} = \int \int \Delta T(v_c, b) f_{v_c}(v_c) f_b(b) \, \mathrm{d}b \, \mathrm{d}v_c, \tag{5.5}$$

where $f_{v_c}(v_c)$ and $f_b(b)$ are the distributions of collision velocities and impact parameters, respectively. Evaluation of this expression as detailed in Appendix 5.A yields $\overline{\Delta T} = 56.3 \pm 0.9$ mK for 262 laser-cooled Ca^+ ions colliding with room-temperature H_2 background gas molecules.

Thus, a time- and collision-strength-averaged temperature $\overline{T}$ can be calculated:

$$\bar{T} = \frac{1}{\Delta t} \int_{t_0}^{t_0+\Delta t} T_{eq} + \overline{\Delta T} e^{-\lambda t} dt, \tag{5.6}$$

where the averaging length Δt is taken to be the period between collisions $\Delta t = 1/k_{el}$. Using $\overline{\Delta T}$, λ and T_{eq} extracted from the simulations, the mean temperature of the experimental crystal shown in Fig. 5.2 (a) was found to be $\overline{T} = 20 \pm 1$ mK.

In Ref. [141], the same crystal was assigned a temperature of $T = 23$ mK, obtained through use of the frequent, weak collision model of Ref. [87] producing the image shown in Fig. 5.2 (b). The difference between these results is attributed to the large temperature fluctuations in the current model which were previously neglected.

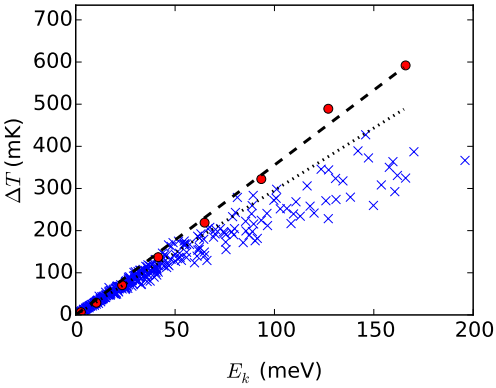

Figure 5.3: Increase in secular temperature ΔT of a Coulomb crystal of 262 Ca^+ ions following a collision with a H_2 molecule at impact parameter $b = 0$ sampled over ≈ 350 simulations (blue crosses) as a function of the kinetic energy E_k of the colliding H_2 molecule. The dotted line is a best fit to indicate the deviation from the linear trend at high E_k. Red circles indicate additional simulations performed with the laser cooling switched off after the collision, and the dashed line is a line of best fit to these data. See text for discussion.

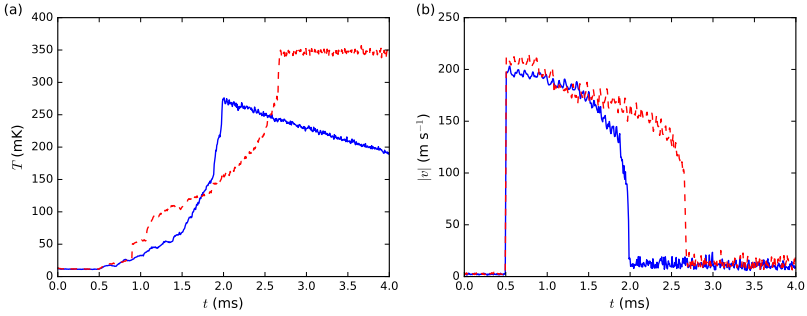

Figure 5.4: (a) Secular temperature T of a Coulomb crystal of 262 Ca^+ ions following the collision of a single ion with a H_2 molecule at a velocity of 3000 m s^{-1} and impact parameter $b = 0$ with (blue solid line) and without (red dashed line) laser cooling applied. (b) Magnitude of the secular velocity $|v|$ of the ejected ion for these two cases. See text for details.

5.3.1 Superstatistical velocity distributions

The effects of the different collision models can be investigated by sampling the secular-velocity distribution of the ions over the period Δt. For the model using frequent weak kicks to all ions, the velocity distribution is Maxwellian for a fixed temperature, as would be expected for a sample in thermal equilibrium. The realistic present model using infrequent, energetic collisions of a single ion with a single background gas molecule does not lead to a system in thermal equilibrium at a fixed temperature. The instantaneous velocity distributions of the ions at a certain point in time are found to be approximately Maxwellian, but change with time, see Fig. 5.5(a). This reflects the considerably faster timescale for the energy redistribution within the crystal than for the cooling of the entire ensemble.

To simplify the analysis, we assume that collisions occur at fixed time intervals Δt, that the temperature rise is instant following a kick, and that the system recools to equilibrium in between. Thus, only the effects of a single collision need to be considered at a time, and the secular-velocity distribution found when sampling over Δt can be written as a time average of the instantaneous thermal distributions taking into account the time-varying temperature for a given temperature rise ΔT:

$$f_v(v|\Delta T) = \frac{1}{\Delta t}\int_{t_0}^{t_0+\Delta t} 4\pi v^2 \sqrt{\left(\frac{m}{2\pi k_\mathrm{B} T(t)}\right)^3} e^{\frac{-mv^2}{2k_\mathrm{B}T(t)}} \mathrm{d}t, \qquad (5.7)$$

where the left-hand side has been written as $f_v(v|\Delta T)$ to emphasize that this represents the distribution following a specified rise in the temperature ΔT. This integral may be evaluated numerically for an arbitrary time-dependent temperature $T(t)$ and can be solved analytically for a temperature of the form given by Eq. (5.4) (see Appendix 5.B). We compare the result of this analytical solution to the distribution obtained numerically for simulations performed at a collision velocity $v_c = 1775$ m s^{-1} and an impact parameter $b = 0$ in Fig. 5.5(b). It can be seen that the distribution has a longer tail at high velocities than a standard Maxwell-Boltzmann distribution due to the periods of high temperature immediately following a collision, and is in very good agreement with the values calculated using Eq. (5.7) with $T(t)$ given by Eq. (5.4).

The two Maxwell-Boltzmann distributions plotted in Fig. 5.5(b) correspond to the time-averaged temperature (Eq. (5.6)) for $v_c = 1775$ m s^{-1},

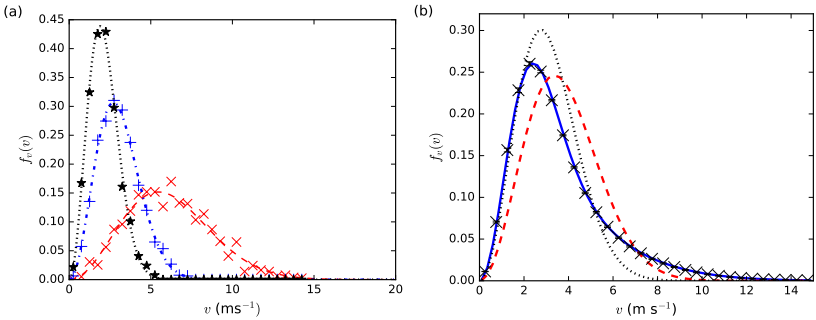

Figure 5.5: (a) Instantaneous secular-velocity distributions $f_v(v)$ of the crystal of 262 Ca^+ ions at times t=2.5 ms (red $\times$), 15 ms (blue +) and 27.5 ms (black $\star$) after a collision with a H_2 molecule. Maxwell-Boltzmann distributions fitted to the numerical results at these times are shown as dashed, dash-dotted and dotted lines, respectively. The data points are averaged over six iterations of the simulation and represent a histogram bin of width $\Delta v = 0.5$ m s^{-1}. (b) Velocity distribution of the ions in the period of time between two collisions from Eq. (5.7) (solid blue line) and the numerical distribution obtained by sampling a simulation over this interval (crosses). The red dashed line is a Maxwell-Boltzmann distribution at the average temperature $\overline{T} = 26$ mK, and the black dotted line is a Maxwell-Boltzmann distribution at $\hat{T} = 18$ mK obtained from a fit to the numerical data. In the simulation, a H_2 velocity of 1775 m s^{-1} and impact parameter $b = 0$ were assumed.

$b = 0$ of $\overline{T} = 26$ mK (red dashed line) and a temperature of $\hat{T} = 18$ mK (black dotted line) obtained from a fit of a Maxwell-Boltzmann distribution to the numerical data (crosses). Neither correctly describe the ion velocities – the distribution for $T = \overline{T}$ overpredicts the peak velocity and for $T = \hat{T}$ the high-velocity tail is lost. For this system, the temperature fluctuations are significant enough that a single static temperature cannot accurately describe the distribution of ion velocities.

The Cartesian components of the secular velocity $v_i,\ i = x, y, z$, can also be sampled over the course of a simulation producing the distribution:

$$f_{v_i}(v_i\ |\Delta T) = \frac{1}{\Delta t}\int_{t_0}^{t_0+\Delta t} \sqrt{\frac{m}{2\pi k_B T(t)}}\, e^{\frac{-mv^2}{2k_B T(t)}}\, \mathrm{d}t \tag{5.8}$$

as shown in Fig. 5.6(a) (see Appendix 5.B for an analytical solution to this

integral). Similar heavy-tailed distributions have previously been observed experimentally for atoms in an optical lattice, and in simulations of ions undergoing buffer-gas cooling [53, 54, 56, 142]. In these cases the velocity distributions are generally a good fit to a q-Gaussian, that is, the result of replacing the function e^{-x^2/σ^2} in a Gaussian distribution by a q-exponential, $e_q(-x^2/\sigma^2)$ (see Chapter 2). Indeed, the data shown in Fig. 5.6(a) can be fit to a q-Gaussian distribution with the parameterisation used in Ref. [53],

$$f_{v_i}^{(q)}(v_i) = \frac{T_0}{(1 + (v_i/\sigma)^2/n)^n}, \tag{5.9}$$

with excellent accuracy. The fit yields a width of the distribution $\sigma = 2.34$ m s^{-1} and an exponent $n = 2.72$. Fig. 5.6(a) also shows the solution of the integral Eq. (5.8) (see Appendix 5.B for the analytic expression). It can be seen that this representation is in excellent agreement with the numerical data and the q-Gaussian function.

The present results can be understood within the framework of the superstatistics of driven non-equilibrium systems, as discussed in Chapter 2 [99]. The time average over an exponentially decaying temperature performed in Eq. (5.7) is mathematically equivalent to an integration over a temperature distribution $f_T(T|\Delta T) \sim 1/(T - T_{eq})$, as demonstrated in Appendix 5.B. It has been shown previously that the low-energy limit of a Maxwell-Boltzmann distribution averaged over a fluctuating temperature is a form of Tsallis distribution [98, 99], and so the fact that the q-Gaussian represents a good fit to the data simply reflects that the ions remain in this low energy regime. Note that the parameterisation of Eq. (5.9) does not match that used in Eq. (2.82), as a result of the fact that Eq. (5.9) corresponds to the form of q-Gaussian obtained from the Tsallis entropy rather than through the superstatistical approach. By equating the two we obtain $1/(k_B\langle\beta\rangle) = 16$ mK and a Tsallis exponent $n_T = 2.22$.

Appendix 5.B also provides an analytical form for the superstatistical parameter $q_s = \langle(1/T)^2\rangle/\langle 1/T\rangle^2$ [99]. At $q_s = 1$, the system follows Maxwell-Boltzmann statistics, and values greater than 1 indicate a greater deviation from Maxwellian behavior. A numerical investigation of this parameter revealed that over a wide range of equilibrium temperatures (1-40 mK) and values of ΔT (10-200 mK), q_s is maximized for $\lambda\Delta t \approx 4$, corresponding to the situation in which the crystal has just recooled to equilibrium before the next collision occurs. For much faster ($\lambda \to \infty$) or much slower ($\lambda \to 0$)

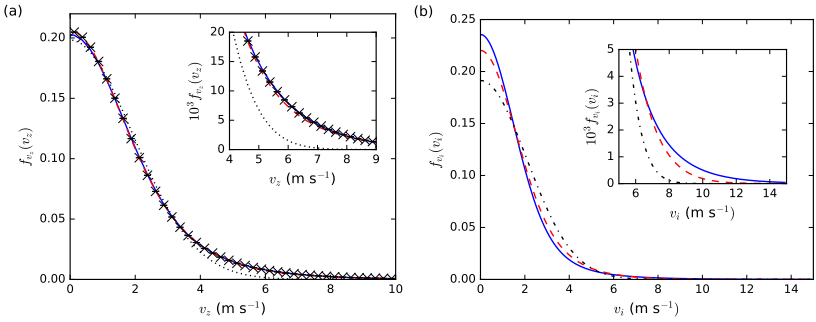

Figure 5.6: (a) Distribution of the axial component v_z of the secular velocity (crosses) sampled during a simulation over 30ms following a collision event with a H_2 molecule with $v = 1775$ m s^{-1} at impact parameter $b = 0$. The red dashed line represents a fit to a q-Gaussian function and the black dotted line to a Gaussian distribution. The blue solid line is a Maxwell-Boltzmann distribution averaged over a time-varying temperature, see text for details. The inset shows the heavy-tailed behaviour of the distributions at high velocities. (b) Superstatistical velocity distributions including the effects of varying temperature increases. The blue solid line shows the results of averaging a Maxwell-Boltzmann velocity distribution over a varying temperature induced by collisions with a range of impact parameters b and velocities v_c causing increases in the temperature $\Delta T(v_c, b)$ followed by a slow return to equilibrium. The red dashed line is calculated using the same averaging procedure but treating all collisions as causing the mean increase in temperature $\overline{\Delta T}$=56.3mK. The black dash-dotted line is a Maxwell-Boltzmann distribution for a fixed temperature equal to the mean $\overline{T}$=20mK. The inset shows the heavy-tailed behavior of the superstatistical distributions.

cooling, $q_s \to 1$ and the Maxwellian limit is recovered. λ, and therefore q_s, can be adjusted by varying the laser-cooling parameters, i.e., laser detuning and intensity.

The discussion above applies to the time interval following a single collision of fixed strength and hence a known value of ΔT. Averaging over the distribution of collision velocities and impact parameters yields

$$f_{v_i}(v_i) = \int_0^\infty f_{v_i}(v_i \,|\Delta T(v_\perp)) f_{v_\perp}(v_\perp)\, \mathrm{d}v_\perp, \tag{5.10}$$

where $v_\perp$ is the normal collision velocity (see Appendix 5.A). Using the results

obtained previously for ΔT, Eq. (5.10) was numerically integrated. The result is plotted in Fig. 5.6(b) and compared to both the distribution $f_{v_i}(v_i \mid \overline{\Delta T})$ obtained using Eq. (5.8) with $\Delta T = \overline{\Delta T} = 56.3$ mK and the Maxwell-Boltzmann distribution at the mean temperature $\overline{T}$ given by Eq. (5.6). It can be seen that averaging over all collisions in this manner leads to a distribution with an even more pronounced tail compared to $f_{v_i}(v_i \mid \overline{\Delta T})$, since this now includes the effects of the most energetic collisions. A further refinement would be relax the requirement that the collisions occur at a fixed interval, i.e., treating Δt as a random variable. In this case, the evolution of the temperature due to a combination of a random delay between collisions and random values of ΔT can be modelled using a jump-diffusion process to obtain $f_T(T)$ [143], allowing for either the direct computation of $\int f_v(v|T) f_T(T) dT$, or the estimation of the parameters for the Tsallis distribution.

5.3.2 Consequences for studies of cold chemistry

As a further example of the consequences of a time-dependent temperature, we now turn to the area of determining rate constants for cold chemical reactions [92, 144]. Take the rate constant of a reaction with an activation energy E_a as given by the Arrhenius equation:

$$k = A e^{\frac{-E_a}{k_B T(t)}}, \tag{5.11}$$

where A is a reaction-specific prefactor. Temperature fluctuations lead to a time-averaged rate constant

$$\bar{k} = \frac{1}{\Delta t} \int_{t_0}^{t_0+\Delta t} A e^{\frac{-E_a}{k_B T(t)}} dt \tag{5.12}$$

differing from the rate constant calculated using a model with $T(t) = \bar{T}$. Furthermore, additionally averaging over collision velocities and impact parameters leads to further changes in the rate constant. Fig. 5.7 shows the rate constants as a function of the activation energy for all three cases: for a fixed temperature, for a time-averaged temperature, and for a time- and collision-averaged temperature. As expected, for $E_a = 0$ (e.g., barrierless Langevin-type ion-neutral processes) the same rate constant is obtained, since in this case k does not depend on the velocity of the ions. However, it can be seen from the figure that for time-varying temperatures, the logarithm of

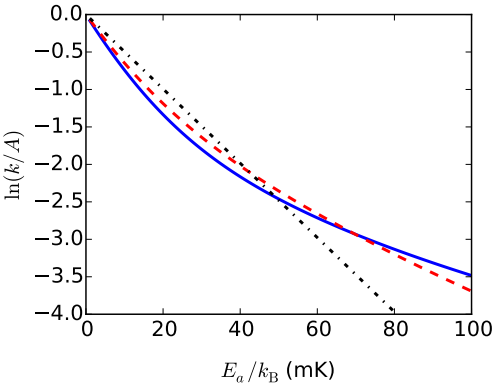

Figure 5.7: Variation of the logarithm of the ratio of the time-averaged reaction rate constant k to the Arrhenius prefactor A as a function of the activation energy E_a averaged over the time-varying temperature for all collision strengths (blue solid line) and for the mean collision strength (red dashed line). The black dash-dotted line indicates the expected behavior for a constant temperature equal to the mean.

the reaction rate is no longer a linear function of the activation energy due to the periods of time spent at higher and lower temperatures. At higher activation barriers, the rate constant for the temperature-varying model is higher than for the fixed-temperature, suggesting that reactions which would be energetically suppressed at the mean temperature can still occur.

5.3.3 Influence of micromotion

The discussion so far focussed on the effect of collisions on the secular motion of the trapped ions. Micromotion is implicitly contained by using a fully time-dependent trap potential in our simulations. However, the effects discussed here are qualitatively different from the micromotion heating of ions in a buffer gas which has been studied in detail in a range of previous publications [20, 53, 54, 56, 145] and is further discussed in Chapter 6. In these works, it was shown that ions undergoing collisions with neutral buffer-gas particles exhibit heavy-tailed velocity distributions caused by micromotion disruption and the resulting dissipation of micromotion energy into the secular motion

("RF heating"). Here, we have shown that a non-Maxwellian behavior of the entire ensemble can also emerge because of an energetic collision of a single ion with a neutral particle. This effect does not depend on the specifics of the ion trap and, in particular, does not require the presence of micromotion. It results from a time-dependent ensemble temperature which exists whenever cooling processes are active in combination with infrequent but strong heating effects.

The effects pertaining to the secular energy of the ions discussed here are expected to be less relevant in large crystals in which the energy content of the ions is clearly dominated by micromotion [45]. We expect them, however, to be significant in small crystals or strings centered on the RF null line of the trap, or for larger ensembles in multipole traps for which the micromotion energies are small. In fact, it has been shown experimentally that a string of sympathetically-cooled light ions located at the centre of a radiofrequency trap exhibits a Tsallis velocity distribution as a result of a combination of recooling to equilibrium due to the coolant ions, and rare heating events due to chemical reactions [57]. In this case, q_s was found to be on the order of 1.07, indicating only a small degree of departure from thermal statistics, but one which nonetheless contributed significantly to the uncertainity of the measurements.

5.4 Summary and conclusions

Using the molecular dynamics simulations described in Chapter 4, the constraints on the validity of previously employed friction-force models for laser cooling were explored and shown to lead to a significant overestimation of the cooling rates for energetic ions. It was demonstrated that the infrequent collisions with background gas molecules lead to superstatistical secular-velocity distributions of the ion ensemble independent of the presence of micromotion and that this behavior is tunable through changing laser-cooling parameters. We also show that the effects discussed here can have consequences for the determination of rate constants of cold chemical reactions with small activation barriers. The system considered here was that of ions being heated by collisions with residual hydrogen molecules, but the methodology and results can be straightforwardly adapted to the heating caused by collisions with untrapped rubidium atoms in the hybrid chip trap.

5.A Averaging collisions over impact parameters

To avoid repeating a large number of simulations for all possible impact parameters, we note that for the elastic isotropic collisions of structureless particles considered here, the effects of a collision at a collisional velocity v_c are entirely described by $v_\perp$, the component of v_c normal to the collision surface, while the tangential component plays no role [146]. The overall effect is that a fast glancing collision can impart the same momentum to an ion as a slow head-on collision, leading to the same rise in temperature. $v_\perp$ can be calculated from v_c, b according to:

$$v_\perp = v_c\sqrt{1-\frac{b^2}{d^2}}, \tag{5.13}$$

where $d = \sqrt{\sigma/\pi}$ is the maximum impact parameter. Since a collision along this velocity component is by definition head on (i.e., $b = 0$), we have:

$$\Delta T(v_c, b) = \Delta T(v_\perp(v_c, b), 0), \tag{5.14}$$

and so the results obtained in Sec. 5.3, Fig. 5.3 can be used to describe a collision with arbitrary impact parameter. Eq. (5.5) can then be replaced with an integration over the probability-distribution function $f_{v_\perp}(v_\perp)$,

$$\overline{\Delta T} = \int \Delta T(v_\perp, 0) f_{v_\perp}(v_\perp)\mathrm{d}v_\perp. \tag{5.15}$$

Under the (for the present case very good) assumption that the total velocity of the ion (including micromotion) is much smaller than the velocity of the colliding molecule, $f_{v_\perp}(v_\perp)$ may be derived in closed form as follows. The distribution for $v_\perp$ can be written in terms of the distributions of the collision velocity v_c and the impact parameter b as [63],

$$f(v_\perp) = \int_0^\infty \int_0^d f_{v_c}(v_c) f_b(b) \delta\left(v_c\sqrt{1-\frac{b^2}{d^2}} - v_\perp\right) \mathrm{d}b\mathrm{d}v_c. \tag{5.16}$$

The velocity of the incoming molecule is taken to follow Maxwell-Boltzmann statistics, and since this is typically much larger than the velocity of the ion, v_c

is approximately equal to this velocity. Thus, v_c is assumed to follow Maxwell-Boltzmann statistics. We assume that collisions occur with equal probability at all points on the cross-section, that is, they are uniformly distributed on the disk with radius d [28]. The probability for a point to be on the circle at a distance b from the centre of the disk is proportional to $2\pi b$ for $b < d$. Thus, after normalisation we obtain the distribution for the impact parameter b,

$$f_b(b) = \frac{2b}{d^2}, \tag{5.17}$$

for $b \in [0, d)$. Evaluating Eq. (5.16) using these distributions produces,

$$f(v_\perp) = \frac{2mv_\perp}{k_\mathrm{B}T}\left[1 - \mathrm{erf}\left(v_\perp\sqrt{\frac{m}{2k_\mathrm{B}T}}\right)\right], \tag{5.18}$$

where $\mathrm{erf}(x)$ is the error function. This distribution may then be used in combination with the values of $\Delta T(v_\perp, 0)$ taken from simulations to evaluate the integral in Eq. (5.15).

5.B Time-averaged velocity distribution

The form of $T(t)$ given by Eq. (5.4) allows for an analytical solution of Eq. (5.7) to be found by substituting:

$$\mathrm{d}T = -\lambda(T - T_{eq})\mathrm{d}t, \tag{5.19}$$

so that Eq. (5.7) can be written as

$$f_v(v) = \frac{-4\pi v^2}{\lambda\Delta t}\int_{T_1}^{T_2}\frac{\sqrt{\left(\frac{m}{2\pi k_\mathrm{B}T}\right)^3}e^{\frac{-mv^2}{2k_\mathrm{B}T}}}{T - T_{eq}}\mathrm{d}T. \tag{5.20}$$

Here, the limits of the integral are given by $T_1 = T_{eq} + \Delta T$ and $T_2 = T_{eq} + \Delta T e^{-\lambda\Delta t}$. The same integral may also be found through considering the temperature distribution $f_T(T)$ as follow. In our case, we aim to determine the temperature during the interval of time spanned by $[t_0, t_0 + \Delta t)$. The distribution of times in this interval is uniform (since, experimentally, we cannot tell at which point a collision has occurred), and equal to $1/\Delta t \mathrm{d}t$. Eq. (5.4) is used to map this time distribution onto a temperature distribution,

$$f_T(T) = f_t(t(T))\frac{\mathrm{d}t}{\mathrm{d}T} = 1/(\lambda\Delta t(T - T_{eq})), \tag{5.21}$$

where $t(T)$ is the inverse function of Eq. (5.4), and $f_T(T)$ is defined in the interval $[T_2, T_1]$. The Maxwell-Boltzmann distribution averaged over an arbitrary temperature distribution is given by

$$f_v(v) = \int 4\pi v^2 \left(\frac{m}{2\pi k_\mathrm{B} T}\right)^{\frac{3}{2}} e^{-\frac{mv^2}{2k_\mathrm{B}T}} f_T(T)\mathrm{d}T \tag{5.22}$$

and substitution of Eq. (5.21) into this equation recovers Eq. (5.20). Using another substitution $u = T_{eq}/T$ gives an integral of the form

$$\int \frac{\sqrt{u}e^{-au}}{u-1} du, \tag{5.23}$$

where $a = mv^2/(2k_\mathrm{B}T_{eq})$ and the prefactor has been omitted. This integral evaluates to,

$$\begin{aligned}\int \frac{\sqrt{u}e^{-au}}{u-1}\mathrm{d}u = e^{-a}\Bigg(&4i\pi\ \mathcal{T}\left[\sqrt{2au}, \frac{i}{\sqrt{u}}\right] \\ &+ \sqrt{\frac{\pi}{a}}\left[e^a - \sqrt{\pi a}\ \mathrm{erfi}\left(\sqrt{a}\right)\right]\mathrm{erf}\left(\sqrt{au}\right)\Bigg)\end{aligned} \tag{5.24}$$

where $\mathcal{T}(h, a)$ is Owen's T function [147], $\mathrm{erfi}(x) = -i\ \mathrm{erf}(ix)$, u and a are both real-valued and greater than zero, and the constant of integration has been neglected. This result cannot be directly obtained using Mathematica, but here we give a derivation for $0 < u < 1$. An application of integration by parts produces,

$$\int \frac{\sqrt{u}e^{-au}}{u-1}\, du = e^{-a}\sqrt{u}\mathrm{Ei}(-a(u-1)) - \frac{1}{2}e^{-a}\int \frac{\mathrm{Ei}(-a(u-1))}{\sqrt{u}}\, du. \tag{5.25}$$

Here, $\mathrm{Ei}(x)$ is the exponential integral [77]. Evaluation of this second integral is achieved by substitution $x = \sqrt{u}$, taking the derivative of it with respect to a and then integrating with respect to x, integrating with respect to a, and

returning to the original variable u. The result is,

$$\begin{aligned}\int \frac{\mathrm{Ei}(-a(u-1))}{\sqrt{u}}\,du = \sqrt{\pi}\left(2\sqrt{\pi}\mathrm{erfi}\left(\sqrt{a}\right) - \frac{2e^a}{\sqrt{a}}\right)\mathrm{erf}\left(\sqrt{a}\sqrt{u}\right) \\ + 2\sqrt{u}\left(\mathrm{Ei}(a-au)\right) \\ - 2\sqrt{u}\left(\frac{\pi\left[1+4\mathcal{T}\left(i\sqrt{2}\sqrt{a}\sqrt{-u},\frac{1}{\sqrt{-u}}\right)\right]}{\sqrt{-u}}\right)\end{aligned} \tag{5.26}$$

where we have assumed that the integrals are convergent to justify this procedure, and where the constants of integration have been neglected. Substituting this into Eq. (5.25) produces Eq. (5.24), which may be verified by differentation.

Eq. (5.24) can be used to obtain the velocity distribution plotted in Fig. 5.5,

$$\begin{aligned}f_v(v|\Delta T) = \frac{4ae^{-a}\sqrt{a\pi}}{\lambda\Delta t\sqrt{v^2}}\Bigg[\left(\mathrm{erfi}\left(\sqrt{a}\right) - \frac{e^a}{\sqrt{a\pi}}\right)\mathrm{erf}\left(\sqrt{\frac{mv^2}{2k_\mathrm{B}T}}\right) \\ -4i\mathcal{T}\left(\sqrt{\frac{mv^2}{k_\mathrm{B}T}}, i\sqrt{\frac{T}{T_{eq}}}\right)\Bigg]_{T=T_1}^{T=T_2},\end{aligned} \tag{5.27}$$

where $T_1 = T_{eq} + \Delta T(v,b)$ and $T_2 = T_{eq} + \Delta T(v,b)\exp(-\lambda\Delta t)$, and the notation $f_v(v|\Delta T)$ is used to emphasize that it applies in the time period following a collision resulting in a temperature increase of ΔT.

The distributions of the individual velocity components v_i with $i = x, y, z$ can be obtained through evaluation of:

$$f_{v_i}(v_i|\Delta T) = -\frac{1}{\lambda\Delta t}\int_{T_1}^{T_2}\frac{\sqrt{\frac{m}{2\pi k_\mathrm{B}T}}e^{\frac{-mv_i^2}{2k_\mathrm{B}T}}}{T-T_{eq}}\mathrm{d}T. \tag{5.28}$$

Integration yields:

$$f_{v_i}(v_i|\Delta T) = \frac{1}{\lambda\Delta t}\sqrt{\frac{m\pi}{2k_{\mathrm{B}}T_{eq}}}e^{-\frac{mv^2}{2k_{\mathrm{B}}T_{eq}}}\left[4i\ \mathcal{T}\left(v\sqrt{\frac{m}{k_{\mathrm{B}}T}}, -i\sqrt{\frac{T}{T_{eq}}}\right)\right. \\ \left. +\mathrm{erf}\left(v\sqrt{\frac{m}{2k_{\mathrm{B}}T}}\right)\mathrm{erfi}\left(v\sqrt{\frac{m}{2k_{\mathrm{B}}T_{eq}}}\right)\right]_{T=T_1}^{T=T_2} \tag{5.29}$$

Additionally of interest is the generalized q_s parameter defined as $\frac{\langle 1/T^2\rangle}{\langle 1/T\rangle^2}$ [99]. In the present case, this can be written as:

$$q_s = \lambda\Delta t\frac{T_{eq}(\frac{1}{T_1}-\frac{1}{T_2}) + \ln\left(\frac{T_2(T_1-T_{eq})}{T_1(T_2-T_{eq})}\right)}{\ln^2\left(\frac{T_2(T_1-T_{eq})}{T_1(T_2-T_{eq})}\right)}. \tag{5.30}$$

5.C Time-averaged Arrhenius rate constant

We now derive an expression for the Arrhenius rate constant taking into account temperature fluctuations. Starting from the time-averaged rate constant given by Eq. (5.12), we change the integration variable using Eq. (5.4):

$$\bar{k} = \int_{T_1}^{T_2} -\frac{Ae^{-\frac{E_a}{k_{\mathrm{B}}T}}}{\lambda\Delta t(T-T_{eq})}\mathrm{d}T, \tag{5.31}$$

Making the substitution $u = T_{eq}/T$ yields:

$$\bar{k} = \frac{A}{\lambda\Delta t}\int_{T=T_1}^{T=T_2}\frac{e^{-\frac{E_a u}{k_{\mathrm{B}}T_{eq}}}}{u} - \frac{e^{-\frac{E_a u}{k_{\mathrm{B}}T_{eq}}}}{(u-1)}\mathrm{d}u. \tag{5.32}$$

The solution of the integral can be written in terms of the exponential integral function $\mathrm{Ei}(x)$,

$$\bar{k} = \frac{A}{\lambda\Delta t}\left[\mathrm{Ei}\left(-\frac{E_a}{k_{\mathrm{B}}T}\right) - e^{-\frac{E_a}{k_{\mathrm{B}}T_{eq}}}\mathrm{Ei}\left(-\frac{E_a\left(1-\frac{T}{T_{eq}}\right)}{k_{\mathrm{B}}T}\right)\right]_{T_1}^{T_2} \tag{5.33}$$

which is plotted in Fig. 5.7.

Chapter 6

Statistical mechanics of a single ion in a neutral buffer gas

When an ion is immersed in a buffer gas of ultracold neutral particles, a surprising phenomenon occurs. Typically, it would be expected that a particle in contact with a heat bath thermalises to the temperature of the heat bath, and in a time-independent trap this is indeed the case. However, if the particle is an ion in a radiofrequency trap, then collisions between the ion and neutral particles results in the exchange of energy between the secular motion and micromotion in addition to the transfer of energy between the ion and the neutral particle. Consequently, even if the buffer gas has no kinetic energy, the secular energy of the ion may be increased by the collision [53, 54, 56]. This behaviour has two important consequences. Firstly, the mean energy of the ion is no longer that which would be predicted assuming thermal equilibrium, but may be many times larger, or even not converge to a fixed value. Secondly, the distributions observed for the position and energy are not those expected for a particle in thermal equilibrium, but are closer to those obtained in the framework of non-extensive entropy, i.e, Tsallis statistics [19, 20, 53]. In this model and following the convention for the parameters established in Chapter

2, the distribution for the energy of the ion is given by,

$$f_E^{(T)}(E) = \left(\frac{n_T}{\langle\beta\rangle}\right)^{-k-1} \frac{\Gamma(k+n_T+1)}{\Gamma(k+1)\Gamma(n_T)} \frac{E^k}{\left(\frac{\langle\beta\rangle E}{n_T}+1\right)^{k+n_T+1}}, \tag{6.1}$$

where E^k represents the density of states, $\langle\beta\rangle > 0$ is a scale parameter, and n_T is the Tsallis exponent. The superscript (T) is used to indicate that $f_E^{(T)}$ follows Tsallis statistics, to distinguish this from other possible forms of f_E. Unlike the exponential decay of the Boltzmann distribution obtained in thermal equilibrium, the Tsallis energy distribution decays following a power-law with an exponent of $-(n_T+1)$, requiring that $n_T > 0$ for the distribution to be normalisable and $n_T > 1$ for the mean energy to converge. Previous work has suggested a variety of models for the exponent, either empirical or based on a simplified one-dimensional model of the collisions, and has assumed that the power-law is due solely to the effects of multiplicative noise [20, 53, 56].

In this chapter, I derive the energy change due to an elastic Langevin collision between an ion and a neutral particle of buffer gas, both in the presence and absence of excess micromotion. The energy distributions are obtained through a superstatistical treatment by mapping this change in energy into a change in the temperature of the ion, obtaining the distribution for the inverse temperature β, and evaluating,

$$f_E(E) = \int_{\beta=0}^{\beta=\infty} \frac{E^k \beta^{k+1}}{\Gamma(k+1)} e^{-E\beta} f_\beta(\beta) \mathrm{d}\beta, \tag{6.2}$$

to produce the energy distribution. I demonstrate that, in the absence of excess micromotion and for a buffer gas of uniform density the resulting energy distribution is given by Tsallis statistics (Eq. (6.1) as demonstrated in Ref. [59]. When excess micromotion is present, it is shown that the power-law exponent at low mass ratio is instead due to the additive noise, and that based on the superstatistical treatment Tsallis statistics remain a good approximation for the observed energy distribution [60]. Finally, the superstatistical method is used to obtain the energy distribution for an ion interacting with a buffer gas held in a harmonic trapping potential, with relevance for both the hybrid chip trap designed in this thesis, and for existing ion-atom hybrid systems. In all cases, the analytical results are confirmed via numerical simulations of the collision process.

6.1 Energy change during ion-neutral collisions

In this section, the change in the secular energy of an ion during a collision with a neutral atom is derived and used to calculate the steady-state mean energies. Due to the complexity of the resulting expressions, only an overview of this procedure is shown here, see Appendix 6.F for more details in the form of a Mathematica notebook.

6.1.1 Motion of an ion in a radiofrequency trap

To summarise the results from Chapter 2, an ion in a radiofrequency trap subject to a combination of the trapping potential and an external, spatially-independent force $g_j(\tau)$ is described by the inhomogenous Mathieu equation,

$$\ddot{r}_j(\tau) + [a_j - 2q_j \cos(2\tau)]r_j(\tau) = g_j(\tau), \tag{6.3}$$

and the solution is given by [80],

$$r_j(\tau) = r_{h,j}(A_j, \phi_j, \tau) + r_{f,j}(\tau), \tag{6.4}$$

where $r_{h,j}(A_j, \phi_j, \tau)$ is the intrinsic motion,

$$r_{h,j}(A_j, \phi_j, \tau) = A_j[\mathrm{ce_j}(\tau)\cos\phi_j - \mathrm{se_j}(\tau)\sin\phi_j], \tag{6.5}$$

and $r_{f,j}(\tau)$ is the forced motion. This latter term is defined by [80],

$$r_{f,j}(\tau) = -\frac{\mathrm{ce_j}(\tau)}{W_j}\int \mathrm{se_j}(\tau)g_j(\tau)d\tau + \frac{\mathrm{se_j}(\tau)}{W_j}\int \mathrm{ce_j}(\tau)g_j(\tau)d\tau, \tag{6.6}$$

where $W_j = \mathrm{ce_j}(0)\dot{\mathrm{se}}_\mathrm{j}(0)$ is the Wronskian. The numerical results presented in this chapter employ a time-independent external force, $g_j(\tau) = g_j$, which for example represents the effects of a uniform static electric field [71]. Substituting this into Eq. (6.6) and evaluating the integrals produces,

$$r_{f,j}(\tau) = \frac{g_j}{W_j}\sum_l\sum_m \frac{c_{2l,j}c_{2m,j}}{\beta_j + 2m}\cos[2(m-l)\tau]. \tag{6.7}$$

The $m = l$ terms correspond to a constant offset of the ion's position while the $m \neq l$ terms are oscillations at multiples of Ω. It is convenient to parameterise the effects of this force in terms of the displacement due to the $m = 0, l = 0$

term,

$$\Delta r_j = \frac{g_j}{\beta_j W_j} c_0^2. \tag{6.8}$$

The energy of the ion is described in terms of the secular energy,

$$E_j = \frac{m_i}{2}\frac{\Omega^2}{4} A_j^2 \beta_j^2 c_{0,j}^2 = \frac{m_i}{2}\omega_j^2 A_j^2 c_{0,j}^2, \tag{6.9}$$

where $\omega_j = \frac{1}{2}\beta_j \Omega$ is the secular frequency. This definition of the energy depends only on the intrinsic motion (see Section 2.5.2). An alternative definition for the ion's energy in terms of the average kinetic energy, including the forced motion, is given in Appendix 6.A.

6.1.2 Ion-neutral collisions

To simplify the problem, it is assumed that collisions are classical, short range, and instantaneous such that the ion's trajectory is defined at all times by Eq. (6.3). The trajectory after the collision must therefore have the same general form as Eq. (6.4), but with the constants of integration A_j, ϕ_j updated to new values,

$$r_j'(\tau) = r_{h,j}(A_j', \phi_j', \tau) + r_{f,j}(\tau), \tag{6.10}$$

where primes indicate post-collision quantities. Note that since $r_{f,j}(\tau)$ does not depend on A_j, ϕ_j it is identical before and after the collision, wheras both the magnitude and phase of the intrinsic motion may be altered. For an instantaneous collision, the ion's position must remain unchanged. Equating $r_j'(\tau)$ and $r_j(\tau)$, then subtracting $r_{f,j}(\tau)$ from both sides produces,

$$r_{h,j}(A_j', \phi_j', \tau) = r_{h,j}(A_j, \phi_j, \tau). \tag{6.11}$$

We assume a model of elastic, hard-sphere collisions in which the post-collision velocity is given by [53, 54, 56, 59] ,

$$\mathbf{v}' = \frac{1}{1+\tilde{m}}\mathbf{v} + \frac{\tilde{m}}{1+\tilde{m}}\mathbf{v_b} + \frac{\tilde{m}}{1+\tilde{m}}\mathrm{R}(\mathbf{v} - \mathbf{v_b}), \tag{6.12}$$

where bold-faced variables indicate vectors, e.g., $\mathbf{v} = (v_x, v_y, v_z)^T$, $\mathbf{v_b}$ is the velocity of the colliding particle of buffer gas, $\tilde{m} = m_b/m_i$ is the buffer gas-to-ion mass ratio, and R is a rotation matrix determined by the scattering

angles. As with the position, the velocity of the ion is given by the sum of the intrinsic and forced motion, $v_j(\tau) = v_{h,j}(A_j, \phi_j, \tau) + v_{f,j}(\tau)$, where the forced term is independent of A_j, ϕ_j and so is unchanged by the collision. We therefore obtain,

$$\mathbf{v'_h} = \frac{1}{1+\tilde{m}}\mathbf{v_h} + \frac{\tilde{m}}{1+\tilde{m}}(\mathbf{v_b} - \mathbf{v_f}) + \frac{\tilde{m}}{1+\tilde{m}}\mathrm{R}[\mathbf{v_h} - (\mathbf{v_b} - \mathbf{v_f})]. \tag{6.13}$$

To simplify the notation, the elements of the right-hand side of this vector equation are denoted $\mathcal{C}_j$ such that $v'_{h,j} = \mathcal{C}_j$. Thus, in terms of A'_j, ϕ'_j and the Mathieu functions, we find,

$$A'_j[\dot{\mathrm{ce}}_j(\tau)\cos\phi'_j - \dot{\mathrm{se}}_j(\tau)\sin\phi'_j] = \mathcal{C}_j. \tag{6.14}$$

Taken together, Eq. (6.11) and Eq. (6.13) indicate that the problem is equivalent to that of an ion with no forced motion colliding with a particle of velocity $\mathbf{v_b} - \mathbf{v_f}$. This is similar to the frame transformation used in Ref. [20] in which the intrinisic micromotion is assigned to the buffer gas, but in the present case is performed only for the forced motion and is valid for all q_j.

The change in the secular energy during a collision is found as follows. The requirement that the position of the ion remains unchanged (Eq. (6.11)) can be expressed as,

$$A'_j[\mathrm{ce_j}(\tau)\cos\phi'_j - \mathrm{se_j}(\tau)\sin\phi'_j] = A_j[\mathrm{ce_j}(\tau)\cos\phi_j - \mathrm{se_j}(\tau)\sin\phi_j], \tag{6.15}$$

which may be solved to obtain ϕ'_j,

$$\phi'_j = \cos^{-1}\left[\frac{A_j}{A'_j}\cos(\phi_j + \delta_{\tau,j})\right] - \delta_{\tau,j}, \tag{6.16}$$

where,

$$\delta_{\tau,j} = \mathrm{atan}\left(\frac{\mathrm{se}_j(\tau)}{\mathrm{ce}_j(\tau)}\right). \tag{6.17}$$

Substituting Eq. (6.16) into Eq. (6.14) produces,

$$\frac{\sqrt{A'^2_j - A_j^2\cos^2(\delta_{\tau,j} + \phi_j)}}{\sqrt{\mathrm{ce}_j(\tau)^2 + \mathrm{se}_j(\tau)^2}} = \frac{A_j\cos(\delta_{\tau,j} + \phi_j)\,cs_j(\tau)}{W_j\sqrt{\mathrm{ce}_j(\tau)^2 + \mathrm{se}_j(\tau)^2}} - \frac{\mathcal{C}_j}{W_j}, \tag{6.18}$$

where,

$$cs_j(\tau) = \mathrm{ce}_j(\tau)\dot{\mathrm{ce}}_j(\tau) + \mathrm{se}_j(\tau)\dot{\mathrm{se}}_j(\tau), \tag{6.19}$$

and the Wronskian $W_j = \mathrm{ce}_j(\tau)\dot{\mathrm{se}}_j(\tau) - \mathrm{se}_j(\tau)\dot{\mathrm{ce}}_j(\tau) = \mathrm{ce}_j(0)\dot{\mathrm{se}}_j(0)$ has been used to simplify the results. Squaring both sides and simplifying further produces,

$$A_j'^2 = A_j^2 \cos^2(\delta_{\tau,j} + \phi_j) + \frac{1}{W_j^2}\Bigg(A_j \cos(\delta_{\tau,j} + \phi_j)\, cs_j(\tau) - \mathcal{C}_j\sqrt{\mathrm{ce}_j(\tau)^2 + \mathrm{se}_j(\tau)^2}\Bigg)^2. \tag{6.20}$$

The collision element $\mathcal{C}_j$ is linear in the amplitudes of the intrinsic motion along each axis, the components of the velocity of the forced motion, and the buffer gas velocity. Hence, expanding Eq. (6.20) will produce an expression containing terms which are the product of two of these, e.g., $A_k A_l$ or $v_{b,k}A_l$ for $k, l \in (x, y, z)$. Using Eq. (6.9) to replace the amplitudes by the secular energies, the components of the secular energy after a collision are,

$$E_j' = \sum_{(k,l)\in(x,y,z)} \Bigg(\eta_{jkl}\sqrt{E_k}\sqrt{E_l} + a_{1,jkl}\sqrt{E_k}v_{b,l} + a_{2,jkl}v_{b,k}v_{b,l} + a_{3,jkl}\sqrt{E_k}v_{f,l} + a_{4,jkl}v_{f,k}v_{f,l} + a_{5,jkl}v_{f,k}v_{b,l}\Bigg), \tag{6.21}$$

where the coefficients η_{jkl} and $a_{i,jkl}$ describe the transfer of energy between the motion along the three coordinate axes and between the different components of the ion's velocity and the velocity of the buffer gas. The coefficients of this expression depend on the elements of the random rotation matrix R, the set of phases ϕ_j, and the time of collision τ.

To gain a better understanding of the collision process, it is useful to average over the collision parameters to obtain the mean post-collision energy for a given set of pre-collision energies, $\langle E_j' | E_x, E_y, E_z\rangle$. To do so, we must introduce some further assumptions. The Langevin model of collisions has been shown to be accurate for the classical trajectories considered here [54, 56] and so we adopt this. This results in two useful simplifications. Firstly, the rotation matrix R is isotropic in this model and so is uncorrelated from the

velocity of the ion and neutral particle. Secondly, collisions occur at a uniform rate which is independent of the energy of the ion, and so τ can be assumed to follow a uniform distribution. We assume that the density of the buffer gas is low and uniformally distributed in space, which results in collisions occuring with equal probability at all points in the ion's trajectory, such that ϕ_j follows a uniform distribution. We also assume that the velocity of the buffer gas follows Maxwell-Boltzmann statistics and is characterised by a fixed temperature T_b. Both the density and the temperature of the buffer gas are taken to remain constant, i.e., the heating of the buffer gas due to the collisions is assumed to be negligible. With these assumptions, the averaging can be performed over ϕ_j, $v_{b,k}$, τ and the elements of the isotropic random rotation matrix by integrating Eq. (6.21) over the distributions of each of these variables in turn, see Appendix 6.F for details and the resulting expression. The a_1, a_3, a_5 coefficients all average to zero, significantly simplifying the expression. Moreover, all the coefficients with $k \neq l$ also average to zero, and to eliminate the resulting redundant subscripts the convention $\langle \eta_{jk} \rangle = \langle \eta_{jkk} \rangle$ is adopted. The remaining terms are given by,

$$\langle E'_j | E_{x,y,z} \rangle = \sum_{k \in (x,y,z)} \left[\langle \eta_{jk} \rangle E_k + \langle a_{4,jk} v_{f,k}^2 \rangle \right] + \kappa_j k_B T_b, \tag{6.22}$$

where the coefficients are defined as,

$$\langle \eta_{jk} \rangle = \frac{\delta_{jk}}{\tilde{m}+1} + \frac{\tilde{m}\kappa_j(3\delta_{jk}+1)}{6\beta_k^2 c_{0,k}^2} \mathcal{M}_j \left[\dot{\mathrm{ce}}_\mathrm{k}(\tau)^2 + \dot{\mathrm{se}}_\mathrm{k}(\tau)^2 \right], \tag{6.23}$$

and,

$$\langle a_{4,jk} v_{f,k}^2 \rangle = \frac{\tilde{m} m_i \Omega^2 \kappa_j}{24} (3\delta_{jk}+1) \mathcal{M}_j \left[v_{f,k}(\tau)^2 \right]. \tag{6.24}$$

In the above expressions, δ_{jk} is the Kronecker delta, κ_j is defined by,

$$\kappa_j = \frac{\tilde{m}}{(1+\tilde{m})^2} \frac{\beta_j^2 c_{0,j}^2}{W_j^2}, \tag{6.25}$$

and the operator $\mathcal{M}_j$ is defined as,

$$\mathcal{M}_j \left[h(\tau) \right] = \lim_{L \to \infty} \frac{1}{2L} \int_{-L}^{L} h(\tau) \left[\mathrm{ce}_\mathrm{j}(\tau)^2 + \mathrm{se}_\mathrm{j}(\tau)^2 \right] d\tau. \tag{6.26}$$

In principle, the above procedure may be adapted to arbitrary distributions for the velocity of the buffer gas by averaging over these in place of the Maxwell-Boltzmann distribution. This would allow for an investigation of the results when, e.g., Fermi-Dirac or Bose-Einstein statistics are required to correctly characterize the buffer gas. In practice, however, such statistics become relevant at collision energies low enough so that a classical description of the motion may no longer be valid. Moreover, at such low energies the long-range nature and finite duration of the ion-neutral interaction introduces an additional heating effect from dislocating the ion from its position in the RF field. At higher collision energies, this heating effect becomes less significant [148]. To simplify both the analytical model and the numerical calculations, we proceed by assuming that the energy of the ion is large enough so that these effects can be neglected.

The mean energy after a large number of collisions can be calculated from Eq. (6.22) as follows. Averaging over the pre-collision energies, corresponding to setting $\langle E_j' | E_x, E_y, E_z \rangle \to \langle E_j' \rangle$ and $E_j \to \langle E_j \rangle$, produces

$$\langle E_j' \rangle = \sum_k \langle \eta_{jk} \rangle \langle E_k \rangle + \langle \epsilon_j \rangle, \tag{6.27}$$

where $\langle \epsilon_j \rangle$ is the sum of the energy-independent terms arising in the averaging procedure. Depending on the values of the $\langle \eta_{jk} \rangle$, the mean energy will either increase with every collision, or tend towards a finite value for which $\langle E_j' \rangle = \langle E_j \rangle$. In the latter case, substituting this equality into Eq. (6.27) and solving for the mean energies produces,

$$\begin{pmatrix} \langle E_x \rangle \\ \langle E_y \rangle \\ \langle E_z \rangle \end{pmatrix} = \left(\mathrm{I}_3 - \begin{pmatrix} \langle \eta_{xx} \rangle & \langle \eta_{xy} \rangle & \langle \eta_{xz} \rangle \\ \langle \eta_{yx} \rangle & \langle \eta_{yy} \rangle & \langle \eta_{yz} \rangle \\ \langle \eta_{zx} \rangle & \langle \eta_{zy} \rangle & \langle \eta_{zz} \rangle \end{pmatrix} \right)^{-1} \cdot \begin{pmatrix} \langle \epsilon_x \rangle \\ \langle \epsilon_y \rangle \\ \langle \epsilon_z \rangle \end{pmatrix}, \tag{6.28}$$

where I_3 is the 3×3 identity matrix. The mean total kinetic energy, $\langle E_{j,K} \rangle$, of the ion including the contributions from the micromotion and the forced motion can then be evaluated from the values of $\langle E_j \rangle$ (see Appendix 6.A),

$$\langle E_{j,K} \rangle = \frac{\langle E_j \rangle}{2\beta_j^2 c_{0,j}^2} \sum_m c_{2m}^2 (\beta + 2m)^2 + \frac{1}{2} m_i \frac{\Omega^2}{4} \overline{v_{f,j}^2}, \tag{6.29}$$

where $\overline{v_{f,j}^2}$ is the mean-square velocity of the forced motion. For simplicity,

however, we will continue to use the secular energy, since for low mass ratios and low values of q_j this is approximately equal for each axis, whereas the time-averaged energy is significantly larger for axes with $q_j \neq 0$ compared to axes with $q_j = 0$ [56]. It is possible that the matrix inversion in Eq. (6.28) cannot be performed or results in a negative energy, corresponding to a breakdown of the assumption that $\langle E'_j \rangle = \langle E_j \rangle$ and implying that the mean energy does not converge to a fixed value. The mass ratio at which this occurs for a given set of trapping parameters is referred to as the critical mass ratio [56], and since it is independent of the ϵ_j, it is unchanged when forced motion is present.

We now focus on the case of in-phase EMM in an ideal linear quadrupole trap defined by q_r and a_z, taking $q_x = -q_y = q_r$, $q_z = 0$, and $a_x = a_y = -a_z/2$. The constant offset in the ion's position caused by the spatially-independent force does not appear in either Eq. (6.11) or Eq. (6.13), and so the most significant effect is the oscillations described by $v_{f,j}(\tau) \propto \sin(2\tau)$. Hence, the present results can also be adapted to the case of excess micromotion due to an RF phase offset, which also results in forced motion with the same form of the velocity [71]. In Fig. 6.1(a), the predicted mean secular energies for the case of excess micromotion along the x-axis and $T_b = 0$ K are shown and compared to the results of numerical simulations (see Appendix 6.B for details), while the results in the absence of EMM but with a nonzero buffer-gas temperature ($T_b = 100$ μK) are shown in Fig. 6.1(b) for comparison. At low mass ratio, there is a clear difference in the qualitative behaviour of the mean energies obtained for the two cases. In this regime, forced motion leads to one high-energy component (E_x) and two components with lower energy (E_y, E_z), and in the limit $\tilde{m} \to 0$ these all converge to 0. In contrast, a nonzero value of T_b results in two high-energy components and one low-energy component which converge to non-zero values as $\tilde{m} \to 0$. Note that the radial and axial components have different mean values even in this limit. As the mass ratio increases, the transfer of energy between the motion along the x and y axes becomes more efficient such that in both cases there are two high-energy and one low-energy component, and the mean energies diverge at the same mass ratio independently of the presence of forced motion. The differences between the two cases are therefore most significant at low mass ratio.

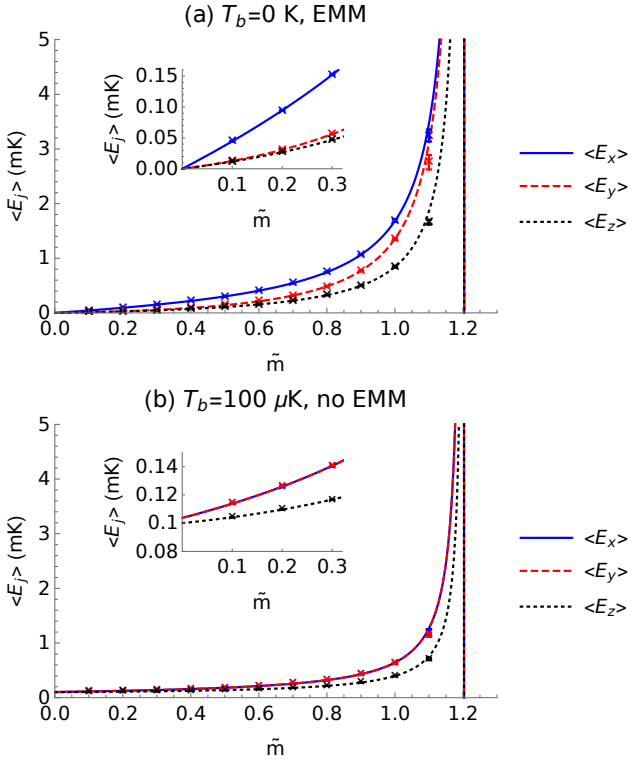

Figure 6.1: (a) The analytically calculated value of the mean secular energy $\langle E_j \rangle$ for $j = x$ (blue solid line), y (red dashed line) and z (black dotted line) as a function of the neutral-to-ion mass ratio, $\tilde{m}$, due to the presence of excess micromotion (EMM) and collisions with a buffer gas of temperature $T_b = 0$ K. The points indicate the results obtained from numerical simulations (10^6 iterations for each value of $\tilde{m}$). The trap parameters correspond to an ideal linear trap with $q_r = 0.2$, $a_z = 0.000625$ and the excess micromotion is generated by a uniform electric field with a magnitude of ≈ 0.5 V/m, corresponding to a displacement of the ion from the centre of the trap by 100 nm along the x-axis. The inset shows the trend as $\tilde{m} \to 0$. Error bars represent the standard error of the mean calculated from the numerical data and are typically smaller than the size of the symbols. (b) As (a), but with a buffer gas temperature of $T_b = 100$ μK and no EMM. In both figures, the vertical asymptote indicates the point at which the mean energy diverges, see main text for details.

6.2 Energy distributions

6.2.1 Reduction to one dimension

It has previously been established that the distribution of the ion's energy does not, in general, follow a thermal distribution regardless of whether or not forced motion is present, and that it closely follows Tsallis statistics in both cases [19, 53, 54, 56, 59]. Before proceeding further, we must first confirm that the Tsallis distributions obtained through numerical simulations can be successfully predicted from our analytical model for the collision process. Very few analytical results are available for three-dimensional recurrence relations with stochastic coefficients such as the one obtained here, especially when the distributions of the coefficients are unknown [149]. To simplify matters, we investigate the distribution of the total secular energy $E = E_x + E_y + E_z$ by making the change of basis,

$$\begin{aligned} E_x &= E \sin^2\theta_\rho \cos^2\phi_\rho, \\ E_y &= E \sin^2\theta_\rho \sin^2\phi_\rho, \\ E_z &= E \cos^2\theta_\rho, \end{aligned} \tag{6.30}$$

where $\theta_\rho, \phi_\rho \in [0, \pi/2)$ describe the relative distribution of the total energy E between the three axes. Briefly, if θ_ρ approaches $\pi/2$, then $E_z << E_x, E_y$, wheras small values of θ_ρ indicate the reverse. Likewise, $\phi_\rho \to 0$ indicates that $E_x > E_y$. The advantage of this basis is that it allows E to be factored out of expressions involving $\sqrt{E_k}\sqrt{E_l}$ in Eq. (6.21), e.g.,

$$\eta_{jxy}\sqrt{E_x}\sqrt{E_y} = E\eta_{jxy}\sin^2\theta_\rho \sin\phi_\rho \cos\phi_\rho. \tag{6.31}$$

Summing over j in Eq. (6.21), applying this change of basis, and neglecting the coefficients with mean values equal to zero, i.e., a_1, a_3, a_5, we obtain,

$$E' = \eta E + \epsilon, \tag{6.32}$$

where η contains the η_{jkl} multiplied by functions of θ_ρ, ϕ_ρ,

$$\eta = \sum_{j,k,l} \eta_{jkl} P_k P_l, \tag{6.33}$$

with $P_x = \sin\theta_\rho \cos\phi_\rho, P_y = \sin\theta_\rho \sin\phi_\rho, P_z = \cos\theta_\rho$. The energy-independent term ϵ is given by,

$$\epsilon = \sum_{j,k,l} a_{2,jkl} v_{b,k} v_{b,l} + a_{4,jkl} v_{f,k}, v_{f,l}. \tag{6.34}$$

As a consequence of the random rotation of the trajectory during a collision, the two angles θ_ρ, ϕ_ρ evolve on a faster timescale than E. For the purposes of determing the evolution of E during a series of collisions, we make two approximations to obtain an effectively one-dimensional system. Firstly, we assume that the angles θ_ρ, ϕ_ρ change sufficiently rapidly compared to E that they may be treated as being effectively random for each collision. Secondly, we approximate that the distributions of these variables are independent of E. Therefore, the correlations between E and θ_ρ, ϕ_ρ can be neglected and these angles incorporated into the multiplicative term η. Under these conditions, Eq. (6.32) is a linear stochastic recurrence relation for the variable E with two noise terms: the multiplicative noise η, and the additive noise ϵ, so-called as they respectively multiply the energy by a random amount or add a random amount to the energy with each collision. The multiplicative term η represents the amplification of the ion's secular energy by the interruption of the intrinsic micromotion, and depends primarily on the mass ratio and the Mathieu parameters. Since η contains contributions from θ_ρ, ϕ_ρ, the distribution of η varies slightly depending on how the energy is distributed between the axes, which is discussed in further detail below. The additive term ϵ describes the energy gained by the ion from the kinetic energy of both the buffer gas and the forced motion. We will later demonstrate that ϵ must have some probability of being non-zero for a steady-state to exist, and moreover that it serves to establish the characteristic scale of the energy distribution in the steady-state.

We next consider the evolution of the mean energy defined by averaging over Eq. (6.32),

$$\langle E' \rangle = \langle \eta \rangle \langle E \rangle + \langle \epsilon \rangle. \tag{6.35}$$

Due to the linearity of averages, $\langle E \rangle = \sum_j \langle E_j \rangle$ [63], and so this expression must be equivalent to that found from summing over j in Eq. (6.27),

$$\sum_j \langle E'_j \rangle = \sum_j \left[\left(\sum_k \langle \eta_{jk} \rangle \langle E_k \rangle \right) + \langle \epsilon_j \rangle \right]. \tag{6.36}$$

By inspection, we conclude that $\langle\epsilon\rangle = \sum_j \langle\epsilon_j\rangle$. Under the assumption that $E, \theta_\rho, \phi_\rho$ are independent, it holds that [63],

$$\langle E_x\rangle = \langle E\rangle\langle\cos^2\phi_\rho\rangle\langle\sin^2\theta_\rho\rangle, \tag{6.37}$$

and likewise $\langle E_y\rangle, \langle E_z\rangle$ can be written as the product of $\langle E\rangle$ and averages of functions of θ_ρ, ϕ_ρ found from Eq. (6.30). Substituting these into Eq. (6.36) and factoring out $\langle E\rangle$, we obtain an expression for $\langle\eta\rangle$ which is most compactly represented as the sum of the elements of the vector found by evaluating,

$$\begin{pmatrix} \langle\eta_{xx}\rangle & \langle\eta_{xy}\rangle & \langle\eta_{xz}\rangle \\ \langle\eta_{yx}\rangle & \langle\eta_{yy}\rangle & \langle\eta_{yz}\rangle \\ \langle\eta_{zx}\rangle & \langle\eta_{zy}\rangle & \langle\eta_{zz}\rangle \end{pmatrix} \begin{pmatrix} \langle\cos^2\phi_\rho\rangle\langle\sin^2\theta_\rho\rangle \\ \langle\sin^2\phi_\rho\rangle\langle\sin^2\theta_\rho\rangle \\ \langle\cos^2\theta_\rho\rangle \end{pmatrix}, \tag{6.38}$$

where the required averages of the angles θ_ρ, ϕ_ρ may be obtained as described in Appendix 6.C. The same result for $\langle\eta\rangle$ is obtained by directly averaging η over all the collision parameters. In the limit where an internal equilibrium of energy holds such that $\langle E_x\rangle = \langle E_y\rangle = \langle E_z\rangle = \frac{1}{3}\langle E\rangle$ and each component of the energy follows a thermal distribution, then the distributions for θ_ρ, ϕ_ρ take simple forms (Appendix 6.C), and averaging yields,

$$\langle\eta\rangle = \frac{1}{3}\sum_{j,k}\langle\eta_{jk}\rangle. \tag{6.39}$$

However, as discussed in Section 6.1.2, the mean values of the components of the secular energy are not in general equal. For a linear trap in the absence of EMM, micromotion interruption preferentially increases the energy of the radial modes (x, y) compared to the axial mode (z), such that typically E_x, E_y are larger than E_z. A correction for this effect is discussed in Appendix 6.C, and is found to slightly alter the obtained values of $\langle\eta\rangle$. When forced motion is present this causes a further shift in the values of $\langle\theta_\rho\rangle, \langle\phi_\rho\rangle$ and thus in $\langle\eta\rangle$. In both cases, the values of the $\langle\eta_{jk}\rangle$ themselves are unaffected, but their contributions to $\langle\eta\rangle$ are magnified when there is more energy present on the relevant axis. That is, if almost all the energy is associated with the motion along the z axis, then $\langle\eta_{xx}\rangle$ contributes very little to $\langle\eta\rangle$, leading to a different value of $\langle\eta\rangle$ than if all the energy is associated with motion along the x axis.

The second-order moment $\langle\eta^2\rangle$ can likewise be calculated in terms of the Mathieu parameters and the mass ratio by means of squaring the analytical

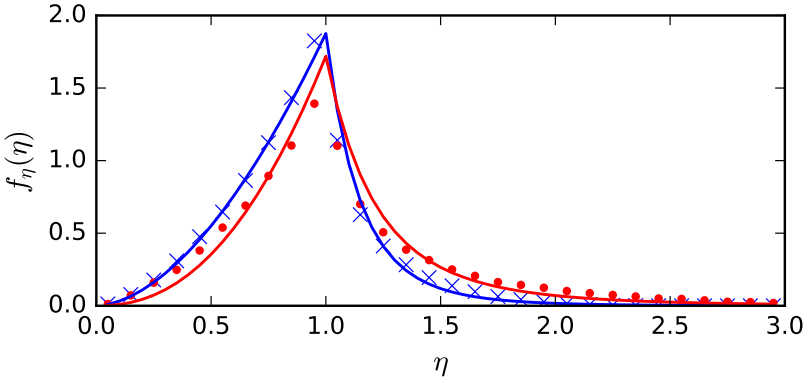

Figure 6.2: Distributions of the energy-transfer factor η in ion-atom collisions for $q = 0.1, \tilde{m} = 0.75$ (blue crosses) and $q = 0.5, \tilde{m} = 1.25$ (red points) starting from a thermal state with ion temperature $T_0 = 1$ mK. The points are binned normalized data from 100'000 numerical simulations of a collision. The lines represent an empirical asymmetric log-Lapace distribution, see text.

expression for η, then averaging over all the collision parameters. In theory, this procedure could be extended to calculate arbitrary moments of η, but in practice the required integrals cannot be evaluated analytically except for integer moments, and even then the analytical averaging of η^2 over all the collision parameters takes a large amount of computational time. In general, knowledge of the distribution of η, $f_\eta(\eta)$, is more useful. Although this distribution is not known in closed form, if a reasonable empirical model for this distribution can be found, then the known values for $\langle\eta\rangle$ and $\langle\eta^2\rangle$ can be used to calculate the parameters for this empirical distribution by means of the method of moments. Fig. 6.2 shows the distributions $f_\eta(\eta)$ obtained through numerical simulations for the cases with $q = 0.1, \tilde{m} = 0.75$ and $q = 0.5, \tilde{m} = 1.25$ which correspond to stable and unstable ion motions, respectively. The solid lines in Fig. 6.2 correspond to log-Laplace distributions of the form [150],

$$f_\eta(\eta) = \frac{1}{\delta}\frac{a_1 a_2}{a_1 + a_2}\begin{cases}\left(\frac{\delta}{\eta}\right)^{a_1+1} & \eta \geq \delta \\ \left(\frac{\eta}{\delta}\right)^{a_2-1} & 0 < \eta < \delta\end{cases} \tag{6.40}$$

with $a_1, a_2 > 0$ which have previously been used to model processes involving multiplicative fluctuations [150]. The parameter δ representing the maximum of the distribution was found to be ≈ 1, reflecting the fact that most collisions result in only minor changes to the ion's energy, and is set equal to 1 from here on. The first two moments of Eq. (6.40) are given by,

$$\langle \eta \rangle = \frac{a_1 a_2}{(1+a_2)(a_1-1)}, \tag{6.41}$$

$$\langle \eta^2 \rangle = \frac{a_1 a_2}{(2+a_2)(a_1-2)}. \tag{6.42}$$

By equating these two expressions to the values of $\langle \eta \rangle, \langle \eta^2 \rangle$ calculated by averaging over the collision parameters, expressions for a_1, a_2 in terms of the Mathieu parameters and mass ratio can be found. As can be seen in Fig. 6.2, this produces a good representation of the form of $f_\eta(\eta)$ obtained numerically for both stable and unstable motion.

6.2.2 The multiplicative model

We first take the case where $T_b = 0$ K and there is no excess micromotion, such that $\epsilon = 0$. The energy after n collisions is given by [59],

$$E_{(n)} = E_{(0)} \prod_{i=1}^{i=n} \eta_{(i)}. \tag{6.43}$$

Here, we use the notation $x_{(n)}$ to indicate the value of the variable x at collision number n. We assume that collisions are infrequent enough that there is no correlation between them, and so the $\eta_{(i)}$ are independent and identically distributed. By taking the logarithm of both sides of Eq. (6.43), we find $\ln E_{(n)} = \ln E_{(0)} + \sum_n \ln \eta_{(i)}$, and so $\ln E_{(n)}$ undergoes a random walk with steps of size $\ln \eta$ [151]. The long-term behaviour of $\ln E_{(n)}$ therefore depends on the sign of $\langle \ln \eta \rangle$ to determine in which direction this random walk is biased. If $\langle \ln \eta \rangle > 0$, then $\ln E_{(n)} \to \infty$ as $n \to \infty$. Conversely, if $\langle \ln \eta \rangle < 0$, then $\ln E_{(n)} \to -\infty$ in this limit, and so the ion's energy tends towards zero. Using the terminology of Ref. [149], we refer to the $\langle \ln \eta \rangle < 0$ situation as the contractive case and $\langle \ln \eta \rangle > 0$ as the divergent case.

Let us now assume that the ion is initially prepared in a thermal state at temperature T_0, as may be the situation after Doppler laser cooling [6, 64].

The resulting distribution for the ion's initial energy E_0 is,

$$f_{E_0}(E_0) = \frac{E_0^k \beta_0^{k+1}}{\Gamma(k+1)} e^{-E_0\beta_0}, \tag{6.44}$$

where $\beta_0 = 1/(k_B T_0)$, Γ is the Gamma function and the pre-exponential factor E^k represents the density of states. The value of k depends on the effective density of states. In the ideal case, this is simply the density of states for a three dimensional harmonic oscillator, leading to $k = 2$. However, as noted in the previous section the mean energy for each axis differs such that not all degrees of freedom are equal. In the extreme case when the energy of one axis is much greater than the others, e.g., $E_x >> E_y, E_z$, then $E \approx E_x$, and so is approximately a one-dimensional system. Hence, the density of states would be much closer to that expected for a one dimensional harmonic oscillator, $k = 0$. In practice, this effect is sufficiently small that we will simply assume that $k = 2$ for the analytical treatment.

We now consider the effects of collisions with the neutral atoms. Initially, we neglect their thermal energy and the excess micromotion, and set $\epsilon = 0$ in Eq. (6.32) such that $E' = \eta E_0$. The general result for the distribution of E' for arbitrary distributions of E_0 and η is [63],

$$f_{E'}(E') = \int_{\eta=0}^{\eta=\infty} \frac{1}{\eta} f_{E_0}(E'/\eta) f_\eta(\eta) \mathrm{d}\eta. \tag{6.45}$$

For the remainder of this section, all integrals are assumed to be over the entire domain of the relevant variables, typically $[0, \infty)$, with the limits omitted for reasons of space. Substituting in Eq. (6.44), we find,

$$f_{E'}(E') = \int \frac{1}{\eta} \frac{(E'/\eta)^k \beta_0^{k+1}}{\Gamma(k+1)} e^{-(E'/\eta)\beta_0} f_\eta(\eta) \mathrm{d}\eta. \tag{6.46}$$

We first consider the case in which every collision multiplies the energy by a fixed amount, η_c. The distribution for η is then given by a Dirac δ function,

$$f_\eta(\eta) = \delta(\eta - \eta_c), \tag{6.47}$$

so that

$$f_{E'}(E') = \frac{E'^k \beta_0^{k+1}}{\eta_c^{k+1}\Gamma(k+1)} e^{-\frac{E'\beta_0}{\eta_c}}. \tag{6.48}$$

This is still a thermal distribution, except that it can now be written in terms of $\beta' = \beta_0/\eta_c$.

We now generalise this approach to an arbitrary $f_\eta(\eta)$ by making the change of variables $\beta' = \beta_0/\eta$ in Eq. (6.46),

$$f_{E'}(E') = \int \frac{E'^k \beta'^{k+1}}{\Gamma(k+1)} e^{-E'\beta'} \frac{\beta_0}{\beta'^2} f_\eta\left(\frac{\beta_0}{\beta'}\right) \mathrm{d}\beta'. \tag{6.49}$$

The energy distribution after a collision can thus be represented by a superposition of thermal states, i.e., using the formalism of superstatistics [98, 99]. In this case we have represented the problem in terms of the inverse temperature β rather than the standard temperature $T = 1/\beta$ to make it more apparent that Eq. (6.49) is linked to the Laplace transform of a function of β. We can now define a distribution for β',

$$f_{\beta'}(\beta') = \frac{\beta_0}{\beta'^2} f_\eta\left(\frac{\beta_0}{\beta'}\right), \tag{6.50}$$

which is used to recast Eq. (6.49) into the form

$$f_{E'}(E') = \int \frac{E'^k \beta'^{k+1}}{\Gamma(k+1)} e^{-E'\beta'} f_{\beta'}(\beta') \mathrm{d}\beta' = \frac{E'^k}{\Gamma(k+1)} \mathcal{L}_{\beta'}^{E'} \left[\beta'^{k+1} f_{\beta'}(\beta')\right], \tag{6.51}$$

where $\mathcal{L}_x^y$ is the Laplace transform from x to y.

We may further extend this to the general case where both β and η are random variables. We start by expressing $f_E(E)$ as a superposition of thermal states as in Eq. (6.2), and using Eq. (6.45) we find that $f_{E'}(E')$ for $E' = \eta E$ is given by [63],

$$f_{E'}(E') = \int\int \frac{1}{\eta} \frac{(E'/\eta)^k \beta^{k+1}}{\Gamma(k+1)} e^{-(E'/\eta)\beta} f_\beta(\beta) f_\eta(\eta) \mathrm{d}\beta \mathrm{d}\eta. \tag{6.52}$$

Making a change of variables $\eta = u$, $\beta = u\beta'$, with $d\beta d\eta = u\, d\beta'\, du$ produces [63],

$$\begin{aligned} f_{E'}(E') &= \int\int \frac{1}{u} \frac{(E'/u)^k (u\beta')^{k+1}}{\Gamma(k+1)} e^{-(E'/u)\beta' u} f_\beta(u\beta') f_\eta(u) u \mathrm{d}\beta' \mathrm{d}u \\ &= \int\int u \frac{(E')^k (\beta')^{k+1}}{\Gamma(k+1)} e^{-E'\beta'} f_\beta(u\beta') f_\eta(u) \mathrm{d}\beta' \mathrm{d}u. \end{aligned} \tag{6.53}$$

The variable u is entirely identical to η and is used only as a placeholder to ensure that the Jacobian for the change of variables is correctly calculated [63]. Replacing u with η then changing the order of integration from $d\beta'\ d\eta$ to $d\eta\ d\beta'$, we find,

$$f_{E'}(E') = \int\int \eta \frac{(E')^k(\beta')^{k+1}}{\Gamma(k+1)} e^{-E'\beta'} f_\beta(\eta\beta') f_\eta(\eta) \mathrm{d}\eta \mathrm{d}\beta'. \tag{6.54}$$

This is equivalent to Eq. (6.51) with $f_{\beta'}(\beta')$defined by,

$$f_{\beta'}(\beta') = \int \eta f_\beta(\eta\beta') f_\eta(\eta) d\eta, \tag{6.55}$$

which is the distribution for $\beta' = \beta/\eta$ [63], generalising the result found previously to the case where both β and η are random variables. Thus, multiplying the energy by a random value is equivalent to dividing the inverse temperature by this value. Using this result and changing variables from the inverse temperature to the standard temperature, it can be shown that for $E' = \eta E$, the relation $T' = \eta T$ holds when both T and η are random variables.

Repeated application of Eq. (6.55) and substitution into Eq. (6.51) can then be performed to obtain the energy distribution of an ion after n collisions. Thus, we formulate a recurrence relation for β after collision number i,

$$\beta_i = \beta_{i-1}/\eta_i. \tag{6.56}$$

In terms of the standard temperature, the equivalent recurrence relation reads $T_i = \eta_i T_{i-1}$. Since the ion is initially in a thermal state, we take β_0 to be constant. After n collisions starting from β_0, we get

$$\beta_n = \beta_0 \prod_{i=1}^{n} 1/\eta_i. \tag{6.57}$$

Each value of η is assumed to be independently and identically distributed, and so by applying the central limit theorem the product $\prod_{i=1}^{n} 1/\eta_i$ is log-normally distributed for large n [63]. Hence, from Eq. (6.50) we write,

$$f_{\beta_n}(\beta_n) = \frac{1}{\sqrt{2\pi n}\sigma\beta_n} \exp[-\frac{(\ln\beta_n - \ln\beta_0 + n\mu)^2}{2n\sigma^2}], \tag{6.58}$$

where $\mu = \langle \ln \eta \rangle$ and $\sigma^2 = \langle (\ln \eta)^2 \rangle - \langle \ln \eta \rangle^2$.

We now return to the energy distribution. By inserting Eq. (6.58) into Eq. (6.51), we obtain,

$$f_{E_n}(E_n) = \int \frac{E_n^k \beta_n^{k+1}}{\Gamma(k)} e^{-E_n \beta_n} \times \frac{1}{\sqrt{2\pi n}\sigma \beta_n} \exp[-\frac{(\ln \beta_n - \ln \beta_0 + n\mu)^2}{2n\sigma^2}] \mathrm{d}\beta_n. \tag{6.59}$$

We use the Laplace integration method [152] to find an approximate analytical solution for $k = 2$ as follows. The integrand of Eq. (6.59) has a maximum at the point $\beta_n = \hat{\beta}$,

$$\hat{\beta} = \beta_0 \exp\left(-n\mu + 2n\sigma^2 - \mathcal{W}\left[\beta_0 E_n n\sigma^2 e^{2n\sigma^2 - \mu n}\right]\right), \tag{6.60}$$

where $\mathcal{W}$ is the Lambert-$\mathcal{W}$ function [152]. We define $g(E_n, \beta_n)$ to be the logarithm of the integrand of Eq. (6.59) such that,

$$f_{E_n}(E_n) = \int \exp(g(E_n, \beta_n)) d\beta_n, \tag{6.61}$$

and then replace $g(E_n, \beta_n)$ with its Taylor series to second order around the point $\beta = \hat{\beta}$. This leads to a Gaussian integral which can be analytically evaluated,

$$f_{E_n}(E_n) = \frac{\hat{\beta}^3 E_n^2}{4\sqrt{\hat{\beta} E_n n\sigma^2 + 1}} \exp\left(-\hat{\beta} E_n\right) \times \left(\mathrm{erf}\left(\sqrt{\frac{\hat{\beta} E_n n\sigma^2 + 1}{2n\sigma^2}}\right) + 1\right) \exp\left(-\frac{n\sigma^2}{2}\left(\hat{\beta} E_n - 2\right)^2\right), \tag{6.62}$$

which is asymptotically correct for $E_n \to \infty$, since as E_n increases, the integral becomes more sharply peaked around $\hat{\beta}$ and the approximation becomes more precise [152]. The same method can be applied for an arbitrary value of k. In the high-energy limit for $k = 0$, the Laplace transform of a log-normal distribution for β has been shown to exhibit an exponential decay [102, 153].

From the general property of the Laplace transform,

$$\mathcal{L}_{\beta}^{E}[\beta^{k+1} f_{\beta}(\beta)] = (-1)^{k+1} \frac{d^{k+1}}{dE^{k+1}} \mathcal{L}_{\beta}^{E}[f_{\beta}(\beta)], \tag{6.63}$$

follows that if the high-energy behavior for $k = 0$ is an exponential decay, then this holds true for any integer value of k. Thus, we conclude that a purely multiplicative model of the heating process does not lead to Tsallis statistics which is characterized by a power-law tail for the distribution at high energies.

In order to test the validity of Eq. (6.62), a series of simulations were performed at a buffer gas temperature $T_b = 0$ K and varying the mass ratio or number of collisions. The results are plotted in Fig. 6.3 along with the distributions computed from Eq. (6.62). The μ and σ parameters were computed from numerical distributions $f_{\eta}(\eta)$ such as the ones shown in Fig. 6.2. At low collision numbers, the agreement is generally poor, which is expected due to the assumption in the derivation of Eq. (6.62) that the central limit theorem can be applied. Moreover, for all collision numbers, the agreement is less good at low energies due to the Laplace integration method being valid only in the limit $E \to \infty$. However, for higher energies and numbers of collisions, Eq. (6.62) becomes an increasingly better representation of the simulated data.

For comparison, the numerical data for 25 collisions at a mass ratio of 1.0 is presented in Fig. 6.3(c) together with the distribution predicted using Eq. (6.62). The red dashed line represents a Tsallis distribution obtained from a maximum-likelihood estimation (MLE) to the numerical data. It can be clearly seen that Tsallis statistics is a poor match for a buffer gas at zero Kelvin, while Eq. (6.62) provides much better agreement.

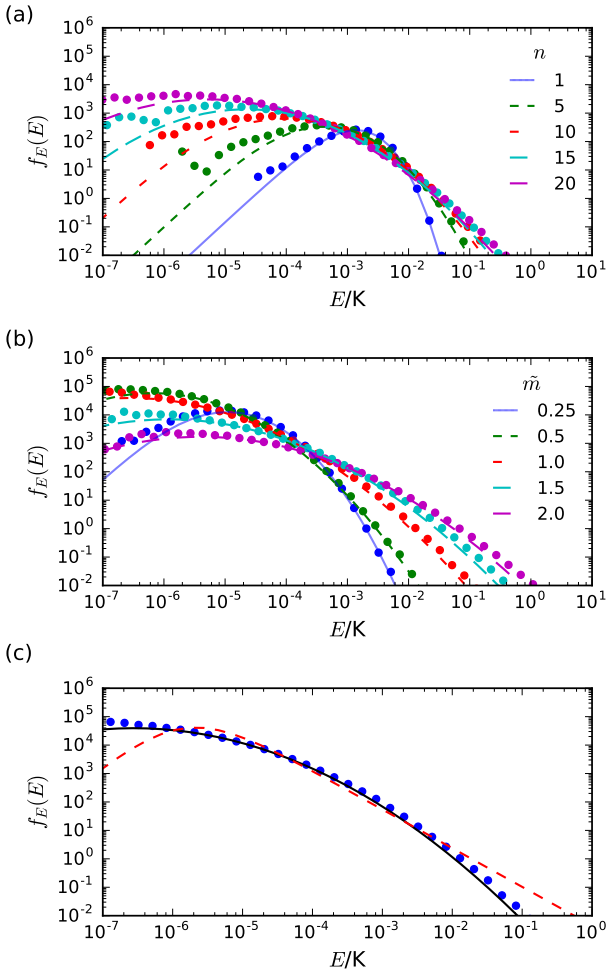

Figure 6.3: (a) Energy distributions of an ion in a RF trap after n collisions with a neutral buffer gas at zero Kelvin with a mass ratio $\tilde{m} = m_b/m_i = 1.5$.
(b) The ion energy distribution after 25 collisions at a range of mass ratios. The lines show corresponding energy distributions computed with Eq. (6.62). (c) Comparison between the ion energy distribution Eq. (6.62) for a buffer gas at 0 K (black dashed line) and a Tsallis distribution (red dashed line) after 25 collisions with $\tilde{m} = 1.0$. In all cases, the points represent numerical data sampled from 100'000 simulations.

6.2.3 Requirement for a lower bound

The energy distribution obtained through the method detailed in the previous section does not converge to a steady-state as the number of collisions increases which is a known property of an unbounded purely multiplicative random process [149, 151, 154, 155]. In the contractive case, each collision on average reduces the energy of the ion no matter how small it may already be, while if $\langle \ln \eta \rangle > 0$ the energy increases on average in each collision. Establishing a steady-state distribution requires either that the energy is bounded from below in the contractive case, or bounded from above in the divergent case [151]. For the model considered at this point, there is no upper bound on the energy. There is, however, a lower bound if at least one of $g_j(\tau)$ or T_b are nonzero, since if this is true, then ϵ may take a non-zero value. Consequently, if $E << \epsilon$, then after a collision $E' = \epsilon$ and so the convergence towards $E = 0$ is interrupted. This applies if ϵ has a non-zero probability to take any non-zero value no matter how small the resulting value may be. This is a result of the fact that when $E \to 0$, it will eventually become smaller than any non-zero value of ϵ. In terms of the random-walk analogy used in Ref. [151], the presence of ϵ corresponds to the introduction of a barrier preventing the energy from reaching the absorbing state at $E = 0$, altering the boundary conditions of the problem and hence leading to a different distribution. The combination of the drift towards this barrier due to η (in the contractive case) and the reflection from it leads to a steady-state energy distribution exhibiting a power-law tail [151]. In contrast, the tail of the distribution obtained from Eq. (6.62) depends on the initial conditions of the ion and does not exhibit a power-law tail for an initially thermal distribution [59, 102].

If the ion's initial energy is large compared to ϵ, then it may take a large number of collisions for E to reach the regime in which ϵ contributes significantly to the outcome of a collision. Consequently, for a small number of collisions the distribution may be close to the one obtained when ϵ is always zero [151]. An order-of-magnitude estimate for the number of collisions required for ϵ to become relevant to the dynamics may be found as follows. We denote this number of collisions n_ϵ and assume that $\langle \eta \rangle < 1$, that $E_{(0)} >> \langle \epsilon \rangle$, and approximate that $\langle E_{(n)} \rangle \approx \langle \eta \rangle^n \langle E_{(0)} \rangle$. By setting $\langle E_{(n_\epsilon)} \rangle = \langle \epsilon \rangle$ we obtain,

$$n_\epsilon = \frac{\ln(\langle \epsilon \rangle / \langle E_0 \rangle)}{\ln(\langle \eta \rangle)}. \tag{6.64}$$

As $\langle \epsilon \rangle \to 0$, the required number of collisions for the additive term to have

an effect increases, but remains finite as long as $\langle\epsilon\rangle \neq 0$. For typical trapping parameters $q = 0.1, a = 0.000625$, $\tilde{m} = 0.1$ and in the absence of excess micromotion, we find $\langle\epsilon\rangle \approx 0.25 k_B T_b$ and $\langle\eta\rangle \approx 0.92$ [59]. Thus, for an ion with an initial temperature of 1 mK, and a hypothetically very low buffer gas temperature of $T_b = 1$ fK, Eq. (6.64) predicts that the ion's energy will be of the same order of magnitude as ϵ after approximately 360 collisions. This does not mean that the distribution has reached the steady-state by this point, but rather that E is in the regime in which ϵ can no longer be neglected. In Fig. 6.4, we plot the energy distributions obtained under these conditions for a varying number of collisions and compare these to the distributions obtained for the same parameters with $T_b = 0$ K. For the distributions corresponding to between 1 and 250 collisions, there is little difference between $T_b = 0$ and $T_b = 1$ fK, since the ion's energy is significantly larger than the additive term due to the temperature of the buffer gas. However, at greater collision numbers it can be seen that this is no longer the case, and a clear difference is visible at 360 collisions, in agreement with the above prediction that this is when ϵ alters the dynamics. For $T_b = 0$ K, the distribution continues to move towards lower and lower values of E as the number of collisions increases, but for $T_b = 1$ fK the distributions for 500 and 1000 collisions are largely identical to each other, and are significantly different to the distributions obtained for the same number of collisions at $T_b = 0$ K. This is due to the influence of the lower bound on the energy caused by ϵ, which in this case prevents E from reaching values more than a few orders of magnitude lower than 10^{-15} K. We reiterate that since E otherwise decreases without limit, any non-zero value of ϵ is sufficient to produce a lower bound and a distribution with a power-law tail after a sufficiently large number of collisions, while if ϵ is always zero, then this lower bound does not exist and a qualitatively different distribution is obtained due to the change in boundary conditions. Although these two distributions are initially close (for the same initial conditions), they diverge as the number of collisions increases.

The form of the energy distribution does not depend on the units of energy apart from a constant scaling factor. That is, if the energy follows a distribution $f_E(E)$ and we define $\tilde{E} = aE$ where a is a positive constant, then the distribution of $\tilde{E}$ is given by [63],

$$f_{\tilde{E}}(\tilde{E}) = \frac{1}{a} f_E(\tilde{E}/a). \tag{6.65}$$

Since ϵ also has units of energy, it follows that we may choose these units such that a non-zero value of ϵ has an arbitrary magnitude without altering $f_E(E)$ beyond applying this scaling transformation. This means that multiplying ϵ by a fixed constant is equivalent to changing the units of energy and therefore effectively applies a scaling factor to $f_E(E)$. This property is why the magnitude of ϵ is unimportant in establishing the steady state, since we may always define units of energy in which ϵ is large, and it is reasonable to assume that the existence of the steady state does not depend on the units in which the energy is measured. The exception is if $\epsilon = 0$ in all cases, since then it will not be non-zero in any units of measurement. A particularly useful choice is to measure the energy in units of the mean energy, that is, taking $a = 1/\langle E \rangle$, assuming that this exists and is not equal to zero. Doing so, we find that if $g_j(\tau) = 0$, then the same distribution for $E/\langle E \rangle$ is obtained for any non-zero value of T_b, see Fig. 6.5(a) for a comparison of $T_b = 1$ fK and $T_b = 1$ MK. Likewise, the same result is obtained when setting $T_b = 0$ K and varying the amount of EMM, see Fig. 6.5(b) for offsets of 1 pm and 1m. Note, however, that if both T_b and $g_j(\tau)$ are nonzero simultaneously then rescaling one does not have the same effect, which we will discuss in more detail later.

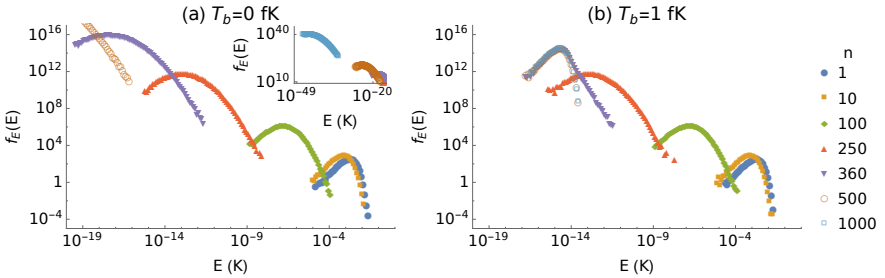

Figure 6.4: The energy distribution of an ion in a linear RF trap with $q_r = 0.1, a_z = 0.000625$, colliding with a buffer gas of neutral-to-ion mass ratio $\tilde{m} = 0.1$ after n collisions. The ion's initial energy is taken from a thermal distribution with a temperature of 1 mK, and the buffer gas temperature is set to either (a) $T_b = 0$ fK or (b) $T_b = 1$ fK. The inset in (a) shows the distributions obtained for $n = 500$ and $n = 1000$ collisions, which are not visible on the scale used for the main figure. 1'000'000 simulations are performed for each combination of collision number and T_b to produce the numerical distributions.

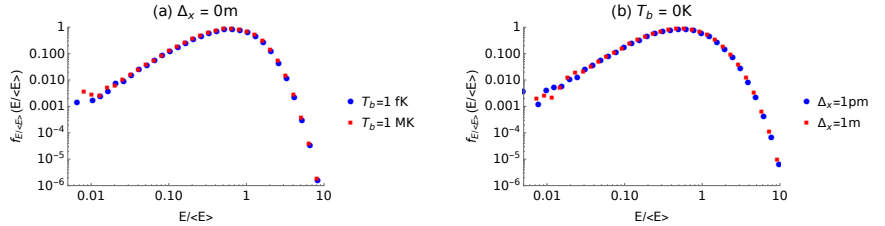

Figure 6.5: (a) The energy distribution of an ion in a RF trap with $q = 0.1, a = 0.000625$, colliding with a buffer gas of neutral-to-ion mass ratio $\tilde{m} = 0.1$ after 1000 collisions with a buffer gas of temperature $T_b = 1$ fK (blue circles) or $T_b = 1$ MK (red squares) in the absence of excess micromotion. (b) As (a), but with $T_b = 0$ K and excess micromotion parameterised by an offset of either $\Delta_x = 1$ pm (blue circles) or $\Delta_x = 1$ m (red squares) along the x-axis. The energies obtained have been rescaled by the mean energy for that distribution to make the similarity between the two distributions more apparent.

6.3 Tsallis statistics

From the above, it is clear that we cannot entirely neglect the effects of the energy contributed from the kinetic energy of the buffer gas or the excess micromotion. We first address the case where there is no excess micromotion, but the buffer gas has a non-zero temperature. From Eq. (6.32), it follows that the model is given by $E' = \eta E + a_2\epsilon_b = \eta E + \epsilon$, where ϵ_b is the total kinetic energy of the buffer gas and a_2 is the result of summing over all $a_{2,jkl}$. For a linear model of this form, the steady-state energy distribution can be expected to decay as a power-law at high energy, and the bulk of the distribution does not depend too strongly on the exact nature of the additive noise [151]. Moreover, it was shown in Ref. [151] that an approximate form for the steady-state distribution of a recurrence relation of this form can be found by replacing the additive noise term with either a lower bound or a constant if the fluctuations in the additive term can be neglected. In the case of a lower bound the resulting distribution is a Pareto distribution [151], and an inverse-Gamma distribution is obtained when the additive noise is treated as a constant [156]. Neither of these are satisfactory solutions for the energy distribution, as they do not converge to the correct thermal distribution (i.e., a Gamma distribution) when the micromotion interruption is negligible and do not produce the correct low-energy behaviour. This is because in this simplified model there is no mechanism which generates the correct density of states, that is, there is nothing which takes into account the fact that E represents the sum of the energy of multiple degrees of freedom.

Let us instead consider the distribution of the temperature of the ion. In this case, the density of states is assumed a priori by including the factor of E^k in the integral converting a temperature distribution to the energy distribution (Eq. (6.2)), and so we do not need to ensure that the temperature distribution explicitly contains an equivalent factor. In Section 6.2.2 it has already been shown that $E' = \eta E$ is equivalent to $T' = \eta T$, and therefore we need only find a representation of the additive term ϵ in the temperature domain. We begin by requiring that the change in the mean energy with each collision,

$$\langle E' \rangle = \langle \eta \rangle \langle E \rangle + \langle \epsilon \rangle, \tag{6.66}$$

is correctly reflected in the change in the mean temperature. Using the result in Appendix. 6.D, this requires that the mean temperature evolves according

to,

$$\langle T' \rangle = \langle \eta \rangle \langle T \rangle + \frac{1}{(k+1)k_B} \langle \epsilon \rangle = \langle \eta \rangle \langle T \rangle + \kappa T_b, \tag{6.67}$$

where $\kappa = \frac{1}{(k+1)} \sum_j \kappa_j$, with κ_j defined as in Eq. (6.25). This suggests that we use a model of the form,

$$T' = \eta T + T_\epsilon, \tag{6.68}$$

where T_ϵ is the equivalent of ϵ in the temperature domain and has a mean value of κT_b. In the limit $T >> \kappa T_b$, this model reduces to $T' = \eta T$ as required, and the additive term prevents the convergence to $T = 0$ such that a steady-state can exist. The distribution of T_ϵ is unknown, and in the absence of a suitable model for this distribution we replace T_ϵ by its mean value, κT_b. As long as the fluctuations in the temperature are dominated by the multiplicative noise this is a reasonable assumption. This is further justified by noting that since ϵ is proportional to the energy of the buffer gas, it follows an approximately thermal distribution, and so its representation in the temperature domain, i.e., T_ϵ, has a narrow distribution around its mean value. Finally, we note also that if the fluctuations in η are also negligible such that $\eta \approx \langle \eta \rangle$, then T' approaches a constant value, corresponding to thermal equilibrium. The energy distribution found by applying Eq. (6.2) is then simply a thermal distribution with the correct density of states, as expected.

Thus, we employ a recurrence relation of the form,

$$T_i = \eta_i T_{i-1} + \kappa T_b. \tag{6.69}$$

From the properties of stochastic recurrence relations, $f_T(T)$ asymptotically approaches a power-law of the form $T^{-(\alpha+1)}$ for large values of T, where the exponent α is defined as [149, 151],

$$\int_{\eta=0}^{\eta=\infty} f_\eta(\eta) \eta^\alpha d\eta = 1. \tag{6.70}$$

Since E also follows a recurrence relation of the same form with the same multiplicative coefficient η, the distribution of E approaches a power-law with the same exponent. To obtain the full form of the energy distribution, however, we require the entire distribution of T and not just the asymptotic behaviour.

Thus, we find an approximate form for the distribution of T, and set the parameters of this distribution to ensure that it has the correct power-law tail. To do so, we convert the discrete recurrence relation for the variable T to a continuous process for the variable $x = \ln T$. In the absence of the additive term κT_b, i.e., for $T_b = 0$ or where $T >> \kappa T_b$, we have $\ln T_i = \ln T_{i-1} + \ln \eta_i$, such that,

$$x_i - x_{i-1} = \ln \eta_i. \tag{6.71}$$

Separating $\ln \eta_i$ into its mean $\mu = \langle \ln \eta \rangle$ and a fluctuating term $\hat{\zeta}(t) = \ln \eta - \langle \ln \eta \rangle$, and replacing $x_i - x_{i-1}$ with $\frac{dx}{dt}$ produces,

$$\frac{dx}{dt} = \mu + \hat{\zeta}(t). \tag{6.72}$$

We must now augment this with a representation of the additive term κT_b, since as demonstrated in Section 6.2.3 and in Ref. [151], there is no steady-state solution in the absence of this term. Following Ref. [151], we rewrite Eq. (6.69) as,

$$\frac{T_i - T_{i-1}}{T_{i-1}} = \eta_i - 1 + \kappa \frac{T_b}{T_{i-1}}. \tag{6.73}$$

Using $(T_i - T_{i-1})/T_{i-1} \approx d \ln T/dt$, this expression can be converted into a Langevin equation for $x = \ln T$,

$$\frac{dx}{dt} = \langle \eta \rangle - 1 + \hat{\eta}(t) + \kappa T_b e^{-x}, \tag{6.74}$$

where η has been decomposed into its mean $\langle \eta \rangle$ and a fluctuating part $\hat{\eta}(t)$. Notice that this approximation leads to a different definition for the constant and the noise term than are used in Eq. (6.72), but to first order $\mu \approx \langle \eta \rangle - 1$ and the variances of $\hat{\eta}(t)$ and $\hat{\zeta}(t)$ are approximately equal [151]. To ensure that the behaviour for both $x \to \infty$ and $x \to -\infty$ is correct, we take Eq. (6.72) and add in the exponential term representing the effects of κT_b, producing,

$$\frac{dx}{dt} = \mu + \hat{\zeta}(t) + \kappa T_b e^{-x}. \tag{6.75}$$

For $x \to \infty$, the exponential term approaches zero, and we recover Eq. (6.72). Conversely, in the limit $x \to -\infty$, the exponential term is large and the remaining terms can be neglected, such that in this limit Eq. (6.75) and

Eq. (6.74) are equivalent.

To proceed, we approximate that $\hat{\zeta}(t)$ follows a Gaussian distribution, justified by an application of the central limit theorem for the fluctuations in x [64]. For this to hold exactly would require that η follows a log-normal distribution. Although η does not follow this form of distribution, it is sufficiently close to enable the derivation of the functional form of $f_x(x)$ and hence $f_T(T)$, but as this is equivalent to using an incorrect distribution in Eq. (6.70) this will produce an inaccurate value for the power-law exponent of $f_T(T)$ [151]. However, by assuming that $\hat{\zeta}(t)$ follows a Gaussian distribution, the probability distribution of x for the Langevin equation Eq. (6.75) is given by an analytically tractable Fokker-Planck equation of the form [64, 151],

$$\frac{\sigma^2}{2}\frac{d^2}{dx^2}f_x(x) - \frac{d}{dx}\left[(\mu + \kappa T_b e^{-x})f_x(x)\right] = 0, \tag{6.76}$$

where $\sigma^2 = \langle(\ln\eta)^2\rangle - \langle\ln\eta\rangle^2$ is the variance of $\hat{\zeta}(t)$ [64]. The boundary conditions are fixed by $f_T(0) \to 0$ and $f_T(\infty) \to 0$, corresponding to $f_x(x) \to 0$ for $x \to \pm\infty$. The corresponding solution of Eq. (6.76) is then given by,

$$f_x(x) = A\exp\left(-\frac{2}{\sigma^2}(\kappa T_b e^{-x} - \mu x)\right), \tag{6.77}$$

where A is a normalization constant. Changing variables back to T produces,

$$f_T(T) = \frac{4^{-\frac{\mu}{\sigma^2}}T^{\frac{2\mu}{\sigma^2}-1}e^{-\frac{2\kappa T_b}{\sigma^2 T}}\left(\frac{\kappa T_b}{\sigma^2}\right)^{-\frac{2\mu}{\sigma^2}}}{\Gamma\left(-\frac{2\mu}{\sigma^2}\right)}, \tag{6.78}$$

where $\mu < 0$ is required for the distribution to be normalizable, which is equivalent to the requirement that $\langle\ln\eta\rangle < 0$ for a steady-state to exist [149]. Defining $\nu = -\frac{2\mu}{\sigma^2}$ and $b = \frac{-\mu}{k_B T_b \kappa}$, we obtain,

$$f_T(T) = \frac{T^{-\nu-1}\left(\frac{\nu}{bk_B}\right)^{\nu}e^{-\frac{\nu}{bTk_B}}}{\Gamma(\nu)}. \tag{6.79}$$

This distribution has the overall form of an inverse-gamma distribution, in agreement with the result obtained in Ref. [156] for multiplicative fluctuations with an additive constant. For large values of T, Eq. (6.79) asymptotically approaches a power-law of the form $T^{-(\nu+1)}$. The definition of $\nu = -\frac{2\mu}{\sigma^2}$

is that which would be found by evaluating Eq. (6.70) with $f_\eta(\eta)$ set to a log-normal distribution defined by $\langle \ln \eta \rangle = \mu, \langle (\ln \eta)^2 \rangle - \mu^2 = \sigma^2$ [151]. As η does not follow log-normal statistics, this is not the correct value for the power-law exponent [151]. Moreover, the values of μ and σ are difficult to directly calculate from the collision model, as this requires averaging $\ln \eta$ over all the collision parameters. No closed-form expression for this result has been found, and so neither ν or b as defined here can be accurately calculated even if they did represent the correct parameters for this distribution. We therefore assume that the distribution of T is of the same form as Eq. (6.79), and reparameterise in terms of two new parameters, $\nu \to n_T$ and $b \to \langle \beta \rangle$,

$$f_T(T) = \frac{T^{-n_T-1} \left(\frac{n_T}{\langle \beta \rangle k_B} \right)^{n_T} e^{-\frac{n_T}{\langle \beta \rangle T k_B}}}{\Gamma(n_T)}. \tag{6.80}$$

to emphasise that these parameters are not equal to the estimates obtained from the Langevin equation approximation, and must instead be obtained through some other means (see Section 6.3.1). Changing variables from T to $\beta = 1/(k_B T)$ produces,

$$f_\beta(\beta) = \frac{1}{\beta \Gamma(n_T)} e^{-\frac{\beta n_T}{\langle \beta \rangle}} \left(\frac{\beta n_T}{\langle \beta \rangle} \right)^{n_T}, \tag{6.81}$$

which is a gamma distribution for β, and where the mean value of this distribution is equal to the parameter $\langle \beta \rangle$. Evaluating Eq. (6.2) using Eq. (6.81) produces the secular energy distribution,

$$f_E^{(T)}(E) = \left(\frac{n_T}{\langle \beta \rangle} \right)^{-k-1} \frac{\Gamma(k + n_T + 1)}{\Gamma(k+1)\Gamma(n_T)} \frac{E^k}{\left(\frac{\langle \beta \rangle E}{n_T} + 1 \right)^{k+n_T+1}}, \tag{6.82}$$

which is a Tsallis energy distribution (Eq. (6.1)). We have therefore shown that Tsallis statistics are physically meaningful for the present problem under the condition that the variance of the thermal fluctuations are sufficiently small so that the additive noise due to the thermal energy of the atoms can be approximated as a constant in the temperature domain, validating their previously empirical usage [19, 20, 53].

6.3.1 Parameter estimation

The Tsallis distribution is parameterised in terms of a scale $\langle\beta\rangle$ and an exponent n_T, and it is of interest to find a method to estimate these two parameters using quantities which can be accurately calculated from the collision model, that is, the first two moments of η and the value of κ. As previously mentioned, for stochastic recurrence relations of the form given by Eq. (6.32), it can be shown that the distribution of E asymptotically approaches a power-law of the form $E^{-(\alpha+1)}$ for large values of E [149, 151]. If the multiplicative fluctuations are more heavy-tailed than the additive noise, then the exponent α is given by Eq. (6.70) [149, 151]. The Tsallis distribution, Eq. (6.82), asymptotically approaches a power-law $E^{-(n_T+1)}$ for large values of E. To ensure that the Tsallis distribution has the correct high-energy behaviour, we require that $n_T = \alpha$, with the value obtained using this expression denoted n_T^*, i.e.,

$$\int_{\eta=0}^{\eta=\infty} f_\eta(\eta)\eta^{n_T^*} d\eta = 1. \tag{6.83}$$

The value of n_T^* which satisfies Eq. (6.83) depends on the form of $f_\eta(\eta)$. In principle, Eq. (6.83) can be evaluated by performing a set of simulations to extract a set of numerical values for η and then numerically solving Eq. (6.83). To avoid the requirement to do so, and to produce a result directly in terms of the Mathieu parameters and mass ratio, we instead find an analytical expression for n_T^* in terms of $\langle\eta\rangle, \langle\eta^2\rangle$, both of which can be calculated from the collision model without performing simulations. As discussed in Section 6.2.2, $f_\eta(\eta)$ can be approximated by a log-Laplace distribution (Eq. (6.40)) with the parameters found from the analytical estimates for $\langle\eta\rangle, \langle\eta^2\rangle$. Substituting Eq. (6.40) into Eq. (6.83) and evaluating the integral, we obtain,

$$n_T^* = a_1 - a_2 = \frac{\langle\eta\rangle - 4\langle\eta^2\rangle + 3\langle\eta\rangle\langle\eta^2\rangle}{\langle\eta\rangle - 2\langle\eta^2\rangle + \langle\eta\rangle\langle\eta^2\rangle}. \tag{6.84}$$

assuming $\delta = 1$ in Eq. (6.40). Since both $\langle\eta\rangle$ and $\langle\eta^2\rangle$ can be calculated in terms of the mass ratio and trapping parameters (Appendix 6.C), this allows for the calculation of n_T^* directly from these values. The choice of the log-Laplace distribution is motivated purely by the observation that the form of $f_\eta(\eta)$ found from numerical simulations closely resembles this distribution, and is used only to provide an expression for n_T^* in terms of $\langle\eta\rangle, \langle\eta^2\rangle$. We assume that the log-Laplace distribution holds in all cases considered here, and

therefore can calculate n_T^* without needing to simulate the entire distribution of η and numerically solve Eq. (6.83). As a result of the fact that this is not the exact distribution, and moreover the values of $\langle\eta\rangle, \langle\eta^2\rangle$ are not known precisely, the value of n_T^* calculated in this manner is not expected to be exact, but we will later demonstrate that it provides a very good approximation when the power-law tail is caused by multiplicative noise.

To fully characterize Eq. (6.82), we also require the value for $\langle\beta\rangle$. From Eq. (6.69), it follows that

$$\langle T\rangle = \langle\eta\rangle\langle T\rangle + \kappa T_b = \frac{\kappa T_b}{1-\langle\eta\rangle}, \tag{6.85}$$

Averaging $T = 1/(k_B\beta)$ over Eq. (6.81), we get,

$$\langle T\rangle = \frac{1}{k_B\langle\beta\rangle}\frac{n_T}{n_T-1}. \tag{6.86}$$

Equating Eqs. (6.85) and (6.86) we find,

$$\langle\beta\rangle = \frac{1}{k_B\kappa T_b}\frac{n_T}{n_T-1}(1-\langle\eta\rangle). \tag{6.87}$$

This derivation is only valid for $n_T > 1$ and $\langle\eta\rangle < 1$. If either of these conditions is not met, the mean temperature diverges and so the above procedure fails, although $\langle\beta\rangle$ still converges to a finite value for $n_T > 0$.

Using these predictions for the parameters, we may now confirm that Tsallis statistics sucessfully describes the energy distributions obtained from numerical simulations. The predicted and numerically simulated distributions are shown in Fig. 6.6 for four different combinations of q_r and $\tilde{m}$, finding excellent agreement. Fig. 6.7 shows a comparison of the values of the parameters n_T and $1/\langle\beta\rangle$ extracted from numerical simulations via maximum-likelihood estimation with their predictions from Eqs. (6.84) and (6.87), respectively. Below the critical mass ratio given by the intersection of the curves with the grey horizontal line in Fig. 6.7 (a), the ion motion is stable. Up to near this point, the predictions for both parameters are very close to the values extracted from numerical data, vindicating the assumptions leading to the derivation of Eq. (6.81). Above the critical mass ratio, the predicted value of $\langle\beta\rangle$ becomes increasingly inaccurate as a result of energy correlations between different coordinate axes not accounted for in the present model (see

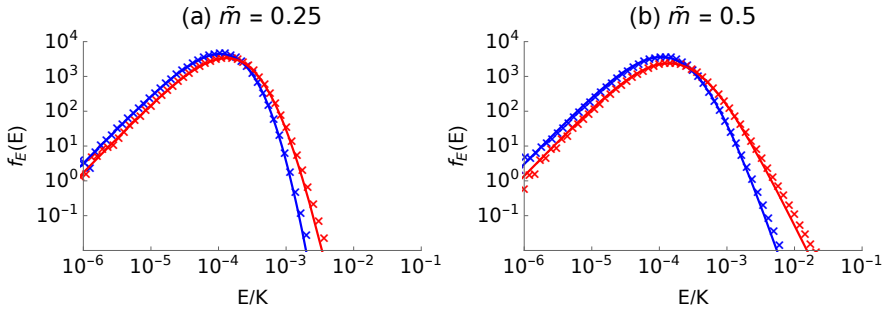

Figure 6.6: (a) The secular energy distribution of an interacting with a buffer gas of temperature 50 μK and neutral-to-ion mass ratio of $\tilde{m} = 0.25$ in a linear radiofrequency trap with $q_r = 0.1$ (blue) and $q_r = 0.5$ (red). The solid lines indicate the predicted distribution from theory and points give the results of numerical simulations (10'000'000 iterations of 500 collisions). (b) As (a), but for a mass ratio of 0.5.

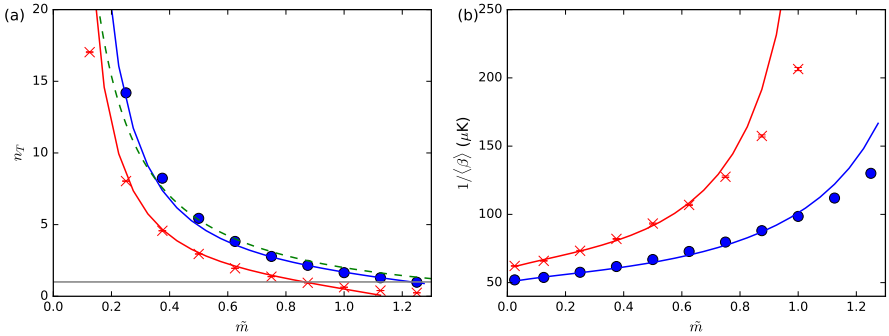

Figure 6.7: (a) Tsallis parameter n_T at Mathieu parameter $q = 0.1$ (blue circles) and $q = 0.5$ (red crosses) as a function of the neutral-to-ion mass ratio $\tilde{m}$ calculated by a maximum likelihood estimation (MLE) of a Tsallis function to the steady-state ion-energy distribution obtained from numerical simulations (100'000 trials per point). The blue and red lines show the predictions using Eq. (6.84). The green dotted line indicates the approximate result for $q < 0.4$ from Ref. [56] and the grey horizontal line indicates the critical exponent $n_T = 1$ below which the mean energy is undefined. (b) As (a) for $1/\langle\beta\rangle$. Error bars correspond to the standard errors of the MLE values and are plotted when larger than the size of the symbols.

[56]). The numerically obtained and predicted values of n_T for $q_r = 0.1$ and $\tilde{m} > 0.2$ are in good agreement with those predicted using the analytical model in Ref. [56], which is based on a simplified one-dimensional collision model. In general the analytical model successfully predicts the observed value of n_T, justifying the use of the empirical log-Laplace distribution for η and confirming that the power-law tail is due to the multiplicative fluctuations of the energy of the ion.

It is also of interest to compare the prediction of this model to the results reported experimentally for the $^{88}Sr^+$ - ^{87}Rb system [19]. For the trapping parameters used in this experiment, the mass ratio of $\tilde{m} \approx 1$ is greater than the critical mass ratio, with the experimental Tsallis exponent found to be $n_T \approx 0.8$. As an initial approximation, we use the distributions for θ_ρ, ϕ_ρ assuming equipartition of energy between the axes (Appendix 6.C), and find $n_T \approx 1.15$. This is clearly inaccurate, since the non-convergence of the mean energies requires that $n_T < 1$, and highlights the importance of using the correct distributions for these two variables. As an improved estimate, we correct for the difference in energy between the axial and radial degrees of freedom as discussed in Appendix 6.C and obtain $n_T = 0.77$, in good agreement with the experimental result. For this system the lower bound on the energy is set by the ion-neutral polarisation potential rather than the temperature of the buffer gas [148], but as this effect is significant only at low energy it appears to behave as if it was another source of additive noise.

6.3.2 Estimation of the Tsallis exponent in the presence of EMM

We now return to the general case where the ion may exhibit excess micromotion in addition to buffer gas having a non-zero kinetic energy. In this case, the additive term ϵ includes a contribution from the forced motion, and the fluctuations in this term may be large in comparison to the fluctuations in η, especially at low mass ratios for which the micromotion interruption is less significant. Under these circumstances, the analytical derivation of Tsallis statistics in the previous section is no longer necessarily valid, as this assumed that the additive noise could be approximated by a constant in the temperature domain. If this is not the case, then $f_T(T)$ may follow a different distribution, such that the superstatistical energy distribution is not given exactly by Tsallis statistics. However, it can be shown that in general, as long as $f_\beta(\beta)$ is sufficiently narrow, then the energy distribution is well approx-

imated by Tsallis statistics at low energies [99]. To be exact, this requires that the product $E\sqrt{(\langle\beta^2\rangle - \langle\beta\rangle^2)}$ is close to zero. In the present case, if the mass ratio is small then the cooling is efficient. Thus, even if the additive noise causes fluctuations in T, these are damped out sufficiently quickly that $f_T(T)$, and thus $f_\beta(\beta)$, are sufficiently narrow that Tsallis statistics can be expected over the range of energies achieved. Conversely, if the mass ratio is large, then the additive fluctuations are effectively negligible compared to the multiplicative term, and so the additive fluctuations may again be treated as effectively constant as in Section 6.3. Thus, in both cases we may reasonably expect that the energy distribution follows Tsallis statistics. Since n_T^* is based only on the multiplicative term, it may not produce the correct result when the mass ratio is small if there are significant fluctuations in the additive noise. Indeed, if ϵ has a heavier tail than η, then the power-law tail of E is defined from $f_\epsilon(\epsilon)$ and not $f_\eta(\eta)$ [149]. Thus, since n_T^* is calculated from $f_\eta(\eta)$, it may produce an incorrect estimate for the power-law tail and hence for n_T if the additive fluctuations are larger than the multiplicative fluctuations.

We therefore introduce another estimator for n_T by matching the moments of the Tsallis distribution to the analytical mean and mean-square energy, which does not require the assumption that the deviation from a thermal distribution is caused by the multiplicative noise. The mean value of the Tsallis distribution is given by,

$$\langle E_T\rangle = \frac{(1+k)}{\langle\beta\rangle}\frac{n_T}{n_T-1}, \tag{6.88}$$

for $n_T > 1$. This mean energy must be equal to the value of the mean energy $\langle E\rangle = \sum_j \langle E_j\rangle$, where the $\langle E_j\rangle$ are calculated in terms of the trapping parameters using Eq. (6.28), as demonstrated in Appendix 6.F. Thus, we have,

$$\frac{n_T}{n_T-1} = \frac{\langle\beta\rangle}{(1+k)}\sum_j \langle E_j\rangle. \tag{6.89}$$

We require a second equation to eliminate $\langle\beta\rangle$, which is obtained from calculating the second moment of the Tsallis distribution $\langle E_T^2\rangle$, and equating this to $\langle E^2\rangle = \sum_j \sum_k \langle E_j E_k\rangle, (j,k) \in (x,y,z)$. The $\langle E_j E_k\rangle$ are found by multiplying together E_j' and E_k' as given by Eq. (6.21), averaging over all the collision parameters and solving for the steady state, analogously to the mean energy. These second-order moments diverge at a lower mass ratio than the

first-order moments, and in terms of the Tsallis distribution are defined only for $n_T > 2$. This requires small values of $\tilde{m}$ and q_j and so we primarily focus on this regime from this point onwards. In terms of these mean energies, we find,

$$\hat{n_T} = \frac{(2+k)\langle E\rangle^2 - 2(1+k)\langle E^2\rangle}{(2+k)\langle E\rangle^2 - (1+k)\langle E^2\rangle}, \tag{6.90}$$

where $\hat{n_T}$ indicates that this is an estimation and is exact only if the distribution exactly follows Tsallis statistics with a known value of k, which following the discussion in the previous section we assume is given by $k = 2$. If the value of $\hat{n_T}$ is in good agreement with n_T^* then we may take this as evidence that the power-law tail is caused primarily by the multiplicative noise. However, if these estimates do not agree, then this indicates that another source of noise must be responsible for the deviation from thermal statistics.

To confirm that the use of Tsallis distributions and the values of $\hat{n_T}$ from Eq. (6.90) are accurate, the distributions obtained from numerical simulations are compared to the distribution predicted using $\hat{n_T}$ for $\tilde{m} = 0.1$ (Fig. 6.8(a)) and $\tilde{m} = 0.5$ (Fig. 6.8(b)), finding good agreement. At low mass ratio $\tilde{m} \approx 0.1$ and for the trapping parameters employed ($q_r = 0.2, a_z = 0.000625$), it is generally assumed that the ion will exhibit a thermal energy distribution. It can be seen in Fig. 6.8(a) that this is approximately true in the absence of forced motion, for which the numerical data and predicted Tsallis distribution are both close to a thermal distribution. However, this does not hold when there is forced motion. The distribution still closely follows Tsallis statistics, but with a more pronounced power-law tail, i.e., a smaller value of n_T. As the mass ratio increases, the distribution for non-zero T_b also deviates from a thermal distribution as expected, see Fig. 6.8(b). At high energies, a small deviation from the Tsallis distribution can be seen, typically accounting for 0.1% of the data set. This is likely a result of the approximations made during the derivation of Tsallis statistics and the assumption that $k = 2$. Nonetheless, the bulk of the distribution is adequately described by the present treatment, and it is clear that there is a difference between the two cases.

In Fig. 6.9 we compare the exponents obtained from numerical simulations to both the predicted value due to multiplicative fluctuations from Ref. [59], n_T^*, and the predicted value from Eq. (6.90), $\hat{n_T}$, as a function of mass ratio, both including and excluding EMM. It can be seen that n_T^* is a good predictor for the observed exponent in the absence of forced motion, as was demonstrated in the previous section. Furthermore, at high mass ratio it also

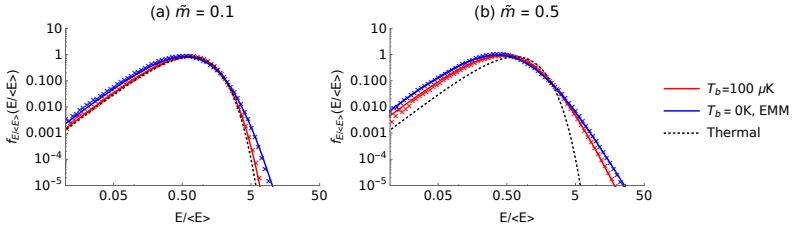

Figure 6.8: The energy distribution for an ion exhibiting excess micromotion colliding with a buffer gas of temperature $T_b = 0$ K (blue, solid) and without excess micromotion colliding with a buffer gas of temperature $T_b = 100$ μK (red, dashed) for (a) $\tilde{m} = m_b/m_i = 0.1$ and (b) $\tilde{m} = m_b/m_i = 0.5$. The data have been scaled by the analytically calculated mean energy to make the difference between the two distributions more apparent. The trapping parameters are given by $q_r = 0.2, a_z = 0.000625$, and when present the excess micromotion is defined by a static electric field such that the equilibrium position is displaced by 100 nm along the x-axis. The solid lines indicate the predicted Tsallis distributions while the dotted line gives the distribution for an ion in thermal equilibrium. Each distribution is obtained from 10'000'000 iterations of the numerical simulation and binned into logarithmically spaced bins, normalised by the bin width.

successfully predicts the exponent when forced motion is present, which is found to approach the value in the absence of forced motion. However, at low mass ratio there is no longer an agreement between n_T and n_T^*, demonstrating that the multiplicative model with an additive constant does not fully explain the dynamics in the regime of a low mass ratio with forced motion. In contrast, $\hat{n_T}$ remains reasonably accurate over all mass ratios. Both $\hat{n_T}$ and the numerical simulations show that at low mass ratio the Tsallis exponent does not diverge to infinity if the ion is subject to forced motion, i.e. a thermal distribution is not obtained in this case.

The discrepancy at low mass ratio between the value of n_T obtained from numerical simulations compared to the value estimated from $f_\eta(\eta)$, n_T^*, implies that the multiplicative fluctuations due to the micromotion interruption are not the only cause of the deviation from thermal statistics when forced motion is present. Thus, another source of fluctuations in the temperature must have an influence on n_T. We therefore re-examine the assumption that the additive fluctuations lead to a fixed increase in the temperature with each collision. In Eq. (6.13), it is demonstrated that the velocity of the forced mo-

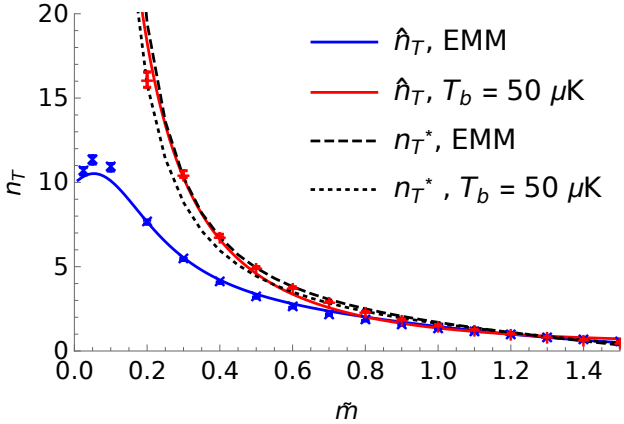

Figure 6.9: A comparison of the analytically estimated and numerically simulated values of the Tsallis exponent n_T as a function of mass ratio for a buffer gas with $T_b = 0$ K and a static electric field resulting in an offset of 100 nm (blue, lower) and a buffer gas with a temperature of $T_b = 50$ μK with no offset (red). The data points give the values found from maximum-likelihood estimation performed on the numerical data. The error bars indicate the calculated standard error and are typically smaller than the size of the symbols. The blue (lower) and red solid lines show the predicted value of the exponent from the analytically calculated mean and mean-square energy, denoted $\hat{n_T}$ in the main text. The dashed and dotted lines show the prediction from the multiplicative coefficient η, n_T^*, for the two cases [59]. The trap parameters are given by $q_r = 0.1, a_z = 0.000625$ and 200'000 simulations are performed for each data point.

tion may be assigned to the buffer gas, but there is an important distinction between the thermal motion of the buffer gas and the forced motion in that the latter does not follow a thermal distribution. To lowest order, the velocity of the in-phase EMM, i.e., the derivative of Eq. (6.7) with respect to τ, is described by $v_{f,j}(\tau) = |v| \sin(2\tau)$. When sampled at random collision times, $v_{f,j}^2$ follows a bimodal distribution with peaks of equal height at $0, |v|^2$, in contrast to the single peak for a thermal distribution [157]. To demonstrate the importance of this, we perform simulations of an ion in a time-independent harmonic trap, i.e., in the pseudopotential approximation, undergoing collisions with a buffer gas with a velocity given by $v = |v| \sin(2\tau)$. This leads to the results shown in Fig. 6.10(a), with the distribution close to that found

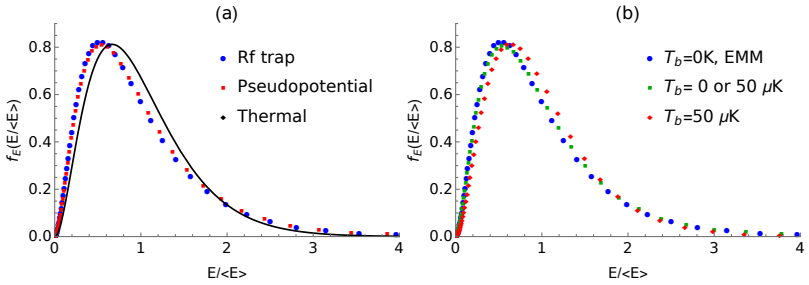

Figure 6.10: The energy distributions obtained for an ion in a linear RF trap ($q_r = 0.1, a_z = 0.000625$) interacting with a buffer gas of mass ratio $\tilde{m} = m_b/m_i = 0.1$ in different scenarios illustrating the effects of non-thermal buffer gas velocity distributions. (a) Distribution obtained in a time-dependent trapping potential with excess micromotion corresponding to an offset of 100 nm along the x-axis (blue circles), compared to the distribution obtained for an ion in a harmonic pseudopotential colliding with atoms with a velocity given by $v_x = \sin(2\tau)$ (red squares). The frequencies of the pseudopotential trap are set equal to the secular frequencies of the RF trap. The solid line indicates the distribution for a three-dimensional harmonic oscillator at thermal equilibrium. (b) Forced motion and a buffer gas temperature of $T_b = 0$ K (blue circles), a fixed buffer gas temperature of $T_b = 50$ μK (red diamonds), and a buffer gas temperature which is randomly chosen in each collision from either $T_b = 0$ or 50 μK with equal probability (green squares). 10'000'000 simulations are performed for each of the three cases.

when forced motion is present in an RF trap. Thus, a non-thermal velocity distribution of the buffer gas is sufficient to cause the deviation from thermal statistics for the ion even in the absence of the time-dependent trapping potential.

As a toy model to better understand this situation, we assume that each collision samples one of the two peaks of the distribution of v_f^2 as if the ion had collided with a buffer gas of temperature either 0 or T_b with equal probability. The temperature then evolves according to,

$$T' = \eta T + B\langle\epsilon\rangle/(3k_B), \tag{6.91}$$

where B takes values of 0 or 1 with equal probability, and ϵ is defined as for a thermal buffer gas with temperature T_b. In this model, we may view the temperature of the ion as being subject to dichotomous noise in addition

to the multiplicative noise, leading to a different distribution than the one obtained for a fixed atomic temperature [158–160]. However, as shown in Ref. [99], the energy distribution obtained will still approach Tsallis statistics as long as the ion's energy remains low.

To test this interpretation, in Fig. 6.10(b) we show the energy distribution for a simulation in which the atomic temperature is chosen from either $T_b = 0$ or 50 μK with each collision, which produces a distribution close to that observed in the presence of forced motion and which is noticeably different to the one obtained for the same trapping parameters with a fixed buffer gas temperature. It is interesting to compare this to the system discussed in Chapter 5, in which an ensemble of ions underwent a combination of laser cooling with rare collisions with background gas leading to a large amount of heating. Neglecting the heating due to photon recoil, this situation is equivalent to Eq. (6.91) with B biased such that it has only a small probability of taking the value 1 and η fixed to a constant, which we demonstrated leads to Tsallis statistics [52].

So far, we have considered only one of the two sources of additive fluctuations at a time. That is, either EMM is present and $T_b = 0$, or the buffer gas has a finite temperature and there is zero EMM. In this case, the exponent is independent of the magnitude of the fluctuations, since changing T_b or g_j while the other is set to zero is equivalent to multipling the energy by a constant which simply rescales the underlying distribution without changing its form, and so n_T remains unchanged [63]. In the more realistic case in which both forced motion and a non-zero buffer gas temperature are present, the value of n_T obtained depends on the relative proportions of each. In Fig. 6.11, we show the results of applying an electric field of varying magnitude while keeping the temperature of the buffer gas fixed at a non-zero value. It can be seen that the analytical predictions given by $\hat{n_T}$ are in good agreement with the numerical values obtained, and further that for a buffer gas at a temperature $T_b = 50$ μK only a small electric field is required to tune the exponent from one limit to the other. As noted in Ref. [71], uniform electric fields of a magnitude 1 V/m may easily develop during an ion trapping experiment and this is already sufficient to significantly alter the observed Tsallis exponent. Furthermore, since this effect applies even at very low mass ratios it cannot be assumed that in these cases the ion will exhibit a thermal distribution unless the EMM is compensated to a high degree of accuracy such that it contributes a negligible amount of energy compared to the thermal energy of the buffer gas.

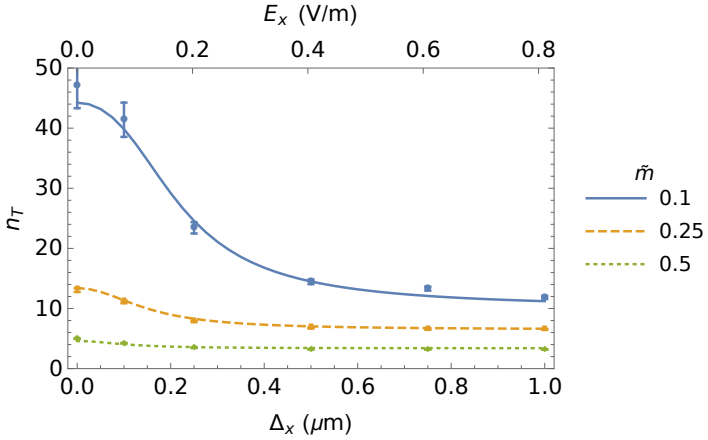

Figure 6.11: The Tsallis exponent n_T as a function of the applied electric field for a fixed buffer gas temperature of 50 μK from numerical simulations (points) and the predicted trend calculated from the mean and mean-square energy, $\hat{n_T}$, (line) for $q_r = 0.1, a_z = 0.000625$ over a range of values of the neutral-to-ion mass ratio, $\tilde{m} = m_b/m_i$. Error bars show the estimated standard error. 200'000 iterations of the numerical simulation per data point.

Let us briefly address the heating effect described in Ref. [148], which arises due to the finite time of interaction between the ion and the atom during which the ion can be displaced in the RF field. By itself, this serves to produce a lower bound on the energy of the ion analogously to the effects of non-zero values of T_b and $v_{f,j}(\tau)$. Moreover, it has been shown numerically and experimentally that, at a mass ratio of $\tilde{m} \approx 1$, this effect does not lead to a change in the observed power-law exponent [19], in agreement with the results obtained here that at high mass ratio the power-law tail is a result of the multiplicative fluctuations. At low mass ratio, however, we have shown that n_T is sensitive to the nature of the additive noise, and the heating effects due to long-range ion-atom interaction may alter the observed value of n_T in this regime if it dominates over the other additive contributions.

6.4 Localised buffer gases

The model of buffer gas cooling predicts that, if m_b/m_i is above a certain ratio, then the ion will on average gain energy from each collision and so cannot be effectively cooled. This is true if collisions occur with equal probability at all points in the ion's trajectory. However, it has been demonstrated numerically and experimentally that this limit can be overcome by ensuring that collisions are more likely when the ion is close to the centre of the trap [20, 21, 55]. At this point, the secular velocity is large compared to the velocity of the micromotion, and so collisions on average cause a greater reduction in the energy of the ion than if they occur closer to the turning points of the ion's motion. By ensuring that collisions preferentially occur at this point then the cooling remains efficient at much greater mass ratios [20, 21]. This is especially relevant for the hybrid chip trap described in Chapter 3, since in this case $\tilde{m} \approx 2$ and so the motion is predicted to be unstable for a uniform buffer gas.

6.4.1 Collisions at the centre of the trap

First, let us consider the extreme case in which collisions may only occur at the centre of the trap, under the assumption that there is no EMM. This may be achieved using the same procedure to calculate the change in energy as described in Section 6.1.2, with the exception that there is now an additional constraint that the collision must occur at the centre of the trap, $r_j(\tau) = 0$ for each $j \in (x, y, z)$, where $r_j(\tau)$ is defined as in Eq. (6.5). That is,

$$A_j(\cos\phi_j \ \mathrm{ce}_j(\tau) - \sin\phi_j \ \mathrm{se}_j(\tau)) = 0, \tag{6.92}$$

which requires that,

$$\tan\phi_j = \frac{\mathrm{ce}_j(\tau)}{\mathrm{se}_j(\tau)}. \tag{6.93}$$

Since $\tan\phi_j$ is periodic, there are two possible solutions to this equation, which physically represents that the velocity may correspond to motion in either the $+j$ or $-j$ direction. This velocity is given by,

$$v_j(\tau) = \pm\frac{A_j W_j}{\sqrt{\mathrm{ce}_j(\tau)^2 + \mathrm{se}_j(\tau)^2}}. \tag{6.94}$$

Note that the velocity at the centre of the trap depends on τ and is not equal to the maximum value of the secular velocity $\pm\beta_j c_0 A_j$, and so we expect micromotion interruption to still play a role in the outcome of a collision even at the centre of the trap.

As a concrete example, we take the case where the initial velocity is given by $(v_0, 0, 0)$, and the post-collision velocity is given by $(0, v_0, 0)$. That is, the ion is initially moving in the $+x$ direction, collides with a stationary particle with $m_b >> m_i$ in the centre of the trap, and the outgoing trajectory is rotated to the $+y$ direction without changing in magnitude. The post-collision phase must also obey Eq. (6.92), and thus,

$$\frac{A_x W_x}{\sqrt{\mathrm{ce}_x(\tau)^2 + \mathrm{se}_x(\tau)^2}} = \frac{A'_y W_y}{\sqrt{\mathrm{ce}_y(\tau)^2 + \mathrm{se}_y(\tau)^2}}. \tag{6.95}$$

Taking $a_x = a_y \approx 0, q_x = -q_y = q_r$, such that $W_x = W_y, \beta_x = \beta_y, c_{0,x} = c_{0,y}$, and using the fact that $E = E_x, E' = E'_y$ we find,

$$\frac{E'}{E} = \frac{\mathrm{ce}_y(\tau)^2 + \mathrm{se}_y(\tau)^2}{\mathrm{ce}_x(\tau)^2 + \mathrm{se}_x(\tau)^2} \approx \frac{1 + q_r \cos(2\tau)}{1 - q_r \cos(2\tau)}. \tag{6.96}$$

where the approximation applies in the limit $q \to 0$. The maximum of this ratio is for $\cos(2\tau) = 1$ and is on the order of $1 + 2|q_r|$, which is much less than the large values that $\frac{E'}{E}$ may take when collisions may occur at any point in the trap (Fig. 6.2). Thus, by limiting collisions to near the centre of the trap, the heating due to micromotion interruption can be greatly reduced, even when the mass of the buffer gas is much greater than the mass of the ion. However, since this ratio may be greater than unity, the ion may still gain energy overall from a collision, even though it takes place at the centre of the trap. This implies that it may be possible for runaway heating to occur even when collisions only take place at the centre of the trap.

We now show that this is the case, and that there is an upper limit to the mass of the neutral particle which can be used to sympathetically cool an ion by collisions at the trap centre. This localised critical mass ratio can be expected to be much greater than the critical mass ratio ≈ 1.4 observed for collisions with a uniform buffer gas due to the reduced effect of micromotion interruption, but may still limit the efficiency of cooling at high mass ratios or at large values of q_j. The post-collision energy is given by Eq. (6.21), as this expression is valid for collisions at an arbitrary point in the trap. However,

in this case the set of phases ϕ_j are determined by Eq. (6.93), such that each $f_{\phi_j}(\phi_j)$ is sharply peaked at the two possible values, which we assume to occur with equal probability. The remaining variables may be averaged over as before, and we arrive at,

$$\begin{aligned}\langle E_j' \rangle =& \frac{\langle E_j \rangle}{(1+\tilde{m})^2} + \kappa_j k_B T_b \\ &+ \sum_k \frac{\tilde{m}^2 c_{0,j}^2 W_k^2 \beta_j^2}{3(1+\tilde{m})^2 c_{0,k}^2 W_j^2 \beta_k^2} \mathcal{M}_j [(\mathrm{ce}_k(\tau)^2 + \mathrm{se}_k(\tau)^2)^{-1}] \langle E_k \rangle,\end{aligned} \tag{6.97}$$

where κ_j and $\mathcal{M}_j$ are defined as in Eqs (6.25) and (6.26). As a further simplification, we assume that the temperature of the buffer gas is negligible, and that each of the three components of the mean energy before the collision are approximately equal in magnitude, i.e., $\langle E_x \rangle = \langle E_y \rangle = \langle E_z \rangle = \frac{1}{3}\langle E \rangle$. The ratio of the post-collision energy, $\langle E' \rangle = \sum_j \langle E_j' \rangle$, to the pre-collision energy $\langle E \rangle$ is then given by,

$$\frac{\langle E' \rangle}{\langle E \rangle} = \frac{1}{(1+\tilde{m})^2} + \frac{\tilde{m}^2}{9(1+\tilde{m})^2} \sum_{j,k} \frac{c_{0,j}^2 W_k^2 \beta_j^2}{c_{0,k}^2 W_j^2 \beta_k^2} \mathcal{M}_j [(\mathrm{ce}_k(\tau)^2 + \mathrm{se}_k(\tau)^2)^{-1}] \tag{6.98}$$

If this ratio is greater than unity, then the ion on average gains energy from each collision, $\langle E' \rangle > \langle E \rangle$, leading to runaway heating. This ratio is calculated as a function of the mass ratio for two different values of q_r for an ideal linear trap, $q_x = -q_y = q_r$, $q_z = 0$, $a_z = 0.000625, a_x = a_y = -\frac{1}{2}a_z$ and plotted in Fig. 6.12 in comparison to the values extracted from numerical simulations, finding excellent agreement. The point at which $\langle E' \rangle / \langle E \rangle$ becomes greater than one is found to be very large for $q_r = 0.1$, and so cooling will usually be possible for most pairs of atoms. In contrast, for $q_r = 0.5$ the ratio is already greater than one at $\tilde{m} \approx 16$. The actual value of the critical mass ratio will deviate from this estimate due to the fact that in general $\langle E_j \rangle \neq \langle E_k \rangle$, and can be found by solving Eq. 6.97 for the steady-state mean energies and finding the point at which this expression diverges [56, 60]. For $q_r = 0.1$ and 0.5, we find $\tilde{m} = 593$ and $\tilde{m} = 17$ respectively, in reasonable agreement with the values found assuming equipartition of energy (592 and 16). This indicates that using a localised buffer gas greatly extends the range of ion-neutral systems for which sympathetic cooling of the ion is possible.

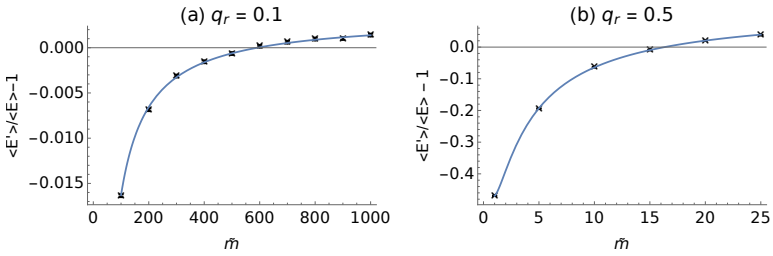

Figure 6.12: The change in the energy due to collisions of an ion of mass m_i with a particle of buffer gas of mass m_b as a function of the mass ratio, $\tilde{m} = m_b/m_i$ when the collisions take place at the centre of a radiofrequency trap. The trap is taken to be an ideal linear trap with $q_x = -q_y = q_r, q_z = 0, a_x = a_y = -a_z/2, a_z = 0.000625$, and velocity of the buffer gas prior to the collision is set equal to zero. Two cases are illustrated, (a) $q_r = 0.1$ and (b) $q_r = 0.5$. The solid lines show the analytical expression obtained by averaging over all the collision parameters, while the points give the results obtained from numerical simulations of a collision at the centre of the trap, with 100'000 simulations per point. Standard errors are smaller than the plot symbols. In all cases, it has been assumed that the ion's energy before the collision is given by a thermal distribution with the same mean energy for the motion along each axis. Values of $\langle E' \rangle / \langle E \rangle > 1$, i.e., points above the horizontal line, indicate that the ion on average gains energy from the collision due to micromotion interruption.

6.4.2 Localised buffer gases

The discussion in the previous section is valid only when collisions may occur only in the exact centre of the trap, requiring that the buffer gas is only present in that one location. We next consider the more physically realistic situation in which the buffer gas has an inhomogenous density with a peak at the centre of the trap, such that collisions are more likely to take place at the centre but may occur elsewhere. The probability that a collision takes place at a given location $\mathbf{r}$ in a time interval Δt is proportional to the density $\rho(\mathbf{r})$ of the buffer gas,

$$p(c|\mathbf{r}) = k_c \Delta t \rho(\mathbf{r}). \tag{6.99}$$

where the notation $c|\mathbf{r}$ indicates the probability of a collision (c) at a specific position $\mathbf{r}$ and where k_c is the collision rate constant. By employing Bayes' theorem, this may be converted to the probability for the ion to be at $\mathbf{r}$ given

that a collision has happened [63],

$$p(\mathbf{r}|c) = \frac{p(c|\mathbf{r})p(\mathbf{r})}{\int p(c|\mathbf{r})p(\mathbf{r})d\mathbf{r}}. \tag{6.100}$$

To proceed, we make the simplification that the density of the buffer gas changes sufficiently slowly such that it depends only on the secular position of the ion, and take the secular position to be given by $r_j = A_j \cos(\phi_j + \omega_j t) = A_j \cos\tilde{\phi}_j$. This approximation does not allow for the situation described previously where all collisions take place at the centre, but is more appropriate for a buffer gas which is not strongly localised, i.e., the density of the buffer gas does not vary significantly over the length scale given by the amplitude of the micromotion, $\approx q_j/2A_j$. For a given value of A_j, the probability for a component of the secular position to take a specific value in the interval $[-A_j, A_j]$ is [161],

$$p(r_j) = \left(\pi\sqrt{A_j^2 - r_j^2}\right)^{-1}, \tag{6.101}$$

and so, assuming that the position for each axis is independent,

$$p(\mathbf{r}) = \prod_{j\in(x,y,z)} p(r_j) = \prod_{j\in(x,y,z)} \left(\pi\sqrt{A_j^2 - r_j^2}\right)^{-1}. \tag{6.102}$$

Typically, the neutral buffer gas is confined in a potential which is approximately harmonic at the centre of the trap, such that the density of the buffer gas follows a Gaussian density distribution,

$$\rho(\mathbf{r}) = \rho_x(r_x)\rho_y(r_y)\rho_z(r_z), \tag{6.103}$$

where,

$$\rho_j(r_j) = \frac{1}{\sqrt{2\pi}\sigma_j} e^{-\frac{r_j^2}{2\sigma_j^2}}. \tag{6.104}$$

The width parameter σ_j is related to the temperature of the buffer gas T_b and the harmonic trapping frequency $\omega_{j,b}$ by,

$$\sigma_j^2 = \frac{k_B T_b}{m_b \omega_{j,b}^2}. \tag{6.105}$$

Substituting Eqs. (6.99), (6.102) and (6.103) into Eq. (6.100) and evaluating the integral produces,

$$p(\mathbf{r}|c) = \prod_{j\in(x,y,z)} \frac{\exp\left(\frac{1}{2}\left(\frac{A_j^2-2r_j^2}{2\sigma_j^2}\right)\right)}{\pi\sqrt{A_j^2-r_j^2}I_0\left(\frac{A_j^2}{4\sigma_j^2}\right)}, \tag{6.106}$$

where $I_n(x)$ is the modified Bessel function of the first kind [77]. Employing a change of variables $r_j = A_j\cos\tilde{\phi}_j$, we obtain the distribution for the instantaneous secular phase for the motion of each axis at the time of a collision,

$$f_{\tilde{\phi}_j}(\tilde{\phi}_j|c) = \frac{1}{2\pi}\frac{e^{-\frac{A_j^2\cos(2\tilde{\phi}_j)}{4\sigma_j^2}}}{I_0\left(\frac{A_j^2}{4\sigma_j^2}\right)}. \tag{6.107}$$

In Fig. 6.13, Eq. (6.107) is plotted for three values of the ratio A_j/σ_j, finding good agreement with the results found from Monte-Carlo simulations of collisions employing the method of Ref. [54] to bias the collision probability according to the density, then extracting the secular phase at the time of the collision. This distribution can be seen to vary from an effectively uniform distribution when $A_j = \frac{1}{2}\sigma_j$, to a sharply peaked distribution when $A_j = 2\sigma_j$. That is, when the ion's amplitude of motion is small compared to the characteristic length scale of the buffer gas density, there is essentially no change. However, as the buffer gas density becomes increasingly strongly localised around the centre of the trap, it is much more likely for ϕ_j to take values which correspond to the ion being at the centre of the trap at the time of a collision, $\tilde{\phi}_j = \pi/2, 3\pi/2$.

Next, we average the expression for the change in energy in a collision (Eq. (6.32)) over the collision parameters as before (Section 6.1.2), substituting $\phi_j \to \tilde{\phi}_j - \beta_j\tau$ and integrating over $f_{\tilde{\phi}_j}(\tilde{\phi}_j)$. By symmetry, any integrals which are linear in $\cos\phi_j$ or $\sin\phi_j$ will vanish. However, the components of η are proportional to $\cos^2\phi_j$ and $\sin^2\phi_j$, which lead to non-zero integrals,

$$\int \cos^2(\tilde{\phi}_j - \beta\tau) f_{\tilde{\phi}_j}(\tilde{\phi}_j) d\tilde{\phi}_j = \frac{1}{2} - \frac{I_1\left(\frac{A_j^2}{4\sigma_j^2}\right)}{2I_0\left(\frac{A_j^2}{4\sigma_j^2}\right)}\cos(2\beta\tau). \tag{6.108}$$

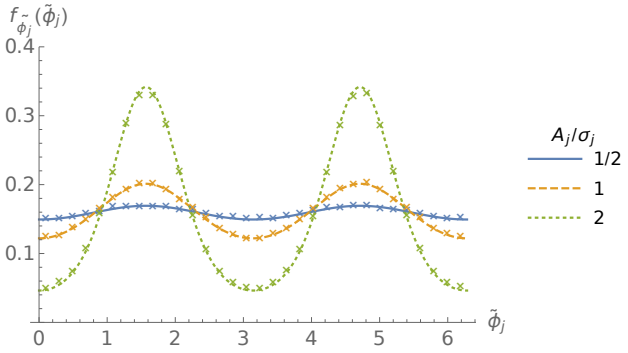

Figure 6.13: Distribution of the instantaneous phase $\tilde{\phi}_j$ at the time of a collision as the result of localisation. The lines indicate the distribution of $\tilde{\phi}_j$ at the time of collision predicted using the analytical model described in the text, while the points indicate the distributions extracted from numerical simulations of collisions in a localised buffer gas. Three ratios of the amplitude of motion A_j to the full width at half maximum of the density distribution of the buffer gas σ are plotted. 500'000 simulations are run for each of the three cases. To ensure a well-defined value of the ratio A_j/σ_j, the numerical simulations are performed using a one-dimensional model of the motion by setting the initial amplitude for the motion along one axis to a constant relative to $\sigma_j = 1$ (in arbitrary units) and the amplitude of the remaining two axes equal to zero, with the Mathieu parameters for the axis with a non-zero amplitude of motion given by $q_j = 0.24, a_j = -0.00036$. The time at which a collision occurs is sampled using the method of Ref. [54], and the value of $\tilde{\phi}_j$ recorded and binned to produce the numerical distributions.

Since A_j^2 is proportional to E_j, the effects of a localised gas are to make η dependent on the secular energy. The ratio of the Bessel functions may be expanded as $I_1(x)/I_0(x) \approx x/2$ for $x < 1/2$ [77], resulting in a term which is linear in E_j. Using the method detailed in Section 6.2.1 to extract the change in E with each collision, we obtain,

$$E' \approx \eta_0 E - \eta_1 E^2 + \epsilon = (\eta_0 - \eta_1 E)E + \epsilon, \tag{6.109}$$

where η_0 is equivalent to η in the absence of localisation, and $\eta_1 > 0$ represents the effects of localisation, which reduces the energy gained in each collision. For this approximation to remain valid, it is necessary that $A_j^2/(4\sigma_j^2) < 1/2$.

Converting A_j^2 to the secular energy using Eq. (6.9) and replacing σ_j with the buffer gas temperature and frequency using Eq. (6.105), this can be expressed as,

$$E_j < \frac{1}{\tilde{m}} k_B T_b \frac{\omega_j^2}{\omega_{j,b}^2}. \tag{6.110}$$

Taking typical neutral trap frequencies $\approx$ 100 Hz and ion trap frequencies $\approx$ 1 MHz, this holds for $E_j/(k_B T_b) < 10^8$. We proceed assuming that E is sufficiently low that the expansion of $\eta \to \eta_0 - \eta_1 E$ remains valid. An expression for $\langle \eta_1 \rangle$ is given in Appendix 6.F, with the averages over θ_ρ, ϕ_ρ and τ left unevaluated, as the averaging over the angles requires the unknown distributions for these two, while the average over τ must be done either numerically or by expanding the Mathieu functions in terms of a Fourier series. From this expression, it can be seen that η_1 inversely proportional to the temperature of the buffer gas T_b and contains terms dependent on the ratios $\omega_{j,b}/\omega_j$. Thus, the impact of localisation is increased by decreasing the temperature of the buffer gas or by increasing the stiffness of the potential used to confine the buffer gas, both of which correspond to decreasing the $1/e$ radius of the buffer gas. As a result of the fact that Eq. (6.109) is non-linear in the energy, closed-form expressions for the mean energy no longer exist. That is, the expression for $\langle E_j \rangle$ depends on $\langle E_j^2 \rangle$, which in turn depends on higher powers of the energy. We therefore do not investigate the steady-state energies, but proceed directly to obtaining the steady-state energy distribution.

6.4.3 The energy distribution due to localised buffer gases

In Section 6.3, it was shown that the energy distribution for an ion undergoing collisions described by a recurrence relation of the form $E' = \eta E + \epsilon$ can be obtained by finding an equivalent recurrence relation for the temperature and converting this to a Langevin equation for the variable $x = \ln T$. The effect of localisation is to introduce an additional term into the recurrence relation for the energy of the form $\eta_1 E^2$, and we must modify the recurrence relation for the temperature to include an equivalent term. Based on the relation between the mean energy and mean temperature, this implies that the temperature recurrence relation contains a term proportional to T^2, see Appendix 6.D. Thus, we take a model of the form:

$$T' = (\eta_0 - 4 k_B \langle \eta_1 \rangle T) T + \kappa T_b, \tag{6.111}$$

where the proportionality factor of $4k_B$ arises from the relation between $\langle E^2 \rangle$ and $\langle T^2 \rangle$ (Appendix 6.D). Since localisation only becomes significant at high energies (temperatures), the bulk of the distribution is only weakly sensitive to this effect, and so the fluctuations in η_1 are neglected to ensure that there is only one source of noise present. Using the same procedure as before (see Section 6.3) to derive a Langevin equation for $x = \ln T$ produces,

$$\frac{dx}{dt} = \mu + \hat{\zeta}(t) + \kappa T_b e^{-x} - 4k_B \langle \eta_1 \rangle e^x, \tag{6.112}$$

where $\mu = \langle \ln \eta_0 \rangle$ and $\hat{\zeta}(t)$ has a variance of $\langle (\ln \eta_0)^2 \rangle - \mu^2$. In comparison to Eq. (6.75) this has an additional term proportional to e^x, which acts as an effective force causing a repulsion from large values of x. Solving the associated Fokker-Planck equation for x [64, 151] (see Appendix 6.E) and changing variables from x to β produces a generalised inverse Gaussian distribution [162],

$$f_\beta^{(L)}(\beta) = \frac{2^{\nu-1} \left(\frac{1}{\beta}\right)^{1-\nu} \left(\frac{b}{\nu E_\ell}\right)^{-\frac{\nu}{2}} e^{-\frac{\beta\nu}{b} - \frac{1}{4\beta E_\ell}}}{K_\nu \left(\sqrt{\frac{\nu}{bE_\ell}}\right)}, \tag{6.113}$$

where $K_y(z)$ is the modified Bessel function of the second kind with index y and argument z [77], $b = \frac{-\mu}{\kappa k_B T_b}$, $\nu = -2\mu/\sigma^2$, and $E_\ell = \sigma^2/(32\langle \eta_1 \rangle)$. The superscript (L) is used here to indicate that this is the distribution appropriate for a localised buffer gas. By taking the limit $\langle \eta_1 \rangle \to 0$, Eq. (6.113) reduces to the Gamma distribution obtained for the uniform buffer gas, wheras if instead the limit $\kappa T_b \to 0$ is applied, an inverse-Gamma distribution is obtained [162]. Eq. (6.113) therefore generalises two of the common cases observed in superstatistics [101]. Substituting Eq. (6.113) into Eq. (6.2) with $k = 2$ and evaluating the integral, we find,

$$f_E^{(L)}(E) = \left(\frac{b}{\nu E_\ell}\right)^{\frac{3}{2}} \frac{E^2}{\left(\frac{bE}{\nu} + 1\right)^{\frac{3+\nu}{2}}} \frac{K_{3+\nu}\left(\sqrt{\frac{E}{E_\ell} + \frac{\nu}{bE_\ell}}\right)}{16 K_\nu \left(\sqrt{\frac{\nu}{bE_\ell}}\right)}, \tag{6.114}$$

which has the form of a gamma-generalised inverse Gaussian distribution [163], but here will be referred to as a Bessel-Tsallis distribution, reflecting the fact that the asymptotic behaviour is determined by the Bessel function and that it reduces to a Tsallis distribution in the limit $E_\ell \to \infty$, which will

be demonstrated shortly. The distribution is normalisable as long as $E_\ell > 0$ and the ratio b/ν is positive, i.e., both b and ν have the same sign. This condition is met for the definitions given here, since of the set of variables $\mu, \sigma, \kappa, k_B, T_b$ only μ can take non-positive values, but if the parameters are found numerically this must either be enforced as an additional constraint, or the substitution $\tilde{b} = b/\nu$ made with the constraint $\tilde{b} > 0$.

To gain a better understanding of this distribution, we consider two asymptotic limits for the modified Bessel function. When the argument of this function is close to zero, i.e., if $E_\ell >> E, \nu/b$, the Bessel function may be approximated by [77],

$$K_y(z) \approx \frac{1}{2}\Gamma(y)\left(\frac{z}{2}\right)^{-y}, \tag{6.115}$$

where $\Gamma(y)$ is the Gamma function. By replacing the Bessel functions in Eq. (6.114) with this approximation and simplifying the result, we find,

$$f_E^{(L)}(E) \approx \frac{E^2 b^3 \Gamma(\nu+3)}{2\Gamma(\nu)}\left(\frac{1}{bE/\nu+1}\right)^{\nu+3}, \tag{6.116}$$

which is equivalent to Eq. (6.1) with $k = 2$, $b = \langle\beta\rangle$ and $\nu = n_T$. Thus, when $E_\ell \to \infty$, the distribution converges to Tsallis statistics. This corresponds to $\langle\eta_1\rangle \to 0$, i.e., the effects of localisation becoming negligible. For large values of the argument, the Bessel function asymptotically approaches the form [77],

$$K_{3+\nu}\left(\sqrt{\frac{E}{E_\ell}+\frac{\nu}{bE_\ell}}\right) \sim e^{-\sqrt{\frac{E}{E_\ell}+\frac{\nu}{bE_\ell}}}. \tag{6.117}$$

For large values of E, Eq. (6.114) therefore asymptotically approaches zero as $e^{-\sqrt{E/E_\ell}}$. This leads to a slower asymptotic decay than the exponential function used in Ref. [20], but a faster decay than the power-law tail of the Tsallis distribution. The parameter E_ℓ controls the rate of this decay, with a small value of E_ℓ, i.e., a large value of $\langle\eta_1\rangle$, causing the distribution to more rapidly approach zero. The exact dependency of E_ℓ on the trapping parameters is complex, but in general $E_\ell \propto k_B T_b$, and decreases as the ratio $\omega_{j,b}/\omega j$ increases. This reflects that as the density of the buffer gas becomes increasingly strongly peaked at the centre, i.e., at lower temperatures or larger values of $\omega_{j,b}$, the effects of localisation become significant at lower energies.

In Fig. 6.14(a), the distributions obtained from numerical simulations of

a calcium ion interacting with a rubidium buffer gas are plotted, with the trapping parameters set to reproduce those of the hybrid chip trap (Chapter 3). By fitting the parameters of the Bessel-Tsallis distribution (Eq. (6.114)) to these results using a numerical maximum-likelihood estimation we find an excellent agreement, confirming the validity of the above method to establish the overall form for the energy distribution. Note that the high-energy tail of this distribution lies above the region in which the expansion of $\eta \to \eta_0 - \eta_1 E$ is formally valid, but it appears to remain sufficiently accurate to produce the correct form for the energy distribution.

Instead of treating b, ν, E_ℓ as numerical parameters, it would be useful to calculate these analytically in terms of the Mathieu parameters, trapping frequencies of the neutral trap, and the mass ratio. This is significantly more challenging. The distributions for θ_ρ, ϕ_ρ are unknown, preventing the evaluation of the moments of η_0 and η_1, and in the absence of expressions for the steady-state mean energies the approximations detailed in Appendix 6.C to estimate these distributions cannot be used. Furthermore, the parameters μ and σ are the mean and standard deviation of $\ln \eta_0$, which cannot be directly evaluated from the collision model. These may be estimated using the empirical log-Laplace distribution for η_0 (Eq. (6.40)) parameterised in terms of $\langle \eta_0 \rangle, \langle \eta_0^2 \rangle$, but this is not particularly accurate even when these two values are known, i.e., when the distributions of θ_ρ, ϕ_ρ have simple forms such as when equipartition of energy holds. Calculating the moments of η_0 and η_1 using the equipartition distributions for θ_ρ, ϕ_ρ (Appendix 6.C), then defining $f_\eta(\eta)$ through the use of the method of moments based on $\langle \eta_0 \rangle, \langle \eta_0^2 \rangle$ to estimate μ and σ produces a poor fit to the numerical data, as can be seen in Fig. 6.14(a). This is due to a combination of the fact that $f_\eta(\eta)$ is only known approximately, such that the moments of $\ln \eta$ cannot be accurately calculated, and the fact that equipartition of energy between the axes does not hold in the steady-state.

Thus, we take an alternative approach. By performing numerical simulations of the collision process with a localised buffer gas for a large (≈ 500) number of collisions to allow the energy distribution to reach the steady state, then simulating an additional collision with an atom of zero velocity, we obtain a numerical estimate for the ratio $E'/E = \eta = \eta_0 - \eta_1 E$. By obtaining a large number of pairs of values of E, η a linear regression can be performed to obtain estimates of $\langle \eta_0 \rangle, \langle \eta_1 \rangle$. For this regression, only pre-collision energies $E < 200 k_B$ K are used to ensure that it remains in the low-energy regime for which the linear expansion is valid, corresponding to 98% of the set of

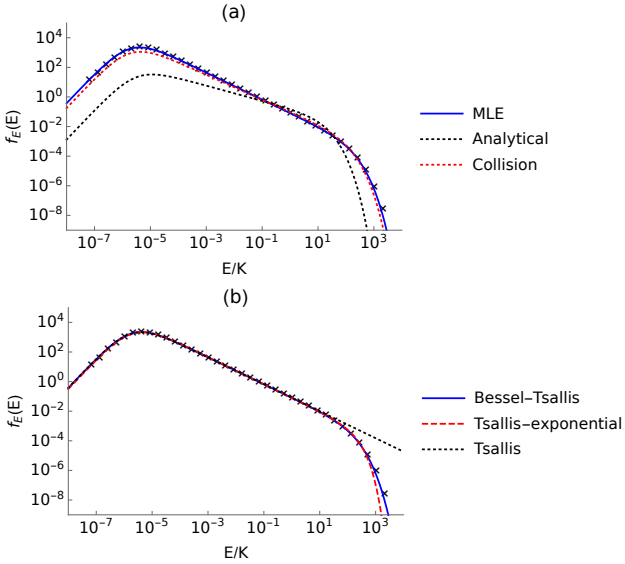

Figure 6.14: Secular energy distribution in the presence of localisation, showing a comparison between numerical data (points) and different models for the distribution. The Mathieu parameters are calculated for the surface-electrode ion trap discussed in Chapter 3 at operating conditions of $V_{RF} = 200$V, $\Omega_{RF} = 20 \times 2\pi$ MHz, and an axial frequency of $120 \times 2\pi$ kHz. The buffer gas has a mass of $m_b = 87$, a temperature of 1 μK and follows a Gaussian density distribution corresponding to trapping frequencies of $(100, 45, 188)$ Hz to match the properties of rubidium trapped in the magnetic chip trap. (a) Comparison of different methods for the estimation of the parameters of the Bessel-Tsallis distribution, showing the maximum-likelihood estimate (MLE) parameters (solid blue line), analytically calculated parameters (dotted black line), and parameters calculated numerically from the change in energy during a single collision (dashed red line). (b) Comparison between distributions using MLE parameters, showing the Bessel-Tsallis distribution (blue line), Tsallis distribution multiplied by an exponential cutoff e^{-E/E_a} as in Ref. [20] (dashed red line). A Tsallis distribution is also shown (black dotted line) as the limiting case of the Bessel-Tsallis distribution. The numerical data consists of 10'000'000 iterations of simulations each consisting of 500 collisions, while the numerical MLE is calculated using a subset consisting of the first 1'000'000 simulations due to the long computational time required to perform the numerical optimisation with larger sets.

10'000'000 values of E, E'. If, instead, a uniform buffer gas is used, then the ratio $E'/E = \eta_0$, and the set of values found in this manner used to calculate μ and σ as the mean and standard deviation of $\ln \eta_0$. The values of $\mu, \sigma, \langle \eta_1 \rangle$ found from 1'000'000 iterations of these two simulations are listed in Table 6.1 and compared to the values obtained when equipartition of energy between the motion of each axis holds, calculated both through the analytical model and through simulations of the same type as performed to calculate the steady state values, but without allowing the system to reach the steady state before extracting E'/E. Notice that in the steady-state, μ is much larger than the equipartition value, wheras $\langle \eta_1 \rangle$ decreases significantly. Calculating b, ν, l using the steady-state values for $\mu, \sigma, \langle \eta_1 \rangle$ leads to a greatly improved fit to the numerical data (Fig. 6.14(a)). Note that the values of b, ν, E_ℓ calculated using in this manner are not expected to produce an exact fit to the numerical data as a result of the fact that Eq. (6.114) is derived by replacing the distribution of η by a log-normal distribution. That is, the parameters calculated using μ and σ produce the steady-state energy distribution corresponding to a hypothetical log-normal distribution of η, rather than the actual distribution of η. Nonetheless, the difference is sufficiently small that the overall form of Eq. (6.114) is correct, and the parameters calculated using μ and σ are sufficiently accurate to validate the theory.

In a previous study of the cooling of an ion by a localised buffer gas (Refs. [20, 164]), an empirical distribution of the form,

$$f_E^{(H)}(E) \propto \frac{E^k}{(1+cE)^n} e^{-E/E_a}, \tag{6.118}$$

was employed to describe the energy distribution, that is, a Tsallis energy distribution multiplied by an exponential cutoff e^{-E/E_a}. The scale of this exponential cutoff, E_a, represents the combined energy of the micromotion and thermal energy of the buffer gas at a distance of σ_j from the centre of the trap [20, 164]. At low energy, $e^{-E/E_a} \approx 1$ and so Eq. (6.118) reduces to the Tsallis distribution. For $E >> E_a$, the asymptotic decay of this distribution is proportional to e^{-E/E_a}, in contrast to the asymptotic decay of $e^{-\sqrt{E/E_\ell}}$ for the distribution given by Eq. (6.114). In Fig. 6.14(b), a comparison of these two distributions is made with the parameters obtained from numerical maximum-likelihood estimation. Although both accurately capture the majority of the distribution, there is a slight disagreement at high energy, with the Bessel-Tsallis distribution appearing a better match to the numerical data

Parameter	Analytical	Simulation (equipartition)	Simulation (steady state)
$\langle\eta_0\rangle$	1.126	1.125 ± 0.003	1.144 ± 0.002
$k_B\langle\eta_1\rangle$	0.0036	0.004 ± 0.001	0.00067 ± 0.00003
μ	0.0362	0.0047 ± 0.0005	0.020 ± 0.002
σ^2	0.152	0.226 ± 0.001	0.240 ± 0.001

Table 6.1: A summary of the parameters describing the change in energy of an ion in a radiofrequency trap undergoing collisions with a buffer gas of zero kinetic energy, which causes the secular energy of the ion to evolve according to $E' = \eta_0 E - \eta_1 E^2$, with $\mu = \langle \ln \eta_0 \rangle$ and $\sigma^2 = \langle (\ln \eta_0)^2 \rangle - \mu^2$. Three methods are used to calculate these parameters: the analytical model of the collisions evaluated assuming equipartition of energy, numerical simulations of a collision performed with the ion's energy assuming equipartition of energy between axes, and numerical simulations performed in which the ion's energy distribution has reached the steady-state in which equipartition of energy no longer applies. Errors for values found from simulations are the standard error. The simulations performed assuming equipartition of energy sample the ion's initial energy for each axis from a thermal distribution of temperature T_0, where T_0 is the same for each axis in a given simulation, but for each simulation is chosen uniformly from the interval [0K,1K) to ensure that the energies sampled span several orders of magnitude and are not peaked around one mean energy.

in this case. This may be due to a difference in the numerical simulations performed here compared to Ref. [20], as here there is an axial component to the trapping potential and the adiabatic approximation is not employed. Moreover, we note that the distribution derived here is not valid for highly localised buffer gases, very high mass ratios, or large values of the q_j parameters due to breakdowns of the assumptions used to derive this distribution, chiefly, those used to find $f_{\phi_j}(\phi_j)$ and the expansion of $I_1(x)/I_0(x) \approx x/2$, and it may be the case that the exponential-Tsallis is more appropriate under these circumstances. Nonetheless, these approximations appear valid for the system considered here, as evidenced by the fact that the Bessel-Tsallis distribution is found to be a very good match to the numerical data. Both distributions are an improvement over the standard Tsallis distribution, which can clearly be seen to fail to describe the tail of the numerical distribution once the effects of localisation become significant.

6.5 Summary and conclusions

In this chapter, the change in the energy of an ion undergoing a Langevin-type collision with a buffer gas particle has been derived and used to investigate the steady-state energy distribution achieved by the ion after a large number of collisions. It has been shown that either the presence of excess micromotion or a non-zero temperature for the buffer gas is required to ensure that this distribution converges to a steady state, and that the distribution is well-approximated by Tsallis statistics. Excess micromotion has been shown to substantially change the power-law exponent obtained for small mass ratios compared to the exponent obtained for a non-zero buffer gas temperature. The model has been further extended to take into account the consequences of a non-uniform buffer gas density, and the form of the energy distribution has been derived in the limit in which the buffer gas density follows a Gaussian density distribution which changes slowly compared to the amplitude of the motion of the ion. By comparison to numerical simulations, this is shown to describe the energy distribution of a calcium ion in the hybrid trap undergoing collisions with co-trapped rubidium atoms.

6.A Total kinetic energy of an ion in an RF trap

In the main text, the ion's energy is characterised in terms of the secular energy, which represents the energy associated with the lowest-frequency mode of motion. The procedure used to calculate the effects of a collision, however, requires only that this energy be proportional to A_j^2, and so also applies to the time-averaged kinetic energy of the intrinsic motion used in Ref. [56]. Furthermore, for the purposes of, e.g., calculating reaction rates the total time-averaged kinetic energy, including contributions from the secular motion, instrinsic micromotion, and forced motion, may be required, as this represents the kinetic energy avaliable during collisions. The velocity of the ion is,

$$v_j(\tau) = A_j[\mathrm{c\dot{e}_j}(\tau)\cos\phi_j - \mathrm{s\dot{e}_j}(\tau)\sin\phi_j] + v_{f,j}(\tau), \tag{6.119}$$

where dots indicates the derivative with respect to τ. To simplify the notation, we define,

$$v_{h,j}(\tau) = A_j[\cos\phi_j \mathrm{c\dot{e}_j}(\tau) - \sin\phi_j \mathrm{s\dot{e}_j}(\tau)], \tag{6.120}$$

where the index h indicates that this is the solution to the homogenous equation. The average kinetic energy is given by [56],

$$E_{j,K} = \frac{1}{2} m_i \frac{\Omega^2}{4} \Theta[v_j(\tau)^2], \tag{6.121}$$

where the prefactor of $\Omega^2/4$ handles the conversion from the units of time used in the Mathieu equation to SI units, and the operator $\Theta[h(\tau)]$ is defined by,

$$\Theta[h(\tau)] = \lim_{L\to\infty} \frac{1}{2L} \int_{-L}^{L} h(\tau) d\tau. \tag{6.122}$$

We may write Eq. (6.121) as,

$$E_{j,K} = \frac{1}{2} m_i \frac{\Omega^2}{4} (I_1 + 2I_2 + I_3), \tag{6.123}$$

where,

$$I_1 = \Theta[v_{h,j}(\tau)^2], \tag{6.124}$$

$$I_2 = \Theta[v_{h,j}(\tau) v_{f,j}(\tau)], \tag{6.125}$$

and,

$$I_3 = \Theta[v_{f,j}(\tau)^2]. \tag{6.126}$$

To evaluate I_1, we use the Fourier series definitions of the Mathieu functions to write,

$$v_{h,j}(\tau) = -A_j \sum_m c_{2m,j}(\beta_j + 2m) \sin[(\beta_j + 2m)\tau + \phi_j]. \tag{6.127}$$

Using this expression, we may evaluate I_1 term-by-term to produce,

$$I_1 = A_j^2 \frac{1}{2} \sum_m c_{2m,j}^2 (\beta_j + 2m)^2. \tag{6.128}$$

Note that $\frac{1}{2} m_i \frac{\Omega^2}{4} I_1$ corresponds to the time-averaged kinetic energy of the intrinsic motion and is proportional to A_j^2 [56]. For the ion's trajectory to remain bounded, the forced motion cannot contain any frequency components which coincide with the frequencies of the intrinsic motion [80]. That is, when expressed as a Fourier series, it cannot contain terms with frequencies given by $\beta + 2m$ for any integer m. Hence, when $v_{f,j}$ is written in terms of a Fourier series and substituted into I_2, this integral must average to zero due to the orthogonality of sine and cosine functions [77]. The third integral cannot be evaluated without specifying the external force and so we shall simply denote this result as $\overline{v_{f,j}^2}$. Thus,

$$E_{j,K} = \frac{1}{2} m_i \frac{\Omega^2}{4} \left[\sum_m [A_j^2 \frac{1}{2} c_{2m,j}^2 (\beta_j + 2m)^2] + \overline{v_{f,j}^2} \right]. \tag{6.129}$$

Recall that the secular energy of the ion is given by $E_j = \frac{m_i}{2} \frac{\Omega^2}{4} A_j^2 \beta_j^2 c_{0,j}^2$. Hence,

$$E_{j,K} = \frac{1}{2} E_j \sum_m \frac{c_{2m,j}^2 (\beta_j + 2m)^2}{\beta_j^2 c_{0,j}^2} + \frac{m_i}{2} \frac{\Omega^2}{4} \overline{v_{f,j}^2}. \tag{6.130}$$

Since Eq. (6.130) is a linear function of E_j, we may obtain the ensemble average simply by replacing E_j by $\langle E_j \rangle$, which is obtained as described in the main text.

6.B Numerical methods

In principle, the collision process may be numerically simulated by means of a molecular-dynamics simulation as described in Chapter 4, with the addition of a check at each timestep to see of a collision with a neutral atom should occur. In practice, however, the requirement to simulate large numbers of these collisions means that this approach is infeasible. Instead, the simulations are performed by making use of the analytical solutions to the Mathieu equations as described in Ref. [53]. Given the position and velocity at a time τ_1, $r(\tau_1), v(\tau_1)$, in the absence of excess micromotion the position and velocity at a time τ_2 are found by multiplication by the fundamental matrix [80],

$$\begin{pmatrix} r_j(\tau_2) \\ v_j(\tau_2) \end{pmatrix} = \Phi_j(\tau_2, \tau_1) \begin{pmatrix} r_j(\tau_1) \\ v_j(\tau_1) \end{pmatrix}. \tag{6.131}$$

The fundamental matrix is given by,

$$\Phi_j(\tau_2, \tau_1) = \Psi_j(\tau_2)\Psi_j^{-1}(\tau_1), \tag{6.132}$$

where,

$$\Psi_j(\tau) = \begin{pmatrix} \mathrm{ce}_j(\tau) & \mathrm{se}_j(\tau) \\ \dot{\mathrm{ce}}_j(\tau) & \dot{\mathrm{se}}_j(\tau) \end{pmatrix}. \tag{6.133}$$

When excess micromotion is present, this approach must be modified to take the external force into account. With the same definition of the fundamental matrix, the position and velocity at τ_2 are given by [80],

$$\begin{pmatrix} r(\tau_2) \\ v(\tau_2) \end{pmatrix} = \Phi(\tau_2, \tau_1) \begin{pmatrix} r(\tau_1) \\ v(\tau_1) \end{pmatrix} + \Phi(\tau_2, \tau_1) \int_{\tau_1}^{\tau_2} \Phi(\tau, \tau_1)^{-1} \begin{pmatrix} 0 \\ g_j(\tau) \end{pmatrix} d\tau \tag{6.134}$$

Thus, the system may be directly advanced from one collision to the next without needing to numerically integrate the ion's trajectory inbetween, if τ_2 is chosen to be the time of the next collision. If collisions occur at a constant rate Γ_c, then $\tau_2 - \tau_1$ is distributed according to an exponential distribution with parameter Γ_c, and so generating a random value from this distribution allows calculation of τ_2 given τ_1. A collision is applied by calculating a new set of values for the velocity of the ion given the pre-collision velocity, the velocity of the buffer gas, and an isotropic random rotation matrix [165]. The simulation is then advanced to the next collision until a predefined number of

collisions have been sampled. To find the steady-state distribution, the total number of collisions per iteration is typically set to 300–500 to ensure that the distribution has converged.

The numerical simulations were implemented initially in Mathematica and then, to improve the computational speed, in a C++ program. For the majority of the simulations performed in this work, the collision rate is a constant but this may be altered to model a varying collision rate due to an energy-dependent cross-section or a non-uniform buffer gas density distribution, as is the case for the simulations performed in Section 6.4 [20, 54]. The density and temperature of the buffer gas is fixed for all simulations performed, see [54] for a discussion of how they may be updated after each collision to model the heating of the buffer gas by the ion. The Mathieu functions were evaluated up to the $m = \pm 5$ Fourier terms with coefficients calculated using Miller's algorithm, and the characteristic exponent was found through numerical integration [77, 166]. The energy drift in the absence of collisions after 300 propagations was found to be $E_{300}/E_0 < 10^{-5}$ for $q = 0.5$. The extraction of n_T from numerically calculated values of the energy was performed using maximum likelihood estimation to avoid the systematic errors introduced by performing linear regression on the tail of the binned data, and furthermore eliminating the need to choose appropriate bin sizes and a cutoff point [167–169]. This estimation treats $k, n_T, \langle\beta\rangle$ as free parameters to be found from the unbinned data and is performed using Mathematica [170]. The errors on the parameters found via MLE are calculated from the estimated Fisher matrix [63]. The analytical expressions for the mean energies were evaluated using Mathematica's built-in implementations of the Mathieu functions, which were also used to validate the implementations in the C++ program.

6.C Averaging over η

The factor η is a function of nine random variables – the three initial secular phases $\phi_{0,j}$, the time τ, the three variables x_1, x_2, x_3 used in the random rotation matrix given in Ref. [165], and θ_ρ, ϕ_ρ which describe the relative distribution of the secular energy between the three axes. Of these, the $\phi_{0,j}$ are uniformly distributed on $[0, 2\pi)$ for a homogenous buffer gas, and the three rotation matrix variables x_1, x_2, x_3 are uniformly distributed on $[0, 1)$. The angles θ_ρ and ϕ_ρ are the angular components in spherical coordinates of a vector ρ with magnitude $|\rho|^2 = E$, where the components of ρ are linearly

proportional to the amplitudes of motion, $\rho_j = c_{0,j}\beta_j A_j$. Since these amplitudes are all positive, the angles θ_ρ, ϕ_ρ are limited to the interval $[0, \pi/2)$, and are defined by,

$$\phi_\rho = \tan^{-1}\left(\frac{A_y c_{0,y}\beta_y}{A_x c_{0,x}\beta_x}\right) = \tan^{-1}\sqrt{\frac{E_y}{E_x}}, \tag{6.135}$$

and,

$$\begin{aligned}\theta_\rho &= \cos^{-1}\frac{A_z c_{0,z}\beta_z}{\sqrt{(A_x c_{0,x}\beta_x)^2 + (A_y c_{0,y}\beta_y)^2 + (A_z c_{0,z}\beta_z)^2}} \\ &= \cos^{-1}\sqrt{\frac{E_z}{E_x + E_y + E_z}}.\end{aligned} \tag{6.136}$$

The probability distributions for these angles may be found as follows. In the ideal case, the energy for each axis is independent and follows a thermal distribution with the same value of the temperature T_0 for each axis. Under these conditions, the joint distribution for the variable E_x, E_y, E_z is given by the product of three Boltzmann distributions [63],

$$f_{E_x,E_y,E_z}(E_x, E_y, E_z) = \left(\frac{1}{k_B T_0}\right)^3 e^{-\frac{E_x+E_y+E_z}{k_B T_0}}. \tag{6.137}$$

These components of the secular energy are related to the two angles and the total secular energy by,

$$\begin{aligned}E_x &= E\sin^2\theta_\rho\cos^2\phi_\rho, \\ E_y &= E\sin^2\theta_\rho\sin^2\phi_\rho, \\ E_z &= E\cos^2\theta_\rho,\end{aligned} \tag{6.138}$$

and making this change of variables in Eq. (6.137) produces [63],

$$f_{E,\phi_\rho,\theta_\rho}(E, \phi_\rho, \theta_\rho) = \frac{2E^2 e^{-\frac{E}{k_B T_0}}\sin(2\phi_\rho)\sin^3(\theta_\rho)\cos(\theta_\rho)}{(k_B T_0)^3}. \tag{6.139}$$

This distribution can be factored into the form $f_E(E) f_{\phi_\rho}(\phi_\rho) f_{\theta_\rho}(\theta_\rho)$, indicating that in this case these three variables are also independent of each other.

This produces,

$$f_{\phi_\rho}(\phi_\rho) = \sin(2\phi_\rho), 0 < \phi_\rho < \pi/2, \tag{6.140}$$

and

$$f_{\theta_\rho}(\theta_\rho) = 4\cos\theta_\rho \sin^3\theta_\rho, 0 < \theta_\rho < \pi/2, \tag{6.141}$$

and $f_E(E)$ is found to have the expected form for the total energy of a three-dimensional harmonic oscillator,

$$f_E(E) = \frac{E^2}{2(k_B T_0)^3} e^{-\frac{E}{k_B T_0}}. \tag{6.142}$$

We may make use of these distributions and the expression for η to calculate $\langle\eta\rangle$ and $\langle\eta^2\rangle$ by averaging it in turn over each of these distributions. The integrations over $\phi_{x,y,z}, x_1, x_2, x_3, \phi_\rho, \theta_\rho$ may be performed analytically, leaving only the integration over τ to be performed. In theory, this integration could also be performed analytically through use of the Fourier series expansions of the Mathieu functions, but in practice we simply perform this integration numerically using the built-in Mathematica routines to avoid the evaluation of the quadruple sums arising from products of the form $\mathrm{ce}_j(\tau)^2\mathrm{ce}_k(\tau)^2$. We find that the remaining function of τ is periodic and so numerically integrating over a single period is sufficient to calculate $\langle\eta\rangle$ and $\langle\eta^2\rangle$ in terms of the Mathieu parameters and the mass ratio. As shown in Fig. 6.15, the mean value calculated using this procedure and the stated distributions for the random variables involved is in excellent agreement with the values found from simulations in the limit where the components of the energy of the ion follow thermal distributions with the same temperature for each axis.

In practice, especially at higher mass ratios and values of the Mathieu q parameter, this assumption of thermal equilibrium breaks down. In the main text, it was demonstrated that the energy distribution deviates from thermal statistics, that there is no equipartition of energy between axes, i.e., $\langle E_x\rangle \neq \langle E_z\rangle$, and that at sufficiently high mass ratios $\langle E_j\rangle$ becomes undefined, see Fig. 6.1. Under these conditions, the distributions for θ_ρ, ϕ_ρ derived above are no longer valid. This follows from the fact that the different mean energies for each axis imply that the energy distribution cannot be the same for each axis, and can be seen by plotting the distribution of θ_ρ extracted from numerical simulations as shown in Fig. 6.16. When the energy for each axis is thermally distributed and equipartition of energy applies, the distribution for θ_ρ is well-described by Eq. (6.141), both sampled over all energies and using a subset

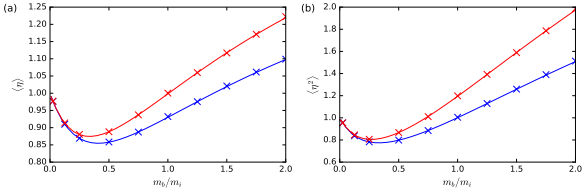

Figure 6.15: (a) A comparison of the mean value of η extracted from numerical simulation (points) to the analytical predictions in the text (lines) for $q_R = 0.1$ (blue) and $q_R = 0.5$ (red). Points represent the result of 100'000 simulations, error bars corresponding to the standard error are not visible on this scale. (b) As (a), except for the mean value of η^2. In both cases, the expressions are calculated assuming that equipartition of energy applies between all three spatial degrees of freedom.

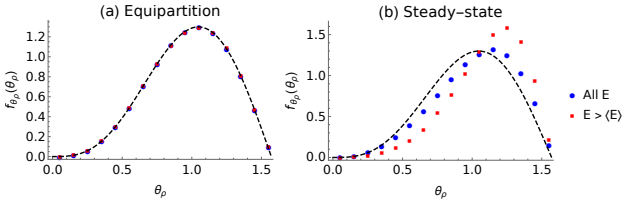

Figure 6.16: The distribution of the parameter θ_ρ, shown for (a) thermal equilibrium with equipartition of energy between the axes and (b) the steady-state energy distribution for an ion in an ideal linear radiofrequency trap defined by $q_x = 0.1, a_z = 0.000625$ interacting with a buffer gas of equal mass. The blue circles indicate the distribution obtained when sampling over all values of the total energy, wheras the red squares indicate the subset with $E > \langle E\rangle$. The dashed black line gives the analytical distribution for θ_ρ when thermal equilibrium is assumed. The distributions including all energies are sampled from 1'000'000 data points, while the reduced sets correspond to 423'100 data points in (a) and 185'960 data points in (b).

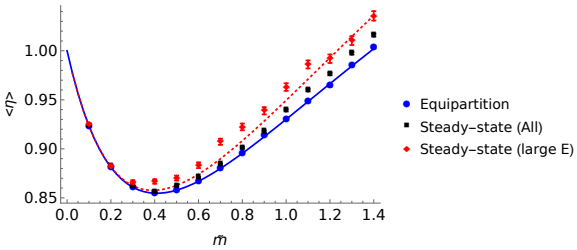

Figure 6.17: The value of $\langle\eta\rangle$ as a function of the neutral to ion mass ratio, $\tilde{m} = m_b/m_i$ for the same trapping parameters as Fig. 6.16. The solid blue line gives the analytical prediction when equipartition of energy holds finding excellent agreement with the results of numerical simulations in this limit (blue points). Black squares indicate the steady-state value of $\langle\eta\rangle$ averaged over all energies. Calculating $\langle\eta\rangle$ in the steady-state using the largest 10% of pre-collision energies produces a larger increase (red diamonds). An analytical model calculated using a correction for the breakdown of equipartition (red dashed line, see text) produces a more accurate representation of this change in $\langle\eta\rangle$. The error bars correspond to the standard error and all points indicate the average of 100'000 values of η.

limited to values of the energy greater than the mean, $E > \langle E\rangle$. However, once the energy distribution has reached the steady-state, this is no longer the case. It can be seen that θ_ρ is shifted to larger values in general compared to the equipartition value, indicating that more energy is in the radial modes than in the axial. Moreover, it is also demonstrated that θ_ρ is not entirely independent of E, as a difference in the distributions can be seen when sampling θ_ρ over all values of E when compared to the subset of this sample for which $E > \langle E\rangle$. This corresponds to a breakdown of the assumption that $E, \theta_\rho, \phi_\rho$ are independent, but applies only for the most energetic ions, and does not appear to alter the accuracy of these results too significantly.

In order to correct for this effect, an improved approximation for the distributions of these angles is derived as follows. We now approximate that the energies are described by thermal distributions but incorporate the difference in mean energy by taking a different temperature for each axis For a linear trap with radial frequency, we set $T_x = T_y = \xi T_z$, where $\xi < 1$ reflects the decreased mean energy of the axial motion. Taking the joint distribution to be the product of these individual distributions, applying the change of variables to $E, \theta_\rho, \phi_\rho$, and integrating over E and ϕ_ρ produces the marginal distribution

for θ_ρ,

$$f_{\theta_\rho}(\theta_\rho) = \frac{4\xi^2 \sin^3(\theta_\rho)\cos(\theta_\rho)}{\left((1-\xi)\cos^2(\theta_\rho)+\xi\right)^3}. \tag{6.143}$$

The required value of ξ is approximately equal to $\langle E_z\rangle/\langle E_x\rangle$, which for low mass ratios can be calculated using the analytical expression for these mean energies. The mean energies diverge for masses above the critical mass ratio, but the expression obtained for ξ in this manner remains continuous even above the critical mass ratio.

As a result of the breakdown of equipartition, not only does $\langle\eta\rangle$ deviate from the value calculated assuming equipartition of energy, but is also slightly dependent on the energy due to the correlation between θ_ρ, ϕ_ρ and E. This effect is plotted as a function of mass ratio in Fig. 6.17 by comparing the values of $\langle\eta\rangle$ obtained when equipartition of energy holds to those found in the steady state. It can be seen that $\langle\eta\rangle$ differs from the equipartition value, and moreover, that $\langle\eta\rangle$ increases slightly when considering only the largest values of the pre-collision energy, i.e., those for which more of the energy is in the radial modes. The difference between these values is only a few percent, and for the purposes of obtaining the steady-state distribution of E we assume that η is approximately independent of E. The analytical values of $\langle\eta\rangle$ calculated using the above distribution for θ_ρ are shown as the dashed line in Fig. 6.17. Although this slightly overestimates $\langle\eta\rangle$ averaged over all pre-collision energies, it is more accurate in the limit $E >> \langle\epsilon\rangle$ for which the effects of the multiplicative fluctuations are most significant. The values of $\langle\eta\rangle, \langle\eta^2\rangle$ calculated using this method work reasonably well to predict the values of the Tsallis exponent n_T, validating the use of this correction.

6.D Moments of superstatistical distributions

For a general energy distribution which can be expressed as a superposition of thermal states, i.e.,

$$f_E(E) = \int \frac{E^k}{(k_B T)^{k+1}\Gamma(k+1)} f_T(T) e^{-\frac{E}{k_B T}}\, dT, \tag{6.144}$$

the moments are given by,

$$\langle E^n \rangle = \int E^n f_E(E) dE = \int \int E^n \frac{E^k}{(k_B T)^{k+1} \Gamma(k+1)} f_T(T) e^{-\frac{E}{k_B T}} dT dE. \tag{6.145}$$

Exchanging the order of integration to first integrate over E produces,

$$\langle E^n \rangle = \int k_B^n T^n \frac{\Gamma(k+n+1)}{\Gamma(k+1)} f_T(T) dT, \tag{6.146}$$

and integration with respect to T produces,

$$\langle E^n \rangle = k_B^n \frac{\Gamma(k+n+1)}{\Gamma(k+1)} \langle T^n \rangle, \tag{6.147}$$

which is the superstatistical generalisation of the result expected from equipartition. Thus, if the mean change in energy in a collision is given by,

$$\langle E' \rangle = \langle \eta \rangle \langle E \rangle + \langle \epsilon \rangle, \tag{6.148}$$

this may be represented in the temperature domain by,

$$(k+1) k_B \langle T' \rangle = (k+1) k_B \langle \eta \rangle \langle T \rangle + \langle \epsilon \rangle. \tag{6.149}$$

In the absence of EMM, $\langle \epsilon \rangle = \sum_j \kappa_j k_B T_b$, see Eq. (6.25) and so,

$$\langle T' \rangle = \langle \eta \rangle \langle T \rangle + T_b \frac{1}{k+1} \sum_j \kappa_j. \tag{6.150}$$

6.E The Bessel-Tsallis distribution

When the buffer gas follows a Gaussian density distribution, the mean energy evolves in each collision according to,

$$\langle E' \rangle = \langle \eta_0 \rangle \langle E \rangle - \langle \eta_1 \rangle \langle E^2 \rangle + \langle \epsilon \rangle, \tag{6.151}$$

and using Eq. (6.147) we obtain

$$\langle T' \rangle = \langle \eta_0 \rangle \langle T \rangle - 4 k_B \langle \eta_1 \rangle \langle T^2 \rangle + \frac{\langle \epsilon \rangle}{3 k_B}. \tag{6.152}$$

Assuming that there is no EMM and neglecting the fluctuations in both the additive term and η_1, a suitable recurrence relation for the random variable T is,

$$T' = \eta_0 T - 4k_B\langle\eta_1\rangle T^2 + \kappa T_b. \tag{6.153}$$

In terms of the variable $x = \ln T$, this is equivalent to a Langevin equation of the form[151],

$$\frac{dx}{dt} = \mu + \hat{\zeta}(t) + \kappa T_b e^{-x} - 4\langle\eta_1\rangle k_B e^x, \tag{6.154}$$

Here, $\hat{\zeta}(t)$ represents the fluctuations of $\ln\eta_0$ around its mean value of $\mu = \langle\ln\eta_0\rangle$. Under the assumption that $\hat{\zeta}(t)$ is Gaussian white noise, this gives rise to a Fokker-Planck equation for the probability distribution $f_x(x)$ [151],

$$\frac{\sigma^2}{2}\frac{d^2}{dx^2}f_x(x) - \frac{d}{dx}\left[(\mu + \kappa T_b e^{-x} - 4\langle\eta_1\rangle k_B e^x) f_x(x)\right] = 0, \tag{6.155}$$

where σ^2 is the variance of $\hat{\zeta}(t)$. Subject to the boundary conditions that $f_x(x) \to 0$ for $x \to \pm\infty$, the steady-state distribution for T is,

$$f_T^{(L)}(T) = \frac{2^{\nu-1}\left(\frac{b}{\nu}\right)^{-\frac{\nu}{2}} T^{-\nu-1}\left(\frac{k_B^2}{E_\ell}\right)^{-\frac{\nu}{2}} e^{-\frac{\nu}{bk_BT} - \frac{k_BT}{4E_\ell}}}{K_\nu\left(\sqrt{\frac{\nu}{bE_\ell}}\right)}, \tag{6.156}$$

where $K_y(z)$ is the modified Bessel function of the second kind with order y and argument z, and the superscript (L) is used to indicate that this is the distribution obtained in the presence of a localised buffer gas. The parameters are defined in terms of the coefficients of Eq. (6.155) as,

$$b = \frac{-\mu}{k_B\kappa T_b}, \tag{6.157}$$

$$\nu = \frac{-2\mu}{\sigma^2}, \tag{6.158}$$

$$E_\ell = \frac{\sigma^2}{32\langle\eta_1\rangle}. \tag{6.159}$$

If $E_\ell > 0$, then the distribution is normalisable as long as the ratio $b/\nu > 0$. For $E_\ell < 0$ no steady-state exists, and we proceed assuming $E_\ell > 0$ and $b/\nu > 0$.

The energy distribution is defined as before,

$$f_E^{(L)}(E) = \int E^k \beta^{k+1} \frac{1}{\Gamma(k+1)} f_\beta(\beta) e^{-\beta E} d\beta. \tag{6.160}$$

Changing the variable in Eq. (6.156) to $\beta = 1/(k_B T)$ to find $f_\beta(\beta)$, then evaluating Eq. (6.160) produces,

$$f_E^{(L)}(E) = \frac{E^k \left(\frac{bE}{\nu}+1\right)^{-\frac{1}{2}(k+\nu+1)} \left(\frac{b}{\nu E_\ell}\right)^{\frac{k+1}{2}} K_{k+\nu+1}\left(\sqrt{\frac{E}{E_\ell}+\frac{\nu}{bE_\ell}}\right)}{2^{k+1}\Gamma(k+1)K_\nu\left(\sqrt{\frac{\nu}{bE_\ell}}\right)}. \tag{6.161}$$

The moments of this distribution are difficult to evaluate directly due to the complexity of integrals involving the Bessel function. However, the moments of Eq. (6.156) may be easily calculated by evaluating $\int T^n f_T(T) dT$, and applying Eq. (6.147) produces,

$$\langle E^n \rangle = \frac{2^n \Gamma(k+n+1)\left(\frac{b}{\nu E_\ell}\right)^{-\frac{n}{2}} K_{\nu-n}\left(\sqrt{\frac{\nu}{bE_\ell}}\right)}{\Gamma(k+1)K_\nu\left(\sqrt{\frac{\nu}{bE_\ell}}\right)}. \tag{6.162}$$

The mean energy $\langle E \rangle$ evaluated using this expression is defined as long as $E_\ell > 0$ and $b/\nu > 0$. However, as demonstrated in Section 6.4.1, the mean energy may diverge even if collisions occur only at the centre of the trap. This corresponds to a breakdown of the assumption that η can be expanded as $\eta \to \eta_0 + \eta_1 E$, since for high energies the linear approximation of the ratio of Bessel functions used to obtain this result is no longer valid.

Analytical expressions for the maximum-likelihood estimates of the parameters b, ν, E_ℓ have not yet been obtained due to the complexity of derivatives of the Bessel function with respect to ν. Thus, the estimation is performed numerically with respect to the parameters $\tilde{b} = b/\nu, \nu, E_\ell$. The use of $\tilde{b}$ ensures that this parameter is strictly positive, reducing the range of values to optimise over and eliminating the constraint that b must have the same sign as ν.

6.F Mathematica notebooks

In the following pages, extracts from a Mathematica notebook are provided detailing how the change in energy during a collision is calculated and used to obtain the mean steady-state energies in Chapter 6. Note that for reasons of space the output is necessarily truncated in places. An expression for the mean value of η_1, that is, the linear coefficient for the model of $\eta = \eta_0 - \eta_1 E$ is also given in terms of an average over the distributions of $\tau, \theta_\rho, \phi_\rho$.

```
(*Define an isotropic rotation matrix following J.Arvo,Graphics Gems III,117 (1992).*)
RandomRotationMatrix[x1_, x2_, x3_] :=
 ({{-Cos[2 π x1] (1 - 2 x3 Cos[2 π x2]^2) - 2 x3 Cos[2 π x2] Sin[2 π x1] Sin[2 π x2],
    -(1 - 2 x3 Cos[2 π x2]^2) Sin[2 π x1] + 2 x3 Cos[2 π x1] Cos[2 π x2] Sin[2 π x2], 2 Sqrt[1 - x3] Sqrt[x3]
     Cos[2 π x2]}, {2 x3 Cos[2 π x1] Cos[2 π x2] Sin[2 π x2] + Sin[2 π x1] (1 - 2 x3 Sin[2 π x2]^2),
    2 x3 Cos[2 π x2] Sin[2 π x1] Sin[2 π x2] - Cos[2 π x1] (1 - 2 x3 Sin[2 π x2]^2),
    2 Sqrt[1 - x3] Sqrt[x3] Sin[2 π x2]}, {2 Sqrt[1 - x3] Sqrt[x3] Cos[2 π x1] Cos[2 π x2] -
     2 Sqrt[1 - x3] Sqrt[x3] Sin[2 π x1] Sin[2 π x2], 2 Sqrt[1 - x3] Sqrt[x3] Cos[2 π x2] Sin[2 π x1] +
     2 Sqrt[1 - x3] Sqrt[x3] Cos[2 π x1] Sin[2 π x2], -1 + 2 (1 - x3)}})
(*To avoid computationally slow simplifications following integration,
we also define it purely in terms of the matrix elements,
and define a set of rules for converting this to the trig definitions later.*)
RandomRotationMatrixNoTrig = {{rxx, rxy, rxz}, {ryx, ryy, ryz}, {rzx, rzy, rzz}};
replaceMatrixTrig =
  Transpose[{Flatten[RandomRotationMatrixNoTrig], Flatten[RandomRotationMatrix[x1, x2, x3]]}] /.
   {a_, b_} :> a → b;
```

```
(*Define the ion's trajectory in terms of the homogenous motion
  (parameterised with amplitude and phase) and a forced motion term*)
IonTrajectory = A_j Cos[ϕ_j] ce[a_j, q_j, τ] - A_j Sin[ϕ_j] se[a_j, q_j, τ] + rf_j[g_j, τ]
(*The velocity is the derivative with respect to τ - the conversion to SI is handled later  *)
IonVelocity =  D[IonTrajectory, τ]
IonTrajectoryPostCollision =
 IonTrajectory /. {Subscript[A, j] → Subscript[(A'), j], Subscript[ϕ, j] → Subscript[(ϕ'), j]}
IonVelocityPostCollision = IonVelocity /.
  {Subscript[A, j] → Subscript[(A'), j], Subscript[ϕ, j] → Subscript[(ϕ'), j]}
```

$$ce[a_j, q_j, \tau]\, \text{Cos}[\phi_j]\, A_j - se[a_j, q_j, \tau]\, \text{Sin}[\phi_j]\, A_j + rf_j[g_j, \tau]$$

$$rf_j^{(0,1)}[g_j, \tau] + \text{Cos}[\phi_j]\, A_j\, ce^{(0,0,1)}[a_j, q_j, \tau] - \text{Sin}[\phi_j]\, A_j\, se^{(0,0,1)}[a_j, q_j, \tau]$$

$$ce[a_j, q_j, \tau]\, \text{Cos}[\phi'_j]\, A'_j - se[a_j, q_j, \tau]\, \text{Sin}[\phi'_j]\, A'_j + rf_j[g_j, \tau]$$

$$rf_j^{(0,1)}[g_j, \tau] + \text{Cos}[\phi'_j]\, A'_j\, ce^{(0,0,1)}[a_j, q_j, \tau] - \text{Sin}[\phi'_j]\, A'_j\, se^{(0,0,1)}[a_j, q_j, \tau]$$

```
(*The phase after a collision is given by:*)
Subscript[ϕPrimePlus, j] = ArcCos[Subscript[A, j] / Subscript[(A'), j] Cos[Subscript[ϕ, j] +
      ArcTan[ce[Subscript[a, j], Subscript[q, j], τ], se[Subscript[a, j], Subscript[q, j], τ]]]] -
  ArcTan[ce[Subscript[a, j], Subscript[q, j], τ], se[Subscript[a, j], Subscript[q, j], τ]]
Subscript[ϕPrimeMinus, j] = -ArcCos[Subscript[A, j] / Subscript[(A'), j] Cos[Subscript[ϕ, j] +
       ArcTan[ce[Subscript[a, j], Subscript[q, j], τ], se[Subscript[a, j], Subscript[q, j], τ]]]] -
  ArcTan[ce[Subscript[a, j], Subscript[q, j], τ], se[Subscript[a, j], Subscript[q, j], τ]]
```

$$\text{ArcCos}\left[\frac{\text{Cos}[\text{ArcTan}[ce[a_j, q_j, \tau], se[a_j, q_j, \tau]] + \phi_j]\, A_j}{A'_j}\right] - \text{ArcTan}[ce[a_j, q_j, \tau], se[a_j, q_j, \tau]]$$

$$-\text{ArcCos}\left[\frac{\text{Cos}[\text{ArcTan}[ce[a_j, q_j, \tau], se[a_j, q_j, \tau]] + \phi_j]\, A_j}{A'_j}\right] - \text{ArcTan}[ce[a_j, q_j, \tau], se[a_j, q_j, \tau]]$$

```
(*Substituting these into IonTrajectoryPostCollision produces the position before
  the collision as required. The sign convention should be chosen such that the A_j>
 0 but does not affect the post-collision energy, as this is A'_j^2*)

IonTrajectoryPostCollision /. Subscript[(ϕ'), j] → Subscript[ϕPrimePlus, j] // FullSimplify
IonTrajectoryPostCollision /. Subscript[(ϕ'), j] → Subscript[ϕPrimeMinus, j] // FullSimplify
```

$$\left(ce[a_j, q_j, \tau]\, \text{Cos}[\phi_j] - se[a_j, q_j, \tau]\, \text{Sin}[\phi_j]\right) A_j + rf_j[g_j, \tau]$$

$$\left(ce[a_j, q_j, \tau]\, \text{Cos}[\phi_j] - se[a_j, q_j, \tau]\, \text{Sin}[\phi_j]\right) A_j + rf_j[g_j, \tau]$$

```
(*Next, we set up the vectors containing the ion's post-collision velocity,
both in terms of A' and in terms of the pre-collision velocities put into the collision model
  The velocities of the neutral buffer gas here
  are defined with respect to the reduced time τ and not the SI time.

*)
velPrimeLeft = {IonVelocityPostCollision /. j → x,
   IonVelocityPostCollision /. j → y, IonVelocityPostCollision /. j → z};
velInitial = { IonVelocity /. j → x, IonVelocity /. j → y, IonVelocity /. j → z};
velNeutral = {vbx, vby, vbz};
velPrimeRight = 1 / (1 + m̃) velInitial + m̃ / (1 + m̃) velNeutral +
   m̃ / (1 + m̃) RandomRotationMatrixNoTrig. (velInitial - velNeutral);

(*We eliminate the set of ϕ' by using the relations found earlier.We have two choices of phi'
 and here we evaluate both. The two lead to the same expression for the change in energy,
the proof of which is omitted for space but easily verified.*)
velPrimeLeft2 =
  ((velPrimeLeft /. {Subscript[(ϕ'), x] → (Subscript[ϕPrimePlus, j] /. j → x), Subscript[(ϕ'), y] →
           (Subscript[ϕPrimePlus, j] /. j → y), Subscript[(ϕ'), z] →
           (Subscript[ϕPrimePlus, j] /. j → z)} // TrigExpand) /. Cos[x_] :→ TrigExpand[Cos[x]]) //.
    a_ / Sqrt[b_] - c_ / Sqrt[b_] :→ (a - c) / Sqrt[b] //. a_ / Sqrt[b_] + c_ / Sqrt[b_] :→
    (a + c) / Sqrt[b];
velPrimeLeft2Minus = ((velPrimeLeft /. {Subscript[(ϕ'), x] → (Subscript[ϕPrimeMinus, j] /. j → x),
          Subscript[(ϕ'), y] → (Subscript[ϕPrimeMinus, j] /. j → y), Subscript[(ϕ'), z] →
           (Subscript[ϕPrimeMinus, j] /. j → z)} // TrigExpand) /. Cos[x_] :→ TrigExpand[Cos[x]]) //.
    a_ / Sqrt[b_] - c_ / Sqrt[b_] :→ (a - c) / Sqrt[b] //. a_ / Sqrt[b_] + c_ / Sqrt[b_] :→
    (a + c) / Sqrt[b];
```

```
(*Next, A' must be isolated and squared for each of the components.
  This isn't the most computationally efficient way of doing so,
but it avoids needing to define each and every step of the process.

*)


Assuming[{(A')x > 0},
 PostCollisionAmplitudeSqX = ((A')x /. Solve[velPrimeLeft2[[1]] == velPrimeRight[[1]], (A')x])^2
]
Assuming[{Subscript[(A'), y] > 0}, PostCollisionAmplitudeSqY =
   (Subscript[(A'), y] /. Solve[velPrimeLeft2[[2]] == velPrimeRight[[2]], Subscript[(A'), y]])^2]
Assuming[{Subscript[(A'), z] > 0}, PostCollisionAmplitudeSqZ =
   (Subscript[(A'), z] /. Solve[velPrimeLeft2[[3]] == velPrimeRight[[3]], Subscript[(A'), z]])^2]
```

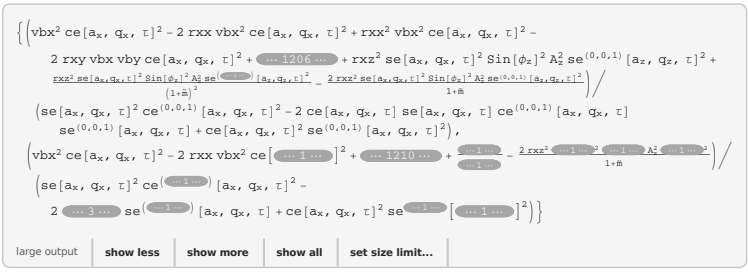

large output | show less | show more | show all | set size limit...

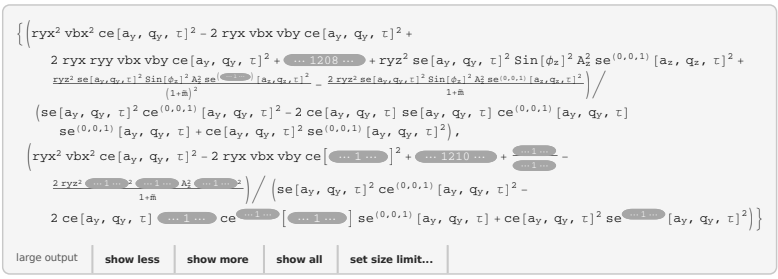

large output | show less | show more | show all | set size limit...

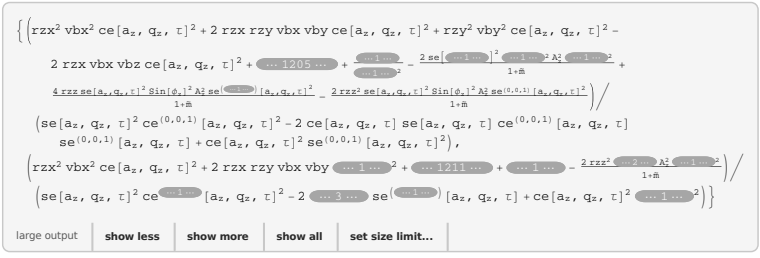

large output | show less | show more | show all | set size limit...

```
(*The amplitude squared can be converted to the energy by choosing a convention
 for the definition of the energy.A convenient choice is the secular energy,
for which Subscript[E,j]==Subscript[m,i]/2 Ω^2/4 Subscript[c0,j]^2 Subscript[β,j]^2
  Subscript[A,j]^2. Redefining the amplitudeToEnergyRule allows for alternate
  definitions of the energy.This is in SI units due to the factor of Ω^2/4,
and so at the same time we must convert the velocity of the buffer gas to SI units.*)
amplitudeToEnergyRule =
 Aj → Sqrt[Subscript[En, j]] / (Ω Subscript[c0, j] Subscript[β, j] Sqrt[(Subscript[m, i] / 2 1 / 4)])
amplitudeToEnergySet = {(amplitudeToEnergyRule /. j → x),
   (amplitudeToEnergyRule /. j → y), (amplitudeToEnergyRule /. j → z)}

(*Making this substitution produces the analytical
 expressions for the change in energy during a collision.*)
EnPrimeX =
 (Subscript[En, x] / Subscript[A, x]^2 /. amplitudeToEnergySet)  PostCollisionAmplitudeSqX[[1]] /.
   {vbx → vbx * 2 / Ω, vby → vby * 2 / Ω, vbz → vbz * 2 / Ω} /. amplitudeToEnergySet
EnPrimeY = (Subscript[En, y] / Subscript[A, y]^2 /. amplitudeToEnergySet) PostCollisionAmplitudeSqY[[
      1]] /. {vbx → vbx * 2 / Ω, vby → vby * 2 / Ω, vbz → vbz * 2 / Ω} /. amplitudeToEnergySet
EnPrimeZ = (Subscript[En, z] / Subscript[A, z]^2 /. amplitudeToEnergySet) PostCollisionAmplitudeSqZ[[
      1]] /. {vbx → vbx * 2 / Ω, vby → vby * 2 / Ω, vbz → vbz * 2 / Ω} /. amplitudeToEnergySet
```

$$A_j \to \frac{2\sqrt{2}\ \sqrt{En_j}}{\Omega\, c0_j \sqrt{m_i}\ \beta_j}$$

$$\left\{A_x \to \frac{2\sqrt{2}\ \sqrt{En_x}}{\Omega\, c0_x \sqrt{m_i}\ \beta_x},\ A_y \to \frac{2\sqrt{2}\ \sqrt{En_y}}{\Omega\, c0_y \sqrt{m_i}\ \beta_y},\ A_z \to \frac{2\sqrt{2}\ \sqrt{En_z}}{\Omega\, c0_z \sqrt{m_i}\ \beta_z}\right\}$$

$$\Big(\Omega^2\, c0_x^2\, m_i\, \beta_x^2 \Big(\frac{4\, vbx^2\, ce[a_x,q_x,\tau]^2}{\Omega^2} - \frac{8\, rxx\, vbx^2\, ce[a_x,q_x,\tau]^2}{\Omega^2} + \frac{4\, rxx^2\, vbx^2\, ce[\langle\langle 1\rangle\rangle]^2}{\Omega^2} - \frac{\langle\langle 1\rangle\rangle}{\Omega^2} + \langle\langle 1206\rangle\rangle + \frac{8\, rxz^2\, \langle\langle 2\rangle\rangle\, En_x\, \langle\langle 1\rangle\rangle^2}{\Omega^2\, c0_z^2\, m_i\, \beta_z^2} + \frac{8\, rxz^2\, se[a_x,q_x,\tau]^2\, Sin[\phi_x]^2\, En_x\, se^{\langle\langle 1\rangle\rangle}[a_x,q_x,\tau]^2}{\Omega^2\,(1+\bar{m})^2\, c0_z^2\, m_i\, \beta_z^2} - \frac{16\, rxz^2\, se[a_x,q_x,\tau]^2\, Sin[\phi_x]^2\, En_x\, se^{(0,0,1)}[a_x,q_x,\tau]^2}{\Omega^2\,(1+\bar{m})\, c0_z^2\, m_i\, \beta_z^2}\Big)\Big) \Big/ \Big(8\,\big(se[a_x,q_x,\tau]^2\, ce^{(0,0,1)}[a_x,q_x,\tau] - 2\, ce[a_x,q_x,\tau]\, se[a_x,q_x,\tau]\, ce^{(0,0,1)}[a_x,q_x,\tau] \\ se^{(0,0,1)}[a_x,q_x,\tau] + ce[a_x,q_x,\tau]^2\, se^{(0,0,1)}[a_x,q_x,\tau]^2\big)\Big)$$

large output | show less | show more | show all | set size limit...

$$\Big(\Omega^2\, c0_y^2\, m_i\, \beta_y^2 \Big(\frac{4\, ryx^2\, vbx^2\, ce[a_y,q_y,\tau]^2}{\Omega^2} - \frac{8\, ryx\, vbx\, vby\, ce[a_y,q_y,\tau]^2}{\Omega^2} + \frac{8\, ryx\, ryy\, vbx\, vby\, ce[\langle\langle 1\rangle\rangle]^2}{\Omega^2} + \langle\langle 1208\rangle\rangle + \frac{8\,\langle\langle 4\rangle\rangle\,\langle\langle 1\rangle\rangle^2}{\Omega^2\, c0_z^2\, m_i\, \beta_z^2} + \frac{8\, ryz^2\, se[\langle\langle 1\rangle\rangle]^2\, \langle\langle 1\rangle\rangle^2\, En_y\, se^{\langle\langle 1\rangle\rangle}[a_y,q_y,\tau]^2}{\Omega^2\,(1+\bar{m})^2\, c0_z^2\, m_i\, \beta_z^2} - \frac{16\, ryz^2\, se[a_y,q_y,\tau]^2\, Sin[\phi_y]^2\, En_y\, se^{(0,0,1)}[a_y,q_y,\tau]^2}{\Omega^2\,(1+\bar{m})\, c0_z^2\, m_i\, \beta_z^2}\Big)\Big) \Big/ \Big(8\,\big(se[a_y,q_y,\tau]^2\, ce^{(0,0,1)}[a_y,q_y,\tau] - 2\, ce[a_y,q_y,\tau]\, se[a_y,q_y,\tau]\, ce^{(0,0,1)}[a_y,q_y,\tau] \\ se^{(0,0,1)}[a_y,q_y,\tau] + ce[a_y,q_y,\tau]^2\, se^{(0,0,1)}[a_y,q_y,\tau]^2\big)\Big)$$

large output | show less | show more | show all | set size limit...

$$\Big(\Omega^2\, c0_z^2\, m_i\, \beta_z^2 \Big(\frac{4\, rzx^2\, vbx^2\, ce[a_z,q_z,\tau]^2}{\Omega^2} + \frac{8\, rzx\, rzy\, vbx\, vby\, ce[a_z,q_z,\tau]^2}{\Omega^2} + \langle\langle 1211\rangle\rangle + \frac{32\, rzz\, se[\langle\langle 1\rangle\rangle]^2\, \langle\langle 1\rangle\rangle^2\, En_z\, se^{\langle\langle 1\rangle\rangle}[a_z,q_z,\tau]^2}{\Omega^2\,(1+\bar{m})\, c0_z^2\, m_i\, \beta_z^2} - \frac{16\, rzz^2\, se[a_z,q_z,\tau]^2\, Sin[\phi_z]^2\, En_z\, se^{(0,0,1)}[a_z,q_z,\tau]^2}{\Omega^2\,(1+\bar{m})\, c0_z^2\, m_i\, \beta_z^2}\Big)\Big) \Big/ \Big(8\,\big(se[a_z,q_z,\tau]^2\, ce^{(0,0,1)}[a_z,q_z,\tau] - 2\, ce[a_z,q_z,\tau]\, se[a_z,q_z,\tau]\, ce^{(0,0,1)}[a_z,q_z,\tau] \\ se^{(0,0,1)}[a_z,q_z,\tau] + ce[a_z,q_z,\tau]^2\, se^{(0,0,1)}[a_z,q_z,\tau]^2\big)\Big)$$

large output | show less | show more | show all | set size limit...

```
(*Next we average over the collision parameters,
     i.e. integrating over their distribution function. The trick here is to use
       Collect[] and a dummy function Lock to stop Mathematica from trying to over-
      simplify the results and leave them in a form which is more amenable to further averaging.
        The assumptions here are that ϕx,ϕy,ϕz are uniformly distributed in [0,2Pi),
    that the buffer gas velocity follows a thermal distribution with a fixed
     temperature for each axis, and the random rotation is isotropic with
     the three parameters (x1,x2,x3) uniformly distributed in [0,1). This
  section of code defines the collection and integration routine for these.

)
AverageOver2Pi[expr_, var_] :=
 Integrate[Collect[expr, {Cos[var], Sin[var]}, Lock] / (2 Pi), {var, 0, 2 Pi}] /. Lock[x_] :> x
AverageOverOneTrig[expr_, var_] :=
 Integrate[Collect[expr, {Cos[2 Pi var], Sin[2 Pi var]}, Lock] , {var, 0, 1}] /. Lock[x_] :> x
AverageOverThermalVelDist[expr_, var_] := Assuming[{kb > 0, Tb > 0, mb > 0},
   Integrate[ (Collect[expr, var, Lock] Sqrt[mb / (2 Pi kb Tb)]  Exp[-mb var^2 / (2 kb Tb)] ),
    {var, -Infinity, Infinity}]] /. Lock[x_] :> x
(*This function then applies these for ϕx,ϕy,ϕz,x1,x2,x3, vbx,vby,vbz *)

AverageOverCollision[expr_] := (
  ExprPhaseAnglesAveraged =  AverageOver2Pi[
    AverageOver2Pi[AverageOver2Pi[expr, Subscript[ϕ, x]],   Subscript[ϕ, y]], Subscript[ϕ, z]] ;
ExprPhaseAnglesRotationAveraged = Integrate[ Collect[
      AverageOverOneTrig[  AverageOverOneTrig[ExprPhaseAnglesAveraged /. replaceMatrixTrig, x1],
       x2], x3,   Lock], {x3, 0, 1}] /. Lock[x_] :> x;
AverageOverThermalVelDist[ AverageOverThermalVelDist[AverageOverThermalVelDist[
      ExprPhaseAnglesRotationAveraged, vbx], vby], vbz] /. Subscript[m, b] -> m̃ Subscript[m, i]


 )

 (*First, we apply the averaging procedure to the post-
  collision energies. This may take a few minutes, especially on slower computers.*)
EnPrimeXPhaseAnglesRotationThermalAveraged = AverageOverCollision[EnPrimeX];
EnPrimeYPhaseAnglesRotationThermalAveraged = AverageOverCollision[EnPrimeY];
EnPrimeZPhaseAnglesRotationThermalAveraged = AverageOverCollision[EnPrimeZ];
```

```
(*The integrals over tau can't be performed analytically in closed form for the exact
 Mathieu functions, but these expressions can be cleaned up a bit further. First,
note that the Wronskian Wj =ce se' - ce' se is present in most of the denominators,
and is a constant.   Then, Collect[] is used to factor out tau,
which conveniently separates the post-collision energy out into components proportional to Ej,
Tb, and the forced motion. *)
makeWronskiX =
  ce[Subscript[a, x], Subscript[q, x], τ] D[se[Subscript[a, x], Subscript[q, x], τ], τ] → Subscript[W,
     x] + se[Subscript[a, x], Subscript[q, x], τ] D[ce[Subscript[a, x], Subscript[q, x], τ], τ];
makeWronskiY = makeWronskiX /. x → y;
makeWronskiZ = makeWronskiX /. x → z;
gatherTauTerms[input_] :=
 Collect[Collect[Distribute[tauIntegral[input]] //. tauIntegral[a_ b_] :> a tauIntegral[b] /;
       FreeQ[a, τ] && ! NumericQ[a] /. tauIntegral[a_] :> a /; FreeQ[a, τ], _tauIntegral, prefactor],
   _prefactor] //. tauIntegral[a_] + tauIntegral[b_] :> tauIntegral[a + b]

EnPrimeXAveraged = (EnPrimeXPhaseAnglesRotationThermalAveraged // Expand) /.
   Power[expr_, n_] :> Power[expr /. makeWronskiX , n] /; n < 0 ;
EnPrimeXAveraged2 = (gatherTauTerms[EnPrimeXAveraged] // FullSimplify) /. makeWronskiX /.
    tauIntegral[expr_] :> expr /; FreeQ[expr, τ] /. prefactor[expr_] :> expr /.
  tauIntegral[a_ b_] :> a tauIntegral[b] /; NumericQ[a]

EnPrimeYAveraged = (EnPrimeYPhaseAnglesRotationThermalAveraged // Expand) /.
   Power[expr_, n_] :> Power[expr /. makeWronskiY, n] /; n < 0;
EnPrimeYAveraged2 = (gatherTauTerms[EnPrimeYAveraged] // FullSimplify) /. makeWronskiY /.
    tauIntegral[expr_] :> expr /; FreeQ[expr, τ] /. prefactor[expr_] :> expr /.
  tauIntegral[a_ b_] :> a tauIntegral[b] /; NumericQ[a]

EnPrimeZAveraged = (EnPrimeZPhaseAnglesRotationThermalAveraged // Expand) /.
   Power[expr_, n_] :> Power[expr /. makeWronskiZ, n] /; n < 0;
EnPrimeZAveraged2 = (gatherTauTerms[EnPrimeZAveraged] // FullSimplify) /. makeWronskiZ /.
    tauIntegral[expr_] :> expr /; FreeQ[expr, τ] /. prefactor[expr_] :> expr /.
  tauIntegral[a_ b_] :> a tauIntegral[b] /; NumericQ[a]
```

$$\frac{En_x}{1+\tilde{m}} + \frac{1}{(1+\tilde{m})^2 W_x^2}\tilde{m}\, c0_x^2 k_b T_b \beta_x^2 \text{tauIntegral}\left[ce[a_x, q_x, \tau]^2 + se[a_x, q_x, \tau]^2\right] +$$
$$\frac{1}{24(1+\tilde{m})^2 W_x^2}\Omega^2 \tilde{m}^2 c0_x^2 m_i \beta_x^2 \text{tauIntegral}\Big[$$
$$\left(ce[a_x, q_x, \tau]^2 + se[a_x, q_x, \tau]^2\right)\left(4\, rf_x^{(0,1)}[g_x, \tau]^2 + rf_y^{(0,1)}[g_y, \tau]^2 + rf_z^{(0,1)}[g_z, \tau]^2\right)\Big] + \frac{1}{3(1+\tilde{m})^2 W_x^2}$$
$$2\tilde{m}^2 En_x \text{tauIntegral}\left[\left(ce[a_x, q_x, \tau]^2 + se[a_x, q_x, \tau]^2\right)\left(ce^{(0,0,1)}[a_x, q_x, \tau]^2 + se^{(0,0,1)}[a_x, q_x, \tau]^2\right)\right] +$$
$$\left(\tilde{m}^2 c0_x^2 En_y \beta_x^2 \text{tauIntegral}\left[\left(ce[a_x, q_x, \tau]^2 + se[a_x, q_x, \tau]^2\right)\left(ce^{(0,0,1)}[a_y, q_y, \tau]^2 + se^{(0,0,1)}[a_y, q_y, \tau]^2\right)\right]\right)/$$
$$\left(6(1+\tilde{m})^2 c0_y^2 W_x^2 \beta_y^2\right) +$$
$$\left(\tilde{m}^2 c0_x^2 En_z \beta_x^2 \text{tauIntegral}\left[\left(ce[a_x, q_x, \tau]^2 + se[a_x, q_x, \tau]^2\right)\left(ce^{(0,0,1)}[a_z, q_z, \tau]^2 + se^{(0,0,1)}[a_z, q_z, \tau]^2\right)\right]\right)/$$
$$\left(6(1+\tilde{m})^2 c0_z^2 W_x^2 \beta_z^2\right)$$

$$\frac{En_y}{1+\tilde{m}} + \frac{1}{(1+\tilde{m})^2 W_y^2}\tilde{m}\, c0_y^2 k_b T_b \beta_y^2 \text{tauIntegral}\left[ce[a_y, q_y, \tau]^2 + se[a_y, q_y, \tau]^2\right] + \frac{1}{24(1+\tilde{m})^2 W_y^2}\Omega^2 \tilde{m}^2 c0_y^2 m_i \beta_y^2$$
$$\text{tauIntegral}\left[\left(ce[a_y, q_y, \tau]^2 + se[a_y, q_y, \tau]^2\right)\left(rf_x^{(0,1)}[g_x, \tau]^2 + 4\, rf_y^{(0,1)}[g_y, \tau]^2 + rf_z^{(0,1)}[g_z, \tau]^2\right)\right] +$$
$$\left(\tilde{m}^2 c0_y^2 En_x \beta_y^2 \text{tauIntegral}\left[\left(ce[a_y, q_y, \tau]^2 + se[a_y, q_y, \tau]^2\right)\left(ce^{(0,0,1)}[a_x, q_x, \tau]^2 + se^{(0,0,1)}[a_x, q_x, \tau]^2\right)\right]\right)/$$
$$\left(6(1+\tilde{m})^2 c0_x^2 W_y^2 \beta_x^2\right) + \frac{1}{3(1+\tilde{m})^2 W_y^2}$$
$$2\tilde{m}^2 En_y \text{tauIntegral}\left[\left(ce[a_y, q_y, \tau]^2 + se[a_y, q_y, \tau]^2\right)\left(ce^{(0,0,1)}[a_y, q_y, \tau]^2 + se^{(0,0,1)}[a_y, q_y, \tau]^2\right)\right] +$$
$$\left(\tilde{m}^2 c0_y^2 En_z \beta_y^2 \text{tauIntegral}\left[\left(ce[a_y, q_y, \tau]^2 + se[a_y, q_y, \tau]^2\right)\left(ce^{(0,0,1)}[a_z, q_z, \tau]^2 + se^{(0,0,1)}[a_z, q_z, \tau]^2\right)\right]\right)/$$
$$\left(6(1+\tilde{m})^2 c0_z^2 W_y^2 \beta_z^2\right)$$

```
En_z/(1+m̃) + 1/(1+m̃)^2 W_z^2 m̃ c0_z^2 k_b T_b β_z^2 tauIntegral[ce[a_z, q_z, τ]^2 + se[a_z, q_z, τ]^2] + 1/(24 (1+m̃)^2 W_z^2) Ω^2 m̃^2 c0_z^2 m_i β_z^2
   tauIntegral[(ce[a_z, q_z, τ]^2 + se[a_z, q_z, τ]^2) (rf_x^(0,1)[g_x, τ]^2 + rf_y^(0,1)[g_y, τ]^2 + 4 rf_z^(0,1)[g_z, τ]^2)] +
 (m̃^2 c0_z^2 En_x β_z^2 tauIntegral[(ce[a_z, q_z, τ]^2 + se[a_z, q_z, τ]^2) (ce^(0,0,1)[a_x, q_x, τ]^2 + se^(0,0,1)[a_x, q_x, τ]^2)]) /
   (6 (1+m̃)^2 c0_x^2 W_x^2 β_x^2) +
 (m̃^2 c0_z^2 En_y β_z^2 tauIntegral[(ce[a_z, q_z, τ]^2 + se[a_z, q_z, τ]^2) (ce^(0,0,1)[a_y, q_y, τ]^2 + se^(0,0,1)[a_y, q_y, τ]^2)]) /
   (6 (1+m̃)^2 c0_y^2 W_z^2 β_y^2) + 1/(3 (1+m̃)^2 W_z^2)
  2 m̃^2 En_z tauIntegral[(ce[a_z, q_z, τ]^2 + se[a_z, q_z, τ]^2) (ce^(0,0,1)[a_z, q_z, τ]^2 + se^(0,0,1)[a_z, q_z, τ]^2)]

(*
The remaining tauIntegral functions can all be seen
 to be of the form tauIntegral[(ce[a_j,q_j,τ]^2+se[a_j,q_j,τ]^2) h(τ)] ,
and so when these expressions are averaged with respect to τ this leads to the m_j[h(τ)]
 operator defined in the text. Note that M_j[1] ( i.e., the terms proportional to T_b ) is
 equal to 1. The form given in Eqs.(21) through (24) can then be obtained by inspection
 and using the linearity of Subscript[m,j][h (τ)] with respect to h(τ) where necessary.*)


EnPrimeXAveraged2 /.
  tauIntegral[(ce[Subscript[a, x], Subscript[q, x], τ]^2 + se[Subscript[a, x], Subscript[q, x], τ]^2)
     expr_] :> m_x[expr] /. tauIntegral[
   (ce[Subscript[a, x], Subscript[q, x], τ]^2 + se[Subscript[a, x], Subscript[q, x], τ]^2) ] :> 1

EnPrimeYAveraged2 /.
  tauIntegral[(ce[Subscript[a, y], Subscript[q, y], τ]^2 + se[Subscript[a, y], Subscript[q, y], τ]^2)
     expr_] :> Subscript[m, y][expr] /. tauIntegral[
   (ce[Subscript[a, y], Subscript[q, y], τ]^2 + se[Subscript[a, y], Subscript[q, y], τ]^2)] :> 1

EnPrimeZAveraged2 /.
  tauIntegral[(ce[Subscript[a, z], Subscript[q, z], τ]^2 + se[Subscript[a, z], Subscript[q, z], τ]^2)
     expr_] :> Subscript[m, z][expr] /. tauIntegral[
   (ce[Subscript[a, z], Subscript[q, z], τ]^2 + se[Subscript[a, z], Subscript[q, z], τ]^2)] :> 1


En_x/(1+m̃) + m̃ c0_x^2 k_b T_b β_x^2/(1+m̃)^2 W_x^2 + 1/(24 (1+m̃)^2 W_x^2) Ω^2 m̃^2 c0_x^2 m_i β_x^2 m_x[4 rf_x^(0,1)[g_x, τ]^2 + rf_y^(0,1)[g_y, τ]^2 + rf_z^(0,1)[g_z, τ]^2] +
 1/(3 (1+m̃)^2 W_x^2) 2 m̃^2 En_x m_x[ce^(0,0,1)[a_x, q_x, τ]^2 + se^(0,0,1)[a_x, q_x, τ]^2] +
 (m̃^2 c0_x^2 En_y β_x^2 m_x[ce^(0,0,1)[a_y, q_y, τ]^2 + se^(0,0,1)[a_y, q_y, τ]^2]) / (6 (1+m̃)^2 c0_y^2 W_x^2 β_y^2) +
 (m̃^2 c0_x^2 En_z β_x^2 m_x[ce^(0,0,1)[a_z, q_z, τ]^2 + se^(0,0,1)[a_z, q_z, τ]^2]) / (6 (1+m̃)^2 c0_z^2 W_x^2 β_z^2)

En_y/(1+m̃) + m̃ c0_y^2 k_b T_b β_y^2/(1+m̃)^2 W_y^2 + 1/(24 (1+m̃)^2 W_y^2) Ω^2 m̃^2 c0_y^2 m_i β_y^2 m_y[rf_x^(0,1)[g_x, τ]^2 + 4 rf_y^(0,1)[g_y, τ]^2 + rf_z^(0,1)[g_z, τ]^2] +
 (m̃^2 c0_y^2 En_x β_y^2 m_y[ce^(0,0,1)[a_x, q_x, τ]^2 + se^(0,0,1)[a_x, q_x, τ]^2]) / (6 (1+m̃)^2 c0_x^2 W_y^2 β_x^2) +
 1/(3 (1+m̃)^2 W_y^2) 2 m̃^2 En_y m_y[ce^(0,0,1)[a_y, q_y, τ]^2 + se^(0,0,1)[a_y, q_y, τ]^2] +
 (m̃^2 c0_y^2 En_z β_y^2 m_y[ce^(0,0,1)[a_z, q_z, τ]^2 + se^(0,0,1)[a_z, q_z, τ]^2]) / (6 (1+m̃)^2 c0_z^2 W_y^2 β_z^2)

En_z/(1+m̃) + m̃ c0_z^2 k_b T_b β_z^2/(1+m̃)^2 W_z^2 + 1/(24 (1+m̃)^2 W_z^2) Ω^2 m̃^2 c0_z^2 m_i β_z^2 m_z[rf_x^(0,1)[g_x, τ]^2 + rf_y^(0,1)[g_y, τ]^2 + 4 rf_z^(0,1)[g_z, τ]^2] +
 (m̃^2 c0_z^2 En_x β_z^2 m_z[ce^(0,0,1)[a_x, q_x, τ]^2 + se^(0,0,1)[a_x, q_x, τ]^2]) / (6 (1+m̃)^2 c0_x^2 W_z^2 β_x^2) +
 (m̃^2 c0_z^2 En_y β_z^2 m_z[ce^(0,0,1)[a_y, q_y, τ]^2 + se^(0,0,1)[a_y, q_y, τ]^2]) / (6 (1+m̃)^2 c0_y^2 W_z^2 β_y^2) +
 1/(3 (1+m̃)^2 W_z^2) 2 m̃^2 En_z m_z[ce^(0,0,1)[a_z, q_z, τ]^2 + se^(0,0,1)[a_z, q_z, τ]^2]
```

```
(*For the purposes of actually evaluating these expressions, though,
it's more convenient to keep them in the tauIntegral format. The integrals over tau can be
 evaluated either analytically using the Fourier series expansions of the Mathieu functions,
or numerically by defining values for the Mathieu stability parameters and using the built-
 in Mathematica functions. The latter is more convenient for calculating the mean energies,
as it avoids the complex expressions for the coefficients. To demonstrate the former,
we set all the EMM to zero and leave only the thermal energy,
then replace the Mathieu functions with their expansions from m =-1 to m = 1,
i.e., the secular motion and first-order micromotion. *)
```

```
MathieuFourierApproxReplace = {
   ce[Subscript[a, j_], Subscript[q, j_], τ] :> Subscript[c0, j] Cos[Subscript[β, j] τ] +
     Subscript[c2, j] Cos[(Subscript[β, j] + 2) τ] + Subscript[cm2, j] Cos[(Subscript[β, j] - 2) τ],
   se[Subscript[a, j_], Subscript[q, j_], τ] :> Subscript[c0, j] Sin[Subscript[β, j] τ] +
     Subscript[c2, j] Sin[(Subscript[β, j] + 2) τ] + Subscript[cm2, j] Sin[(Subscript[β, j] - 2) τ],
   se^(0,0,1)[Subscript[a, j_], Subscript[q, j_], τ] :> Cos[τ (-2 + Subscript[β, j])] Subscript[cm2, j]
      (-2 + Subscript[β, j]) + Cos[τ Subscript[β, j]] Subscript[c0, j] Subscript[β, j] +
     Cos[τ (2 + Subscript[β, j])] Subscript[c2, j] (2 + Subscript[β, j]),
ce^(0,0,1)[Subscript[a, j_], Subscript[q, j_], τ] :> -Sin[τ (-2 + Subscript[β, j])] Subscript[cm2, j]
      (-2 + Subscript[β, j]) - Sin[τ Subscript[β, j]] Subscript[c0, j] Subscript[β, j] -
     Sin[τ (2 + Subscript[β, j])] Subscript[c2, j] (2 + Subscript[β, j])
  };


EnPrimeXAveraged2 /. rf_j_^(0,1)[Subscript[g, j_], τ]^2 :> 0 /. MathieuFourierApproxReplace /.
 tauIntegral[x_] :> Integrate[Expand[x] / (2 Pi), {τ, -Pi, Pi}]
EnPrimeYAveraged2 /. rf_j_^(0,1)[Subscript[g, j_], τ]^2 :> 0 /. MathieuFourierApproxReplace /.
 tauIntegral[x_] :> Integrate[Expand[x] / (2 Pi), {τ, -Pi, Pi}]
EnPrimeZAveraged2 /. rf_j_^(0,1)[Subscript[g, j_], τ]^2 :> 0 /. MathieuFourierApproxReplace /.
 tauIntegral[x_] :> Integrate[Expand[x] / (2 Pi), {τ, -Pi, Pi}]
```

$$\frac{En_x}{1+\tilde{m}} + \frac{\tilde{m}\, c0_x^2 \left(c0_x^2 + c2_x^2 + cm2_x^2\right) k_b\, T_b\, \beta_x^2}{\left(1+\tilde{m}\right)^2 W_x^2} + \frac{1}{3\left(1+\tilde{m}\right)^2 W_x^2} 2\,\tilde{m}^2\, En_x$$
$$\left(cm2_x^4 \left(-2+\beta_x\right)^2 + c0_x^4 \beta_x^2 + 4\, c2_x^2\, cm2_x^2 \beta_x^2 + c2_x^4 \left(2+\beta_x\right)^2 + 4\, c0_x^2 \left(cm2_x^2 \left(-1+\beta_x\right)^2 + c2_x\, cm2_x \beta_x^2 + c2_x^2 \left(1+\beta_x\right)^2\right)\right) +$$
$$\frac{1}{6\left(1+\tilde{m}\right)^2 c0_y^2 W_x^2 \beta_y^2} \tilde{m}^2\, c0_x^2\, En_y\, \beta_x^2 \left(2\, c2_x\, c2_y\, cm2_x\, cm2_y \left(-4+\beta_y^2\right) +$$
$$2\, c0_x\, c0_y \left(c2_x + cm2_x\right) \beta_y \left(cm2_y \left(-2+\beta_y\right) + c2_y \left(2+\beta_y\right)\right) + c0_x^2 \left(cm2_y^2 \left(-2+\beta_y\right)^2 + c0_y^2 \beta_y^2 + c2_y^2 \left(2+\beta_y\right)^2\right) +$$
$$c2_x^2 \left(cm2_y^2 \left(-2+\beta_y\right)^2 + c0_y^2 \beta_y^2 + c2_y^2 \left(2+\beta_y\right)^2\right) + cm2_x^2 \left(cm2_y^2 \left(-2+\beta_y\right)^2 + c0_y^2 \beta_y^2 + c2_y^2 \left(2+\beta_y\right)^2\right)) +$$
$$\frac{1}{6\left(1+\tilde{m}\right)^2 c0_z^2 W_x^2 \beta_z^2} \tilde{m}^2\, c0_x^2\, En_z\, \beta_x^2 \left(2\, c2_x\, c2_z\, cm2_x\, cm2_z \left(-4+\beta_z^2\right) +$$
$$2\, c0_x\, c0_z \left(c2_x + cm2_x\right) \beta_z \left(cm2_z \left(-2+\beta_z\right) + c2_z \left(2+\beta_z\right)\right) + c0_x^2 \left(cm2_z^2 \left(-2+\beta_z\right)^2 + c0_z^2 \beta_z^2 + c2_z^2 \left(2+\beta_z\right)^2\right) +$$
$$c2_x^2 \left(cm2_z^2 \left(-2+\beta_z\right)^2 + c0_z^2 \beta_z^2 + c2_z^2 \left(2+\beta_z\right)^2\right) + cm2_x^2 \left(cm2_z^2 \left(-2+\beta_z\right)^2 + c0_z^2 \beta_z^2 + c2_z^2 \left(2+\beta_z\right)^2\right))$$

$$\frac{En_y}{1+\tilde{m}} + \frac{\tilde{m}\, c0_y^2 \left(c0_y^2 + c2_y^2 + cm2_y^2\right) k_b\, T_b\, \beta_y^2}{\left(1+\tilde{m}\right)^2 W_y^2} +$$
$$\left(\tilde{m}^2\, c0_y^2\, En_x \left(c2_x^2 \left(c2_y^2 + cm2_y^2\right) \left(2+\beta_x\right)^2 + 2\, c2_x\, c2_y\, cm2_x\, cm2_y \left(-4+\beta_x^2\right) + \left(c2_y^2 + cm2_y^2\right) \left(cm2_x^2 \left(-2+\beta_x\right)^2 + c0_x^2 \beta_x^2\right) +\right.\right.$$
$$\left.\left.2\, c0_x\, c0_y \left(c2_y + cm2_y\right) \beta_x \left(cm2_x \left(-2+\beta_x\right) + c2_x \left(2+\beta_x\right)\right) + c0_y^2 \left(cm2_x^2 \left(-2+\beta_x\right)^2 + c0_x^2 \beta_x^2 + c2_x^2 \left(2+\beta_x\right)^2\right)\right) \beta_y^2\right) /$$
$$\left(6\left(1+\tilde{m}\right)^2 c0_x^2 W_y^2 \beta_x^2\right) + \frac{1}{3\left(1+\tilde{m}\right)^2 W_y^2} 2\,\tilde{m}^2\, En_y \left(cm2_y^4 \left(-2+\beta_y\right)^2 + c0_y^4 \beta_y^2 + 4\, c2_y^2\, cm2_y^2 \beta_y^2 +\right.$$
$$\left.c2_y^4 \left(2+\beta_y\right)^2 + 4\, c0_y^2 \left(cm2_y^2 \left(-1+\beta_y\right)^2 + c2_y\, cm2_y \beta_y^2 + c2_y^2 \left(1+\beta_y\right)^2\right)\right) +$$
$$\frac{1}{6\left(1+\tilde{m}\right)^2 c0_z^2 W_y^2 \beta_z^2} \tilde{m}^2\, c0_y^2\, En_z\, \beta_y^2 \left(2\, c2_y\, c2_z\, cm2_y\, cm2_z \left(-4+\beta_z^2\right) +$$
$$2\, c0_y\, c0_z \left(c2_y + cm2_y\right) \beta_z \left(cm2_z \left(-2+\beta_z\right) + c2_z \left(2+\beta_z\right)\right) + c0_y^2 \left(cm2_z^2 \left(-2+\beta_z\right)^2 + c0_z^2 \beta_z^2 + c2_z^2 \left(2+\beta_z\right)^2\right) +$$
$$c2_y^2 \left(cm2_z^2 \left(-2+\beta_z\right)^2 + c0_z^2 \beta_z^2 + c2_z^2 \left(2+\beta_z\right)^2\right) + cm2_y^2 \left(cm2_z^2 \left(-2+\beta_z\right)^2 + c0_z^2 \beta_z^2 + c2_z^2 \left(2+\beta_z\right)^2\right))$$

$$\frac{En_z}{1+\tilde{m}} + \frac{\tilde{m}\, c0_z^2 \left(c0_z^2 + c2_z^2 + cm2_z^2\right) k_b\, T_b\, \beta_z^2}{\left(1+\tilde{m}\right)^2 W_z^2} +$$
$$\left(\tilde{m}^2\, c0_z^2\, En_x \left(c2_x^2 \left(c2_z^2 + cm2_z^2\right) \left(2+\beta_x\right)^2 + 2\, c2_x\, c2_z\, cm2_x\, cm2_z \left(-4+\beta_x^2\right) + \left(c2_z^2 + cm2_z^2\right) \left(cm2_x^2 \left(-2+\beta_x\right)^2 + c0_x^2 \beta_x^2\right) +\right.\right.$$
$$\left.\left.2\, c0_x\, c0_z \left(c2_z + cm2_z\right) \beta_x \left(cm2_x \left(-2+\beta_x\right) + c2_x \left(2+\beta_x\right)\right) + c0_z^2 \left(cm2_x^2 \left(-2+\beta_x\right)^2 + c0_x^2 \beta_x^2 + c2_x^2 \left(2+\beta_x\right)^2\right)\right) \beta_z^2\right) /$$
$$\left(6\left(1+\tilde{m}\right)^2 c0_x^2 W_z^2 \beta_x^2\right) + \left(\tilde{m}^2\, c0_z^2\, En_y \left(c2_y^2 \left(c2_z^2 + cm2_z^2\right) \left(2+\beta_y\right)^2 + 2\, c2_y\, c2_z\, cm2_y\, cm2_z \left(-4+\beta_y^2\right) +\right.\right.$$
$$\left.\left.\left(c2_z^2 + cm2_z^2\right) \left(cm2_y^2 \left(-2+\beta_y\right)^2 + c0_y^2 \beta_y^2\right) + 2\, c0_y\, c0_z \left(c2_z + cm2_z\right) \beta_y \left(cm2_y \left(-2+\beta_y\right) + c2_y \left(2+\beta_y\right)\right) +\right.\right.$$
$$\left.\left.c0_z^2 \left(cm2_y^2 \left(-2+\beta_y\right)^2 + c0_y^2 \beta_y^2 + c2_y^2 \left(2+\beta_y\right)^2\right)\right) \beta_z^2\right) / \left(6\left(1+\tilde{m}\right)^2 c0_y^2 W_z^2 \beta_y^2\right) + \frac{1}{3\left(1+\tilde{m}\right)^2 W_z^2}$$
$$2\,\tilde{m}^2\, En_z \left(cm2_z^4 \left(-2+\beta_z\right)^2 + c0_z^4 \beta_z^2 + 4\, c2_z^2\, cm2_z^2 \beta_z^2 + c2_z^4 \left(2+\beta_z\right)^2 + 4\, c0_z^2 \left(cm2_z^2 \left(-1+\beta_z\right)^2 + c2_z\, cm2_z \beta_z^2 + c2_z^2 \left(1+\beta_z\right)^2\right)\right)$$

```
(*If values for qⱼ,aⱼ are known it's much more convenient to simply perform
 the integration over tau numerically. Here we again set the EMM to zero,
but as long as the functional form for this is known it can be used.*)
SetTrapParameters = {qx → 0.2, qy → -0.2, qz → 0, ax → -0.000625 / 2, ay → -0.000625 / 2, az → 0.000625};
ReplaceMathieu = { ce[a_, q_, t_] :↦ MathieuC[a, q, t], se[a_, q_, t_] :↦ MathieuS[a, q, t],
   ce^(0,0,1)[a_, q_, t_] :↦ MathieuCPrime[a, q, t], se^(0,0,1)[a_, q_, t_] :↦ MathieuSPrime[a, q, t]};
EnPrimeXAveraged2Numeric = EnPrimeXAveraged2 /. rfj_^(0,1)[Subscript[g, j_], τ]^2 :> 0 /.
    SetTrapParameters /. ReplaceMathieu /. tauIntegral[x_] :↦ NIntegrate[x / (2 Pi), {τ, -Pi, Pi}]
EnPrimeYAveraged2Numeric = EnPrimeYAveraged2 /.
rfj_^(0,1)[Subscript[g, j_], τ]^2 :> 0 /.
  SetTrapParameters /. ReplaceMathieu /.
 tauIntegral[x_] :> NIntegrate[x / (2 Pi), {τ, -Pi, Pi}]
EnPrimeZAveraged2Numeric = EnPrimeZAveraged2 /.
rfj_^(0,1)[Subscript[g, j_], τ]^2 :> 0 /.
  SetTrapParameters /. ReplaceMathieu /.
 tauIntegral[x_] :> NIntegrate[x / (2 Pi), {τ, -Pi, Pi}]
```

NIntegrate::izero :
Integral and error estimates are 0 on all integration subregions. Try increasing the value of the MinRecursion option. If value of integral may be 0, specify a finite value for the AccuracyGoal option. »

$$0. + \frac{En_x}{1+\tilde{m}} + \frac{0.0265018\,\tilde{m}^2\,En_x}{(1+\tilde{m})^2\,W_x^2} + \frac{1.\,\tilde{m}\,c0_x^2\,k_b\,T_b\,\beta_x^2}{(1+\tilde{m})^2\,W_x^2} + \frac{0.00672569\,\tilde{m}^2\,c0_y^2\,En_y\,\beta_x^2}{(1+\tilde{m})^2\,c0_y^2\,W_x^2\,\beta_y^2} + \frac{0.000104167\,\tilde{m}^2\,c0_z^2\,En_z\,\beta_x^2}{(1+\tilde{m})^2\,c0_z^2\,W_x^2\,\beta_z^2}$$

NIntegrate::izero :
Integral and error estimates are 0 on all integration subregions. Try increasing the value of the MinRecursion option. If value of integral may be 0, specify a finite value for the AccuracyGoal option. »

$$0. + \frac{En_y}{1+\tilde{m}} + \frac{0.0265018\,\tilde{m}^2\,En_y}{(1+\tilde{m})^2\,W_y^2} + \frac{1.\,\tilde{m}\,c0_y^2\,k_b\,T_b\,\beta_y^2}{(1+\tilde{m})^2\,W_y^2} + \frac{0.00672569\,\tilde{m}^2\,c0_y^2\,En_x\,\beta_y^2}{(1+\tilde{m})^2\,c0_x^2\,W_y^2\,\beta_x^2} + \frac{0.000104167\,\tilde{m}^2\,c0_y^2\,En_z\,\beta_y^2}{(1+\tilde{m})^2\,c0_z^2\,W_y^2\,\beta_z^2}$$

NIntegrate::izero :
Integral and error estimates are 0 on all integration subregions. Try increasing the value of the MinRecursion option. If value of integral may be 0, specify a finite value for the AccuracyGoal option. »

$$0. + \frac{En_z}{1+\tilde{m}} + \frac{0.000416667\,\tilde{m}^2\,En_z}{(1+\tilde{m})^2\,W_z^2} + \frac{1.\,\tilde{m}\,c0_z^2\,k_b\,T_b\,\beta_z^2}{(1+\tilde{m})^2\,W_z^2} + \frac{0.00668839\,\tilde{m}^2\,c0_z^2\,En_x\,\beta_z^2}{(1+\tilde{m})^2\,c0_x^2\,W_z^2\,\beta_x^2} + \frac{0.00668839\,\tilde{m}^2\,c0_z^2\,En_y\,\beta_z^2}{(1+\tilde{m})^2\,c0_y^2\,W_z^2\,\beta_y^2}$$

```
(*Finally, in the steady-state the mean energy is unchanged by a collision,
that is, <(E')ⱼ> == <Eⱼ> , and so the expressions found can be used to obtain the steady-
 state mean energies by averaging over Eⱼ. As these expressions are linear in the energy,
this doesn't require the distributions to be known,
and we can simply replace each energy component by its mean value.

  We could use the analytical expressions instead,
but here the numeric ones are used due to being less complicated.
*)

EnergyEqX = MeanEnₓ == EnPrimeXAveraged2Numeric /. {Enₓ → MeanEnₓ, Enᵧ → MeanEnᵧ, En_z → MeanEn_z}
EnergyEqY =
 Subscript[MeanEn, y] == EnPrimeYAveraged2Numeric /. {Subscript[En, x] → Subscript[MeanEn, x],
   Subscript[En, y] → Subscript[MeanEn, y], Subscript[En, z] → Subscript[MeanEn, z]}
EnergyEqZ = Subscript[MeanEn, z] == EnPrimeZAveraged2Numeric /.
  {Subscript[En, x] → Subscript[MeanEn, x],
   Subscript[En, y] → Subscript[MeanEn, y], Subscript[En, z] → Subscript[MeanEn, z]}
```

$$\text{MeanEn}_x == 0. + \frac{\text{MeanEn}_x}{1+\tilde{m}} + \frac{0.0265018\,\tilde{m}^2\,\text{MeanEn}_x}{(1+\tilde{m})^2\,W_x^2} + \frac{1.\,\tilde{m}\,c0_x^2\,k_b\,T_b\,\beta_x^2}{(1+\tilde{m})^2\,W_x^2} + \frac{0.00672569\,\tilde{m}^2\,c0_x^2\,\text{MeanEn}_y\,\beta_x^2}{(1+\tilde{m})^2\,c0_y^2\,W_x^2\,\beta_y^2} + \frac{0.000104167\,\tilde{m}^2\,c0_x^2\,\text{MeanEn}_z\,\beta_x^2}{(1+\tilde{m})^2\,c0_z^2\,W_x^2\,\beta_z^2}$$

$$\text{MeanEn}_y == 0. + \frac{\text{MeanEn}_y}{1+\tilde{m}} + \frac{0.0265018\,\tilde{m}^2\,\text{MeanEn}_y}{(1+\tilde{m})^2\,W_y^2} + \frac{1.\,\tilde{m}\,c0_y^2\,k_b\,T_b\,\beta_y^2}{(1+\tilde{m})^2\,W_y^2} + \frac{0.00672569\,\tilde{m}^2\,c0_y^2\,\text{MeanEn}_x\,\beta_y^2}{(1+\tilde{m})^2\,c0_x^2\,W_y^2\,\beta_x^2} + \frac{0.000104167\,\tilde{m}^2\,c0_y^2\,\text{MeanEn}_z\,\beta_y^2}{(1+\tilde{m})^2\,c0_z^2\,W_y^2\,\beta_z^2}$$

$$\text{MeanEn}_z == 0. + \frac{\text{MeanEn}_z}{1+\tilde{m}} + \frac{0.000416667\,\tilde{m}^2\,\text{MeanEn}_z}{(1+\tilde{m})^2\,W_z^2} + \frac{1.\,\tilde{m}\,c0_z^2\,k_b\,T_b\,\beta_z^2}{(1+\tilde{m})^2\,W_z^2} + \frac{0.00668839\,\tilde{m}^2\,c0_z^2\,\text{MeanEn}_x\,\beta_z^2}{(1+\tilde{m})^2\,c0_x^2\,W_z^2\,\beta_x^2} + \frac{0.00668839\,\tilde{m}^2\,c0_z^2\,\text{MeanEn}_y\,\beta_z^2}{(1+\tilde{m})^2\,c0_y^2\,W_z^2\,\beta_y^2}$$

```
(*This can then be solved directly for the steady-
 state mean energies. The Wronskians and Mathieu exponents are calculated explicitly,
and the approximation that c0 = 1 used. In general,
c0 should be calculated using the recurrence relation for the Mathieu Fourier coefficients..*)
```

```
Solve[({EnergyEqX, EnergyEqY, EnergyEqZ} /.
    {Subscript[β, j_] ↦ MathieuCharacteristicExponent[Subscript[a, j], Subscript[q, j]],
     c0_j ↦ 1, W_j ↦ MathieuC[a_j, q_j, 0] MathieuSPrime[a_j, q_j, 0]}) /.
  SetTrapParameters, {MeanEn_x, MeanEn_y, MeanEn_z}]
```

$$\left\{\left\{\text{MeanEn}_x \to -\left(\left(-1.\left(-\frac{0.175544\,\tilde{m}^4}{(1.+\tilde{m})^4}-\frac{0.35044\,\tilde{m}^2}{(1.+\tilde{m})^3}+\frac{0.35044\,\tilde{m}^2}{(1.+\tilde{m})^2}\right)\left(0.-\frac{5.55112\times10^{-17}\,\tilde{m}^3\,k_b\,T_b}{(1.+\tilde{m})^4}\right)+\left(\frac{0.178984\,\tilde{m}^4}{(1.+\tilde{m})^4}+\right.\right.\right.\right.$$
$$\left.\left.\left.\left.\frac{0.173699\,\tilde{m}^2}{(1.+\tilde{m})^3}-\frac{0.173699\,\tilde{m}^2}{(1.+\tilde{m})^2}\right)\left(0.-\frac{0.521096\,\tilde{m}^3\,k_b\,T_b}{(1.+\tilde{m})^4}-\frac{1.04219\,\tilde{m}\,k_b\,T_b}{(1.+\tilde{m})^3}+\frac{1.04219\,\tilde{m}\,k_b\,T_b}{(1.+\tilde{m})^2}\right)\right)\Big/$$
$$\left(-\frac{0.185793\,\tilde{m}^8}{(1.+\tilde{m})^8}-\frac{0.609507\,\tilde{m}^6}{(1.+\tilde{m})^7}-\frac{0.59551\,\tilde{m}^4}{(1.+\tilde{m})^6}+\frac{0.609507\,\tilde{m}^6}{(1.+\tilde{m})^6}-\frac{0.173699\,\tilde{m}^2}{(1.+\tilde{m})^5}+\frac{1.19102\,\tilde{m}^4}{(1.+\tilde{m})^5}+\right.$$
$$\left.\frac{0.521096\,\tilde{m}^2}{(1.+\tilde{m})^4}-\frac{0.59551\,\tilde{m}^4}{(1.+\tilde{m})^4}-\frac{0.521096\,\tilde{m}^2}{(1.+\tilde{m})^3}+\frac{0.173699\,\tilde{m}^2}{(1.+\tilde{m})^2}\right)\Big),$$

$$\text{MeanEn}_y \to -\left(\left(1.44775\left(-1.05827\times10^{-28}\,k_b\,T_b-4.23309\times10^{-28}\,\tilde{m}\,k_b\,T_b+1.26993\times10^{-27}\,\tilde{m}^2\,k_b\,T_b+\right.\right.\right.$$
$$\left.\left.\left.2159.77\,\tilde{m}^3\,k_b\,T_b+948.437\,\tilde{m}^4\,k_b\,T_b-63.7232\,\tilde{m}^5\,k_b\,T_b+1.\,\tilde{m}^6\,k_b\,T_b\right)\right)\Big/\left(\left(-32.8616+1.\,\tilde{m}\right)\right.$$
$$\left.\left(1.45887\times10^{-14}+5.83549\times10^{-14}\,\tilde{m}-1.75065\times10^{-13}\,\tilde{m}^2+91.2984\,\tilde{m}^3-39.113\,\tilde{m}^4-31.7559\,\tilde{m}^5+1.\,\tilde{m}^6\right)\right)\Big),$$

$$\text{MeanEn}_z \to \left(0.0953433\left(3.01694\times10^{-11}\,k_b\,T_b+1.1976\times10^{-10}\,\tilde{m}\,k_b\,T_b-3.65705\times10^{-10}\,\tilde{m}^2\,k_b\,T_b-\right.\right.$$
$$\left.\left.31467.4\,\tilde{m}^4\,k_b\,T_b+2995.03\,\tilde{m}^5\,k_b\,T_b-94.8628\,\tilde{m}^6\,k_b\,T_b+1.\,\tilde{m}^7\,k_b\,T_b\right)\right)\Big/\left(\tilde{m}\left(-32.8616+1.\,\tilde{m}\right)\right.$$
$$\left.\left.\left(1.45887\times10^{-14}+5.83549\times10^{-14}\,\tilde{m}-1.75065\times10^{-13}\,\tilde{m}^2+91.2984\,\tilde{m}^3-39.113\,\tilde{m}^4-31.7559\,\tilde{m}^5+1.\,\tilde{m}^6\right)\right)\right\}\Big\}$$

$$\langle \eta_1 \rangle =$$

$$-\int\int\int \frac{1}{\left(1+\tilde{m}\right)^2 k_B T_b} f_\tau[\tau]\, f_{\Theta_p}[\Theta_p]\, f_{\phi_p}[\phi_p] \left(\frac{1}{4\, c0_x^2\, W_x^2\, \omega_x^2} \cos[\phi_p]^4\, \tilde{m}^2 \sin[\Theta_p]^4\, \omega_{x,b}^2 \left(se[a_x, q_x, \tau]\, ce^{(0,0,1)}[a_x, q_x, \tau] - ce[a_x, q_x, \tau]\, se^{(0,0,1)}[a_x, q_x, \tau] \right) \left(\left(\cos[2\,\tau\,\beta_x]\, se[a_x, q_x, \tau] - ce[a_x, q_x, \tau] \sin[2\,\tau\,\beta_x] \right) ce^{(0,0,1)}[a_x, q_x, \tau] + \left(ce[a_x, q_x, \tau] \cos[2\,\tau\,\beta_x] + se[a_x, q_x, \tau] \sin[2\,\tau\,\beta_x] \right) se^{(0,0,1)}[a_x, q_x, \tau] \right) + \frac{1}{12\, c0_x^2\, W_x^2\, \omega_x^2} \cos[\phi_p]^4\, \tilde{m}^3 \sin[\Theta_p]^4\, \omega_{x,b}^2 \left(\left(\cos[2\,\tau\,\beta_x] \left(-2\, ce[a_x, q_x, \tau]^2 + se[a_x, q_x, \tau]^2 \right) - 3\, ce[a_x, q_x, \tau]\, se[a_x, q_x, \tau] \sin[2\,\tau\,\beta_x] \right) ce^{(0,0,1)}[a_x, q_x, \tau]^2 - \left(ce[a_x, q_x, \tau]^2 + se[a_x, q_x, \tau]^2 \right) \sin[2\,\tau\,\beta_x]\, ce^{(0,0,1)}[a_x, q_x, \tau]\, se^{(0,0,1)}[a_x, q_x, \tau] - \left(\cos[2\,\tau\,\beta_x] \left(ce[a_x, q_x, \tau]^2 - 2\, se[a_x, q_x, \tau]^2 \right) + 3\, ce[a_x, q_x, \tau]\, se[a_x, q_x, \tau] \sin[2\,\tau\,\beta_x] \right) se^{(0,0,1)}[a_x, q_x, \tau]^2 \right) - \frac{1}{24\, c0_x^4\, W_x^2\, \beta_x^2\, \omega_x^2} \cos[\phi_p]^4\, \tilde{m}^3 \left(ce[a_y, q_y, \tau]^2 + se[a_y, q_y, \tau]^2 \right) \sin[\Theta_p]^4\, c0_y^2\, \beta_y^2\, \omega_{x,b}^2 \sin[\Theta_p]^4\, c0_x^2\, \beta_x^2\, \omega_{x,b}^2 \left(2 \sin[2\,\tau\,\beta_x]\, ce^{(0,0,1)}[a_x, q_x, \tau]\, se^{(0,0,1)}[a_x, q_x, \tau] + \cos[2\,\tau\,\beta_x] \left(ce^{(0,0,1)}[a_x, q_x, \tau]^2 - se^{(0,0,1)}[a_x, q_x, \tau]^2 \right) \right) + \frac{1}{4\, c0_y^2\, W_y^2\, \omega_y^2} \tilde{m}^2 \sin[\Theta_p]^4 \sin[\phi_p]^4\, \omega_{y,b}^2 \left(se[a_y, q_y, \tau]\, ce^{(0,0,1)}[a_y, q_y, \tau] - ce[a_y, q_y, \tau]\, se^{(0,0,1)}[a_y, q_y, \tau] \right) \left(\left(\cos[2\,\tau\,\beta_y]\, se[a_y, q_y, \tau] - ce[a_y, q_y, \tau] \sin[2\,\tau\,\beta_y] \right) ce^{(0,0,1)}[a_y, q_y, \tau] + \left(ce[a_y, q_y, \tau] \cos[2\,\tau\,\beta_y] + se[a_y, q_y, \tau] \sin[2\,\tau\,\beta_y] \right) se^{(0,0,1)}[a_y, q_y, \tau] \right) + \frac{1}{12\, c0_y^2\, W_y^2\, \omega_y^2} \tilde{m}^3 \sin[\Theta_p]^4 \sin[\phi_p]^4\, \omega_{y,b}^2 \left(\left(\cos[2\,\tau\,\beta_y] \left(-2\, ce[a_y, q_y, \tau]^2 + se[a_y, q_y, \tau]^2 \right) - 3\, ce[a_y, q_y, \tau]\, se[a_y, q_y, \tau] \sin[2\,\tau\,\beta_y] \right) ce^{(0,0,1)}[a_y, q_y, \tau]^2 - \left(ce[a_y, q_y, \tau]^2 + se[a_y, q_y, \tau]^2 \right) \sin[2\,\tau\,\beta_y]\, ce^{(0,0,1)}[a_y, q_y, \tau]\, se^{(0,0,1)}[a_y, q_y, \tau] - \left(\cos[2\,\tau\,\beta_y] \left(ce[a_y, q_y, \tau]^2 - 2\, se[a_y, q_y, \tau]^2 \right) + 3\, ce[a_y, q_y, \tau]\, se[a_y, q_y, \tau] \sin[2\,\tau\,\beta_y] \right) se^{(0,0,1)}[a_y, q_y, \tau]^2 \right) - \frac{1}{24\, c0_y^4\, W_x^2\, \beta_y^2\, \omega_x^2} \tilde{m}^3 \left(ce[a_x, q_x, \tau]^2 + se[a_x, q_x, \tau]^2 \right) \sin[\Theta_p]^4 \sin[\phi_p]^4\, c0_x^2\, \beta_x^2\, \omega_{y,b}^2 \left(2 \sin[2\,\tau\,\beta_y]\, ce^{(0,0,1)}[a_y, q_y, \tau]\, se^{(0,0,1)}[a_y, q_y, \tau] + \cos[2\,\tau\,\beta_y] \left(ce^{(0,0,1)}[a_y, q_y, \tau]^2 - se^{(0,0,1)}[a_y, q_y, \tau]^2 \right) \right) - \frac{1}{24\, c0_y^4\, W_z^2\, \beta_y^2\, \omega_y^2} \tilde{m}^3 \left(ce[a_z, q_z, \tau]^2 + se[a_z, q_z, \tau]^2 \right) \sin[\Theta_p]^4 \sin[\phi_p]^4\, c0_z^2\, \beta_z^2\, \omega_{y,b}^2 \left(2 \sin[2\,\tau\,\beta_y]\, ce^{(0,0,1)}[a_y, q_y, \tau]\, se^{(0,0,1)}[a_y, q_y, \tau] + \cos[2\,\tau\,\beta_y] \left(ce^{(0,0,1)}[a_y, q_y, \tau]^2 - se^{(0,0,1)}[a_y, q_y, \tau]^2 \right) \right) + \frac{1}{4\, c0_z^2\, W_z^2\, \omega_z^2} \cos[\Theta_p]^4\, \tilde{m}^2\, \omega_{z,b}^2 \left(se[a_z, q_z, \tau]\, ce^{(0,0,1)}[a_z, q_z, \tau] - ce[a_z, q_z, \tau]\, se^{(0,0,1)}[a_z, q_z, \tau] \right) \left(\left(\cos[2\,\tau\,\beta_z]\, se[a_z, q_z, \tau] - ce[a_z, q_z, \tau] \sin[2\,\tau\,\beta_z] \right) ce^{(0,0,1)}[a_z, q_z, \tau] + \left(ce[a_z, q_z, \tau] \cos[2\,\tau\,\beta_z] + se[a_z, q_z, \tau] \sin[2\,\tau\,\beta_z] \right) se^{(0,0,1)}[a_z, q_z, \tau] \right) + \frac{1}{12\, c0_z^2\, W_z^2\, \omega_z^2} \cos[\Theta_p]^4\, \tilde{m}^3\, \omega_{z,b}^2 \left(\left(\cos[2\,\tau\,\beta_z] \left(-2\, ce[a_z, q_z, \tau]^2 + se[a_z, q_z, \tau]^2 \right) - 3\, ce[a_z, q_z, \tau]\, se[a_z, q_z, \tau] \sin[2\,\tau\,\beta_z] \right) ce^{(0,0,1)}[a_z, q_z, \tau]^2 - \left(ce[a_z, q_z, \tau]^2 + se[a_z, q_z, \tau]^2 \right) \sin[2\,\tau\,\beta_z]\, ce^{(0,0,1)}[a_z, q_z, \tau]\, se^{(0,0,1)}[a_z, q_z, \tau] - \left(\cos[2\,\tau\,\beta_z] \left(ce[a_z, q_z, \tau]^2 - 2\, se[a_z, q_z, \tau]^2 \right) + 3\, ce[a_z, q_z, \tau]\, se[a_z, q_z, \tau] \sin[2\,\tau\,\beta_z] \right) se^{(0,0,1)}[a_z, q_z, \tau]^2 \right) - \frac{1}{24\, c0_z^4\, W_x^2\, \beta_z^2\, \omega_z^2} \cos[\Theta_p]^4\, \tilde{m}^3 \left(ce[a_x, q_x, \tau]^2 + se[a_x, q_x, \tau]^2 \right) c0_x^2\, \beta_x^2\, \omega_{z,b}^2 \left(2 \sin[2\,\tau\,\beta_z]\, ce^{(0,0,1)}[a_z, q_z, \tau]\, se^{(0,0,1)}[a_z, q_z, \tau] + \cos[2\,\tau\,\beta_z] \left(ce^{(0,0,1)}[a_z, q_z, \tau]^2 - se^{(0,0,1)}[a_z, q_z, \tau]^2 \right) \right) - \frac{1}{24\, c0_y^4\, W_y^2\, \beta_z^2\, \omega_z^2} \cos[\Theta_p]^4\, \tilde{m}^3 \left(ce[a_y, q_y, \tau]^2 + se[a_y, q_y, \tau]^2 \right) c0_y^2\, \beta_y^2\, \omega_{z,b}^2 \left(2 \sin[2\,\tau\,\beta_z]\, ce^{(0,0,1)}[a_z, q_z, \tau]\, se^{(0,0,1)}[a_z, q_z, \tau] + \cos[2\,\tau\,\beta_z] \left(ce^{(0,0,1)}[a_z, q_z, \tau]^2 - se^{(0,0,1)}[a_z, q_z, \tau]^2 \right) \right) \right) d\tau\, d\Theta_p\, d\phi_p$$

Chapter 7

Conclusions and outlook

The main goals of this thesis were to increase the degree of control with which ultracold hybrid ion-neutral systems may be manipulated, and to better understand the dynamics of trapped particles to allow for a more accurate interpretation of experimental results. To achieve the first goal, a miniaturised hybrid ion-neutral chip trap has been designed, combining elements from the surface electrode ion trap and magnetic atom trap to produce a device capable of co-trapping these two species. Compared to currently existing macroscopic devices, this enables a much more precise control of the location of the trapped particles and the shape of the trapping potentials, allowing for increased control of the collision energy by manipulating the overlap of the trapped particles. Unfortunately, it was not possible to verify that the design for the hybrid chip proposed here would function experimentally due to the issues with assembling the vacuum chamber. In particular, the deposition of a layer of epoxy of thickness less than 0.5 mm while producing a reliable vaccum seal remains unsolved. One possible solution would be to redesign the chip to incorporate a groove for the cuvette to rest in, such that any excess epoxy accumulates in this trench. Alternatively, the chip could be mounted in a large vacuum chamber with a sufficient number of viewports to enable the optical access required for the mirror-MOT, and high-density electrical feedthroughs used to supply the required set of currents and voltages.

In this thesis, it has been shown that systems of trapped ions may exhibit deviations from thermal statistics due to their interactions with neutral particles under two different regimes: rare collisions with hot neutral particles,

and frequent collisions with ultracold neutrals. The former case arises due to the difference in time scales between the heating and recooling, and applies to any ensemble of confined particles, not only ions. All that is required is a system that is weakly coupled to a heat bath and subject to infrequent heating events. The latter case is due to the process of micromotion interruption and so requires that the ion is in a radiofrequency trap. This is less universal, but is relevant for the growing number of experiments involving ions in radiofrequency traps co-trapped with neutral atoms. In both cases, these results enable the improved comparison of experimental data to theoretical results by ensuring that, for example, reaction rates are calculated taking into account the non-thermal distributions obtained in these traps. The relevant distributions have been found analytically under a range of circumstances, improving on the previous empirical treatments and achieving the second goal: it is now possible to predict both the form and the parameters for these distributions, enabling a greater understanding of the dynamics of trapped ions and a better comparison of theory to experiment.

Although the model for ion-neutral sympathetic cooling discussed in Chapter 6 validates the previously empirical usage of Tsallis statistics and provides an analytical form for the distribution in the presence of a localised buffer gas, there are a number of improvements yet to be made. The accuracy of the model is limited by the conversion of the three components of the secular energy into the total energy and a pair of coordinates which are averaged over to produce a one-dimensional model. This produces an analytically tractable result, but serves only as an approximation, and moreover the distributions of these two coordinates are not known analytically and are presently treated using approximations. To fully describe this system, a three-dimensional treatment is required to obtain the joint distribution for the three components of the secular energy. There is also only a limited amount of experimental evidence with which to validate the analytical model developed here. The hybrid ion-atom chip trap developed in this thesis would be the ideal tool to enable these investigations, as the trapping potentials for both the ions and the neutral atoms can be flexibly tuned and the impact on the steady-state energy distribution determined. By simply filling the vapour cell with rubidium cooled via optical molasses in the absence of a trapping potential, the result is a uniform buffer gas. This is not stable for the Ca^+–Rb system, but allows for a study of the distribution described in Section 6.2.1, since the gain in energy due to micromotion fluctuations is sufficiently large that the thermal energy of the rubidium rapidly becomes irrelevant. Moreover, if a

charge-exchange process occurs, then the resulting Rb^+–Rb system is stable with respect to micromotion interruption, resulting in Tsallis statistics. If, instead, the rubidium is held in a magnetic or magneto-optical trap, then the Ca^+–Rb system is stable due to the localisation effect, leading to the distribution derived in Section 6.4.3. This distribution is dependent on the ratio of the trapping frequencies of the two traps, and so simply altering the current in a magnetic trap to change the aspect ratio of the neutral trap leads to a change in the energy distribution of a trapped ion. It would therefore be possible to validate the whole range of distributions derived in Chapter 6 using the hybrid chip.

Bibliography

[1] J. Anderson and J. Fenn, Phys. Fluids **8**, 780 (1965).

[2] H. L. Bethlem and G. Meijer, Int. Rev. Phys. Chem. **22**, 73 (2003).

[3] A. Trimeche, M. N. Bera, J.-P. Cromiéres, J. Robert, and N. Vanhaecke, Eur. Phys. J. D **65**, 263 (2011).

[4] S. D. Hogan, M. Motsch, and F. Merkt, Phys. Chem. Chem. Phys. **13**, 18705 (2011).

[5] D. J. Wineland and W. M. Itano, Phys. Rev. A **20**, 1521 (1979).

[6] H. J. Metcalf and P. van der Straten, *Laser Cooling and Trapping* (Springer, New York 1999).

[7] E. S. Shuman, J. F. Barry, and D. DeMille, Nature **467**, 820 (2010).

[8] I. Kozyryev, L. Baum, K. Matsuda, B. L. Augenbraun, L. Anderegg, A. P. Sedlack, and J. M. Doyle, Phys. Rev. Lett. **118**, 173201 (2017).

[9] R. Grimm, M. Weidemüller, and Y. B. Ovchinnikov, Optical dipole traps for neutral atoms, in *Advances in Atomic, Molecular, and Optical Physics* (Elsevier 2000), volume 42, pp. 95–170.

[10] T. Bergeman, G. Erez, and H. J. Metcalf, Phys. Rev. A **35**, 1535 (1987).

[11] F. G. Major, V. N. Gheorghe, and G. Werth, *Charged Particle Traps* (Springer, Berlin and Heidelberg 2005).

[12] R. E. March and J. F. Todd, *Quadrupole Ion Trap Mass Spectrometry* (John Wiley & Sons, Hoboken 2005), 2nd edition.

[13] R. Folman, P. Krüger, J. Schmiedmayer, J. Denschlag, and C. Henkel, Microscopic atom optics: From wires to an atom chip, in *Advances in Atomic, Molecular and Optical Physics* (Elsevier 2002), volume 48, pp. 263–356.

[14] S. Seidelin, J. Chiaverini, R. Reichle, J. J. Bollinger, D. Leibfried, J. Britton, J. H. Wesenberg, R. B. Blakestad, R. J. Epstein, D. B. Hume, W. M. Itano, J. D. Jost, C. Langer, R. Ozeri, N. Shiga, and D. J. Wineland, Phys. Rev. Lett. **96**, 253003 (2006).

[15] M. H. Steinecker, D. J. McCarron, Y. Zhu, and D. DeMille, ChemPhysChem **17**, 3664 (2016).

[16] H. Williams, S. Truppe, M. Hambach, L. Caldwell, N. Fitch, E. Hinds, B. Sauer, and M. Tarbutt, New. J. Phys. **19**, 113035 (2017).

[17] W. W. Smith, O. P. Makarov, and J. Lin, J. Mod. Opt. **52**, 2253 (2005).

[18] F. Hall, Cold ion-neutral reactions, Ph.D. thesis, University of Basel (2013).

[19] Z. Meir, T. Sikorsky, R. Ben-shlomi, N. Akerman, Y. Dallal, and R. Ozeri, Phys. Rev. Lett. **117**, 243401 (2016).

[20] B. Höltkemeier, P. Weckesser, H. López-Carrera, and M. Weidemüller, Phys. Rev. Lett. **116**, 233003 (2016).

[21] S. Dutta, R. Sawant, and S. Rangwala, Phys. Rev. Lett. **118**, 113401 (2017).

[22] E. J. Salumbides, J. C. J. Koelemeij, J. Komasa, K. Pachucki, K. S. E. Eikema, and W. Ubachs, Phys. Rev. D **87**, 112008 (2013).

[23] P. Jansen, H. L. Bethlem, and W. Ubachs, J. Chem. Phys. **140**, 010901 (2014).

[24] C. Surko and R. Greaves, Phys. Plasmas **11**, 2333 (2004).

[25] J. Danielson, D. Dubin, R. Greaves, and C. Surko, Rev. Mod. Phys. **87**, 247 (2015).

[26] J. I. Cirac and P. Zoller, Phys. Rev. Lett. **74**, 4091 (1995).

[27] P. Rabl, D. DeMille, J. M. Doyle, M. D. Lukin, R. J. Schoelkopf, and P. Zoller, Phys. Rev. Lett. **97**, 033003 (2006).

[28] M. Brouard and C. Vallance, eds., *Tutorials in Molecular Reaction Dynamics* (The Royal Society of Chemistry, Oxford 2012).

[29] M. T. Bell and T. P. Softley, Mol. Phys. **107**, 99 (2009).

[30] S. Haze, R. Saito, M. Fujinaga, and T. Mukaiyama, Phys. Rev. A **91**, 032709 (2015).

[31] T. Sikorsky, Z. Meir, R. Ben-shlomi, N. Akerman, and R. Ozeri, Nat. Commun. **9**, 920 (2018).

[32] A. Kilaj, H. Gao, D. Rösch, U. Rivero, J. Küpper, and S. Willitsch, Nat. Commun. **9** (2018).

[33] P. Puri, M. Mills, C. Schneider, I. Simbotin, J. A. Montgomery, R. Côté, A. G. Suits, and E. R. Hudson, Science **357**, 1370 (2017).

[34] D. Rösch, S. Willitsch, Y.-P. Chang, and J. Küpper, J. Chem. Phys. **140**, 124202 (2014).

[35] K. M. Jones, E. Tiesinga, P. D. Lett, and P. S. Julienne, Rev. Mod. Phys. **78**, 483 (2006).

[36] C. Chin, R. Grimm, P. Julienne, and E. Tiesinga, Rev. Mod. Phys. **82**, 1225 (2010).

[37] L. D. Carr, D. DeMille, R. V. Krems, and J. Ye, New J. Phys. **11**, 055049 (2009).

[38] C. J. Pethick and H. Smith, *Bose-Einstein Condensation in Dilute Gases* (Cambridge University Press 2001).

[39] J. D. Prestage, A. Williams, L. Maleki, M. J. Djomehri, and E. Harabetian, Phys. Rev. Lett. **66**, 2964 (1991).

[40] J. N. Tan, J. J. Bollinger, B. Jelenkovic, and D. J. Wineland, Phys. Rev. Lett. **75**, 4198 (1995).

[41] D. H. E. Dubin, Phys. Rev. E **53**, 5268 (1996).

[42] F. Diedrich, E. Peik, J. M. Chen, W. Quint, and H. Walther, Phys. Rev. Lett. **59**, 2931 (1987).

[43] M. Drewsen, C. Brodersen, L. Hornekær, J. S. Hangst, and J. P. Schiffer, Phys. Rev. Lett. **81**, 2878 (1998).

[44] M. Block, A. Drakoudis, H. Leuthner, P. Seibert, and G. Werth, J. Phys. B **33**, L375 (2000).

[45] F. H. J. Hall, P. Eberle, G. Hegi, M. Raoult, M. Aymar, O. Dulieu, and S. Willitsch, Mol. Phys. **111**, 2020 (2013).

[46] P. Bowe, L. Hornekaer, C. Brodersen, M. Drewsen, J. S. Hangst, and J. P. Schiffer, Phys. Rev. Lett. **82**, 2071 (1999).

[47] S. Haze, M. Sasakawa, R. Saito, R. Nakai, and T. Mukaiyama, Phys. Rev. Lett. **120**, 043401 (2018).

[48] Y. Moriwaki, M. Tachikawa, Y. Maeno, and T. Shimizu, Jpn. J. Appl. Phys. **31**, L1640 (1992).

[49] R. Côté, V. Kharchenko, and M. D. Lukin, Phys. Rev. Lett. **89**, 093001 (2002).

[50] C. Zipkes, S. Palzer, C. Sias, and M. Köhl, Nature **464**, 388 (2010).

[51] S. Schmid, A. Härter, and J. Hecker Denschlag, Phys. Rev. Lett. **105**, 133202 (2010).

[52] I. Rouse and S. Willitsch, Phys. Rev. A **92**, 053420 (2015).

[53] R. G. DeVoe, Phys. Rev. Lett. **102**, 063001 (2009).

[54] C. Zipkes, L. Ratschbacher, C. Sias, and M. Köhl, New J. Phys. **13**, 053020 (2011).

[55] D. Goodman, I. Sivarajah, J. Wells, F. Narducci, and W. Smith, Phys. Rev. A **86**, 033408 (2012).

[56] K. Chen, S. T. Sullivan, and E. R. Hudson, Phys. Rev. Lett. **112**, 143009 (2014).

[57] J. Biesheuvel, J. P. Karr, L. Hilico, K. S. E. Eikema, W. Ubachs, and J. C. J. Koelemeij, Nat. Commun. **7**, 10385 (2016).

[58] S. J. Schowalter, A. J. Dunning, K. Chen, P. Puri, C. Schneider, and E. R. Hudson, Nat. Commun. **7** (2016).

[59] I. Rouse and S. Willitsch, Phys. Rev. Lett. **118**, 143401 (2017).

[60] I. Rouse and S. Willitsch, Phys. Rev. A **97**, 042712 (2018).

[61] W. Phillips, Rev. Mod. Phys. **70**, 721 (1998).

[62] C. F. Foot, *Atomic Physics* (Oxford University Press, Oxford 2005).

[63] K. Riley, M. Hobson, and S. Bence, *Mathematical Methods For Physics and Engineering* (Cambridge University Press, Cambridge 2010), 3rd edition.

[64] J. Honerkamp, *Statistical Physics: An Advanced Approach with Applications* (Springer, Berlin 2002), 2nd edition.

[65] A. Steane and C. Foot, EPL **14**, 231 (1991).

[66] S. Stenholm, Rev. Mod. Phys. **58**, 699 (1986).

[67] W. M. Itano and D. J. Wineland, Phys. Rev. A **25**, 35 (1982).

[68] J. Reichel and V. Vuletić, eds., *Atom Chips* (Wiley-VCH, Weinheim 2011).

[69] S. Wildermuth, P. Krüger, C. Becker, M. Brajdic, S. Haupt, A. Kasper, R. Folman, and J. Schmiedmayer, Phys. Rev. A **69**, 030901 (2004).

[70] W. Neuhauser, M. Hohenstatt, P. Toschek, and H. Dehmelt, Phys. Rev. Lett. **41**, 233 (1978).

[71] D. J. Berkeland, J. D. Miller, J. C. Bergquist, W. M. Itano, and D. J. Wineland, J. Appl. Phys. **83**, 5025 (1998).

[72] J. Chiaverini, R. B. Blakestad, J. Britton, J. D. Jost, C. Langer, D. Leibfried, R. Ozeri, and D. J. Wineland, Quantum Inf. Comput. **5**, 419 (2005).

[73] ElectroMagneticWorks, Inc., EMS 2017 x64 SP 2.0 (2017).

[74] H. G. Dehmelt, Adv. At. Mol. Phys. **3**, 53 (1968).

[75] D. Gerlich, Adv. Chem. Phys. **82**, 1 (1992).

[76] M. Drewsen and A. Brøner, Phys. Rev. A **62**, 045401 (2000).

[77] F. W. J. Olver, D. W. Lozier, R. F. Boisvert, and C. W. Clark, eds., *NIST Handbook of Mathematical Functions* (Cambridge University Press, New York, NY 2010).

[78] J. E. Fulford, D. Nhu-Hoa, R. J. Hughes, R. E. March, R. F. Bonner, and G. J. Wong, J. Vac. Sci. Technol. **17**, 829 (1980).

[79] D. Douglas, A. Berdnikov, and N. Konenkov, Int. J. Mass Spectrom. **377**, 345 (2015).

[80] W. E. Boyce, R. C. DiPrima, and D. B. Meade, *Boyce's Elementary Differential Equations and Boundary Value Problems* (Wiley, NJ 2017), 11th edition.

[81] R. Blatt, P. Zoller, G. Holzmüller, and I. Siemers, Z. Phys. D **4**, 121 (1986).

[82] I. Siemers, R. Blatt, T. Sauter, and W. Neuhauser, Phys. Rev. A **38**, 5121 (1988).

[83] L. Hand and J. Finch, *Analytical Mechanics* (Cambridge University Press 2008).

[84] E. I. Dashevskaya, A. I. Maergoiz, J. Troe, I. Litvin, and E. E. Nikitin, J. Chem. Phys. **118**, 7313 (2003).

[85] B. Gao, Phys. Rev. A **78**, 012702 (2008).

[86] B. Gao, Phys. Rev. A **88**, 022701 (2013).

[87] C. B. Zhang, D. Offenberg, B. Roth, M. A. Wilson, and S. Schiller, Phys. Rev. A **76**, 012719 (2007).

[88] T. Baba and I. Waki, Appl. Phys. B **74**, 375 (2002).

[89] V. L. Ryjkov, X. Zhao, and H. A. Schuessler, Phys. Rev. A **71**, 033414 (2005).

[90] K. Chen, S. T. Sullivan, W. G. Rellergert, and E. R. Hudson, Phys. Rev. Lett. **110**, 173003 (2013).

[91] Y. S. Nam, E. B. Jones, and R. Blümel, Phys. Rev. A **90**, 013402 (2014).

[92] S. Willitsch, Int. Rev. Phys. Chem. **31**, 175 (2012).

[93] L. Hornekær, N. Kjærgaard, A. M. Thommesen, and M. Drewsen, Phys. Rev. Lett. **86**, 1994 (2001).

[94] C. G. Townsend, N. H. Edwards, C. J. Cooper, K. P. Zetie, C. J. Foot, A. M. Steane, P. Szriftgiser, H. Perrin, and J. Dalibard, Phys. Rev. A **52**, 1423 (1995).

[95] T. Guénault, *Statistical Physics* (Springer 2007), 2nd edition.

[96] C. Tsallis, J. Stat. Phys. **52**, 479 (1988).

[97] C. Tsallis, *Introduction to Nonextensive Statistical Mechanics* (Springer, New York 2009), 1st edition.

[98] C. Beck, Phys. Rev. Lett. **87**, 180601 (2001).

[99] C. Beck and E. Cohen, Physica A **322**, 267 (2003).

[100] F. Sattin, Eur. Phys. J. B **49**, 219 (2006).

[101] C. Beck, Contin. Mech. Thermodyn. **16**, 293 (2004).

[102] H. Touchette and C. Beck, Phys. Rev. E **71**, 016131 (2005).

[103] F. H. J. Hall, M. Aymar, N. Bouloufa-Maafa, O. Dulieu, and S. Willitsch, Phys. Rev. Lett. **107**, 243202 (2011).

[104] A. Härter and J. Hecker Denschlag, Contemp. Phys. **55**, 33 (2014).

[105] L. Deslauriers, S. Olmschenk, D. Stick, W. K. Hensinger, J. Sterk, and C. Monroe, Phys. Rev. Lett. **97**, 103007 (2006).

[106] S. Du, M. B. Squires, Y. Imai, L. Czaia, R. A. Saravanan, V. Bright, J. Reichel, T. Hänsch, and D. Z. Anderson, Phys. Rev. A **70**, 053606 (2004).

[107] P. Treutlein, Coherent manipulation of ultracold atoms on atom chips, Ph.D. thesis, Ludwig Maximilian University of Munich (2008).

[108] A. Mokhberi, Scalable microchip ion traps and guides for cold molecular ions, Ph.D. thesis, University of Basel (2016).

[109] M. G. House, Phys. Rev. A **78**, 033402 (2008).

[110] R. Schmied, New J. Phys. **12**, 023038 (2010).

[111] Z. K. Fisher, Shuttling of ions for characterization of a microfabricated ion trap, B.Sc thesis, Massachusetts Institute of Technology (2012).

[112] J. J. Abbott, Rev. Sci. Instrum. **86**, 054701 (2015).

[113] I. Grant and W. Phillips, *Electromagnetism*, Manchester Physics Series (Wiley 2010).

[114] W. Hänsel, J. Reichel, P. Hommelhoff, and T. Hänsch, Phys. Rev. Lett. **86**, 608 (2001).

[115] R. Kersevan and J.-L. Pons, J. Vac. Sci. Technol. **27**, 1017 (2009).

[116] R. Kersevan and M. Ady, Molflow+, http://cern.ch/molflow (2009).

[117] D. Harra, J. Vac. Sci. Technol. **13**, 471 (1976).

[118] R. Calder and G. Lewin, Br. J. Appl. Phys. **18**, 1459 (1967).

[119] S. Urabe, K. Hayasaka, M. Watanabe, H. Imajo, R. Ohmukai, and R. Hayashi, Appl. Phys. B **57**, 367 (1993).

[120] S. X. Wang, G. Hao Low, N. S. Lachenmyer, Y. Ge, P. F. Herskind, and I. L. Chuang, J.of Appl. Phys. **110**, 104901 (2011).

[121] D. A. Steck, Rubidium 87 d line data revision 2.1.5, https://steck.us/alkalidata/ (2015).

[122] W. C. Swope, H. C. Andersen, P. H. Berens, and K. R. Wilson, J. Chem. Phys **76**, 637 (1982).

[123] B. Leimkuhler and C. Matthews, *Molecular Dynamics With Deterministic and Stochastic Numerical Methods*, Interdisciplinary Applied Mathematics (Springer 2015).

[124] N. A. S. Database, http://physics.nist.gov/cgi-bin/AtData/main_asd, Version 2.0 (1999).

[125] P. Eberle, A. D. Dörfler, C. von Planta, K. Ravi, and S. Willitsch, ChemPhysChem **17**, 3769 (2016).

[126] M. Marciante, C. Champenois, A. Calisti, J. Pedregosa-Gutierrez, and M. Knoop, Phys. Rev. A **82**, 033406 (2010).

[127] P. W. Atkins, *Physical Chemistry* (Oxford University Press 1994), 5th edition.

[128] J. D. Jackson, *Classical Electrodynamics* (Wiley, New York 1994), 3rd edition.

[129] A. Safavi-Naini, P. Rabl, P. F. Weck, and H. R. Sadeghpour, Phys. Rev. A **84**, 023412 (2011).

[130] J. Sedlacek, A. Greene, J. Stuart, R. McConnell, C. Bruzewicz, J. Sage, and J. Chiaverini, Phys. Rev. A **97**, 020302 (2018).

[131] M. Gehm, K. O'Hara, T. Savard, and J. Thomas, Phys. Rev. A **58**, 3914 (1998).

[132] T. Matthey, T. Cickovski, S. S. Hampton, A. Ko, Q. Ma, M. Nyerges, T. Raeder, T. Slabach, and J. A. Izaguirre, ACM Trans. Math. Softw. **30**, 237 (2004).

[133] P. Eastman, M. S. Friedrichs, J. D. Chodera, R. J. Radmer, C. M. Bruns, J. P. Ku, K. A. Beauchamp, T. J. Lane, L.-P. Wang, D. Shukla, T. Tye, M. Houston, T. Stich, C. Klein, M. R. Shirts, and V. S. Pande, J. Chem. Theory Comput. **9**, 461 (2013).

[134] G. Gioumousis and D. P. Stevenson, J. Chem. Phys. **29**, 294 (1958).

[135] M. Germann, Dipole-Forbidden Vibrational Transitions in Molecular Ions, Ph.D. thesis, University of Basel (2016).

[136] A. Mokhberi and S. Willitsch, New J. Phys. **17**, 045008 (2015).

[137] I. Bloch, M. Greiner, O. Mandel, T. W. Hänsch, and T. Esslinger, Phys. Rev. A **64**, 021402 (2001).

[138] S. Pollock, Integration of Magneto Optical Traps in Atom Chips, Ph.D. thesis, Imperial College London (2010).

[139] B. Roth, A. Ostendorf, H. Wenz, and S. Schiller, J. Phys. B: At. Mol. Opt. Phys. **38**, 3673 (2005).

[140] K. Okada, M. Wada, T. Takayanagi, S. Ohtani, and H. A. Schuessler, Phys. Rev. A **81**, 013420 (2010).

[141] A. Mokhberi and S. Willitsch, Phys. Rev. A **90**, 023402 (2014).

[142] P. Douglas, S. Bergamini, and F. Renzoni, Phys. Rev. Lett. **96**, 110601 (2006).

[143] E. Daly and A. Porporato, Phys. Rev. E **81**, 061133 (2010).

[144] S. Willitsch, M. T. Bell, A. D. Gingell, S. R. Procter, and T. P. Softley, Phys. Rev. Lett. **100**, 043203 (2008).

[145] F. G. Major and H. G. Dehmelt, Phys. Rev. **170**, 91 (1968).

[146] J. Brey, J. Dufty, and A. Santos, J. Stat. Phys. **87**, 1051 (1997).

[147] D. B. Owen, Ann. Math. Statist. **27**, 1075 (1956).

[148] M. Cetina, A. T. Grier, and V. Vuletić, Phys. Rev. Lett. **109**, 253201 (2012).

[149] D. Buraczewski, E. Damek, and T. Mikosch, *Stochastic Models with Power-Law Tails: The Equation $X = AX + B$* (Springer 2016), 1st edition.

[150] T. J. Kozubowski and K. Podgórski, Int. Math. J **3**, 467 (2003).

[151] D. Sornette and R. Cont, J. Phys. I **7**, 431 (1997).

[152] S. Asmussen, J. L. Jensen, and L. Rojas-Nandayapa, Methodol. Comput. Apply. Probab. **18**, 441 (2016).

[153] P. Rabassa and C. Beck, Entropy **16**, 5523 (2014).

[154] D. G. Champernowne, Econ. J. **63**, 318 (1953).

[155] M. Mitzenmacher, Internet Math. **1**, 226 (2004).

[156] T. S. Biró and A. Jakovác, Phys. Rev. Lett. **94**, 132302 (2005).

[157] B. C. Arnold and R. A. Groeneveld, J. Am. Stat. Assoc. **75**, 173 (1980).

[158] J. Sancho, J. Math. Phys. **25**, 354 (1984).

[159] A. A. Dubkov, P. N. Makhov, and B. Spagnolo, Physica A **325**, 26 (2003).

[160] C. Vaca, K. Chen, E. Hudson, and A. J. Levine, arXiv preprint arXiv:1510.06465 (2015).

[161] R. Robinett, Am. J. Phys. **63**, 823 (1995).

[162] E. Hammerstein, Generalized hyperbolic distributions: theory and applications to CDO pricing, Ph.D. thesis, Universität Freiburg (2010).

[163] E. Gómez-Déniz, E. Calderín-Ojeda, and J. M. Sarabia, Commun. Stat. Theory Methods **42**, 919 (2013).

[164] B. Höltkemeier, P. Weckesser, H. López-Carrera, and M. Weidemüller, Phys. Rev. A **94**, 062703 (2016).

[165] J. Arvo, Graphics Gems III pp. 117–120 (1992).

[166] H. Früchting, J. Res. Nat. Stand. Sec. B **73**, 21 (1969).

[167] C. R. Shalizi, arXiv preprint math/0701854 (2007).

[168] E. P. White, B. J. Enquist, and J. L. Green, Ecology **89**, 905 (2008).

[169] A. Clauset, C. R. Shalizi, and M. E. Newman, SIAM Rev. **51**, 661 (2009).

[170] Wolfram Research, Inc., *Mathematica 10.2.0.0* (Wolfram Research, Inc., Champaign, Illinois 2015).

Appendix A

List of publications

- "Energy distributions of an ion in a radiofrequency trap immersed in a buffer gas under the influence of additional external forces", I. Rouse and S. Willitsch, *Physical Review A* **97** (2018).
- "Superstatistical energy distributions of an ion in an ultracold buffer gas", I. Rouse and S. Willitsch, *Physical Review Letters* **118** (2017).
- "Superstatistical velocity distributions of cold trapped ions in molecular dynamics simulations", I. Rouse and S. Willitsch, *Physical Review A* **92** (2015).